Gesellschaft für Anlagen-
und Reaktorsicherheit
(GRS) gGmbH

ATHLET-CD

Validation

GRS-P-4 / Vol. 3
Rev. 5

Gesellschaft für Anlagen-
und Reaktorsicherheit
(GRS) gGmbH

GRS-P-4 / Vol. 3
Rev. 5

Gesellschaft für Anlagen-
und Reaktorsicherheit
(GRS) gGmbH

ATHLET-CD 3.5

Validation

T. Hollands
A. Di Nora
C. Köllein
L. Lovasz
P. Pandazis
L. Tiborcz
A. Wielenberg

December 2025

AC²
ATHLET-CD

GRS-P-4 / Vol. 3
Rev. 5

Keywords

AC², ATHLET-CD, quality assurance, severe accidents, system code, validation, validation matrix

Abstract

This report describes the validation status of ATHLET-CD, which is the best-estimate severe accident extension of the system thermal-hydraulics code ATHLET. ATHLET-CD allows to simulate design extension conditions with core degradation, severe accidents with core melt, radioactive releases and their transport within the reactor pressure boundary and the behaviour of corium in the lower head as well as vessel failure. ATHLET-CD is part of the GRS system code package AC². This report is part of the overall documentation for the release AC² 2025.

This report starts with a brief overview of ATHLET-CD. Then, the general validation strategy for ATHLET is described, the validation matrices for ATHLET-CD are presented and the validation calculations on specific tests in these matrices are referenced. In addition, participations in International Standard Problems with ATHLET-CD are briefly summarized. In a separate chapter, the quality assurance procedures for performing validation for ATHLET-CD are explained in some detail. Thereafter, validation calculations on in total 9 tests and the TMI-2 accident for the current release ATHLET-CD 3.5.0 are presented and compared to experimental data and to ATHLET-CD 3.4.3 results.

Overall, ATHLET-CD 3.5.0 has been demonstrated to be validated for severe accident simulations in LWR reactors (PWR including WWER and BWR). ATHLET-CD 3.5.0 is also validated for severe accident analyses in the spent fuel pool of LWR reactors. No claims on the validation status (or applicability) of ATHLET-CD 3.5.0 for reactor designs with working fluids other than water are made.

Acknowledgements

The development and validation of ATHLET-CD and the associated documentation are funded by the German Federal Ministry for the Environment, Climate Action, Nature Conservation and Nuclear Safety (BMUKN) based on decisions of the German Bundestag.

Over the more than 40 years of continuous validation of ATHLET-CD and its predecessors, a very large number of people, both former GRS employees as well as external experts have contributed to the current version of ATHLET-CD. Here, we want a acknowledge the work of those experts who have made major contributions to the validation of ATHLET-CD: Henrique Austregesilo, Christine Bals, Josef Bestele, Walter Erdmann, Wolfgang Luther, Klaus Trambauer, B. M. Schmitz, Johann-Dietrich Schubert, Sebastian Weber.

Thanks are due also to Christoph Bratfisch, Christian Bratfisch, Udo Brockmeier, Martin Bruder, Michael Buck, Manfred Bürger, Tilman Drath, Florian Gremme, Klaus Dieter Hocke, Matthias Jobst, Ingo Kleinhietpaß, Marco K. Koch, P. Kruse, K. Müller, N. Pohl, Alfred Schatz, Polina Tusheva, Hermann Unger and Hermann-Josef Wagner.

Table of Contents

List of Figures

List of Tables

1 Overview of ATHLET-CD

The severe accident code **ATHLET-CD** in the code system AC^2 covers the phenomena related to core degradation in a **PWR, BWR** or **VVER** type reactor. Similar to other relevant code systems, ATHLET-CD also divides the core region radially into concentric rings, axially into different nodes /LOV 21a/.

In each ring at a given height, all fuel rods behave identically, and they are represented by a so-called hypothetical representative fuel rod. This summarizes the extensive properties of all fuel rods within the given ring. This assumption is necessary because in a typical reactor there are many thousands of fuel pins. Simulating each of these fuel rods would make the calculation prohibitively expensive.

ATHLET-CD /LOV 25/ consists of several modules, which are shown in Fig. 1.1. These interact between each other and with **ATHLET** /SCH 25/ during an ATHLET-CD simulation. In addition, full AC^2 simulations are possible by using the coupling interfaces to **COCOSYS** /ARN 23/ as shown below.

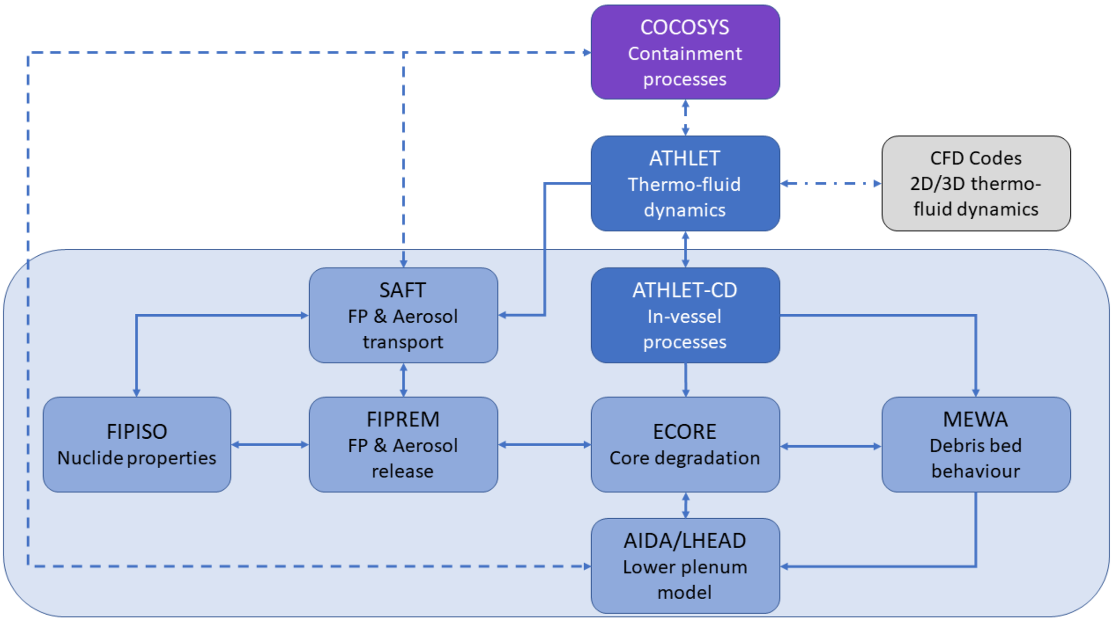

Fig. 1.1 Modular structure of ATHLET-CD

The module **ECORE** calculates the core heat-up, the oxidation effects and the core degradation phenomena. In particular, the implemented models consider the following phenomena:

- Mechanical fuel rod behaviour (ballooning),
- Oxidation of zirconium and boron carbide,
- Melting of metallic and ceramic components,
- Freezing,
- Re-melting and re-freezing,
- Formation and dissolution of blockages.

Heat balance equations are solved for the fuel (and for the absorber material), for the cladding and for the melt/crust, taking the following terms into account:

- Decay power generation in fuel, melt and crust
- Power of the oxidation of cladding, melt and crust
- Axial heat conduction of fuel and cladding
- Radial heat transfer between fuel, cladding, melt, crust and fluid
- Axial and radial heat transfer via thermal radiation
- Heat transferred via moving material

As the temperature rises due to insufficient cooling, five different mechanisms can lead to melting inside a fuel rod:

- Eutectic interaction between solid UO_2 and solid zircaloy
- Melting of the metallic zircaloy of the cladding
- Dissolution of the UO_2 pellets by liquid zircaloy
- Melting of the ZrO_2 layer of the cladding
- Melting of the UO_2 pellets

In the early phase of a core melt accident, the melting of the metallic zircaloy of the cladding and the dissolution of the UO_2 pellets caused by liquid zircaloy are particularly relevant. The interaction between solid UO_2 and solid zircaloy influences the dissolution of fuel pellets only slightly. In fact, the dissolution of UO_2 and ZrO_2 occurs during the melting and in the late phase of a core melt accident. Blockage formation is considered during the melting processes. The computer code limits the flow of coolant and melt if the free area for the flow is reduced due to material relocation.

For the simulation of debris beds a specific model, **MEWA**, is under development at IKE Stuttgart with its own thermal-hydraulic equation system, coupled to the ATHLET-thermo-fluid-dynamics on the outer boundaries of the debris bed. The transition of the simulation of the core zones from ECORE to MEWA depends on the degree of degradation in the zone.

The cladding oxidation model calculates the oxidation of zirconium and the associated hydrogen generation which is important to consider with increasing temperature of the core. The power generated by the oxidation is a substantial part of the total core heat. The oxidation is simulated only in the material zone adjacent to the oxidizing surface. If the material in this zone is completely oxidized the process is terminated, however the oxidation process continues after the melting point of Zr is reached. The oxidation rate is calculated by means of several empirical correlations based on a parabolic law, which is derived from the analytical solution of the diffusion equation. Besides the oxidation in a steam environment, an approach is formulated to consider also nitride formation (air ingress). The reaction rate is also expressed as an Arrhenius function. The parameters for the empirical correlations are determined on the basis of single effect tests performed at KIT.

The user has two options to define the fission/decay power of the reactor core. It is possible to define the power via a time dependent function or by using the **OREST/FIPISO** modules. These modules calculate the decay power and the fission product inventory after shutdown, using the user defined burn-up history and initial fissile material content of the core. The modules take 1296 isotopes separately into account using the appropriate property of each isotope (half time, decay power, etc.).

The module **FIPREM** is responsible for the fission product release from the fuel rods. Fission product release is calculated if the cladding fails. Cladding failure criteria can be a constant user-defined parameter, like the proportion of oxidized/not oxidized cladding material, or the user can use dedicated models, which constantly calculate the deformation of the cladding due to the heat up and oxidation. The release calculation is mainly based on the Antoine approach, where the release rate depends on the temperature of the fuel, system pressure and the partial pressure of the released material. For several relevant fission products that are sensitive to the oxidizing and reducing conditions the amount of available oxygen is also considered. The released fission product is calculated nodewise, adding the fission product to the fluid channel next to the fuel rods. The transport of these fission products and aerosols within the cooling circuit is calculated by the module **SAFT**.

The power due to the alpha and beta decay of the released fission products is added to the surrounding structures, while their gamma decay power leaves the system without any absorption. At the same time the core power is appropriately reduced to account for the released material.

The transport module **SAFT** has been derived from **SOPHAEROS** (ASTEC version 2.0). It computes the transport of fission products and aerosols in the reactor coolant system (RCS) through the gas flow to the containment, simulating the main vapour-phase and aerosol phenomena with the help of mechanistic and semi-empirical models. It considers five physical states: suspended vapour/aerosol, vapour condensed on structural surfaces, aerosol deposited on structural surfaces, and vapour sorbed on structural surfaces. The chemical modelling is based on the calculation of thermodynamic chemical equilibrium in each control volume while its method utilizes a transient approach based on the deviation from the equilibrium. The energy involved in chemical reactions as well as the carrier gas mass changes are neglected. The chemical speciation can change with temperature, carrier gas composition, and concentration of the different gaseous species. SAFT is also able to model branching, which enables the simulation to predict more realistically the FP and aerosol behaviour, particularly during plant simulations.

In ATHLET-CD, there are two modules available to model the relocated molten material behaviour in the lower head: the module **AIDA** and **LHEAD**.

AIDA is an integral simulation module, coupled via GCSM Library to ATHLET-CD (IOPT: 15). It is also possible to run AIDA stand-alone, without ATHLET-CD. In coupled mode, AIDA starts after the failure of the grid plate (PWR) or after the failure of the control rod guide tubes (BWR), triggered via GCSM signal. The relocation of the molten material from the core into the lower head is governed by ECORE under the sub-keyword MTLP-SIG. The relocation process is not modelled in detail, the molten material fills the lower head instantaneously at the beginning of the AIDA calculation. AIDA simulates:

- the thermal behaviour of the molten corium pool, including pool segregation,
- the crust formation between corium and wall,

- the heat transfer through the crust and RPV wall,
- external vessel cooling,
- the wall damage and failure.

The lower head wall consists of a hemispherical and a cylindrical part. The heat conduction through the wall is solved two-dimensionally with a finite difference method, hence a detailed nodalisation of the wall is necessary. The corium pool is calculated with simplified, zero-dimensional balance equations and additional empirical correlations are used to determinate the heat fluxes. Homogeneous or stratified (two-layer) pool configuration models are available. The distribution of the decay heat in the pool between the layers is defined via user-input. In coupled mode, the upper heat transfer of the corium pool is governed via GCSM signals from ATHLET. Also, the boundary conditions of the heat transfer through the RPV wall are defined per GCSM signal and the input data. The modelling of transient external vessel cooling is possible with predefined or calculated heat transfer coefficients, considering also boiling conditions. In coupled mode the material properties are given from ECORE, in stand-alone calculations they are defined via input data.

The damage and the failure of the RPV wall can be calculated via four different failure models. The AIDA module is equipped also with a wall-ablation model. In this case a wall failure is predicted with a simple failure criterion taking into account the pressure difference, the temperature, the remaining wall thickness and the mass of the corium as well as the mass of the vessel wall under the corium pool. Within an AC^2 simulation, AIDA can provide the transferred heat through the wall as well as the mass and energy data of corium after a vessel failure for the containment module COCOSYS, if it is also activated.

The model LHEAD offers an alternative to the late phase module AIDA. LHEAD is part of the module ECORE. In LHEAD it is possible to use a more detailed nodalisation of the lower head fluid domain and, thus, it allows a simplified modelling of the lower head structures and the phenomena in the lower plenum. Especially for the simulation of late phase accidents in BWR such detailed modelling is of interest in order to consider special structures like penetrations through the vessel like control rod guide tubes.

1.1 Code Handling and Code Coupling

ATHLET-CD is implemented as plug-in `core_degradation` in ATHLET and due to that the whole functionality of ATHLET and its input is valid for ATHLET-CD. ATHLET-CD provides also a restart capability like ATHLET. Additionally, ATHLET-CD can be executed serial and parallel, but in parallel runs only the ATHLET part is able to be parallelised. The whole range of ATHLET auxiliary programs can also be applied for ATHLET-CD.

ATHLET is also closely linked with the GRS computer programs **SUSA** and **MCDET**. Both enable uncertainty and sensitivity analyses of ATHLET simulation results

ATHLET-CD is part of the **AC² software package**, which comprises the GRS codes ATHLET, ATHLET-CD and COCOSYS, complemented by the interactive simulator software ATLAS (Fig. 1.2).

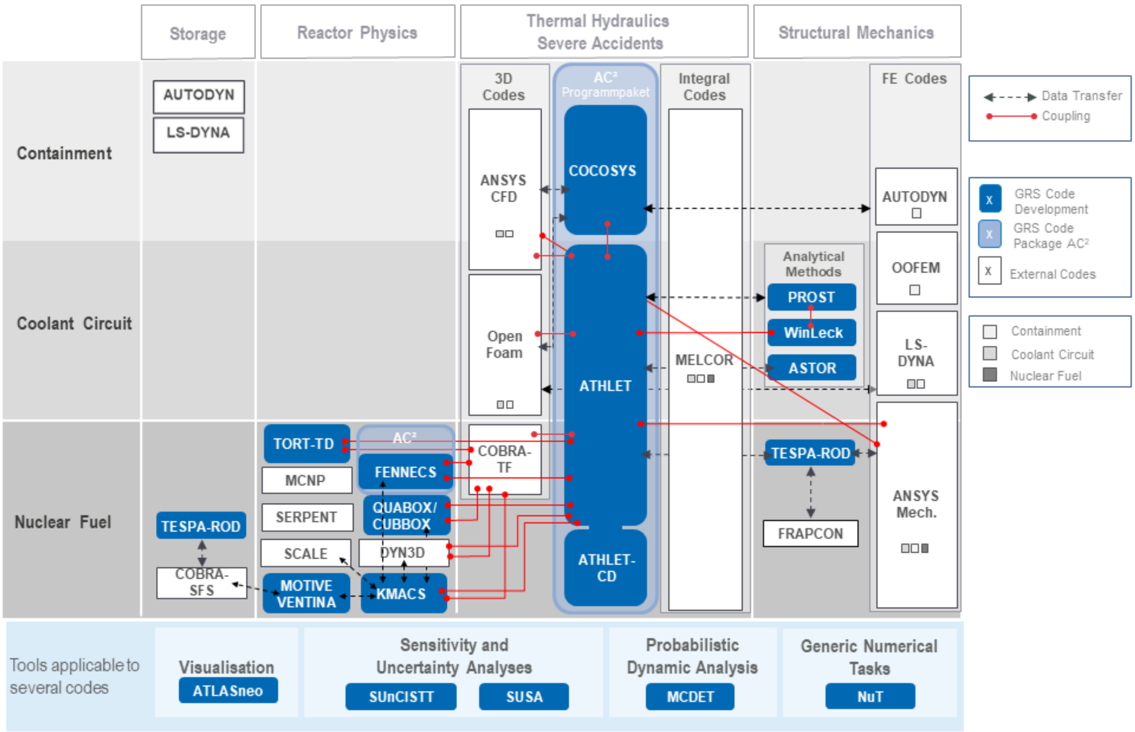

Fig. 1.2 GRS nuclear simulation chain and code coupling

For further information see the ATHLET-CD documentation /LOV 25/.

1.2 Validation

The development of ATHLET-CD has been accompanied by a systematic and comprehensive validation program. The validation is mainly based on pre- and post-test calculations of separate effects tests, integral system tests including the major **International Standard Problems**, as well as on actual plant transients. A well-balanced set of tests has been derived from the **CSNI Code Validation Matrix**. The tests cover phenomena, which are expected to be relevant for all types of events of the envisaged ATHLET-CD range of application for all common LWRs including advanced reactor designs with up-to-date passive safety systems.

As ATHLET-CD extends ATHLET and makes full use of ATHLET models, the validation of ATHLET completes and complements the validation of ATHLET-CD and vice versa. For this reason, validation for phenomena and processes not related to severe accident phenomenology are not included in this report, but only in the ATHLET validation report /HOL 25/.

.

2 General Validation Strategy

2.1 Objectives and Definitions

Severe accident computer codes extending system codes like ATHLET-CD aim to simulate the progression of a design extension condition scenario in the severe accident phase as realistic as feasible ('best estimate') given the status of knowledge on severe accident phenomena while allowing the simulation to be done on a standard PC within days or at most weeks. These computer codes are used to investigate

- the progression of core degradation, cladding oxidation up to core melting, corium formation and relocation,
- the generation and transport of hydrogen in the reactor pressure boundary during severe accidents,
- the release of radionuclides from degraded and molten fuel and their transport within the reactor pressure boundary and to the containment,
- the behaviour of corium and core debris in the lower plenum of a reactor vessel and the failure of vessel walls,
- the feasibility and effectiveness of preventive as well as mitigative emergency operating procedures,
- the adequacy of severe accident management guidance for the plant.

For predicting the overall behaviour of the plant during a severe accident scenario, the processes in and interactions with the containment, including a potential accidental release to the environment, ATHLET-CD can be coupled to COCOSYS for AC² calculations.

The process carried out by comparing code predictions with experimental measurements or measurements in a reactor plant (if available) is called validation /IAEA 16/, /GRS 21/. A code or code model is considered validated when sufficient testing has been performed to ensure an acceptable level of predictive accuracy over the range of conditions for which the code is foreseen to be applied. Accuracy is a measure of the difference between measured and calculated quantities taking into account uncertainties and biases in both. Bias is a measure, usually expressed statistically, of the systematic difference between a true mean value and a predicted or measured mean. Uncertainty is a measure of the scatter in experimental or predicted data /CSNI 89/. The acceptable level of accuracy is judgmental and will vary depending on the specific problem or question to be addressed by the code. The procedure for specifying, qualitatively or quantitatively, the accuracy of code predictions is also called code assessment.

The international literature often distinguishes between the terms 'validation' and 'verification'. A mathematical model, or the corresponding computer code, is verified if it is demonstrated that the code behaves as intended, i.e. that it is a proper mathematical representation of the conceptual model, and that the equations are correctly encoded and solved. Verification may include the demonstration of convergence of the calculated results during a process of reduction of time steps and the size of the nodes of simulation. Also, the comparison of selected results with exact mathematical solutions and with the results obtained by similar codes may fall under the term verification. In this context, the comparison with measured values is not part of the verification process, it is rather a validation task. The term verification, however, had often been used synonymously with validation and qualification /CSNI 89/. In the past, the term verification was used in the frame of the ATHLET-CD code validation work, including comparisons between calculations and measurements.

Given that there is still substantial lack of knowledge as well as a lack of experimental data for validation for some phenomena and processes, particularly under realistic conditions without significant scaling distortions, the general validation strategy for ATHLET-CD places more emphasis on code-to-code comparisons and benchmarks than the strategy for ATHLET presented in its validation report /HOL 23/. In addition and as recommended in IAEA SSG-2, Rev. 1 /IAEA 19/, verification and quality assurance procedures during the development are more important. The overall quality assurance strategy for ATHLET-CD development is similar to ATHLET and described in the ATHLET-CD User’s Manual /LOV 25/ and the Programmer’s Manual of ATHLET /JAC 25/.

2.2 Validation Matrices

As ATHLET-CD extends ATHLET, for which substantial validation is performed independently /HOL 25/. Phenomena and processes also relevant for design basis and design extension conditions without core degradation are not addressed in this report. The validation for ATHLET-CD shows, however, that the models, material characteristics and correlations from ATHLET are also adequate and within their range of applicability for severe accident analyses with ATHLET-CD. The following is therefore limited to severe accident phenomenology for which ATHLET-CD provides own models.

The validation of codes is mainly based on pre-test and post-test calculations of separate effects tests, integral system tests, and accidents in commercial plants. An enormous amount of test data, usable for code validation, has been accumulated in the last decades. Comparable to the report /NEA 87/ compiled by the Task Group on the Status and Assessment of Codes for Transients and ECC of the OECD, validation matrices were derived for severe accidents in 1996 /HAS 96/ and updated in 2001 /NEA 01/. These reports contain a cross reference matrix and a list of these experiments including the test objective and special interest for validation.

To systemize the selection of tests for code validation, the so-called 'Cross Reference Matrices' have been established. Based on these matrices, phenomenologically well-founded sets of experiments have been defined, for which comparison of measured and calculated parameters form a basis for establishing the uncertainty range of test calculation results. The matrices also permit identification of areas where further research may be justified. In the Cross Reference Matrices developed in /HAS 96/ and /NEA 01/, relevant phenomena or processes, which could occur during transients or loss-of-coolant accidents in different types of NPPs are given. In addition to the phenomena, suitable experimental facilities covering these effects and the test types of interest are shown. The relationship between phenomenon and test type indicates which phenomena are expected to occur in which test types. The relationship between test facility and phenomenon indicates the suitability of the test facilities for code validation of the different phenomena, and the relationship between test type and test facility indicates which test types are performed in which test facilities.

The systematic validation of the ATHLET-CD computer code is based on a well-balanced set of integral and separate effects tests derived from the CSNI proposal and current test series /HAS 96/, /NEA 01/, /HAS 96/, /HAS 18/. In the following, the validation cross reference matrices as applied for ATHLET-CD are shown (Tab. 2.2 and Tab. 2.7), with Tab. 2.1 summarizing the keys used in these matrices.

Tab. 2.1 Keys to the ATHLET-CD validation matrices

Key Test	Scale of 1 to 2: most to least suitable for code validation
Selection Criteria	
0.1 Data/Documentation	1 = complete/full; 2 = incomplete/preliminary
	* = available in electronic form
0.2 Boundary Condition	1 = well-defined; 2 = partially defined
0.3 Dominant Characteristic	E = Exploratory; M = Model development
	P = Parameter range investigation; R = Reactor typical;
	S = international Standard problem; U = Unique test
Heat Source	
1.1 Reactor	Y = Yes; n = no (includes fission heat from driver core)
1.2 Heating Method	D = Decay; E = Electrical; F = Fission; M = Micro-wave; W = Wall
	F = Fresh; T = Trace (.lt. 1MWd/kg);
1.3 Burn-up	M = Medium; H = High (.gt. 40 MWd/kg)
Initial Conditions	
2.1 Heated Length	S = Small (.le. 0.5 m); M = Medium; L = Large (.gt. 1.5 m)
2.2 Fuel Rods	S = Small (.le. 15); M = Medium; L = Large (.gt. 45)
2.3 Spacer Grid Zirconium	Y = Yes; n = no
2.4 Spacer Grid Inconel	Y = Yes; n = no
2.5 Control Assembly AIC	Y = Yes; n = no
2.6 Control Assembly B4C	Y = Yes; n = no
2.7 Core Support Struct.	Y = Yes; n = no
2.8 Initial Fuel Debris	Y = Yes; n = no
2.9 Crust Prefabricated	Y = Yes; n = no
2.10 Preoxidation	n = none; S = Small (.lt. 0.01 mm);
	M = Medium; L = Large (.gt. 0.05 mm); T = Total
Boundary Conditions	
3.1 Heat-up Rate	L = Low (.le. 0.3 K/s); M = Medium; H = High (.gt. 1 K/s)
3.2 System Pressure	L = Low (.le. 0.5 MPa); M = Medium; H = High (.gt. 3.0 MPa)
3.3 Gas Injection	n = none; A = Air or O2; S = Steam; H = H2; I = Inert
3.4 Steam Starved	Y = global starvation; n = no or only local starvation
3.5 Boil Down	Y = Yes; n = no
3.6 Reflood	n = none; L = at Low temperature;
	H = at High temperature (.gt. 1800 K); S = rapid cooling by Steam
	Y = Yes; n = no
3.7 Possible Flow Bypass	
Experimental Conditions	
4.1 Clad Ballooning	Y = Yes; n = no
4.2 Oxidation Excursion	Y = Yes; n = no
4.3 Non-Fuel Melt	Y = Yes; n = no
4.4 Fuel Dissolution	Y = Yes; n = no
4.5 Ceramic Melt	Y = Yes; n = no
4.6 Particulate Debris	Y = Yes; n = no Q = from Quench-induced shattering
4.7 Melt Pool	Y = Yes; n = no
4.8 Crust Failure	Y = Yes; n = no
4.9 Structure Ablation	Y = Yes; n = no
4.10 Fission Product Rel.	Y = Yes; n = no; A = fuel Aerosol
	--- indicates not applicable, no clear distinction possible, or insufficient data available to make a valid assignment

Tab. 2.2 Validation Matrix, Integral Experiments with Key Test Scale = 1 /NEA 01/

Test Characteristic	CORA-13	CORA-28	CORA-33	CORA-W2	PHÉBUS-B9+	PBF-1-4	ACRR-ST-1	ACRR-DF-4	LOFT LP-FP-2	PHÉBUS -FPT1	ACRR-MP-1	ACRR-MP-2	TMI- 2
Key Test	1	1	1	1	1	1	1	1	1	1	1	1	1
Data/Documentation	1*	1*	1*	1*	1*	1*	1*	1*	1*	1*	1*	1*	1
Boundary Condition	2	2	2	2	2	2	1	1	2	1	2	1	3
Dominant Characteristic	S	P	U	S	S	R	U	U	R	S	U	U	R
1.1 Reactor	n	n	n	n	n	n	n	n	Y	n	n	n	Y
1.2 Heating Method	E	E	E	E	F	F	F	F	D	F	F	F	FD
1.3 Burn-up	F	F	F	F	F	M	M	F	T	M	F	F	M
2.1 Heated Length	M	M	M	M	M	M	S	S	L	M	S	S	L
2.2 Fuel Rods	M	M	M	M	M	M	S	S	L	M	M	M	L
2.3 Spacer Grid Zirconium	Y	Y	Y	n	n	n	n	n	n	Y	n	n	n
2.4 Spacer Grid Inconel	Y	n	n	Y	Y	Y	n	n	Y	n	n	n	Y
2.5 Control Assembly AIC	Y	n	n	n	n	Y	n	n	Y	Y	n	n	Y
2.6 Control Assembly B4C	n	Y	Y	Y	n	n	n	Y	n	n	n	n	Y
2.7 Core Support Struct.	N	n	n	n	n	n	n	n	Y	n	n	n	Y
2.8 Initial Fuel Debris	n	n	n	n	n	n	n	n	n	n	Y	Y	n
2.9 Crust Prefabricated	n	n	n	n	n	n	n	n	n	n	Y	Y	n
2.10 Preoxidation	n	M	n	n	n	n	n	n	n	n	T	T	n
3.1 Heat-up Rate	M	M	L	M	L	MH	H	H	H	M	L	L	LM
3.2 System Pressure	L	L	L	L	M	H	L	M	M	L	L	L	H
3.3 Gas Injection	SI	SI	SI	SI	SI	SI	HI	S	S	S	I	I	S
3.4 Steam Starved	n	n	Y	n	Y	n	Y	n	n	n	Y	Y	n
3.5 Boil Down	n	n	n	n	n	Y	n	n	Y	n	n	n	Y
3.6 Reflood	Y	n	n	n	n	n	n	n	Y	n	n	n	Y
3.7 Possible Flow Bypass	Y	Y	Y	Y	n	Y	n	n	Y	n	n	n	n
4.1 Clad Ballooning	n	n	n	n	n	Y	n	n	Y	Y	n	n	Y
4.2 Oxidation Excursion	Y	Y	Y	Y	Y	Y	n	Y	Y	Y	n	n	Y
4.3 Non-Fuel Melt	Y	Y	Y	Y	Y	Y	n	Y	Y	Y	n	n	Y
4.4 Fuel Dissolution	Y	Y	Y	Y	Y	Y	Y	Y	Y	Y	n	n	Y
4.5 Ceramic Melt	n	n	n	n	n	Y	n	n	Y	Y	Y	Y	Y
4.6 Particulate Debris	Q	n	n	n	n	Y	n	n	Y	n	Y	Y	Y
4.7 Melt Pool	n	n	n	n	n	Y	n	Y	n	Y	Y	Y	Y
4.8 Crust Failure	n	n	n	n	n	Y	n	n	n	---	n	Y	Y
4.9 Structure Ablation	n	n	n	n	n	n	n	n	n	n	n	n	Y
4.10 Fission Product Rel.	n	n	n	n	n	Y	Y	n	Y	Y	n	n	Y

Tab. 2.3 Validation Matrix, Integral Experiments with Key Test Scale = 2 (1/2) /NEA 01/

Test **Characteristic**	CORA-2	CORA-5	CORA-12	CORA-15	CORA-17	CORA-30	CORA-31	PHÉBUS-C3+	PHÉBUS-AIC	NRU-FLHT-5	ACRR-DF-2
Key Test	2	2	2	2	2	2	2	2	2	2	2
Data/Documentation	1*	2*	2*	2*	2*	2*	1*	1*	1*	2*	1*
Boundary Condition	2	2	2	2	2	2	2	2	1	2	2
Dominant Characteristic	M	M	P	P	P	P	P	P	P	U	E
1.1 Reactor	n	n	n	n	n	n	n	n	n	n	n
1.2 Heating Method	E	E	E	E	E	E	E	F	F	F	F
1.3 Burn-up	F	F	F	F	F	F	F	F	F	FM	F
2.1 Heated Length	M	M	M	M	M	M	M	M	M	L	S
2.2 Fuel Rods	M	M	M	M	M	M	M	M	M	S	S
2.3 Spacer Grid Zirconium	Y	Y	Y	Y	Y	Y	Y	n	Y	Y	n
2.4 Spacer Grid Inconel	Y	Y	n	Y	n	n	Y	Y	n	Y	Y
2.5 Control Assembly AIC	n	Y	Y	Y	n	n	Y	n	Y	n	n
2.6 Control Assembly B4C	n	n	n	n	Y	Y	n	n	n	n	n
2.7 Core Support Struct.	n	n	n	n	n	n	n	n	n	n	n
2.8 Initial Fuel Debris	n	n	n	n	n	n	n	n	n	n	n
2.9 Crust Prefabricated	n	n	n	n	n	n	n	n	n	n	n
2.10 Preoxidation	n	n	n	n	n	n	n	n	n	n	n
3.1 Heat-up Rate	M	M	M	M	M	L	L	H	M	H	H
3.2 System Pressure	L	L	L	L	L	L	L	H	M	M	M
3.3 Gas Injection	SI	SI	SI	SI	SI	SI	SI	SI	SI	S	S
3.4 Steam Starved	n	n	n	n	n	n	n	Y	n	n	n
3.5 Boil Down	n	n	n	n	n	n	n	n	n	Y	n
3.6 Reflood	n	n	Y	n	Y	n	n	n	n	n	n
3.7 Possible Flow Bypass	Y	n	Y	Y	Y	Y	Y	n	n	n	n
4.1 Clad Ballooning	Y	n	n	Y	n	n	n	n	n	n	n
4.2 Oxidation Excursion	Y	Y	Y	Y	Y	Y	Y	n	Y	Y	Y
4.3 Non-Fuel Melt	Y	Y	Y	Y	Y	Y	n	Y	Y	Y	Y
4.4 Fuel Dissolution	Y	Y	Y	Y	Y	Y	Y	Y	n	Y	Y
4.5 Ceramic Melt	n	n	n	n	n	n	n	n	n	n	n
4.6 Particulate Debris	n	n	Q	n	Q	n	n	Y	n	n	n
4.7 Melt Pool	n	n	n	n	n	n	n	n	n	n	Y
4.8 Crust Failure	n	n	n	n	n	n	n	n	n	n	n
4.9 Structure Ablation	n	n	n	n	n	n	n	n	n	n	n
4.10 Fission Product Rel.	n	n	n	n	n	n	n	n	n	Y	n

Tab. 2.4 Validation Matrix, Integral Experiments with Key Test Scale = 2 (2/2) /NEA 01/

Test **Characteristic**	PHÉBUS -FPT0	PHÉBUS -FPT4	SNL-XR1-2	SCARABEE BF	ACRR-DC1	CODEX-AIT1	CODEX-AIT2	QUENCH-01	QUENCH-03	QUENCH-04
Key Test	2	*2*	2	2	2	2	2	2	2	2
Data/Documentation	1*	*1**	1*	1*	1	2*	2*	1*	2*	1*
Boundary Condition	1	*2*	1	2	1	2	2	1*	1*	1*
Dominant Characteristic	U	*U*	E	U	E	E	U	E	P	E
1.4 Reactor	n	*n*	n	n	n	n	n	n	n	n
1.5 Heating Method	F	*F*	E	F	F	E	E	E	E	E
1.6 Burn-up	T	*M*	---	F	F	F	F	---	---	---
2.1 Heated Length	M	*S*	M	S	S	M	M	M	M	M
2.2 Fuel Rods	M	*n*	---	n	n	S	S	M	M	M
2.3 Spacer Grid Zirconium	Y	*n*	---	n	n	Y	Y	Y	Y	Y
2.4 Spacer Grid Inconel	n	*n*	---	n	n	n	n	Y	Y	Y
2.5 Control Assembly AIC	Y	*n*	---	n	n	n	n	n	n	n
2.6 Control Assembly B4C	n	*n*	Y	n	n	n	n	n	n	n
2.7 Core Support Struct.	n	*n*	Y	n	n	n	n	n	n	n
2.8 Initial Fuel Debris	n	*Y*	---	Y	Y	n	n	n	n	n
2.9 Crust Prefabricated	n	*n*	---	n	n	n	n	n	n	n
2.10Preoxidation	n	*T*	---	n	n	M	L	H	n	n
3.1 Heat-up Rate	M	*M*	---	H	L	M	M	M	M	M
3.2 System Pressure	L	*L*	L	L	L	L	L	L	L	L
3.3 Gas Injection	S	*SH*	I	n	I	IA	SA	SI	SI	SI
3.4 Steam Starved	n	*n*	---	Y	Y	n	n	n	n	n
3.5 Boil Down	n	*n*	---	n	n	n	n	n	n	n
3.6 Reflood	n	*n*	---	n	n	n	n	Y	Y	S
3.7 Possible Flow Bypass	n	*Y*	--	n	n	n	n	n	n	n
4.1 Clad Ballooning	Y	---	---	n	n	n	n	n	n	n
4.2 Oxidation Excursion	Y	---	---	n	n	Y	Y	n	Y	Y
4.3 Non-Fuel Melt	Y	*n*	Y	n	n	n	Y	n	n	n
4.4 Fuel Dissolution	Y	*n*	---	n	n	n	Y	n	n	n
4.5 Ceramic Melt	Y	*Y*	---	Y	Y	n	n	n	n	n
4.6 Particulate Debris	n	*Y*	---	n	Y	n	n	n	Q	n
4.7 Melt Pool	Y	*Y*	Y	Y	Y	n	n	n	n	n
4.8 Crust Failure	---	---	Y	n	n	n	n	n	n	n
4.9 Structure Ablation	Y	---	Y	n	n	n	n	n	n	n
4.10 Fission Product Rel.	Y	*Y*	---	n	n	n	A	--	---	-

Tab. 2.5 Validation Matrix, Bundle Separate Effect Experiments with Key Test Scale = 1 and 2 /NEA 01/

Test **Characteristic**	REBEKA-6	PHÉBUS -218	NRU-MT4	MRBT-B6
Key Test	1	2	1	2
Data/Documentation	1	1	1	1
Boundary Condition	2	3	2	2
Dominant Characteristic	S	S	M	M
1.7 Reactor	n	n	n	n
1.8 Heating Method	E	F	F	E
1.9 Burn-up	F	F	F	F
2.1 Heated Length	L	M	L	M
2.2 Fuel Rods	L	M	M	ML
2.3 Spacer Grid Zirconium	---	---	---	---
2.4 Spacer Grid Inconel	N	---	---	---
2.5 Control Assembly AIC	Y	n	n	n
2.6 Control Assembly B4C	n	n	n	n
2.7 Core Support Struct.	n	n	n	n
2.8 Initial Fuel Debris	n	n	n	n
2.9 Crust Prefabricated	n	n	n	n
2.10 Preoxidation	n	n	n	n
3.1 Heat-up Rate	H	H	H	H
3.2 System Pressure	L	H	L	---
3.3 Gas Injection	I	S	S	S
3.4 Steam Starved	n	n	n	n
3.5 Boil Down	n	n	n	n
3.6 Reflood	n	n	n	n
3.7 Possible Flow Bypass	n	n	n	n
4.1 Clad Ballooning	Y	Y	Y	Y
4.2 Oxidation Excursion	---	---	---	---
4.3 Non-Fuel Melt	---	---	---	---
4.4 Fuel Dissolution	---	---	---	---
4.5 Ceramic Melt	---	---	---	---
4.6 Particulate Debris	---	---	---	---
4.7 Melt Pool	---	---	---	---
4.8 Crust Failure	---	---	---	---
4.9 Structure Ablation	---	---	---	---
4.10 Fission Product Rel.	---	---	---	---

Tab. 2.6 Validation Matrix, FCI Experiments with Key Test Scale = 1 and 2 /NEA 01/

Test Characteristic	FARO-L14	FARO-L28	KROTOS 44	FARO-L11	FARO-L31	FARO-L33	KROTOS 58
Key Test	1	1	1	2	2	2	2
Data/Documentation	1	1	2	1	1	2	2
Boundary Condition	1	1	1	1	1	1	1
Dominant Characteristic	S	P	P	P	P	P	P
Material Mass, kg	125	175	1.5	151	92	100	4.5
Composition	Cor1	Cor1	Al_2O_3	Cor2	Cor1	Cor1	Cor1
Metal Content	n	n	n	Y	n	n	n
Initial Temperature, K	3123	3052	2673	2823	2990	3070	3077
Initial Debris	Melt	Melt	Melt	Melt	Melt	Melt	Melt
System Pressure, MPa	5.0	0.5	0.10	5.0	0.22	0.40	0.37
Debris Mass / Water Mass	0.20	0.31	0.045	0.25	0.19	>0.16	0.15
Subcooling, K	0	1	80	2	104	124	125
Gas Phase	Stm/Ar	Stm	He	Stm	Ar	Ar	Ar
Trigger	n	n	Y	n	n	Y	Y
Energetic Interaction	n	n	TE	n	n	TE	TE
Hydrogen Generation	n	Y	n.m.	Y	Y	Y	Y
Peak Pressure Ratio	1.56	3.40	650	2.02	1.20	26.5	26.5
Debris Formation	Pm	n.a.y.	Ts	Tm	Tm	n.a.y.	n.a.y.

Key:		
General	n = no; Y = Yes	
Composition	Cor1 = 80wt%UO_2/20wt%ZrO_2; Cor2 = 77wt%UO_2/19wt%ZrO_2/4wt%Zr; Al_2O_3 = aluminium oxide	
Gas phase	Stm = Steam; Ar = Argon; He = Helium	
Energetic Interaction	n = none; TE = Triggered Explosion	
Total fragmentation (>90%) with small particles, d < 1 mm		Ts
Total fragmentation (>90%) with medium size particles, 1 mm < d < 10 mm		Tm
Total fragmentation (>90%) with large particles, d > 10 mm		Tl
Partial fragmentation with small particles and cake formation		Ps
Partial fragmentation with medium size particles and cake formation		Pm
Partial fragmentation with large particles and cake formation		Pl
Cake formation and little fragmentation (< 10%)		n
Data not measured or not available yet		n.m. / n.a.y.

Tab. 2.7 Cross reference table for late phase separate effects test /NEA 01/

Phenomena	Pool thermal-hydraulics			Gap thermal-hydraulics		Ex-vessel	Gap formation		Fuel coolant interaction	
Test Facility	BALI	RASPLAV-SALT	SIMECO	BENSON	CORCOM	CYBL	FOREVER	LAVA	FARO	KROTOS
Debris bed formation									M	S
Debris bed heat transfer					S					
Pool formation										
Pool thermal-hydraulics	L	M	M							
Pool stratification			sim							
Pool solidification		sim	sim							
Crust thermal behaviour							I	I		
Crust mechanics							I	I		
Upper crust heat transfer										
Lower crust heat transfer				L	S					
Dry RPV cavity										
Wet RPV cavity						L				
RPV elastic deformation										
RPV plastic deformation							I	I		
Vessel failure							I			
Thermal ablation										

Key:

Scaling of facility	L = large,M = medium, S = small
Material	sim = Simulate material
Status of project	I = Investigation intended

Tab. 2.8 Validation cases ATHLET-CD

Test Facility	Test No.	Brief Description	Calculation done by	ATHLET-CD Version	Refer-ence
ACRR	-MP1	Melt progression test	RUB	2.1A, 2.2A	/HOF 10/, /HOL 10/
ACRR	-MP2	Melt progression test	RUB	2.1A, 2.2A	/HOF 10/, /HOL 10/
CODEX	-AIT1	Air ingress	GRS, RUB	2.1A, 3.1A	/PES 19/
CODEX	-AIT3	Steam oxidation and air ingress	GRS	3.1A, 3.2	
CORA	-2	BWR: UO_2 refer., Inconel spacer	GRS	ATHLET-SA	/TRA 90/
CORA	-5	PWR: absorber	GRS	0.2E	/STE 98a/
CORA	-13	PWR: quench initiation at higher temperature	GRS	0.1V, 1.1E, 3.1A, 3.3	Sect. 5.2
CORA	-15	PWR: rods with internal pressure	GRS	3.1A	/KIR 94/ /STE 03/
CORA	-17	BWR: quenching	GRS, RUB	1.1B, 2.2A, 3.2	/STE 00/ /HOF 14/
CORA	-28	BWR: pre-oxidised	GRS, RUB	3.2	/KIR 94/ /STE 03/ /HOF 14/
CORA	-31	BWR: slow initial heat-up (~0.3 K/s)	GRS	1.1I, 2.2A, 3.1A	/AUS 10/
CORA	-33	BWR: dry core conditions, no extra steam injection	GRS	2.2A, 3.2	/STE 03/ /AUS 10/
CORA	-W1	WWER: reference without absorber	GRS	0.1V	
CORA	-W2	WWER: with absorber	GRS	0.1V, 1.0A, 3.1A, 3.3	/KIR 89/ Sect. 5.3
Fukushima Daiichi NPP	Unit 1	Severe accident in a BWR reactor after tsunami-induced long-term SBO			
Fukushima Daiichi NPP	Unit 2	Severe accident in a BWR reactor after tsunami-induced long-term SBO	GRS	3.1 AC² 2019	/WEB 16/ /BAN 18/

Test Facility	Test No.	Brief Description	Calculation done by	ATHLET-CD Version	Refer-ence
Fukushima Daiichi NPP	Unit 3	Severe accident in a BWR reactor after tsunami-induced long-term SBO	GRS	3.1 AC² 2019	/WEB 16/ /BAN 18/
HALDEN	IFA 650.2	LOCA test with a fresh, tight-gap and pressurised PWR rod with Zr-4 cladding with ballooning and fuel failure	GRS	2.0B	/TRA 96/ /STE 03/
HALDEN	IFA 650.3	LOCA test with fuel rods irradiated in a PWR to rod burnups of 82 MWd/kgU	GRS	2.0B	/STE 06/
LIVE	L1	Core melt behaviour in the lower plenum of the reactor pressure vessel and the influence of the cooling of the vessel outer surface with water	GRS	2.2A Update 1, 3.0B	/WEB 12/
LIVE	L4	Influence of external water cooling on the transient melt behaviour at different power levels	GRS	3.0B, 3.2	/HOL 16/
LIVE	L6	Thermal hydraulic behaviour of stratified melt pool in the reactor vessel lower head	GRS	3.0B	
LIVE	L10	Influence of ex-vessel cooling with subcooled water	GRS, RUB	3.2, 3.3	/PES 19/ Sect. 5.9
LIVE	L11	Influence of ex-vessel cooling with boiling water	GRS, RUB	3.2	/PES 19/ Sect. 5.9
LOFT	LP-FP-2	Core degradation with fission product release and transport	GRS	0.1W, 3.0B, 3.2	/TRA 96/ /HOL 16/
NRU	FLHT-2	Early phase melt progression in a PWR bundle under in-reactor conditions with a full-length bundle including fission product release	GRS	0.1T, 2.0A	/KIR 89/ /STE 06/
NRU	FLHT-5	Early phase melt progression in a PWR bundle under in-reactor conditions with a full-length bundle	GRS	2.0A	/STE 06/
PARAMETER	SF1	Top flooding of a degraded core	GRS	2.1A	/STE 06/
PARAMETER	SF2	Simultaneous top and bottom flooding of a degraded core	GRS	2.1B, 3.2	/AUS 10/
PARAMETER	SF3	Top flooding of a degraded core	GRS	2.2A, 3.2	/AUS 10/ /HOF 14/
PARAMETER	SF4	Air ingress with subsequent bottom flooding	GRS	2.2A Update 1, 3.1A	/WEB 12/
PBF	SFD 1-1	Early phase degradation of a fission heated PWR bundle is studied with very high temperatures (> 2800 K).	GRS	0.1P, 0.2G	/KIR 89/, /STE 03/
PBF	SFD 1-4	Early phase degradation of a fission heated PWR bundle is studied under a high system pressure (the highest system pressure used in a well-qualified test) with very high temperatures (> 2800 K)	GRS	1.0A, 1.1L	/STE 03/ /STE 06/

Test Facility	Test No.	Brief Description	Calculation done by	ATHLET-CD Version	Reference
PHÉBUS	B9+	Early phase bundle degradation in the absence of absorber materials, under nuclear heated conditions	GRS	ATHLET-SA, 0.1Q, 1.0A, 1.1K, 3.3	/KIR 89/ /BAL 91/ /STE 99/ /STE 03/ /STE 06/ Sect. 5.1
PHÉBUS	CSD C3+	UO$_2$/Zircaloy reaction within a ZrO2 shell above 2000 K	GRS	1.1K	/STE 06/
PHÉBUS	CSD AIC	PWR control rod failure and the spreading/interaction of the absorber material is studied at temperatures low enough to prevent fuel reactions	GRS	ATHLET-SA, 2.0A	/TRA 90/ /STE 06/
PHÉBUS	FPT0	Transition from early to late phase core degradation and the effect of the degradation on fission product release, for fuel with very low burnup	GRS, RUB	0.2A	/TRA 96/ /POH 99/ /KLE 01/
PHÉBUS	FPT1	Transition from early to late phase core degradation using fuel irradiated to prototypical reactor levels, and the effect of the degradation of such irradiated fuel on fission product release. AIC absorber.	GRS, RUB	1.1I, 3.2, 3.3	/STE 03/ /KLE 03/ /HOF 14/ /JAN 17/ Sect. 5.5 /KRI 22a/, /KRI 22b/, /TIB 22/
PHÉBUS	FPT2	Transition from early to late phase core degradation using fuel irradiated to prototypical reactor levels, and the effect of the degradation of such irradiated fuel on fission product release. AIC absorber.	GRS, RUB	1.2C, 2.1A, 2.1B	/TRA 01/ /KLE 04a/ /STE 06/ /AUS 10/ /HOF 14/
PHÉBUS	FPT3	Transition from early to late phase core degradation using fuel irradiated to prototypical reactor levels, and the effect of the degradation of such irradiated fuel on fission product release. B$_4$C absorber	GRS, RUB	2.1A, 2.2A, 2.2C, 3.1A, 3.2, 3.3	/STE 06/ /DRA 07/ /AUS 10/ /WEB 12/ /HOF 14/ /HOL 16/ Sect. 5.6 /KRI 22a/, /KRI 22b/, /TIB 22/

Test Facility	Test No.	Brief Description	Calculation done by	ATHLET-CD Version	Reference
PHÉBUS	FPT4	Transition from debris bed to melt pool geometry, and associated fission product retention and release	GRS, RUB	1.2G	/TRA 01/ /KLE 04b/
QUENCH	-01	COBE Project: Partial fragmentation of pre-oxidized cladding	GRS	1.1F, 1.2C	/ERD 01/ /TRA 01/ /STE 03/
QUENCH	-03	Delayed flooding: 240 s after temperature escalation has started	RUB	3.1A	/REI 02/
QUENCH	-04	Cool-down behaviour of slightly pre-oxidized cladding by injected cold steam	RUB		/REI 02/
QUENCH	-05	Cool-down behaviour of pre-oxidized cladding by injected cold steam	RUB	1.1G	/REI 02/
QUENCH	-06	OECD-ISP: Prediction of H2 source term by different code systems	GRS, RUB	1.1H, 3.2, 3.3	/REI 02/ /STE 03/ Sect. 5.4
QUENCH	-07	COLOSS Project: Impact of B_4C absorber rod failure on H_2, CO, CO2 and CH_4 generation	GRS, RUB	1.1J, 2.0, 3.2	/STE 06/ /DRA 06/
QUENCH	-08	Reference test to QU-07 without absorber rod	GRS, RUB	1.1L 2.1	/STE 06/ /DRA 06/
QUENCH	-09	COLOSS Project: Impact of B_4C absorber rod failure on H_2, CO, CO_2 and CH_4 generation in steam-starved conditions	GRS	1.1K	/STE 06/
QUENCH	-10	LACOMERA-QUENCH-01: Air ingress during spent fuel storage container accident	GRS	2.0B, 3.2	/STE 06/
QUENCH	-11	LACOMERA-QUENCH-02: Boil-off test with subsequent flooding (SARNET Benchmark)	GRS, RUB	2.1A, 2.1B, 3.2	/STE 06/ /AUS 10/ /JAN 17/
QUENCH	-12	ISTC-1648.2: Physico-chemical behaviour of VVER type cladding (Zr1%Nb) during flooding	RUB		/HOF 14/
QUENCH	-13	SARNET: AgInCd absorber rod, aerosol	RUB	2.2A	/AUS 10/
QUENCH	-15	ACM series: ZIRLO^{TM} cladding	GRS	3.1A, 3.2	
QUENCH	-16	LACOMECO Project: Air ingress (SARNET Benchmark)	GRS, RUB	2.2C, 3.2, 3.3	/WEB 12/ /HOF 14/ /PES 19/ Sect. 5.7

Test Facility	Test No.	Brief Description	Calculation done by	ATHLET-CD Version	Refer-ence
QUENCH	-17	SARNET-2: Debris formation and coolability	GRS, RUB	2.2C	/WEB 12/ /HOL 16/ /JAN 17/
QUENCH	-18	ALISA Project: Air ingress, AgInCd absorber rods	GRS	3.1A, 3.2, 3.3	Sect. 5.8
QUENCH	-19	Bundle wit FeCrAl materials; cooperation with ORNL	GRS	3.2, 3.3.0, 3.3.1	/HOL 19/, /HOL 22a/, /HOL 22b/, /LOV 23/
QUENCH	-20	EC SAFEST: BWR bundle configuration	GRS	3.3.1	/LOV 23/
QUENCH	-L3HT	LOCA bundle test Quench-L3 with otimised ZIRLOTM cladding	RUB	3.3	/STA 22/, /STA 23/
SFP	PWR1	Axial heating and burn propagation in hot neighbour configuration	GRS	2.2B	/WEB 12/
SFP	PWR2	Axial/radial heating and burn propagation in cold neighbour configuration	GRS	2.2C	/WEB 16/
STORM	SR11	Fission product transport	GRS	0.2E SOPHAEROS V2.0	/STE 98b/ /TRA 01/
TMI	Unit-2	Severe accident in a PWR reactor	GRS, RUB	1.2G, 2.0A, 3.1A, 3.2, 3.3	/TRA 01/ /TRA 04/ /DRA 05/ /HOL 16/ Sect. 5.11
WWER-SFP		Postulated loss of cooling in a WWER-SFP	GRS	3.1A AC²-2019	

3 International Standard Problems

Assessing the safety of nuclear installation requires the use of a number of highly specialized tools: computer codes, experimental facilities and their instrumentation, special measurement techniques, methods for testing components and materials, and so on. A highly effective way of increasing confidence in the validity and accuracy of such tools is provided by International Standard Problem (ISP) Exercises in which they are gauged against one another and/or agreed standards /NEA 89/, /NEA 00/. The OECD/CSNI Nuclear Energy Agency promoted International Standard Problems mainly for OECD countries, the IAEA mainly for Eastern European Countries.

The procedure and requirements for set-up and ISP are the same for severe accident ISP like for thermal-hydraulics ISP defined in to /NEA 04/ and detailly described in /HOL 23/. OECD generated a common ISP table including thermal-hydraulics and severe accident ISP for in-vessel and ex-vessel experiments. Tab. 3.1 shows the in-vessel related ISP for severe accident sequences and GRS participation with different codes or modules, currently implemented in AC².

Tab. 3.1 OECD/CSNI International Standard Problems on severe accidents, in-vessel

ISP	Date	Title	CSNI Report No.	GRS participation
28	1992	PHÉBUS SFD B9+: Degradation of a PWR-type core	NEA/CSNI/R(92)17	ATHLET-SA
31	1993	CORA-13: Severe core damage experiment with quenching	NEA/CSNI/R(93)17	ATHLET-CD
34	1994	FALCON ISP-1/-2: Fission product transport	CSNI 1020/01	ATHLET/ TRAP-G
36	1996	CORA-W2: Experiment on severe fuel damage for a WWER bundle	OCDE/GD (96)19	ATHLET-CD
40	1997	STORM SD-11/SR-11: Aerosol deposition and re-suspension in pipes	NEA/CSNI/R(99)4	SOPHAEROS
45	2000	QUENCH-06: Severe core damage experiment with quenching	FZKA 6722	ATHLET-CD
46	1998	PHÉBUS FPT1: Integral experiment on reactor severe accidents	SAM – THENPHEBISP – D005	ATHLET-CD/ COCOSYS

4 Quality Assurance Procedures

The main objective of ATHLET-CD development is providing a simulation code that can be used for deterministic safety analyses of nuclear facilities and to support safety cases submitted to a nuclear regulator. For such a code, there are some high-level requirements to meet, which are formulated in applicable regulation. Experts validating ATHLET-CD should be aware of the overall requirement in IAEA GSR Part 4, Requirement 18: “Any calculational methods and computer codes used in the safety analysis shall undergo verification and validation.” /IAEA 16/, p. 26. Further guidance on quality assurance and the verification and validation of system codes can be found in IAEA SSG-2, Rev. 1, section 5 /IAEA 19/. It is recommended to read this section carefully. In addition, there are applicable norms, e.g. ISO/IEC 90003:2018 or ISO/IEC 25010:2011 and good practices for software development in the nuclear field like e.g. /ODA 00/. Validation of models and software used in the safety assessment of nuclear facilities is required by applicable national regulation in numerous countries, e.g. Germany /BMUB 15/, France /ASN 17/, Spain /CSN 98/, Russia /ROS 12/, U.K. /ONR 19/, and U.S.A. /NRC 05/. Therefore, the validation of ATHLET-CD summarized in this report is an essential part of the overall quality assurance process for ATHLET-CD development.

The software development process implemented at GRS has been defined against this background. Fig. 4.1 below gives an overview of the process. ATHLET-CD is part of the overall AC² development performed at GRS. Therefore, the AC² quality management approach is fully applicable to ATHLET-CD. In short, the process defines the following phases for the actual development process, explained here for a new feature:

- **Design**: Specification of the feature and definition of an implementation, verification, and validation plan
- **Implementation** of the feature in the source code
- **Verification** of the feature with appropriate unit-tests and simple test cases accompanying the development
- **Validation** of the feature against suitable experiments, where the new feature will have a relevant impact, and validation against the set of standard validation cases for ATHLET.

The ATHLET-CD development process is largely identical to the ATHLET development process which is described in detail in the ATHLET Programmer’s Manual /JAC 25/. The

ATHLET-CD User's Manual gives further guidance on how to apply this process to ATHLET-CD development /LOV 25/. In this section, the aspects of the overall quality assurance process relevant for ATHLET-CD validation are explained in more detail.

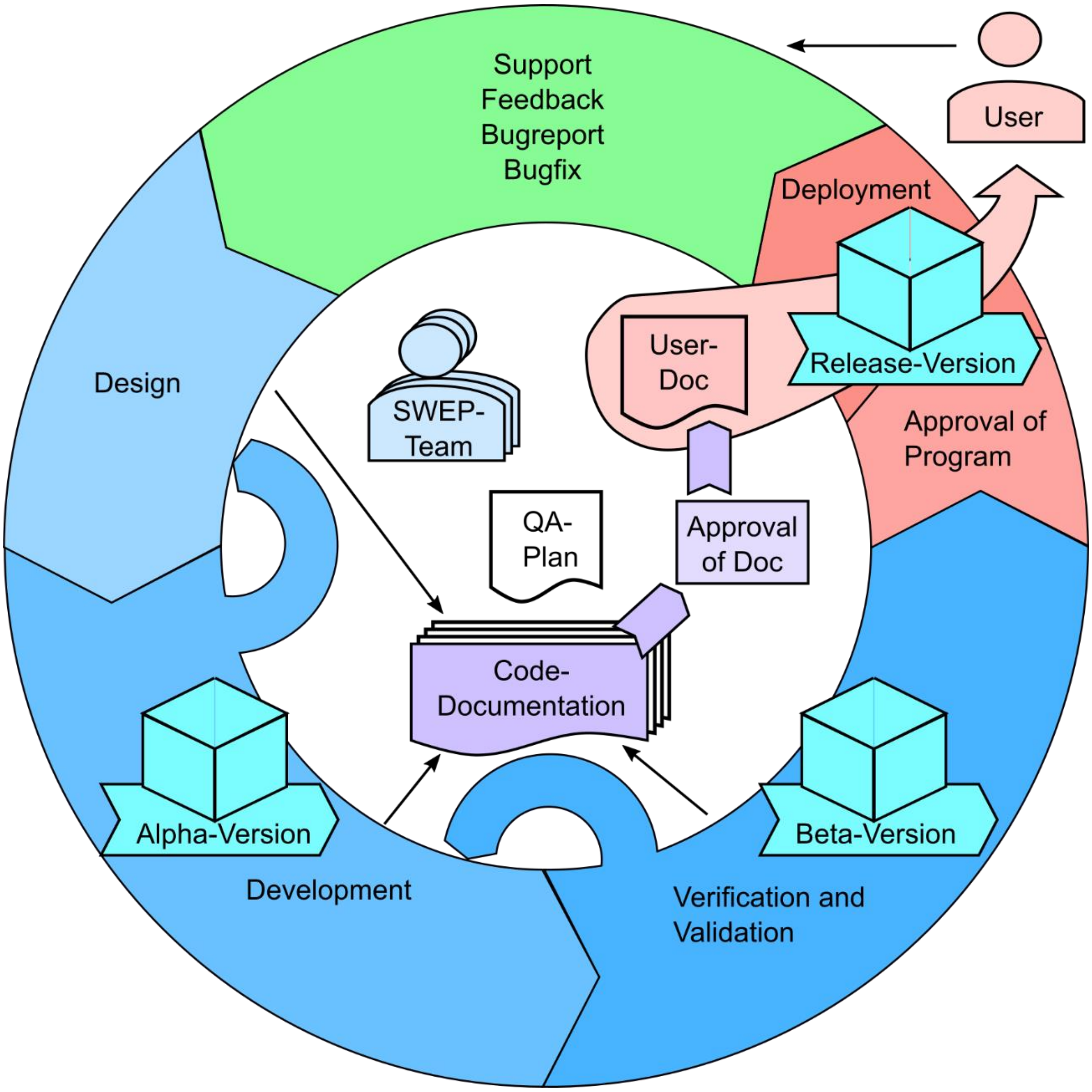

Fig. 4.1 Software development process at GRS /GRS 24/

The **validation** of ATHLET-CD is based on the validation matrices described above. GRS is continuously performing validation of ATHLET-CD both against new test data, standard validation cases and by performing non-regression testing via continuous integration (CI) with the GitLab server operated by GRS. Different to SSG-2, Rev. 1 /IAEA 19/, comparison on ATHLET-CD results against simple basic tests, e.g. single CV simulation models, and checking that the simulation results conform to specified solution, is assigned to the verification phase as it properly happens during code development and implementation. Consequently, ATHLET-CD validation entails SET, integral tests and the accident at TMI-2.

There are two main approaches for validation used for ATHLET-CD:

1. Simulating an experiment or a plant transient with ATHLET-CD and comparing the code results against available **measurement data**. Using expert judgement, it is then concluded if the validation calculation was successful or not, if there are any issues with code performance and predictiveness, and if there are any residual matters.
2. Comparing ATHLET-CD results **against other codes** (integral codes, best-estimate severe accident codes or even CFD codes) for a benchmark case with clearly specified geometry, initial and boundary conditions. Again, using expert judgement, it is then determined if ATHLET-CD adequately simulates the scenario, if deviations between the codes are significant and if there are any indications for code weakness that need to be addressed.

Fortunately, validation against actual plant data for severe accidents is not possible in a lot of cases due to lack of accidents. Still, the accident at TMI-2 /GOL 86/ does play an important role in the validation of ATHLET-CD and with new data becoming available on the Fukushima-Daiichi accidents /TEP 12/ , these will become more important as well. Apart from that, experiments should be preferred over code-to-code validation when feasible. Nonetheless, code-to-code comparisons and benchmarks are an important element of the overall ATHLET-CD validation strategy, as there is a lack of experimental data for severe accident phenomena and scaling distortions as well as corium simulants and electrical heating are an issue in several available experiments.

Whenever feasible, validation should be performed by **independent experts**, i.e. experts not directly involved in the development and implementation of a new feature or model. The validation by GRS will provide some independent validation for new developments eventually, but this aspect should be addressed in the validation plan. Also, validation and plant transient simulations should be done by experts, who are sufficiently familiar with the code, the relevant phenomena, and the reactor technology the validation case applies to. Support from experienced supervisors should be available. This is important for two reasons, firstly for setting up an adequate input deck for the validation case, and secondly for making appropriate expert judgements on the validation results. Moreover, an in-depth understanding of ATHLET-CD models (see the Models and Methods report

/LOV 21a/) or access to the source code will be helpful, particularly if the ATHLET-CD calculation does not arrive at the intended result. For code validation external to GRS, particularly in academia, acquiring the necessary **skills** and **experience** might not always be easy. As GRS supports external validation activities, there are firstly ATHLET-CD trainings offered by GRS available to ATHLET-CD users. Moreover, if external validation activities have been discussed with and endorsed by the ATHLET-CD validation team in advance, GRS validation experts can give advice and support during such activities.

One further important element of **external validation** should be done by code users who apply ATHLET-CD for deterministic safety analyses of nuclear facilities. As is the case for ATHLET /HOL 23/, the input deck should be suitably qualified /IAEA 19/. Due to the fortunate lack of real-life data on accidents, such qualification of ATHLET-CD input decks should be done on commissioning, steady state and transient data as with ATHLET. Consequently, before applying a new version of ATHLET-CD, the code users should validate it against suitable **input deck qualification tests**. For ATHLET-CD, it will be sensible to compare analysis results of a (fast-running) reference severe accident scenario, e.g. a LOCA combined with a long-term SBO. Assessing those results, problems in the input deck or the release version can be discovered. In the latter case, please inform GRS about the issue.

When deciding on **validation cases** to be investigated for ATHLET-CD, the following aspects should be considered:

- The validation case targets one or more models or features recently added to the ATHLET-CD master or release version.
- The validation case is new and has not yet been performed for ATHLET-CD. Also, if the last validation is older than 10 years, a repetition with the recent version is generally sensible.
- The validation case is part of an international benchmark.
- The geometry, materials and the conditions in the test facility are representative of an actual nuclear facility (minimisation of scaling distortions).
- The test facility description is comprehensive and sufficiently detailed for the development and qualification of a detailed ATHLET-CD model.

- The measurement values are of adequate resolution and accuracy for the quantities of interest, the test instrumentation is sufficiently detailed.
- The validation case is suitable for derivation of uncertainty ranges.
- The validation case is suitable for integration into CI on GitLab.

Obviously, ATHLET-CD should be capable of actually performing successfully in the intended validation. It would, e.g., be futile to try to validate ATHLET-CD for the prediction of phase separation in corium on a microscopic scale or for accidents in a sodium-cooled fast reactor, simply because ATHLET-CD lacks important models and will not be able to achieve the validation results with sufficient precision – or at all.

The ATHLET-CD validation matrices are based on a large set of tests, some of which are available publicly and some are subject to confidentiality agreements. For obvious reasons, validation should preferably be done against test results, which are publicly available. Still, GRS is always interested in further validation of its codes. Consequently, if you are interested in contributing to the external validation of ATHLET-CD in the framework of research and education, please contact the ATHLET-CD validation team as to the availability of GRS validation input decks. Conversely, if you want to validate ATHLET-CD against new and or confidential experiments not yet in the ATHLET-CD validation matrix, please contact the ATHLET-CD validation team as well. As GRS is interested in keeping validation cases available, transferring the input deck and validation data to GRS should be explored.

When performing a validation calculation for ATHLET-CD, it is important to clearly define the **scope** of the validation. The following points need to be taken into account.

- Identify the relevant phenomena for which ATHLET-CD is to be validated specifically and derive the relevant model outputs and related measurement data on which ATHLET-CD performance will be judged as a **figure of merit**.
- Identify the modules of ATHLET-CD (besides ECORE) that will need to be utilized to simulate the validation case. Check if the ATHLET-CD module include the **necessary models** for successfully predicting the figures of merits.
- Derive the **nodalisation** required for ATHLET-CD to adequately simulate the facility and the phenomena of interest. Determine if nodalisation studies need to be performed as part of the validation. Consider that there might be competing nodalisation

requirements and constraints from different code modules, e.g. ATHLET thermal-hydraulics, ECORE and SAFT, so that compromises might be necessary.

- Identify the ATHLET-CD models to be varied as **sensitivity cases** for the validation calculation. This should include a comparison of existing ATHLET-CD models vs. a new implementation, but should also consider nodalisation changes, different settings for important correlations (oxidation correlations) or user inputs (e.g. relocation velocity), standard numerics vs. usage of NuT, etc. as applicable and sensible.
- Check, if during the course of the test and/or for the ATHLET-CD simulation the occurring states likely are at or near bifurcation points or more complicated attractors for topologically distinct regions in the phase space of the test (i.e. so-called **cliff-edge effects** are relevant). At least in such cases, performing an **uncertainty analysis** with the GRS method /GLA 08/ should be seriously considered, if feasible. For that, the sample size should be chosen so that several figures of interest can be controlled simultaneously and/or the rank order is comparatively high so that quantiles are better determined. See /HOL 23/ for more information. Given the often commonly long simulation times for severe accident analyses, full uncertainty studies might be necessary to plan from the outset and otherwise resort to essential sensitivity cases.
- Determine the necessary sensitivity cases on simulation model **stability** and **convergence**, e.g. by varying integration settings like `EPS`, `GRESCH`, `HMAX`, or the `FCLIMx` settings under `CW INTEGRAT`. Similarly, determine if both **serial** and **parallel program versions** should be applied and if different settings for NuT should be used during the calculation.
- If applicable, define **restart** points at which the consistency of a restart with the reference calculation can be checked.
- Define acceptance criteria on **mass errors** (both overall as well as for short time periods) as computed by ATHLET/CD.
- Discuss with the ATHLET-CD validation team if the validation case should be prepared for use in the **CI** under GitLab.

The validation calculation should be done based on this scope. The input deck should be refined until either a good agreement of test data to ATHLET-CD predictions is reached, or a conclusion is reached that ATHLET-CD is not adequately simulating the test in question. For this, however, changes to the validation input deck should be limited to those that are firstly necessary to capture the **relevant phenomena** of the scenario and that secondly realistically **applicable to nuclear reactor and facility** input decks. Increasing the resolution of the nodalisation or fine-tuning several of the model parameters accessible via the input away from default values can serve a valid purpose in the context of validation. These would include derivation of nodalisation recommendations, analysing limits and predictiveness of ATHLET-CD models, deriving improvements to existing models, and identifying the need for new models and features. However, for applications where experimental data are missing, such refinements would either not be possible, lead to unreasonable simulation times, or might even lead to the suppression of valid code predictions not in line with user expectations and should therefore be avoided. Consequently, validation calculations should be done with models that are comparable to models used in safety analyses.

Another important question is which ATHLET-CD **version** should be used for validation calculations. The following rules are applicable generically, but for a specific case the ATHLET-CD validation team might decide to select a different version for the validation.

- Validation should support the development effort in a timely manner. Consequently, validation should be performed on adequately stable feature branch or master versions as foreseen in the validation plan of a new development. As these are **alpha versions** of ATHLET, the selection of specific versions as a basis for validation requires coordination between the development and validation team. Similarly, regular non-regression testing via CI should be performed on the master branch and possibly long-running development branches.
- Validation in support of a release obviously needs to happen on the designated **beta versions** defined by the ATHLET development team.
- Participation in **code benchmarks** or similar activities should be done with release versions. If necessary and reasonable, a beta version might be used, if agreed to by the ATHLET validation team.
- **External validation** activities should generally use release versions, unless in support of own or shared developments.

Finally, **non-validation applications** should generally only be done with release versions. This does apply to safety research as well as input model qualification and improvement, unless such activities are included into the validation activities for the current development by the ATHLET-CD validation team. Application of ATHLET-CD for **safety**

analyses in support of safety cases should only be done with release versions. Please note relevant good practice as described in IAEA SSG-2, Rev. 1, for the use of computer codes in safety assessments /IAEA 19/. Importantly, in addition to qualifying the input deck you should consider validating the release version of ATHLET-CD for your purposes against suitable qualification tests for your model.

4.1 Validation supported by GitLab

It is good practice that input decks used for validation are subject to version control, they should therefore be managed via git and/or GitLab. In the ATHLET Programmer's Manual /JAC 25/, a more detailed explanation for using GitLab when developing for ATHLET is given. The overall process for using GitLab to support validation is described in the ATHLET Validation report /HOL 23/ and also transferrable.

Specific to ATHLET-CD validation is the question if the same facility is or will likely be used both for ATHLET and for ATHLET-CD validation (which can be the case). Then, it is recommended to plan and coordinate between the ATHLET and ATHLET-CD validation teams so that the base ATHLET model and the ATHLET-CD are as compatible as feasible.

4.2 Documentation of Validation

The documentation of validation is described in the ATHLET Validation report /HOL 23/. The advice given there is fully applicable also for ATHLET-CD and is not repeated here. Because for the derivation of an ATHLET-CD model significantly more expert judgment on modelling choices will have to be made, and as ATHLET-CD does offer more choices in modelling options without a clear recommendation of a default value or approach, documenting the main modelling choices in an **input deck description** in a traceable manner is even more important than for ATHLET.

4.3 Release Procedures

The overall release procedure for ATHLET-CD (and also AC^2) is described in the ATHLET Programmers Manual /JAC 25/. The following is therefore restricted to the specifics for the validation of ATHLET-CD prior to a release.

Prior to the release of a new ATHLET-CD version, either as a general release or as an internal release (some patch versions might be available only within GRS), a set of experiments from the validation matrices is calculated to check the overall capability of the new code version as the final step of the overall quality assurance process. These tests consist of:

- samples (standardized calculation examples) provided with ATHLET-CD and
- the 'basis' validation cases (including separate effect tests and integral tests).

These basic test cases are supplemented by targeted validation calculations as necessary depending on the changes in the code compared to the previous release. The selected test cases ensure that changes applied to solve one modelling problem do not affect other individual models or the overall simulation capability. A further intention is to compare the results of the new version with those of earlier versions.

For beta versions designated from time-to-time by the ATHLET-CD development team for the used in specific research projects, an analogous by even more simplified process is applied. Relying on the CI performed on the master and GitLab, and considering dedicated verification and validation results performed on alpha versions, it can be concluded in specific cases that a certain tagged commit in the master can be used as a beta version.

In addition to the comparison with the previous versions and experimental data, three kinds of tests are performed on several validation calculations:

- restart tests,
- optimization tests, and
- check of portability.

The restart capability is checked to ensure that all necessary data are stored in the restart file. Usually, a validation calculation is performed in one run, with one or more restart time points defined during the transient. Afterwards, a restart time point is selected, and a restart run is performed. The code must continue the calculation after a restart with identical results in comparison to the original run, if the input is not changed. However, due to known problems in the code, this is not always ensured. While GRS is working on resolving the underlying issues, the user should check if the restart points defined in the input deck (or imposed during coupled calculation with COCOSYS as AC²) produce relevant inconsistencies. In the latter case, please raise this as an issue with the ATHLET-CD development team.

ATHLET-CD can be executed in parallel mode utilizing several CPUs sharing a common memory (SMP computer architecture). This parallelization is based on the OpenMP standard. Parallel ATHLET-CD simulations must provide results which are identical to those achieved with serial applications. Moreover, data conflicts like race conditions must be reliably avoided. These requirements are periodically proven through the comparison of appropriate test cases. However, as the specific models for severe accidents have not yet been parallelized, all parallel mode issues should be ATHLET issues.

Most of the FORTRAN compilers available on different platforms offer several levels of compiler optimization. Optimization is a valuable tool to improve runtime performance, i.e. to reduce the computational time for a given code application. Some options, like loop optimizations or in-lining, can affect processing sequences and can cause significant deviations of calculated results. The adopted procedure for ATHLET-CD is to run one or more validation calculations on a given platform with the debug option (no optimization) of the corresponding compiler, and then to repeat the calculations with the optimization level recommended for the applied compiler (default). Both calculations must produce quasi-identical results (unless the case is at or near an attractor for a cliff-edge effect, see above). Eventual noticeable deviations are investigated thoroughly. They can indicate incorrect programming, or even compiler malfunctions.

One main feature of ATHLET and ATHLET-CD – including its tools – is the that it can be run under Windows as well as Linux. Prior to a code release, a subset of test cases is run on reference Windows and Linux distributions at GRS. Code results between Linux and Windows versions have to be quasi-identical as well. Similarly, the whole AC² distribution including the tools provided therein is tested on these platforms.

5 Selected Validation Calculations for the Current Code Version

This chapter presents the analyses of the integral experiments included in the basis validation matrix. These examples cover a wide range of severe accident phenomena and give an insight into the actual performance of the current code version when applied to new challenging experimental findings.

At present, the following calculations are included in this chapter:

- Phébus SFD-B9+
- CORA-13
- CORA-W2
- QUENCH-06
- Phébus FPT-1
- Phébus FPT-3
- QUENCH-16
- QUENCH-18
- LIVE L-10 und L-11
- TMI-2

The tests cover a wide range of phenomena occurring during a severe accident, different heating methods like electrical or nuclear heating, different scales, different oxidation phenomena as well as fission product release and transport. Finally, the accident TMI-2 is discussed.

5.1 PHÉBUS SFD-B9+ (ISP-28)

The test B9+, performed in January 1989 at the PHÉBUS SFD facility of the French CEA Research Centre CADARACHE, was chosen as the experimental basis for the first international standard problem in the area of severe accidents /ADR 92/. Its objectives were to investigate the main phenomena occurring during the early phases of a severe fuel damage (SFD) accident in a PWR: cladding oxidation, the cladding mechanical behaviour, the simultaneous dissolution of UO_2 and ZrO_2 by molten Zry and melt relocation. ISP-28 was conducted as a “semi-blind” calculation, with given thermal boundary conditions of the shroud surrounding the fuel test bundle.

Fifteen international organizations from 12 countries and with eight different codes participated in this ISP. GRS took part with the code ATHLET-SA, an earlier version of ATHLET-CD.

The current input dataset for ISP-28 is based on a post-test calculation with the code version ATHLET-CD Mod 2.0A/1.1K /ERD 04/.

5.1.1 Test Facility

The PHÉBUS SFD test facility basically consisted of the PHÉBUS driver core supplying the test fuel with nuclear power, a SFD loop located on the vertical axis of the driver core, and a pressurizer water loop working as an independent and external cooling of the SFD loop. The main component of the SFD loop was the test stringer. It consisted of three injection lines (steam, hydrogen, helium) for the gas supply, an electrical superheating device to increase the gas inlet temperature to the level required in the test scenario, the test section, and an exit line, which discharged the gaseous flow to a pressure regulating system and to a storage tank.

The fuel bundle inside the test section consisted of 21 non-irradiated UO_2 fuel rods in a 12.6 mm pitch matrix. The total fissile height was 0.8 m. Two Inconel spacer grids were located on either side of the mid-plane at elevations 138 mm and 661 mm from the bottom of the fissile column. The rods were pressurized with helium at 0.7 MPa in cold conditions.

The insulating shroud of the bundle was a multi-layer structure. The octagonal inner zircaloy liner (0.6 mm thick) was surrounded by a thick porous ZrO_2 layer (94 mm external diameter), a dense ZrO_2 layer (1 mm thick) and an external stainless steel tube (8 mm thick).

Temperature measurements of the fuel, cladding, fluid and shroud at different radial locations and elevations were taken with different types of thermocouples. The hydrogen concentration in the gas mixture at the loop outlet was measured continuously by means of a mass spectrometer.

5.1.2 Test Conduct

The experimental scenario consisted of three phases (Fig. 5.1**Experimental scenario for test SFD-B9+ /ADR 92/**):

- Oxidation phase (from 0 to 8370 s),
- Heat-up phase (from 8370 to 13860 s)
- Final phase (from 13860 s to 18000 s)

The first oxidation phase was performed with pure steam flow. The system pressure, the steam mass flow rate and inlet temperature were kept constant at the following values: 1.9 MPa, 2 g/s and 528 K, respectively. Three power steps (4 kW, 8.8 kW and 11.5 kW) allowed rod temperature levels of 1000 K, 1350 K and 1600 K, respectively, to be reached at the hottest level. Then a slow power increase from 11.5 kW to 14.5 kW during about one hour resulted in a slow heating from 1600 K to about 1800 K. A new power increase from 14.5 kW to 18 kW allowed the effectively complete oxidation of the upper bundle region. Ballooning of the pressurized rods was avoided by the low temperature melting point of the fusible seal in the upper plug of each rod. At the end of the oxidation phase, the cooling gas was switched from steam to helium.

The second heat-up phase was performed with pure helium injection. At a pressure of 1,9 MPa, a helium mass flow rate of 0.5 g/s and an inlet gas temperature of 528 K were kept constant during this high temperature phase. Five power steps were performed leading to a maximum rod temperature of about 2750 K.

During the final phase, step reductions of the nuclear power enabled a slow cooling down in order to keep the previous bundle geometry unchanged. The pressure was reduced to 0.4 MPa at 14153 s. During this phase, a mean helium mass flow rate of 0.5 g/s with an inlet temperature of 528 K was maintained up to the final time of the test at 18000 s /ADR 92/.

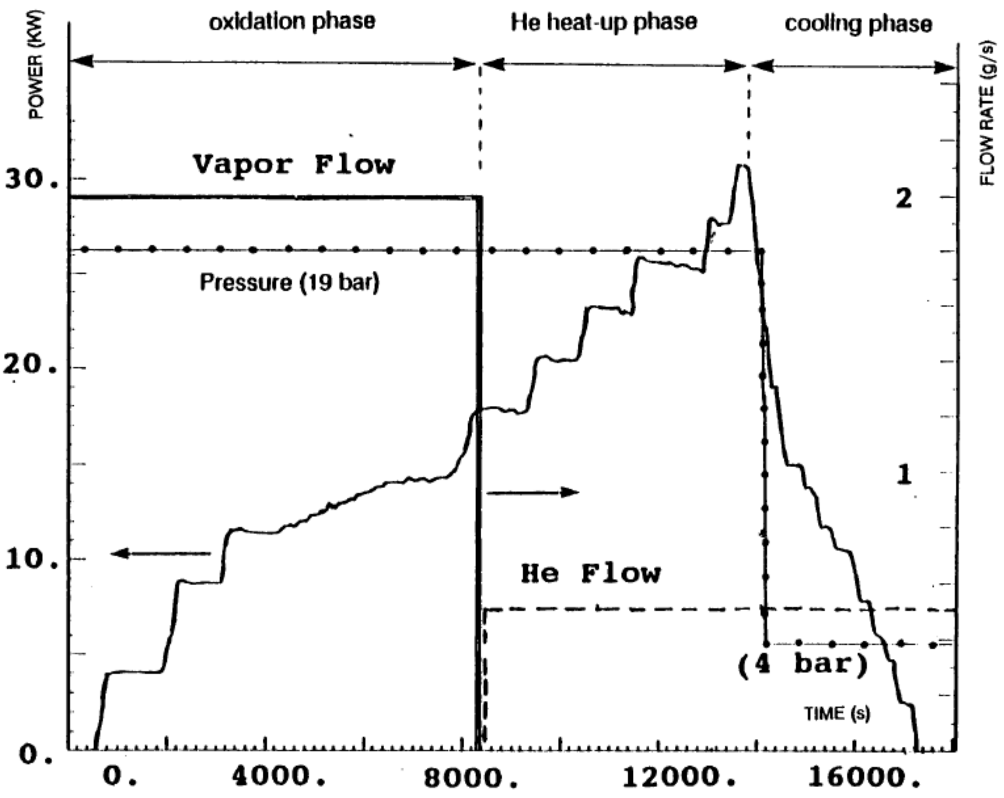

Fig. 5.1 Experimental scenario for test SFD-B9+ /ADR 92/

5.1.3 Input Dataset

5.1.3.1 Nodalisation

The ATHLET-CD nodalisation for the PHÉBUS SFD test section is depicted in Fig. 5.2. It comprises, among others, the bundle fluid channel, represented by one single thermo-fluid object (TFO) and subdivided into 17 axial nodes (15 nodes within the active length). The rod bundle is simulated within the code module ECORE by three concentric rings, an inner ring (`ROD1`) containing the central fuel rod, a second ring containing eight fuel rods (`ROD2`), and an outer ring with the remaining twelve fuel rods (`ROD3`).

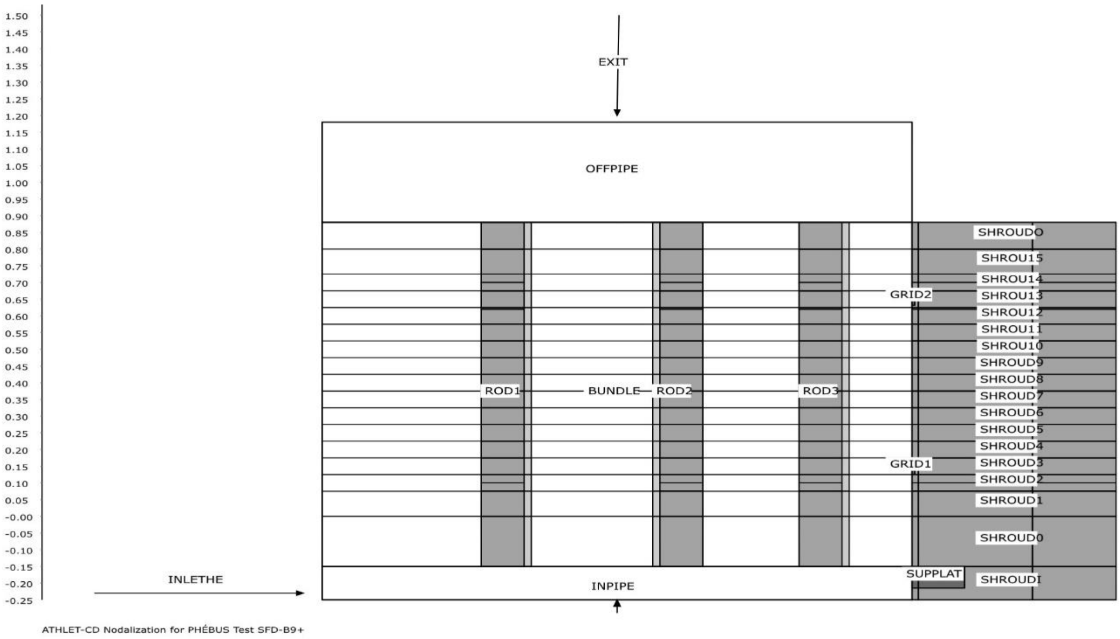

Fig. 5.2 ATHLET-CD Nodalisation for Test SFD-B9+

In addition, the spacer grids, the lower bundle support plate and the shroud with its multi-layer structure have been modelled with heat conduction objects. The thick porous ZrO_2 layer has been combined which the thin dense layer to a single material with average properties. The gap between liner and the porous ZrO_2 layer, filled with helium, has been taken into account by an adequate heat transfer coefficient.

The steam and helium flows have been simulated by fill junctions at the bottom of the bundle.

5.1.3.2 Model Options

The main input parameters and modelling options applied for the simulation of test SFD B9+ are summarized in Tab. 5.1.

Tab. 5.1 Main input parameters and modelling options for test SFD-B9+

Parameter	SFD-B9+
Zr oxidation correlation (IOXMOD = 3)	Leistikow (T < 1800 K) Prater-Courtright (T > 2600 K)
Maximum effective oxide layer thickness (bundle/shroud)	1.0 m
Upper limit of relative steam availability	0.1
Melting temperature of metallic cladding	2030 K

Parameter	**SFD-B9+**
Lower clad failure temperature (low cladding oxidation)	2250 K
Upper clad failure temperature (high cladding oxidation)	2450 K
Minimum oxide layer thickness for upper failure temperature	0.3 mm
Fuel melt temperature (solidus)	2600 K
Fuel melt temperature (liquidus)	2800 K
Metallic melt relocation velocity	0.03 m/s
Ceramic melt relocation velocity	0.03 m/s

The following experimental data have been used as boundary conditions for the calculation: the bundle power (including the changes in the axial profiles due to material relocation, as given in /ADR 92/), the steam and helium mass flow rates and their temperatures at bundle inlet as well as the system pressure.

One of the main sources of uncertainty for the calculation is related to the estimation of the radial heat transfer from the bundle to the external pressurized cooling loop. The main parameter controlling the radial heat transfer is the thermal conductivity of the porous ZrO_2 layer. Considering the information presented in /ADR 92/, the thermal conductivity of the porous layer has been artificially increased in order to get a better agreement with the measured shroud temperatures in different elevations /ERD 04/.

5.1.4 Main Results

The main results of the post-test calculation of test SFD-B9+ are shown in Fig. 5.3 to

Fig. 5.6. In these figures, the red curves refer to the results obtained with the current version 3.5, whereas the blue curves refer to the previous version 3.4. The corresponding experimental results are depicted by the black curves.

Despite the uncertainties related to the radial heat transfer through the shroud, the code can reproduce the thermal evolution in the fuel bundle satisfactorily. In general, the temperatures in the lower bundle regions are overestimated, whereas the temperatures in the upper elevations are slightly underpredicted.

A very good agreement between experiment and calculation could be reached with respect to the bundle oxidation. The dynamics of the oxidation processes (Fig. 5.5) as well as the total amount hydrogen produced (40.8 g against 39.5 g in the experiment) could be well reproduced by the code.

Considerable deviations can be observed with respect to melt relocation and bundle axial profile at the end of the experiment. ATHLET-CD calculates melt accumulation and partial flow blockage (53.5 %) at elevation 0.1 m, whereas the examination performed after the experiment indicated the formation of a partial blockage (51 %) at elevation 0.26 m. The code does not take into account the melting of the upper grid spacer and part of the metallic liner (both simulated as HECU elements), nor the retention capability of the lower grid spacer, which explains part of this finding.

The numerical results of the new code version 3.5, including the computational performance (Fig. 5.6) are almost identical to those of the previous release version 3.4.

5.1.5 Main Findings

Despite the uncertainties in predicting the radial energy transport through the shroud the post-test calculation of test SFD-B9+ shows satisfying results concerning the bundle temperature behaviour compared to the experimental data. A very good agreement could be obtained with respect to cladding oxidation.

The modelling of the dissolution of UO_2 and ZrO_2 by molten Zry could only be assessed qualitatively. The simulation of bundle melting and relocation was impaired by the lack of corresponding models for grid spacers and for the metallic liner.

The new code version does not change the quality of the calculated results. The numerical results are almost identical to those of the previous release version, and very similar to those reported in /ERD 04/.

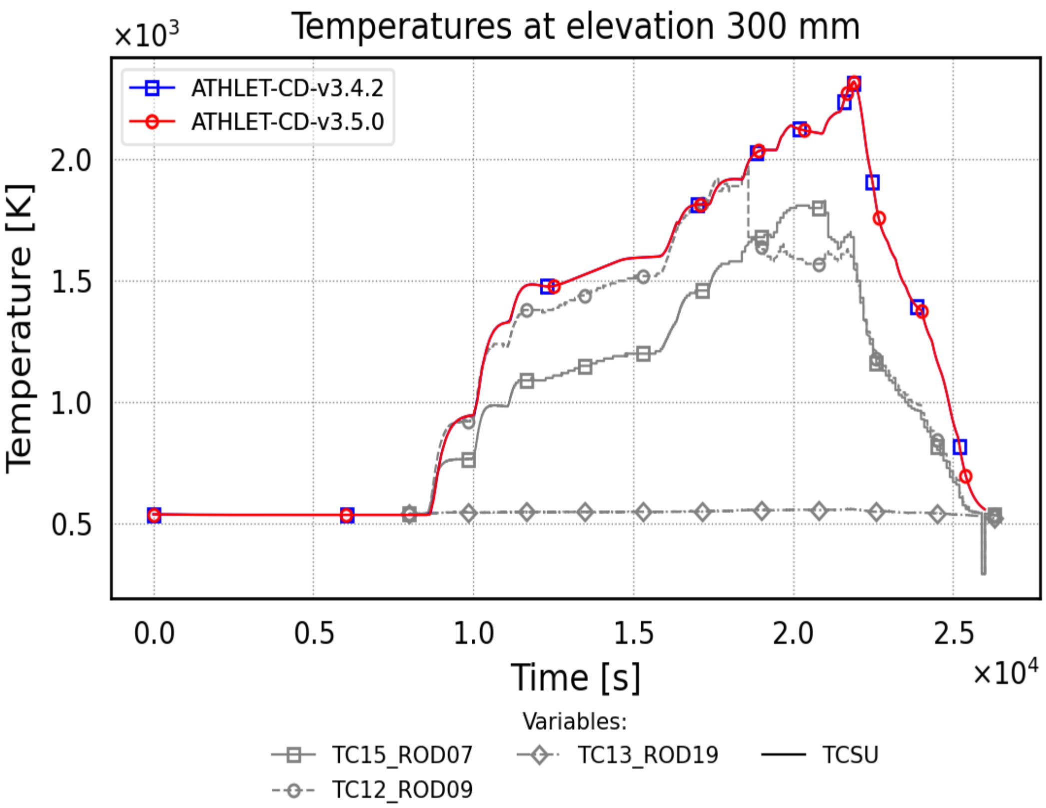

Fig. 5.3 SFD-B9+ – Rod temperatures at elevation 300 mm

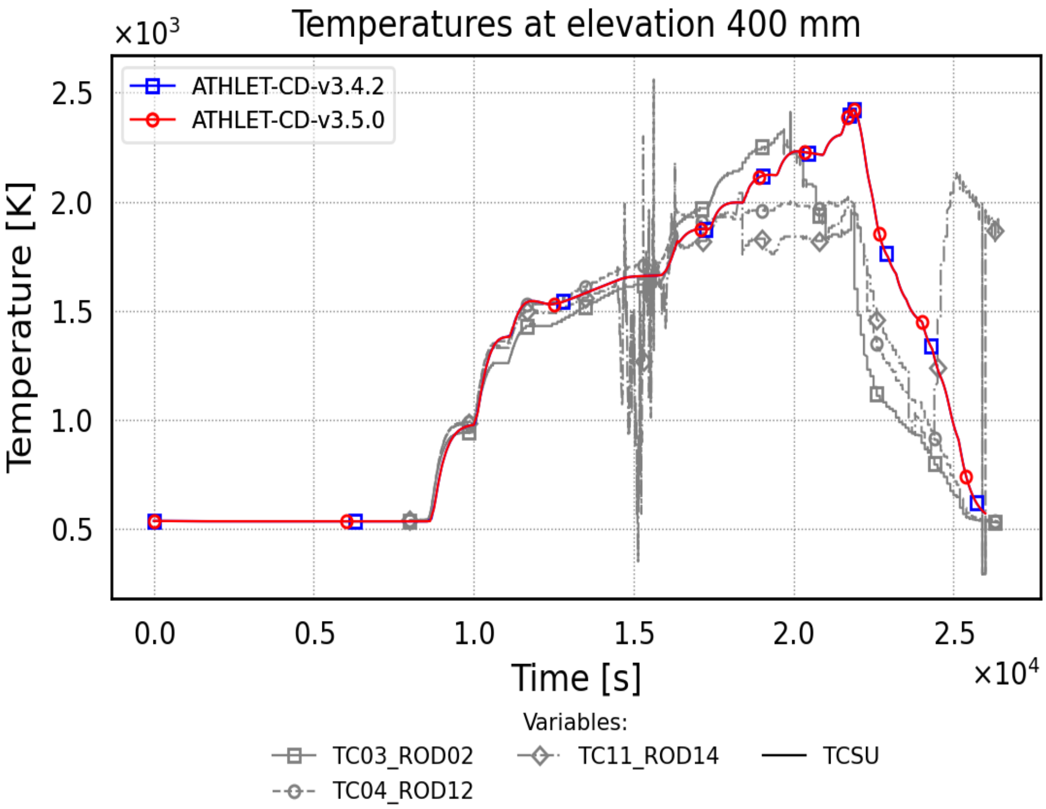

Fig. 5.4 SFD-B9+ – Rod temperatures at elevation 400 mm

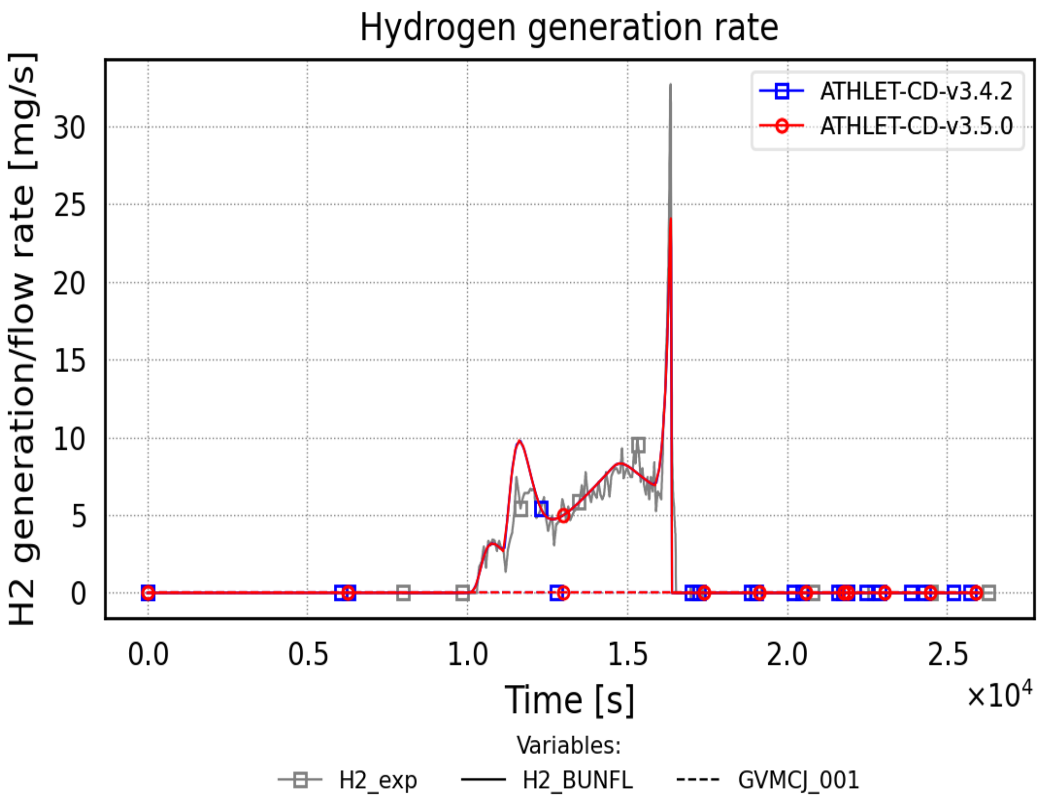

Fig. 5.5 SFD-B9+ – Hydrogen generation rate

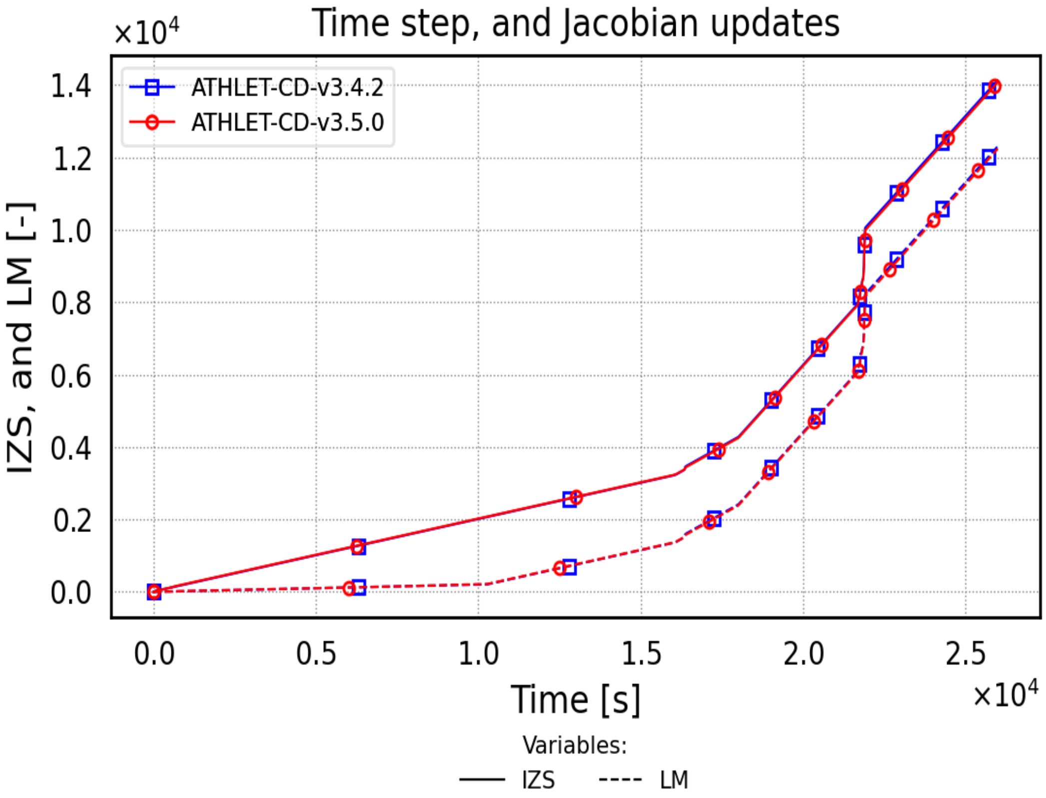

Fig. 5.6 SFD-B9+ – Number of time steps and Jacobian calculations

5.2 CORA-13 (ISP-31)

The out-of-pile experiment CORA-13 has been performed in the former Kernforschungszentrum Karlsruhe (KfK) in November 1990. The main objectives of the test were to investigate the behaviour of PWR during early core degradation and fast cooldown due to bundle refilling. It has been chosen as experimental basis for the International Standard Problem ISP-31, conducted as a “blind” exercise /OEC 93/. Nine organizations with five different codes participated in this ISP. Boundary conditions, which were not measured but which were necessary for test simulation, were estimated with ATHLET-CD.

5.2.1 Test Facility

The CORA experimental program at the Karlsruhe Institute of Technology (KIT, formerly KfK - Kernforschungszentrum Karlsruhe) was conducted between 1987 and 1993. Its main objective was to investigate the integral behaviour of typical light water reactors (LWR) fuel bundles under severe accident conditions. The decay heat was simulated by electrical heating. The test bundles contained all materials normally used in LWR fuel elements: pellets, cladding, grid spacers, absorber rods and guide tubes were typical to those of commercial LWRs concerning their composition and radial dimensions.

A total of 19 tests have been performed in the CORA facility: 11 PWR bundle tests, six BWR bundle tests, and two VVER bundle tests. For test CORA-13, the PWR-typical bundle consisted of 16 heated, 7 unheated and two absorber rods. The absorber material (Ag 80%, In 15%, Cd 5%) was sheathed in stainless steel and surrounded by a Zry-4 guide tube. The bundle was surrounded by a Zry-4 shroud, which in turn was surrounded by an insulating layer of ZrO_2 fibre.

5.2.2 Test Conduct

The general procedure of Test CORA-13 consisted of three main phases /HAG 93/:

- a gas pre-heating phase (0 s -3000 s),
- a transient heat-up phase (3000 s – 4900 s) with a power increase from 6 kW to 27 kW and a steam flow rate of 6 g/s,
- and a cooling phase after 4900 s.

During the gas pre-heat phase, 8 g/s pre-heated argon flowed through the bundle and a low constant electric power input of about 0.65 kW was applied. During this period, the temperature in the insulation reached a level which was high enough to avoid steam condensation. To keep the videoscope windows clear, a total flow of 1 g/s argon was directed to the front of the windows of the videoscopes. The pressure in the system was controlled to 0.22 MPa.

During the transient phase, the temperature increase was initiated by raising the electric power input from 6 to 27 kW at a constant rate. At 3300 s, a steam flow of 6 g/s was added to the system. The cooling phase was initiated by the rise of the quench cylinder at 4870 s and the shutdown of the electric power at 4900 s. The average velocity of the rising quench cylinder was 1 cm/s.

5.2.3 Input Dataset

5.2.3.1 Nodalisation

The input model for the CORA facility (Fig. 5.7) comprises, among others, the bundle fluid channel, composed by two parallel fluid channels connected via cross flow junctions, and subdivided into 13 axial nodes (10 nodes within the heated length). The rod bundle is simulated within the code module ECORE by four concentric rings, an inner ring (`ROD1`) containing the central unheated rod, a second ring containing four heated rods (`ROD2`), a third ring containing six unheated rods and two absorber rods (ROD3) and an outer ring with twelve heated rods (`ROD4`). In addition, the spacer grids, the shroud with its ZrO_2 thermal insulation, and the outer jacket with the three-layer high temperature shield have been simulated.

The argon and steam flows, as well as the quenching by water in Test CORA-13 have been simulated by fill junctions at the bottom of the bundle.

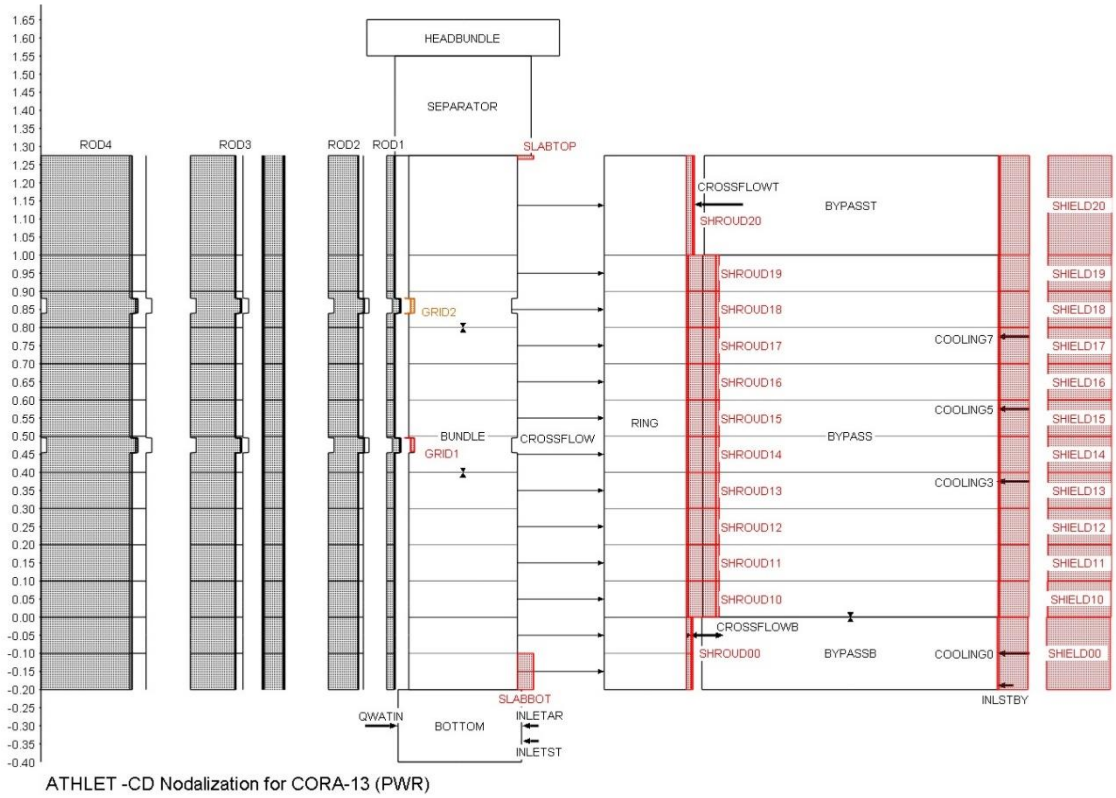

Fig. 5.7 ATHLET-CD Nodalisation for Test CORA-13

5.2.3.2 Model Options

For the simulation of test CORA-13, input parameters and modelling options as recommended by the code user's manual /LOV 21b/ have been applied. For the calculation of Zr oxidation at higher temperatures, however, the correlation of Urbanic-Heidrick has been used instead of the correlation of Prater-Courtright normally applied for the calculation of QUENCH experiments. Tab. 5.2 summarizes the main code input parameters concerning the calculation of Zr oxidation and rod melt and relocation.

For the external resistance per heated rod, which takes into account the voltage drop across the sliding contacts at the rod extremities as well as at the wires connecting the sliding contacts to power supply, a value of 4 mΩ has been used.

Tab. 5.2 Main input parameters and modelling options for test CORA-13

Parameter	CORA-13
Channel flow area (due to slightly different shroud)	0.00527 m^2
Zr oxidation correlation	Cathcart (T < 1800 K) Urbanic-Heidrick (T > 1900 K)
Melting temperature of metallic cladding	2200 K
Lower clad failure temperature (low cladding oxidation)	2200 K
Upper clad failure temperature (high cladding oxidation)	2400 K
Minimum oxide layer thickness for upper failure temperature	0.3 mm
Melt relocation velocity	1 mm/s
Maximum effective oxide layer thickness (bundle/shroud)	0.1 mm
Upper limit of relative steam availability	0.3
External resistance per heated rod	4 mΩ

5.2.4 Main Results

Some of the main results of the post-test calculation of Test CORA-13 with the new version ATHLET-CD 3.5 are depicted in Fig. 5.8 to Fig. 5.12.

Fig. 5.8 shows the calculated and measured temperatures of cladding at the elevation 750 mm from the bottom of the active fuel. The bundle temperatures are satisfactorily reproduced by the code. However, the cladding temperatures at the bottom of active bundle (< 150 mm) were slightly overestimated in comparison to the experiment.

As shown in Fig. 5.10, the total hydrogen production was calculated within the uncertainty of the experimental data. The contribution of the oxidation of fuel rods to the total H_2 production (about 65 %) is also shown in this picture. Version ATHLET-CD 3.5 results are basically the same as for the previous code version 3.4. Additionally, the flooding of the bundle is predicted qualitatively correct compared to the experiment, which is shown in Fig. 5.11 by the calculated top and bottom quench front in comparison to the measured water level.

The simulation results of the new code version are practically identical to those of the previous version. Moreover, as shown in Fig. 5.12, the computational effort for the simulation of the quenching phase is noticeably lower with the new code version 3.5 compared to 3.4 (less time steps, respectively less calculations of Jacobian matrices), but that change is not yet significant.

5.2.5 Main Findings

In general, a good agreement between calculated and measured data with respect to the evolution of cladding temperatures has been obtained, with a slight overestimation at the bottom and a slight underestimation at the top of the active bundle. The hydrogen production has been calculated within the uncertainty of the measured data.

The results of the new version 3.5 are practically identical to those of the previous versions.

One main discrepancy of the calculated results is related to the missing modelling of melt retention due to the spacer grids – respectively not applied for comparison reasons –, leading to a shift of the blockage profile and an overestimation of the temperatures at elevations below the spacer grids. This should be taken into account in the further code development.

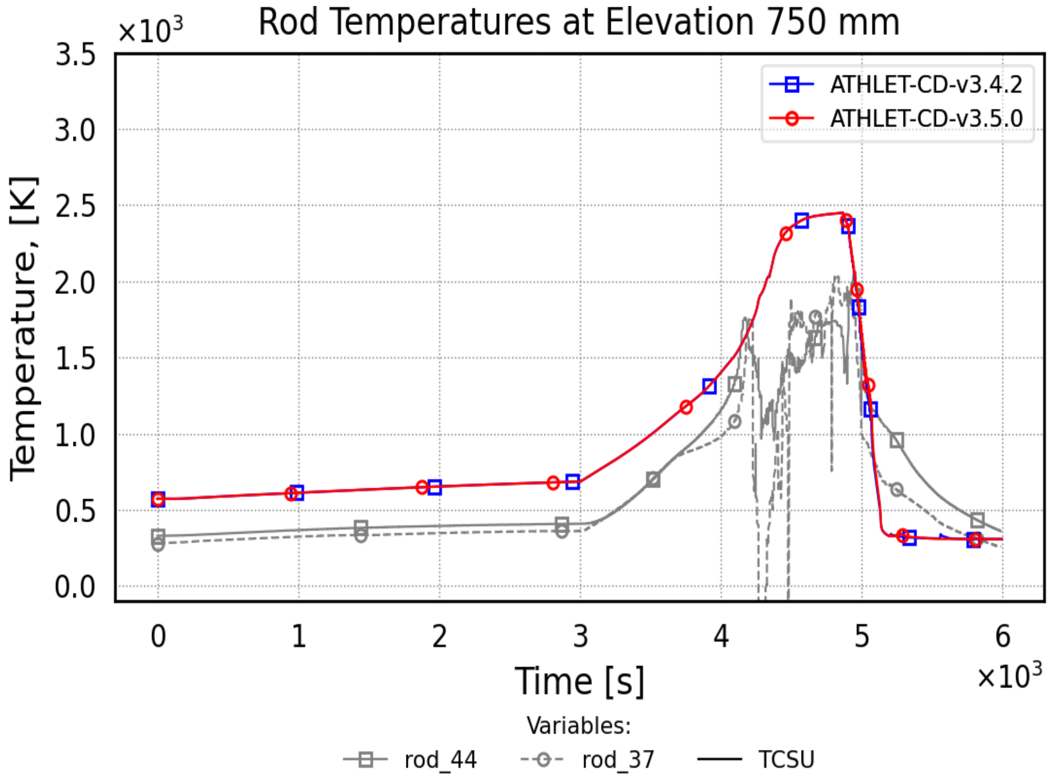

Fig. 5.8 CORA-13 – Bundle temperatures at elevation 750 mm

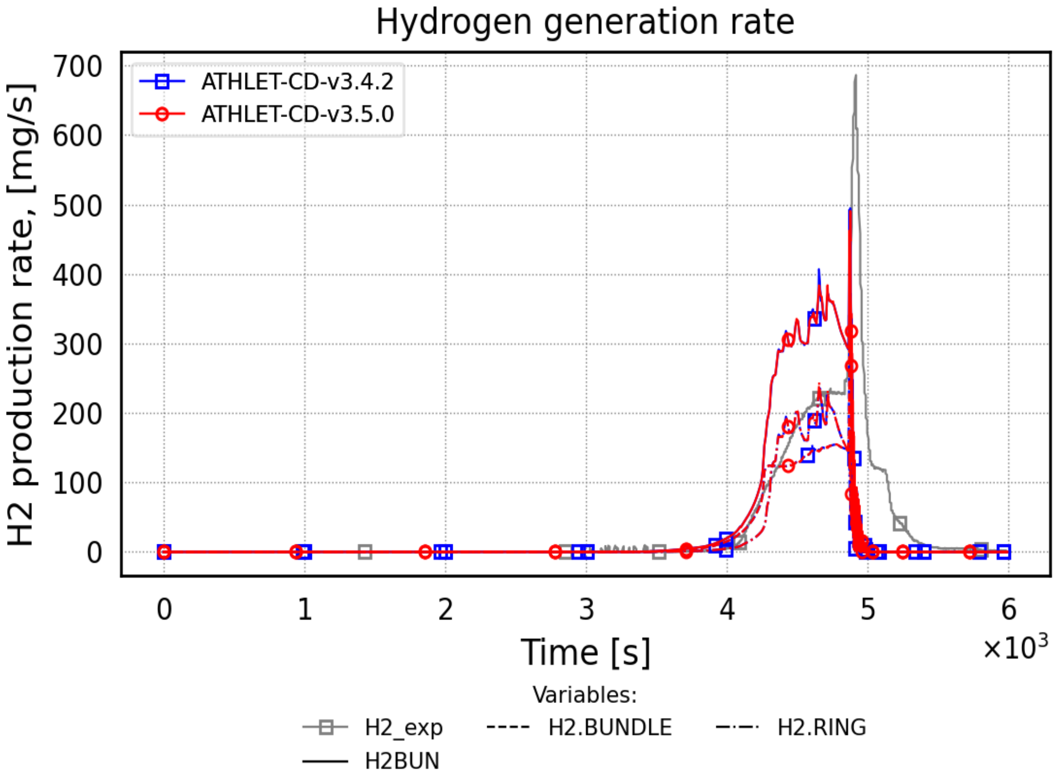

Fig. 5.9 CORA-13 – Total hydrogen production rate

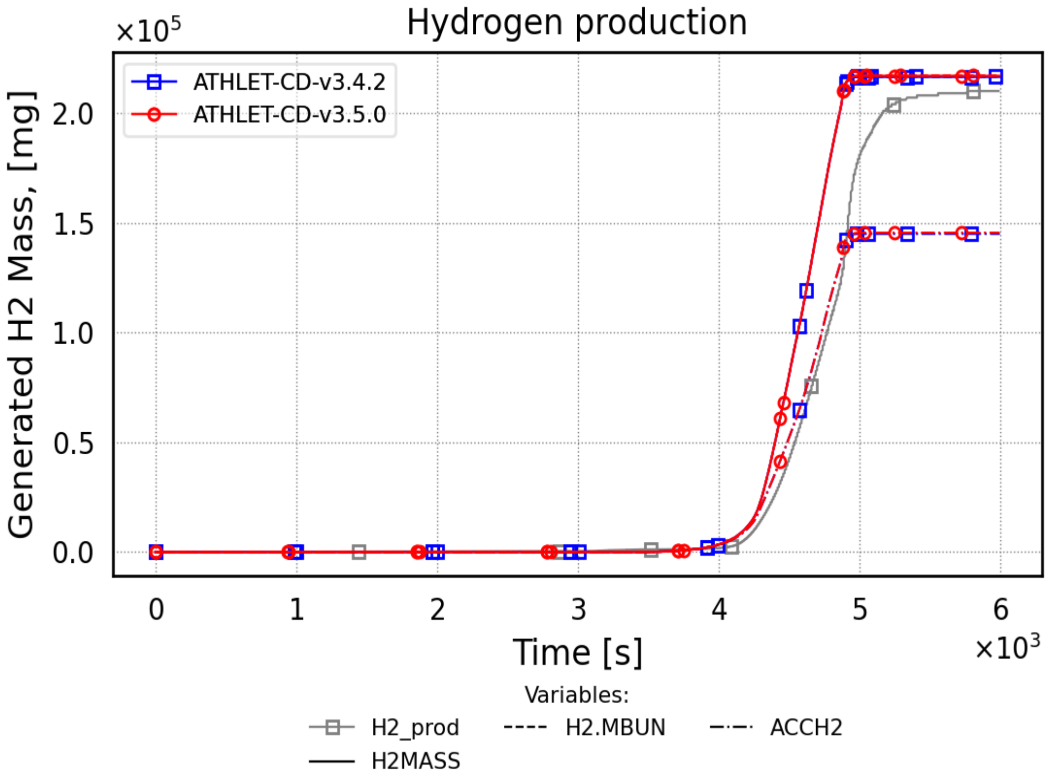

Fig. 5.10 CORA-13 – Total hydrogen production

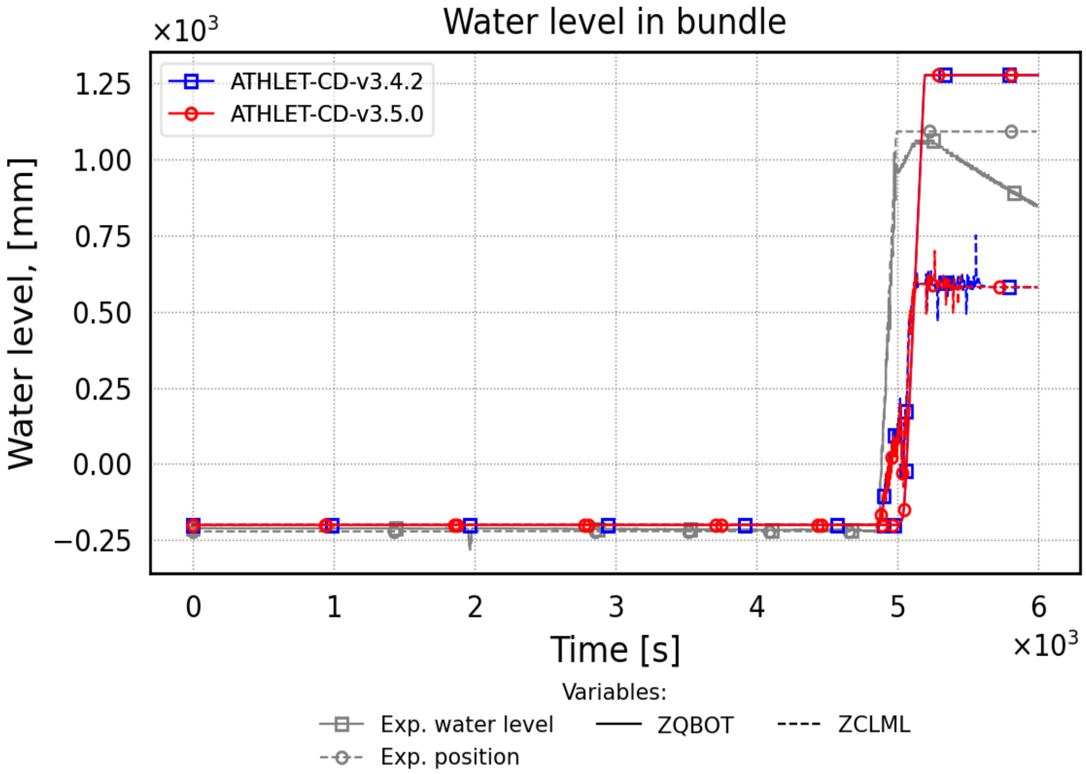

Fig. 5.11 CORA-13 – Water level in the bundle

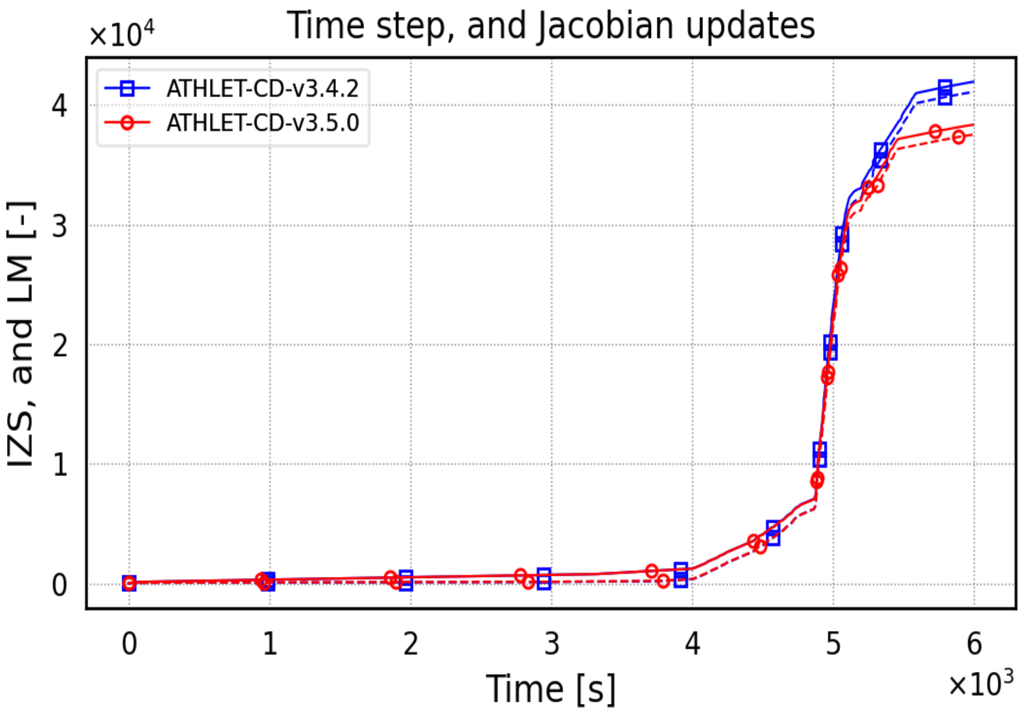

Fig. 5.12 CORA-13 – Number of time steps and Jacobian calculations

5.3 CORA-W2 (ISP-36)

The International Standard Problem ISP-36 was the first VVER-related ISP in the field of severe accidents. The out-of-pile experiment CORA-W2 was conducted in February 1993 at the then Kernforschungszentrum Karlsruhe. The main objectives of this test were the investigation of temperature and material behaviour as well as hydrogen generation of a VVER fuel bundle, especially the influence of the hexagonal grid and the different material combinations (cladding, grid spacers and B_4C absorber rods) compared to western-type PWRs. The experimental data include boundary conditions, bundle temperatures, hydrogen generation and the final bundle configuration after cooldown /OEC 96/.

The ISP-36 was conducted as a “blind exercise” (only thermal initial and boundary conditions were given). Results to the ISP were submitted by 22 participants from 17 international organizations with six different computer codes. GRS took part in the ISP with the code ATHLET-CD Mod 1.1B.

The current input dataset for the ISP-36 is based on a post-test calculation with the code version ATHLET-CD 3.1A /BAL 17/.

5.3.1 Test Facility

The CORA out-of-pile facility was designed to investigate the behaviour of LWR fuel assemblies under severe fuel damage accident conditions. Pellets, cladding, grid spacers and absorber rods are typical to those of the investigated LWR type. In test CORA-W2 original UO_2 pellets, Zr1%Nb cladding, SS grid spacers and B_4C absorbers inside stainless steel cladding were used.

The central part of the facility was the fuel rod bundle, composed of 19 fuel rod simulators. Thirteen of them were electrically heated by central tungsten heating elements. Five rods were unheated and one position within the bundle was filled with the absorber rod and its guide tube. The heated and unheated rods were filled with annular UO_2 pellets. The rod claddings were made of zirconium – 1 % niobium alloy. Three stainless steel grid spacers of 20 mm depth were mounted into the bundle at –5 mm, 210 mm and 610 mm elevations /HAG 94/.

The shroud surrounding the bundle was also made of Zr1%Nb and insulated with a 20 mm thick layer of ZrO_2 fiber material in order to obtain a uniform radial temperature distribution. A high temperature radiation shield surrounded the bundle and shroud assembly. Two videoscopes, at 600 mm and 800 mm, were used in the test to observe the materials behaviour and their relocation during the experiment.

5.3.2 Test Conduct

The general procedure of Test CORA-W2 consisted of three main phases:

- a gas pre-heating phase (0 s-3000 s),
- a transient heat-up phase (3000 s – 4500 s),
- and a cooling phase after 4500 s.

During the pre-heating phase there was a flow of 8 g/s argon through the bundle under a low constant electric power input of about 0.52 kW. In this phase the temperature in the insulation reached a level high enough to avoid steam condensation. At 2760 s, the argon flow was reduced to 6 g/s.

Between 3000 s and 4500 s the electric power was increased from 2 kW to 14.5 kW with a ramp rate of ca. 0.01 kW/s to achieve the initial heat-up rate of 1 K/s. At 3300 s, a constant flow of 4 g/s superheated steam was added to the argon flow. At about 4150 s, the slow temperature rise was followed by a sudden increase caused by increasing electric power together with the energy from the exothermal zirconium-steam reaction.

The electric power supply was turned off at 4500 s, together with the steam supply (test termination by slow cooldown under argon flow). The pressure in the system during the test was controlled to 0.22 MPa.

5.3.3 Input Dataset

5.3.3.1 Nodalisation

The ATHLET-CD input model for the test CORA-W2 (Fig. 5.13) comprises among others the bundle fluid channel, composed by two parallel fluid channels (`BUNDLE` and `RING`) connected via cross flow junctions, and subdivided into 19 axial nodes (10 nodes within the 1000 mm heated length). The rod bundle is simulated within the code module ECORE by three concentric rings, an inner ring (`ROD1`) containing the central heated rod, a second ring containing five unheated rods and the absorber rod (`ROD2`), and an outer ring with twelve heated rods (`ROD3`). In addition, the spacer grids, the shroud with its ZrO_2 thermal insulation, and the outer jacket with the three-layer high temperature shield have been simulated with heat conduction (HECU) objects.

The argon and steam flows have been simulated by fill junctions at the bottom of the bundle.

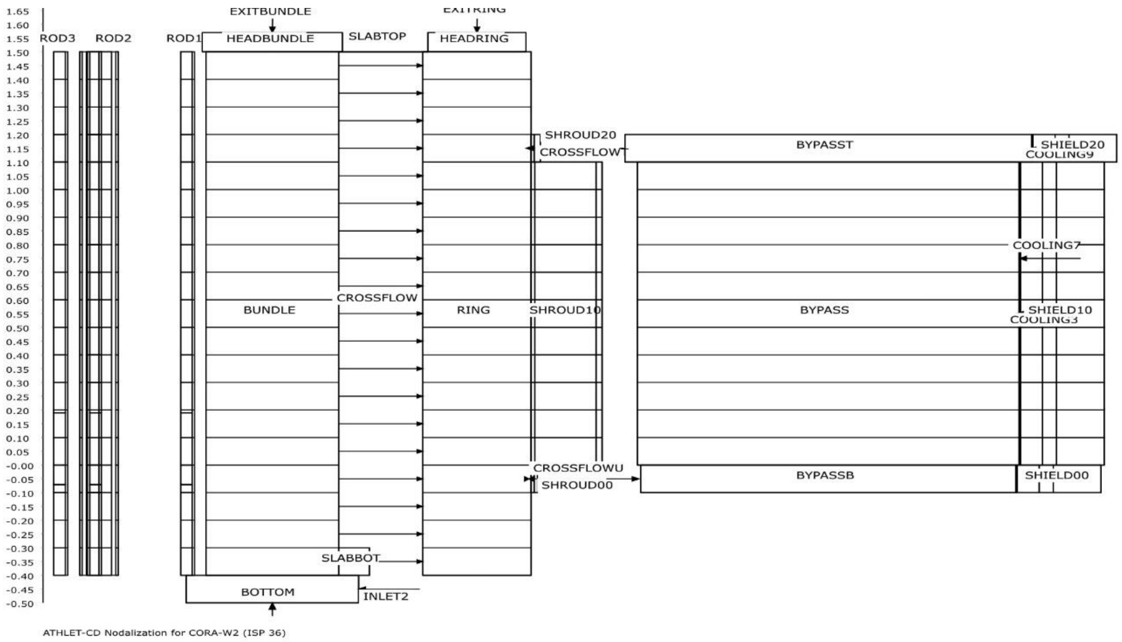

Fig. 5.13 ATHLET-CD Nodalisation for Test CORA-W2

5.3.3.2 Model Options

For the simulation of test CORA-W2, input parameters and modelling options as recommended by the code user's manual /LOV 21b/ have been applied, similar to the simulation of test CORA-13 (ISP-31). For the calculation of Zr oxidation at higher temperatures, the correlation of Urbanic-Heidrick has been used (Input `IOXM` = 2). Furthermore, B_4C oxidation has been also modelled with the recommended option `ICRB4C` = 7 (reaction rates derived from VERDI and BOX data). Tab. 5.3 summarizes the main code input parameters concerning the calculation of Zr oxidation and rod melt and relocation /BAL 17/.For the external resistance per heated rod, which takes into account the voltage drop across the sliding contacts at the rod extremities as well as at the wires connecting the sliding contacts to power supply, a value of 1 mΩ has been used.

Tab. 5.3 Main input parameters and modelling options for test CORA-W2

Parameter	CORA-W2
Zr oxidation correlation	Cathcart (T < 1800 K) Urbanic-Heidrick (T > 1900 K)
Melting temperature of metallic cladding	2200 K
Lower clad failure temperature (low cladding oxidation)	2200 K
Upper clad failure temperature (high cladding oxidation)	2400 K

Parameter	CORA-W2
Minimum oxide layer thickness for upper failure temperature	0.3 mm
Melt relocation velocity	10 mm/s
Liquidus temperature of absorber rods / guide tubes	1523 K
Maximum effective oxide layer thickness (bundle/shroud)	0.1 mm
Upper limit of relative steam availability	0.3
External resistance per heated rod	1 mΩ

5.3.4 Main Results

The main results of the post-test calculation of test CORA-W2 are summarized in Fig. 5.14 and Fig. 5.19, where the black curves refer to the experimental data, the red ones refer to the calculated data with the new version 3.5, and the blue ones refer to the results of the previous release version 3.4.

In general, the measured bundle temperatures at different elevations are satisfactorily reproduced by the code, especially the temperature escalation due to oxidation at the end of the heat-up phase (Fig. 5.14 to Fig. 5.18). During the final cooling phase, after power shutdown, the temperatures calculated at the upper bundle regions are overestimated compared to the measured data. The faster cooling of the bundle after power shutdown was due to a partial rupture of the upper part of the shroud, which has not been simulated in the post-test calculation.

Fig. 5.18 depicts the calculated hydrogen production in comparison to the experiment and results achieved with ATHLET-CD 3.5. The total generation amounts about 93 g, overestimating the experimental value. For this case the improved oxidation model leads to stronger hydrogen generation by the ECORE (incl. melt oxidation) and HECU objects. About 58 % thereof (54.5 g) were produced in the bundle region, including the contribution of the B_4C oxidation (18.1 g) and of the oxidation of the metallic melt (12.0 g). The experimental values available are not sufficient to validate the B_4C oxidation modelling. However, only with consideration of B_4C oxidation it is possible to reproduce the temperature escalation at the end of the heat-up phase and to obtain a good agreement with respect to the total hydrogen production (see also /BAL 17/).

The post-test examination of the test section showed an accumulation of metallic melt in the elevations 200 mm – 300 mm, with a large amount of absorber material at lower elevations. The current ATHLET-CD modelling does not consider B_4C melt and relocation besides the guide tubes. The post-test calculation indicates accumulation of metallic melt and formation of a partial blockage at elevation 300 mm - 400 mm

The results obtained with the new version 3.5 are almost equal to those of the previous release version and also the computational effort is very similar (Fig. 5.19).

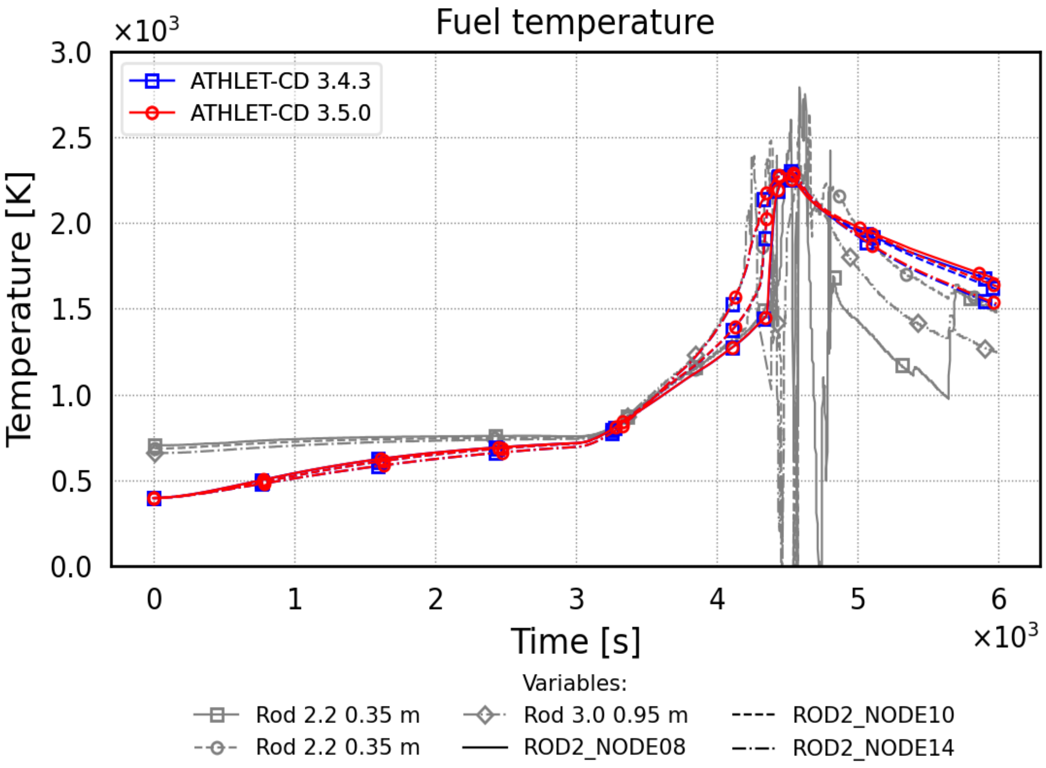

Fig. 5.14 CORA-W2 – Fuel temperatures at elevation 350 mm, 550 mm and 850 mm (intermediate rod)

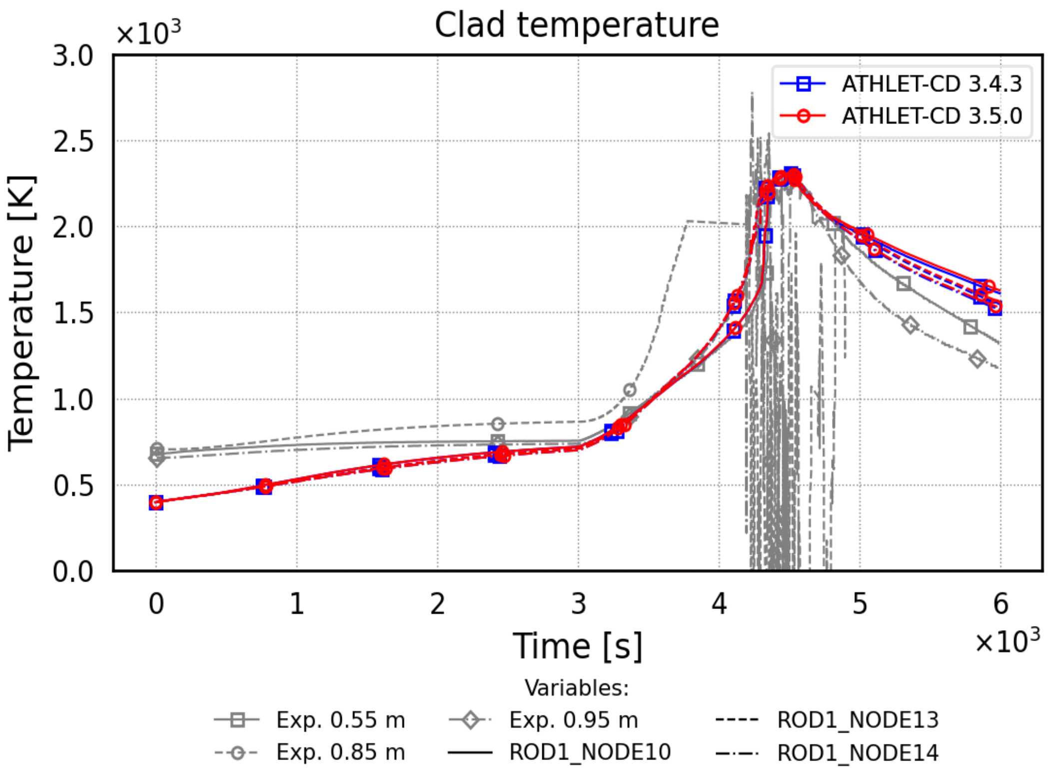

Fig. 5.15 CORA-W2 – Cladding temperatures at elevation 550 mm, 850 mm and 950 mm (inner ROD)

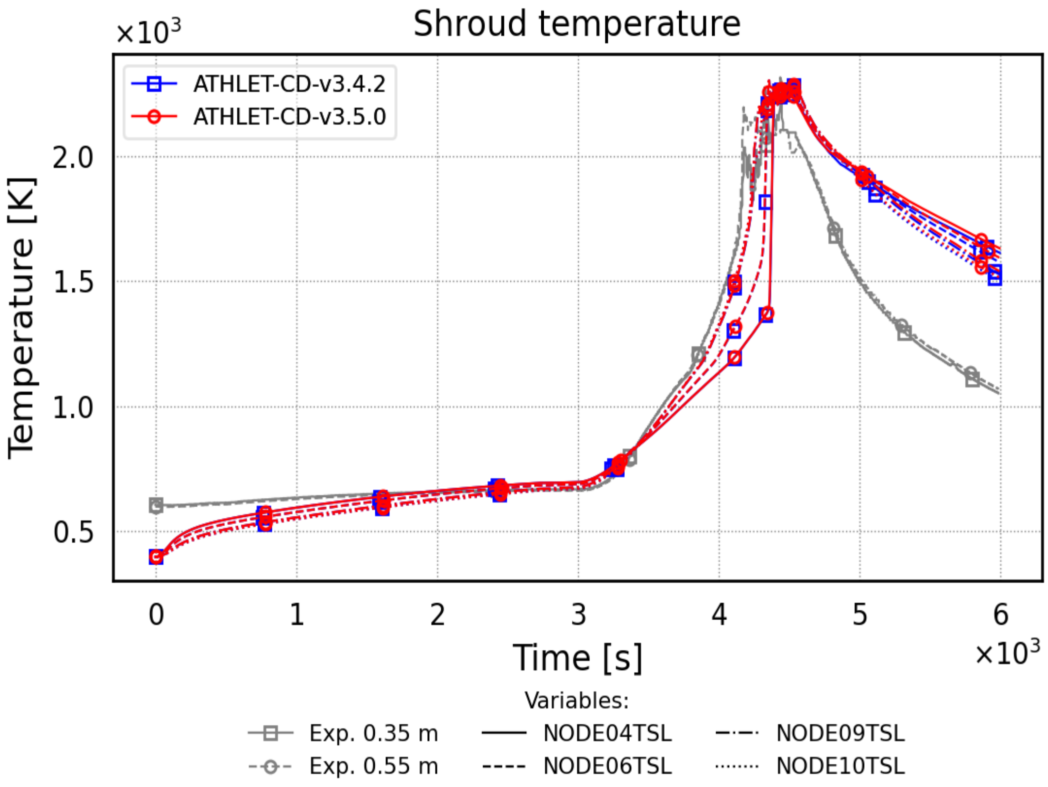

Fig. 5.16 CORA-W2 – Shroud temperatures at elevation 350 mm and 550 mm

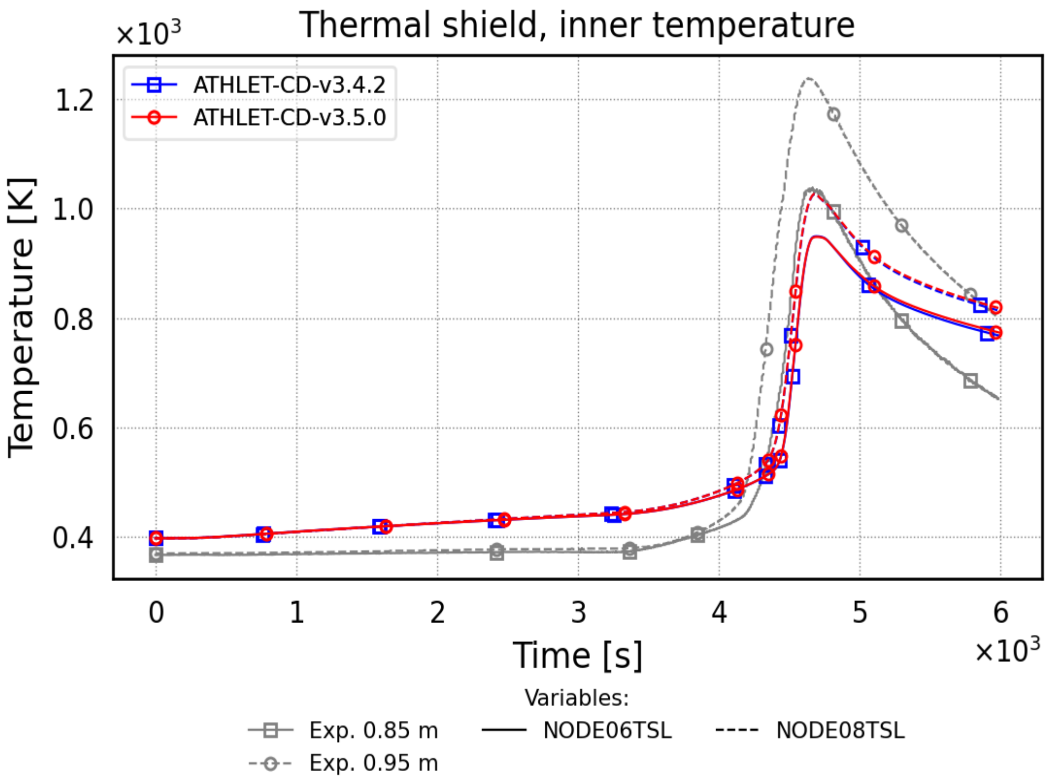

Fig. 5.17 CORA-W2 – Shroud insulation shiel temperatures at elevation 850 mm and 950 mm

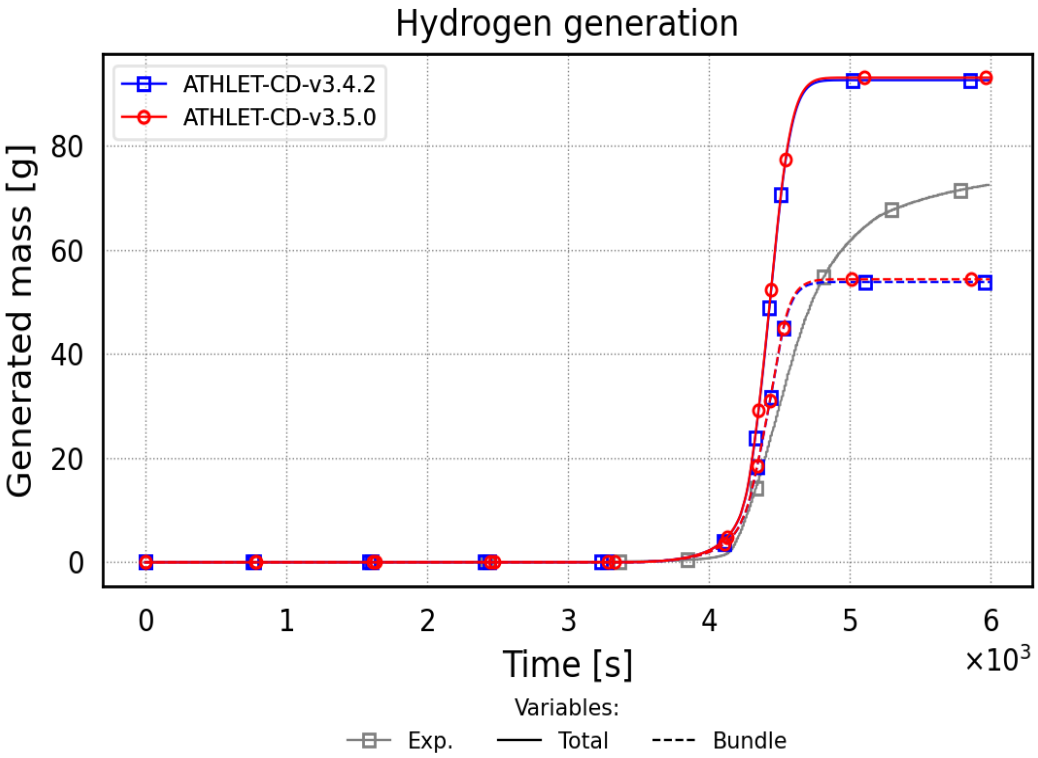

Fig. 5.18 CORA-W2 – Total hydrogen production

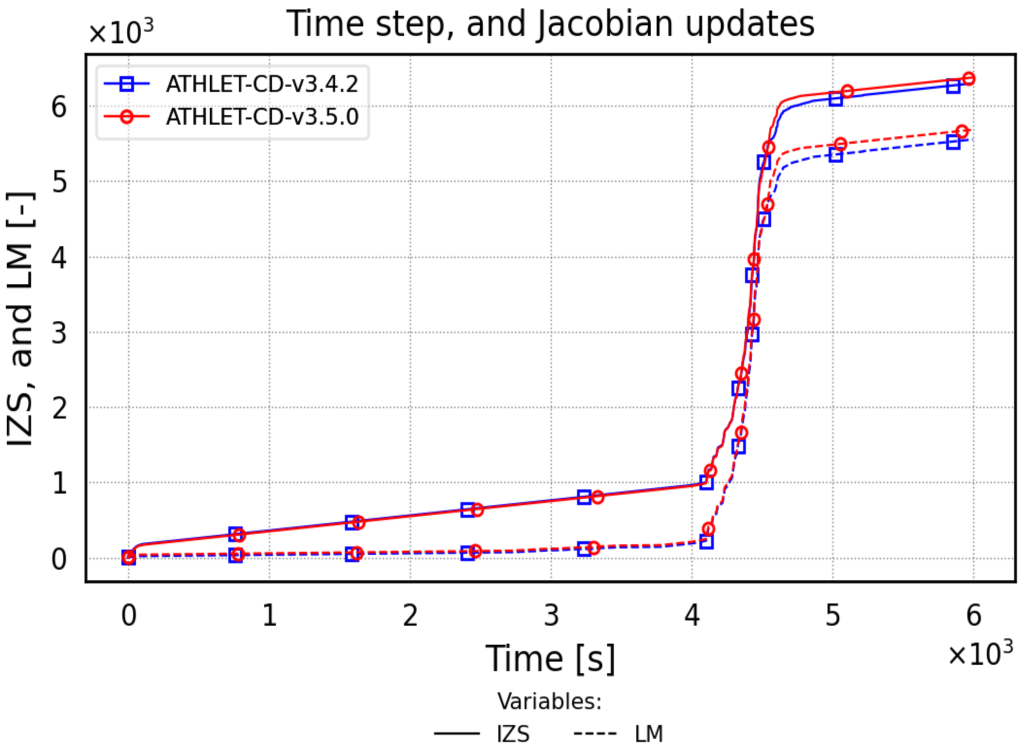

Fig. 5.19 CORA-W2 – Number of time steps and Jacobian calculations

5.3.5 Main Findings

In general, a satisfactory agreement between calculated and measured data with respect to the evolution of bundle temperatures at different elevations has been obtained. The total calculated hydrogen production matches the given experimental value.

The results of the new version 3.5 are practically identical to those of the previous version.

5.4 QUENCH-06 (ISP-45)

The out-of-pile experiment QUENCH-06, selected as the basis for the International Standard Problem ISP-45, was conducted in December 2000 at the then Forschungszentrum Karlsruhe /HER 02/. Its main objective was to investigate the fuel rod bundle behaviour up to and during reflood/quench conditions without severe fuel rod damage prior to reflood initiation.

The ISP-45 was conducted as a “blind exercise” (only thermal initial and boundary conditions were given), followed by an optional open phase after the release of the experimental data. In total 21 participants from 15 countries using eight different codes took part in this exercise. The GRS contribution applied the code version ATHLET-CD 1.2D/1.1G /STE 03/.

5.4.1 Test Facility

The main component of the out-of-pile QUENCH test facility is the test section with the test bundle. Superheated steam from the steam generator and superheater together with argon as a carrier gas enter the test bundle at the bottom. Additionally, to the gas inlet the test section has separate inlets at the bottom to inject water for reflood (bottom quenching).

The bundle is composed of up to 21 heated and unheated fuel rod simulators approximately 2.5 m long. 20 fuel rod simulators are heated over a length of 1024 mm, the one unheated fuel rod simulator is located in the centre of the test bundle. The rod cladding is identical to that used in LWRs: Zircaloy-4, 10.75 mm outside diameter, 0.725 mm wall thickness. Heating is carried out electrically using 6 mm-diameter tungsten heating elements, which are installed in the centre of the rods and which are surrounded by annular ZrO_2 pellets to simulate the fuel pellets. The bundle geometry and most other bundle components (Zry-4 cladding, grid spacers) used are prototypical for Western-type PWRs.

The test section is instrumented with thermocouples (TC) that are attached to the cladding, the shroud, and the cooling jackets at elevations between -250 mm and 1350 mm. Additionally, inside the central rod three centreline TCs and two cladding inner surface TCs were installed, and three centreline TCs were mounted inside three of the four corner rods.

The test bundle is surrounded by a shroud of Zircaloy with a 37 mm thick ZrO_2 fiber insulation up to the upper end of the heated zone and a double-walled cooling jacket of stainless steel. The 6.7 mm annulus of the cooling jacket is cooled by water from the upper end of the test section to the upper end of the heated zone and by argon from the upper end of the heated zone to the bottom of the bundle.

For temperature measurements the test bundle, shroud, and cooling jacket are extensively equipped with thermocouples at different elevations and orientations. Hydrogen production is measured using two mass spectrometers located at two different positions in the circuit, together with a commercial hydrogen analyser /HER 02/.

5.4.2 Test Conduct

The different events and phases of experiment QUENCH-06 are summarized in Tab. 5.4 /HER 02/. As in the previous QUENCH tests the bundle was heated by a series of stepwise increases of electrical power from room temperature to ~600 °C in an atmosphere of flowing argon (3 g/s) and steam (3 g/s). The bundle was stabilized at this temperature for about two hours, the electrical power being about 4 kW. During this time the operation of the various systems was checked. Shortly before the end of this phase data acquisition was started.

At the end of the stabilization period the bundle was ramped up by stepwise increases in power up to about 11 kW to reach ~1473 K, the target temperature for pre-oxidation. The temperature level was maintained for about 4600 s by control of the electrical power to reach the desired oxide layer thickness of about 200 µm. At 6000 s, the electrical power was ramped up at 6 W/s to start the transient phase in the same way as in QUENCH-05. At 6620 s, a corner rod was withdrawn to check the amount of oxidation at that time. Moderate temperature excursions occurred between the 750 mm and 950 mm elevations. The quench phase was initiated when pre-defined criteria similarly to QUENCH-05 were reached. The maximum measured temperature was 2150 K at the 750 mm level coinciding with quench initiation.

Within 5 s approximately 4 kg of water were pre-injected to fill the lower part of the set-up rapidly (fast water injection system). At the same time the quench pump was started to inject water from the bottom of the test section at a rate of ~40 g/s. About 20 s later the electrical power was reduced to 4 kW within 15 s to simulate decay heat level. Quenching of the test section was completed within ~255 s; the steam and electrical power were then shut off, terminating the experiment. During the quench phase the argon injection was switched to the upper plenum to continue to provide carrier gas for quantitative hydrogen detection /HER 02/.

Tab. 5.4 Events and phases of QUENCH-06 /HER 02/

Time (s)	Event	Phase
0	Start of data acquisition	
30	Heat up to about 1500 K	Pre-oxidation
1965	Pre-oxidation at about 1500 K	
6010 6620	Initiation of power transient Initiation of pull-out of corner rod (B)	Power transient
7179	Quench phase initiation Shut down of steam supply Onset of fast water injection Start of quench water pump Detection of clad failure First temperature drop at TFS 2/1	Reflood
7181 7205 7221 7430	Steam mass flow rate zero Onset of electric power reduction Decay heat level reached Onset of final power reduction	Quench
7431 7431 7435 11420	Shut down of quench water injection Electric power < 0.5 kW Quench water mass flow zero End of data acquisition	Post-reflood

5.4.3 Input Dataset

5.4.3.1 Nodalisation

The current input deck used for the post-test calculation of test QUENCH-06 is strongly based on the input deck applied for the participation in ISP-45 /STE 03/. The corresponding nodalisation is depicted in Fig. 5.20.

The test bundle modelling consists basically in the inlet pipe (`INPIPE`), the bundle flow channel (`BUNDLE`, `TOP`) and the outlet pipe (`OFFPIPE`). Superheated vapour, argon and quench water are injected into the inlet pipe (`INPIPE`). After start of the quench phase the steam injection into the bundle is stopped and the injection of argon is switched from the bottom fill to a fill into the upper head (`TOP`). Residual vapour, argon and produced hydrogen exit the system through the outlet pipe (`OFFPIPE`). Inlet and outlet pipes are surrounded by heat structures.

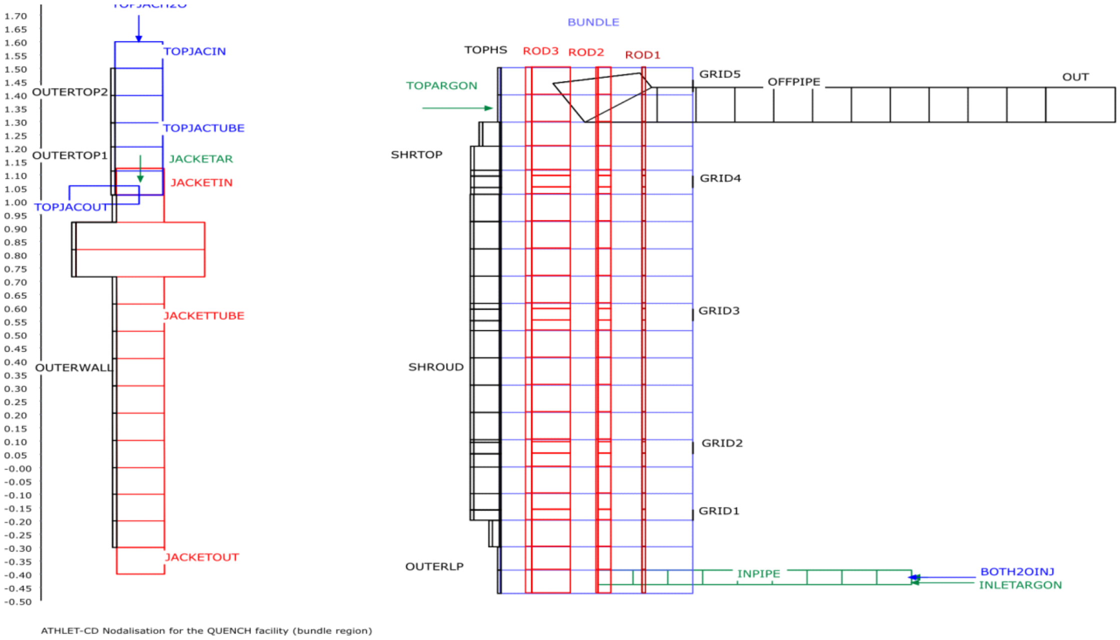

Fig. 5.20 ATHLET-CD Nodalisation for test QUENCH-06

The 21 rod simulators are modelled by 3 rod components (`ROD1`, `ROD2`, `ROD3`), where `ROD1` simulates the central unheated rod, `ROD2` the 8 heated rods of the inner ring and `ROD3` the 12 heated rods of the outer ring. The lower plenum is surrounded by the heat structure `OUTERLP`; within the heated bundle region (`BUNDLE`) and above (`TOP`), the objects `SHROUD` (up to 1.0 m) and `SHRTOP` (up to 1.30 m) simulate the actual shroud. The structure `SHROUD` includes the materials Zircaloy, the ZrO_2 insulation and the steel, which represents the inner wall of the cooling jacket with a radial division of 2, 8 and again 2 layers, respectively. The structure `SHRTOP`, which comprises the region above the insulation, contains argon with a modified thermal conductivity as a second material to correspond to the test facility. The upper plenum is surrounded by the heat structure `TOPHS`.

Outside of the ZrO_2 insulation the channel for counter-current flow cooling with argon (`JACKETTUBE`) is modelled, bordered by the outer steel wall (`OUTERWALL`). Above this TFO, the channel `TOPJACTUBE` simulates the water cooling above the insulation and the objects `OUTERTOP1` and `OUTERTOP2` with their corresponding structures determine the heat transfer to the surrounding within this region.

The lower unheated region with the copper electrode is modelled with 2 and the upper unheated region with the molybdenum electrode with 3 nodes. The heated region of 1 m height is divided into 10 nodes corresponding to the distance of the thermocouples. This axial segmentation is used in the same way for the fluid channel, the rods and the outer structures. The hydraulic diameter of the TFO `BUNDLE` was modified in the lower region so that only 50 % of the actual value was used to consider the influence of perturbances (e. g. inflow, grids) /STE 03/.

The 5 grids are modelled with reduced cross flow area (TFO `BUNDLE`) and as heat conduction (HECU) elements. The upper 4 Zircaloy grids contribute to the oxidation and hydrogen production. The corner rods are not modelled.

5.4.3.2 Model Options

The following main input parameters and modelling options are applied for the post-test calculation of test QUENCH-06:

- the whole system is simulated with the 5-equation model for the two-phase thermal-hydraulics in combination with the drift flux model. The multi-component modelling is applied for the simulation of the argon injection and the outflow of the produced hydrogen;
- the quench front tracking model is activated for the reflood phase; the corresponding input parameters are the standard values recommended in the ATHLET-CD User’s Manual /LOV 21b/;
- the clad failure criterion used is 38 % strain (`IBLOW`=0);
- the correlation of Cathcart (lower temperature region) resp. Prater/Courtright (upper temperature region) (`IOXMOD`=3) is selected for the calculation of oxidation of cladding, grids and inner surface of shroud. This correlation is also applied for the melt oxidation. No transition from parabolic to linear kinetics is considered (`ROXLIM`=`HROXLIM`=1.0);
- the melting temperature of metallic Zircaloy (`TAM`) is 2250 K (α–Zr),
  the start of relocation is at temperatures `TALLOW`=2650 K resp. `TALHIG`=2850 K with `DDTAL` = 0.3 mm (oxide layer thickness for change of criteria);
- the input value for the external resistance is 5 mΩ per rod;

- heat exchange due to radiation is considered from the rods to the shroud and from the shroud to the outer wall.

5.4.4 Main Results

The main results of the post-test calculation of test QUENCH-06 are summarized in the Fig. 5.21 to Fig. 5.26, where the black curves refer to the experimental data, the solid red ones refer to the calculated data with the new version 3.5, and the dashed, blue ones refer to the results of the previous release version 3.4. The given elevations correspond to the values given for the test facility, where the heated length is from 0.0 m to 1.0 m.

Fig. 5.21 and Fig. 5.22 compare the calculated and measured rod cladding temperatures at different elevations. The temperature progression for the whole test shows a good agreement, especially within the pre-oxidation phase. The detailed view to the time of power transient and quenching for the levels 750 mm, 950 mm and 1150 mm reveals some underestimation of the temperature increase rate during the oxidation escalation just before the start of water injection. In /SEP 04/ the maximum measured temperature of the test is given with 2056 K at 950 mm height, while the maximum cladding temperature in the simulation is 1951 K at the same level. Due to the lower cladding temperatures, the cool down after start of quenching proceeds slightly quicker in the calculation but is generally in a satisfactory agreement with measured data.

The diagram of quench front progression (Fig. 5.23) shows complete quenching of the bundle after 7410 s; the time necessary for cooldown is 230 s in the calculation. Fig. 5.23 shows that the quenching of the hottest rod positions at 950 mm elevation needs about 60 s longer in the test than in the simulation.

Considering the release of hydrogen due to the oxidation of the Zircaloy components, the comparison of measured and calculated oxidation heat shows the good agreement achieved by the modelling of the oxidation reactions especially during the pre-oxidation phase (Fig. 5.24). Regarding the integral hydrogen mass (Fig. 5.25), the calculated values of the contribution from the rods only (model ECORE) agree very well with the measured mass derived from the experiment up to the time of escalation just before cool down, whereas the total amount of produced hydrogen including the HECU components (shroud and grids) slightly underestimates the test data (32.6 g compared to 35 g in the experiment /SEP 04/).

The results obtained with the new version 3.5 are almost equal to those of the previous release version 3.4, including computational performance (Fig. 5.26). The increase in time steps during quenching is not yet significant.

5.4.5 Main Findings

In general, a satisfactory agreement between calculated and measured data with respect to the evolution of bundle temperatures at different elevations has been obtained. The oxidation kinetics up to the temperature escalation at the end of the heat-up phase has been well reproduced by the code. The total calculated hydrogen production is slightly higher than the corresponding experimental value.

One main contributor for the uncertainty of code results is the input value for the external resistance of the heater rod. An increase of 10 % of the original value leads to a reduction of about 90 K for the calculated peak cladding temperature and 4.5 g less hydrogen production.

The results of the new version 3.5 are practically identical to those of the previous versions.

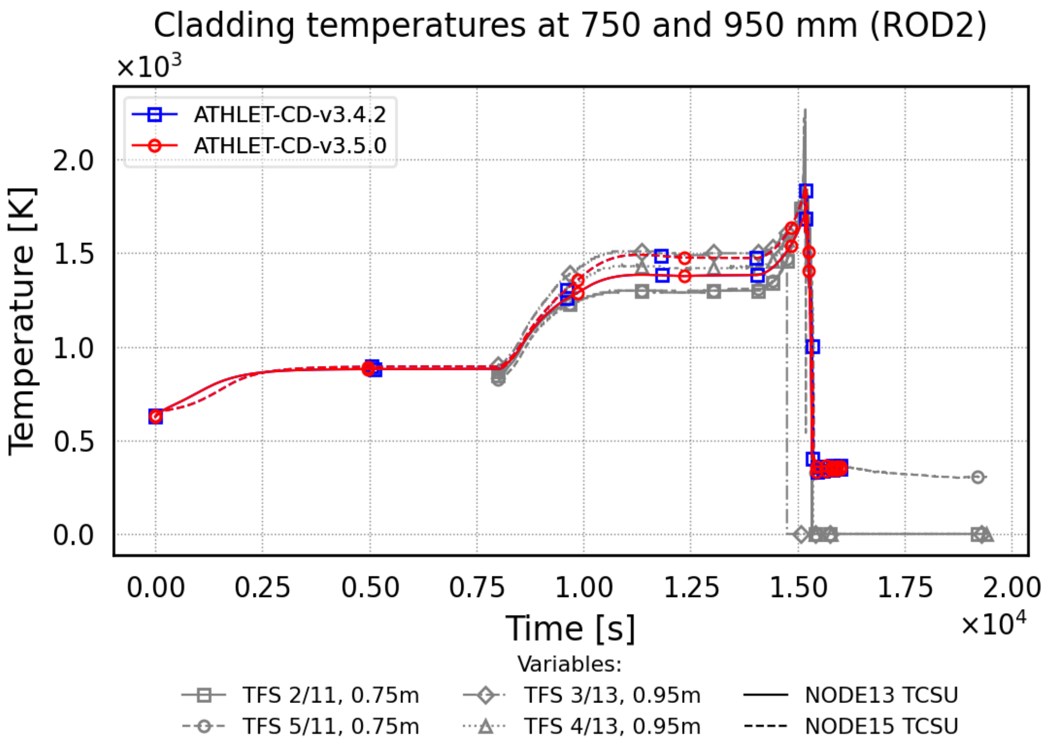

Fig. 5.21 QUENCH-06 – Temperatures at elevation 750 mm and 950 mm

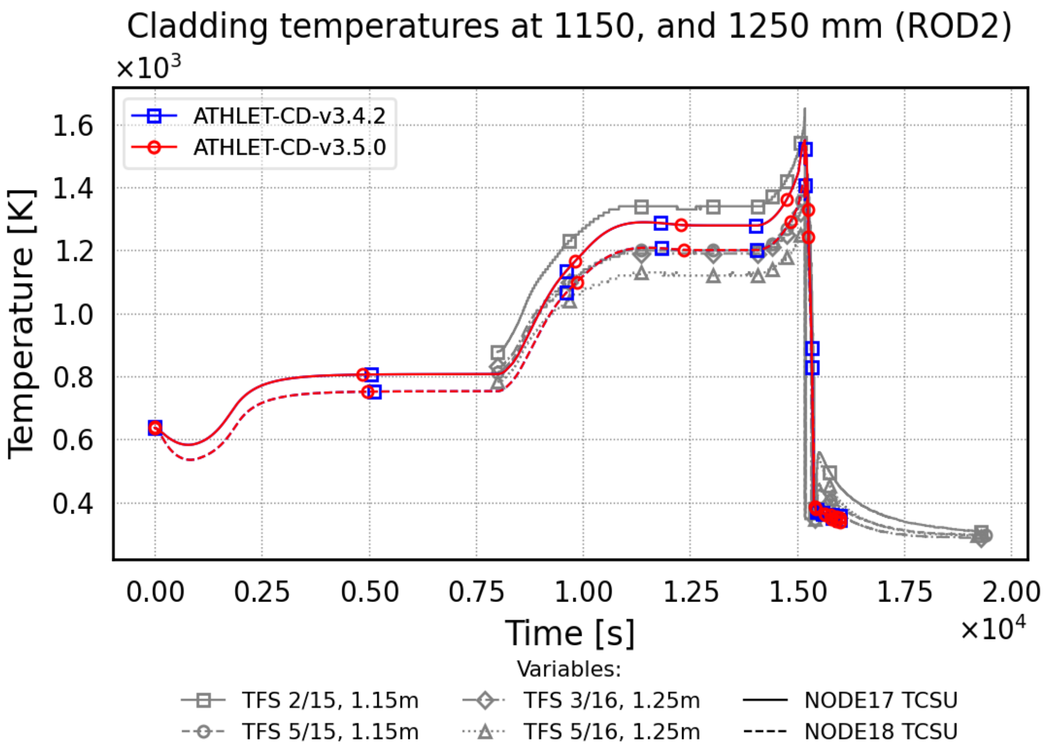

Fig. 5.22 QUENCH-06 – Temperatures at elevation 1150 mm and 1250 mm

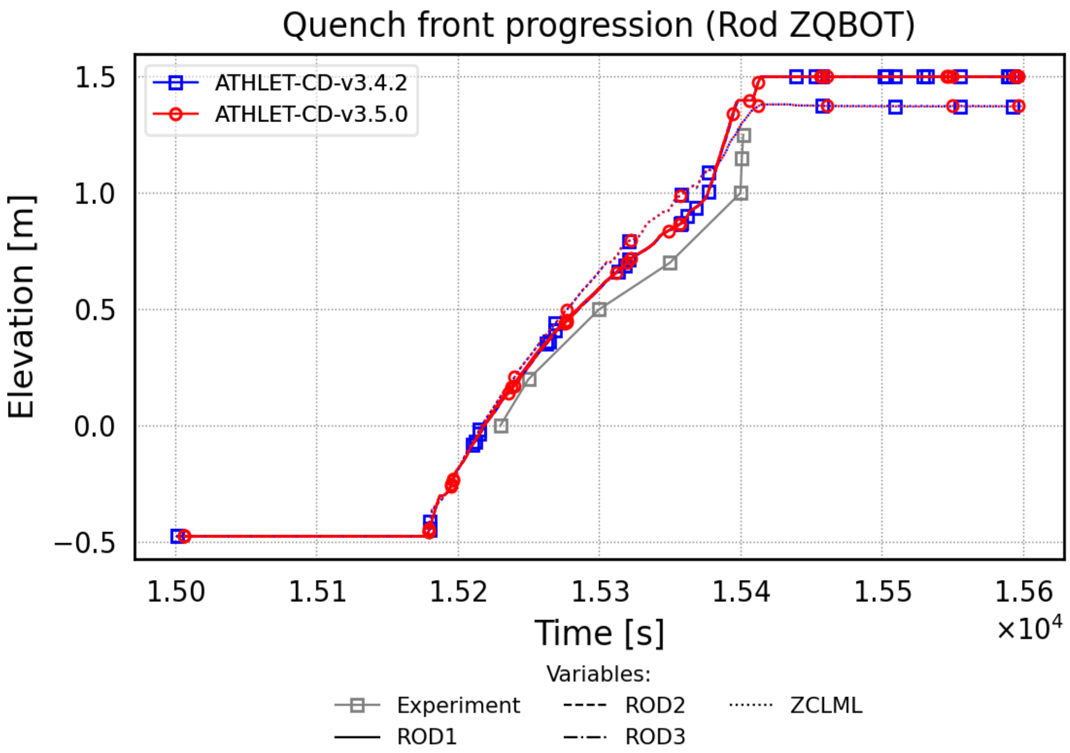

Fig. 5.23 QUENCH-06 – Quench front progression

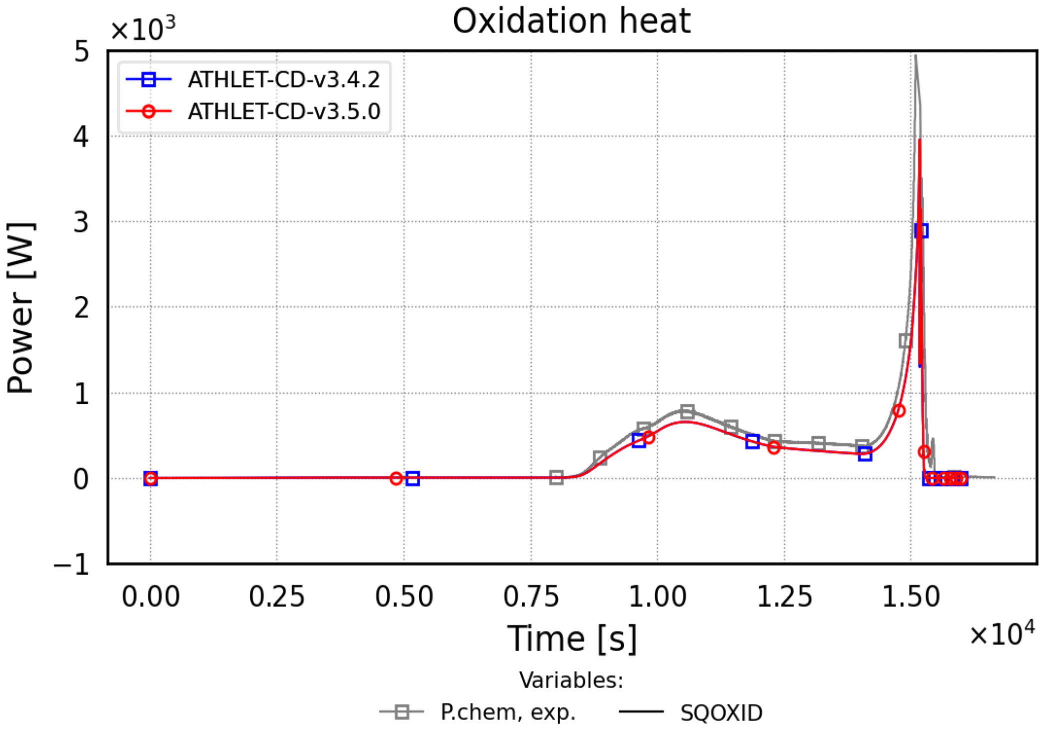

Fig. 5.24 QUENCH-06 – Oxidation heat

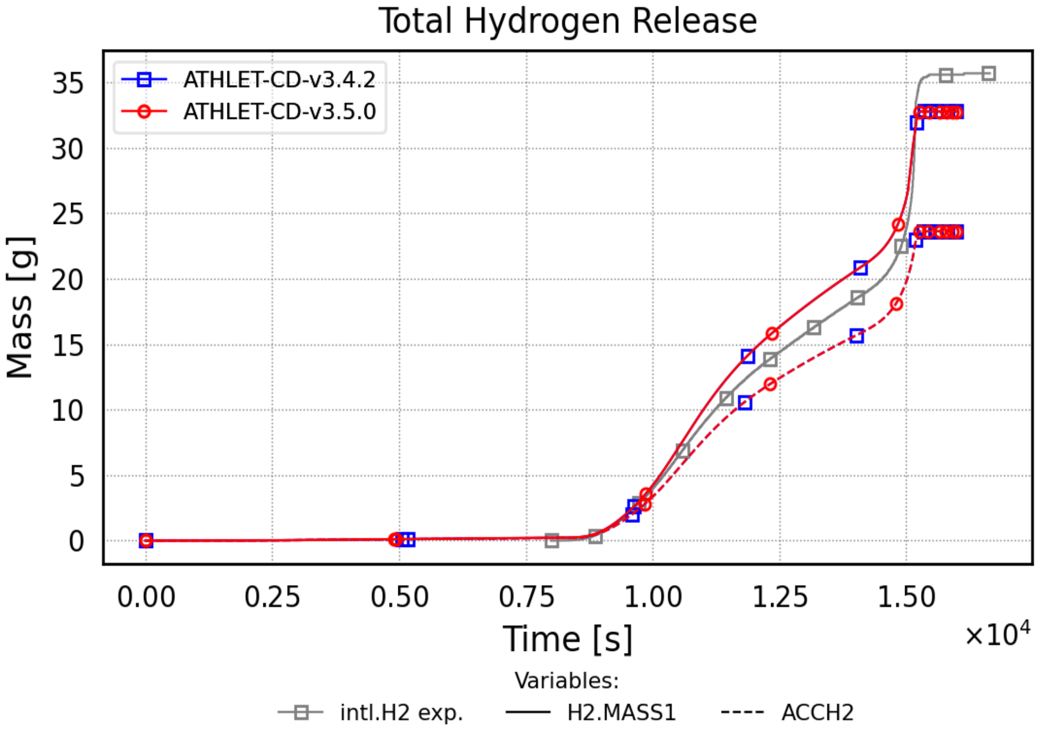

Fig. 5.25 QUENCH-06 – Total hydrogen production

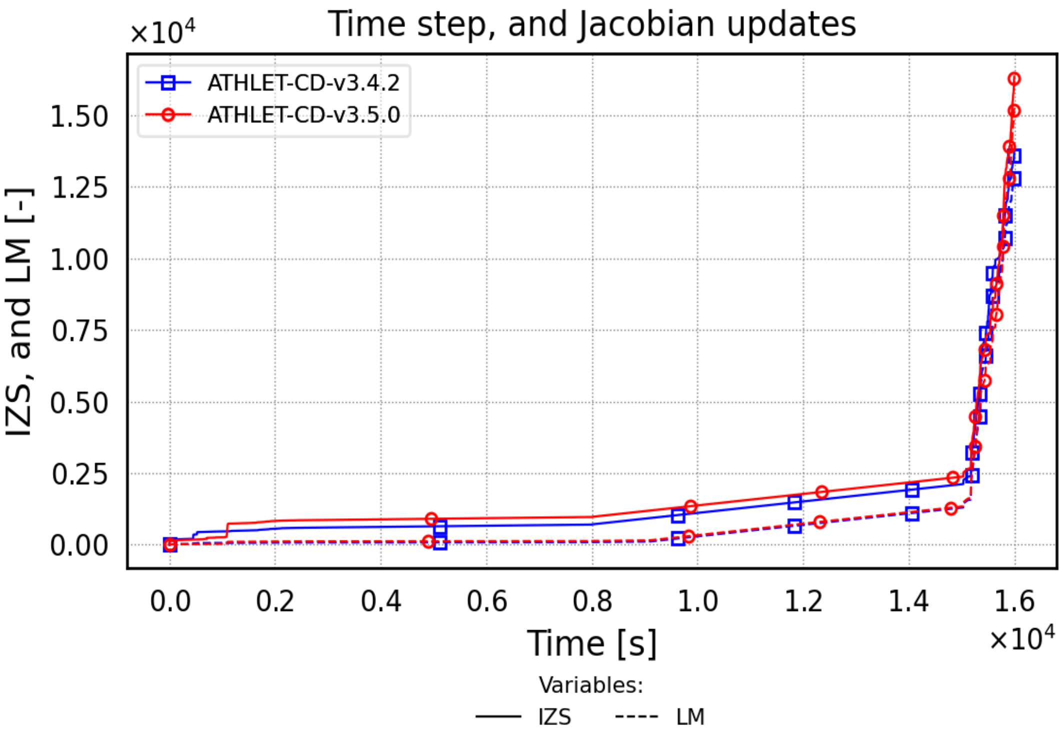

Fig. 5.26 QUENCH-06 – Number of time steps and Jacobian calculations

5.5 PHÉBUS FPT1 (ISP-46)

The in-pile test FPT1, conducted in July 1996 in the PHÉBUS facility at the French research institute CEA – CADARACHE, was selected as the experimental basis for the International Standard Problem ISP-46. The general objective of ISP-46 was to assess the capability of computer codes to model the physical processes taking place during a severe accident in a pressurized water reactor, from the initial stages of core degradation up to the behaviour of fission products released into the containment /CLÉ 03/.

The experiment covered the following physical processes:

- fuel degradation, hydrogen production, release of fission products, fuel and structural materials ('bundle' part of the ISP);
- fission product and aerosol transport in the circuit ('circuit' part of the ISP)
- thermal-hydraulics and aerosol physics in the containment ('containment' part of the ISP);
- iodine chemistry in the containment ('chemistry' part of the ISP).

ISP-46 was organized as an open benchmark. The participants could perform integral calculations covering all four aspects of the exercise, as well as any of the above-mentioned areas in a stand-alone manner. Altogether 33 organizations from 23 countries with 15 different computer codes took place in the exercise. GRS submitted calculations with ATHLET-CD Mod 1.1I for the 'bundle' and 'circuit' parts of the ISP, with COCOSYS for the ‘containment' and 'chemistry' parts, as well as integral calculations with ASTEC and with the coupled codes ATHLET-CD/COCOSYS for the whole experiment /CLÉ 03/.

For the validation calculation described in this technical note only the 'bundle' part of ISP-46 has been considered.

5.5.1 Test Facility

The PHEBUS test reactor (Fig. 5.27) mainly consists of a driver core with a cooling system, the test assembly with a separate cooling circuit, an experimental fission product circuit, including pipes, a steam generator mock-up and a containment vessel. The reduced scale factor compared to a PWR of 900 MW is roughly equal to 1:5000.

The gases and aerosols released from the fuel bundle during the degradation phase are conveyed through pipes to the containment:

- a vertical pipe directly above the bundle,
- an isothermal horizontal pipe simulating the conditions in the hot leg of a PWR,
- a vertical steam generator U-tube, simulating a PWR steam generator,
- an isothermal horizontal pipe leading to the containment tank, simulating the cold leg of a PWR.

The vertical pipe builds up the upper plenum and the riser. The bottom part of the plenum (~0.2 m) is unheated while the remainder of the vertical line and the horizontal pipe are regulated to a temperature of about 975 K. The steam generator U-tube walls are maintained at 425 K as well as the cold leg. The cold leg penetrates the containment (~10 m^3) in the lower part above the sump and ends with an injection cone directed towards the condensers.

The gaseous fission products, the aerosols and the steam/hydrogen effluents are collected in the containment. Part of the bottom of the containment is occupied by a sump to reproduce a representative atmosphere-water exchange surface. Heat transfer and steam condensation phenomena are simulated by a group of three vertical condensers. The condenser surface is divided into two parts: the cooled condensing or 'wet' area and the non-condensing or 'dry' area. The lower part of the condenser is kept dry by heaters.

The radial configuration of the FPT1 test bundle is shown in Fig. 5.28. The bundle consists of 20 fuel rods (2 fresh, 18 irradiated) with 1 absorber rod (AgInCd) in the centre. The rods are 1.13 m long with a UO_2 column of 1 m in length. The spacing between the rods in the test assembly are maintained by two spacer grids which are fixed with four Zry stiffeners. These are located close to the inner surface of the shroud and strengthen the assembly.

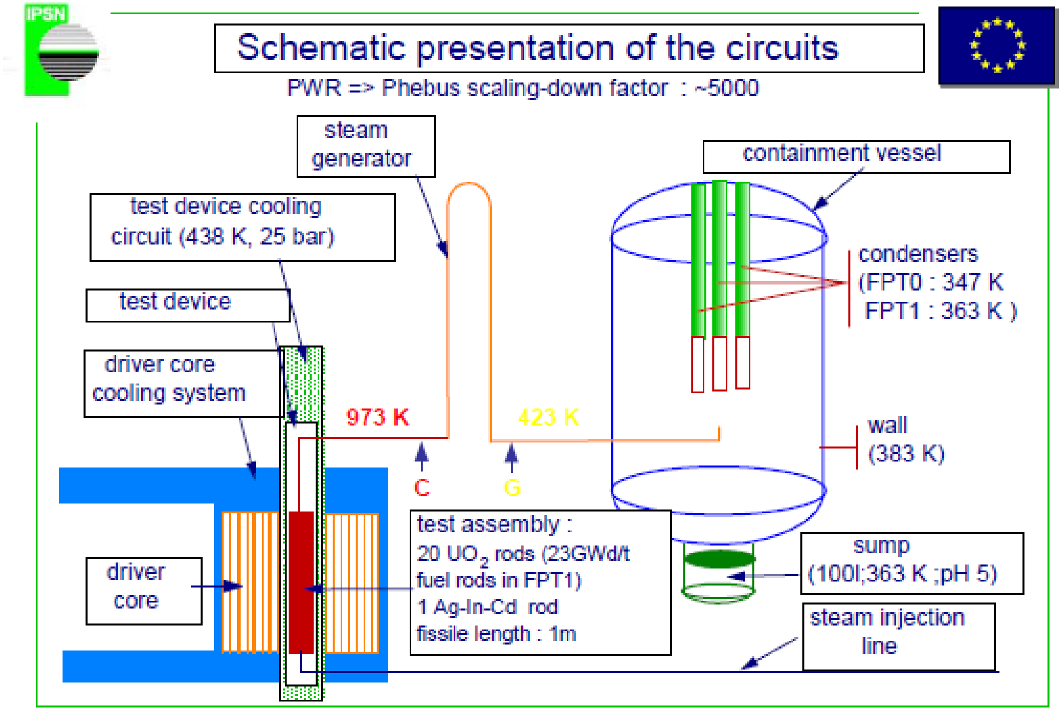

Fig. 5.27 Schematic representation of PHÉBUS FB circuit /JAC 00/

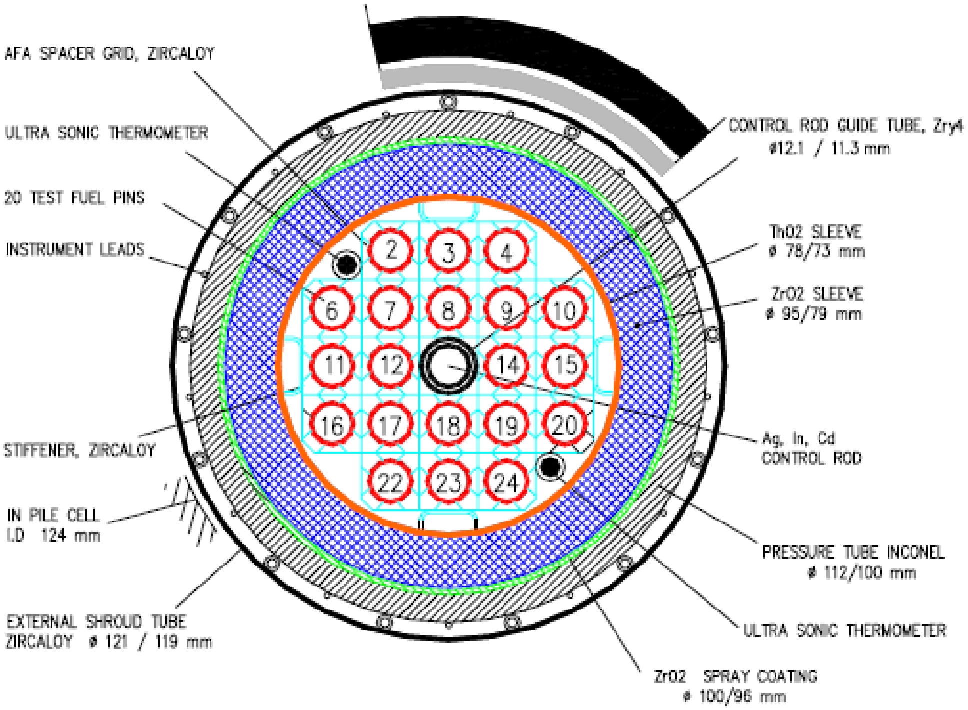

Fig. 5.28 Radial configuration of the FPT1 bundle /JAC 00/

The test bundle is surrounded by an insulating zirconia shroud to limit the radial heat losses. It is built up of three annular structures composed of a thoria inner layer (ThO_2), an insulated region of porous zirconia (ZrO_2) and a pressure tube of Inconel with a flame-spray-coated high density zirconia layer (ZrO_2) on its inner surface. Inside the shroud are two gaps between the three structures with temperature-dependent width. The outer pressure tube is cooled with water at a temperature of 438 K. The two rods containing fresh fuel, the control rod, the stiffener and the shroud are instrumented with thermocouples at various elevations and radial positions. At the periphery of the bundle two ultrasonic thermometers enable improved control of the temperature beyond the failure temperatures of thermocouples and rods.

5.5.2 Test Conduct

The preparations for test FPT1 started with a re-irradiation phase of several days in order to generate short-lived fission products in the fuel. Short-lived fission products are easily detectable by γ-spectrometry measurements, and their activity is necessary to initiate radiolysis phenomena in the containment. This re-irradiation phase was followed by a transition phase, with bundle dry-out and heat-up of the outlet line, to establish the boundary conditions for the experimental circuits. The experiment itself started with the degradation phase by injecting steam into the bundle and gradually increasing the core nuclear power. This bundle degradation phase, which lasted about 5 h, was followed by three other phases restricted to the containment: the aerosol, the washing and the chemistry phases. For the post-test calculation described in this report, only the degradation phase has been considered.

The degradation phase can be divided into two main periods. The preliminary period, which lasted about 7900 s, was devoted to the thermal calibration of the test bundle. It was followed by the temperature transient and degradation period which ended with the shutdown of the nuclear power at 17039 s. After a cooling period the bundle degradation phase was ended with the containment isolation after about 18660 s.

During the thermal calibration period the bundle power was increased in three steps up to about 3.9 kW. During this time the injected steam flow rate was reduced from about 1.8 g/s down to 0.5 g/s. In this period the stabilization of the temperature in the system was reached. Then the pre-oxidation period started by increasing the nuclear power and the steam flow rate. Shortly after the increase of the power, the cladding oxidation and the hydrogen generation started. At ~9000 s the power was stabilized at about 9.15 kW for about 6 min. This period ended with onset of runaway oxidation.

During the following oxidation period, the onset of the temperature escalation in the bundle was observed ~15 min after the stabilization of the steam mass flow rate at 2.2 g/s. Many of the thermocouples failed during this period. After the runaway oxidation, the nuclear power was then stabilized at about 25.7 kW for ~23 min. After 14580 s, the final heat-up period with a progressive increase of the power started. The steam flow rate was reduced to 1.5 g/s. The liquefaction of the materials in the bundle, the fuel relocation and a rapid increase of the temperatures in the lower levels of the shroud were observed. This was associated with a cooling of the upper part, which corresponds to a rapid solid fuel rod slumping situation. A second temperature peak in the lower part of the shroud then led to the condition for the reactor shutdown. The bundle degradation phase ended with a cooling period. The steam injection of 1.5 g/s was stopped after 18617 s, and the containment was isolated from the circuit after 18660 s.

A more detailed description of the test facility and of the test conduct can be found in the FPT1 Final Report /JAC 00/.

5.5.3 Input Dataset

The input deck used for the post-test calculation of test FPT1 is based on the dataset used in the GRS contribution to ISP-46 /ERD 01/, /ERD 02/. The main modifications are related to new ATHLET/ATHLET-CD code features, as well as to the objective of keeping, to the extent reasonable, the same input options and model parameters for the calculation of all PHÉBUS bundle tests. All necessary information concerning geometry, material properties, initial and boundary conditions have been taken from the FPT1 Final Report /JAC 00/ and from the ISP-46 comparison report /CLÉ 03/.

5.5.3.1 Nodalisation

The ATHLET-CD nodalisation for the test facility is shown in Fig. 5.29. The steam is injected via a fill component into the object `INLET` at the bottom of the test section. The steam not consumed during the steam/zirconium reaction, the generated hydrogen and the released fission products and aerosols leave the test bundle to the upper plenum and the vertical line, which are modelled here as one object `PLENUM` (5 nodes). The gas is then conveyed through the horizontal `HOTPIP` (6 nodes), the steam generator `STGEN` (14 nodes) and the horizontal `COLPIP` (5 nodes) to the containment `CONTAN` (time-dependent object).

Fig. 5.30 shows a more detailed scheme of the bundle section. The bundle is modelled by three thermal-hydraulic concentric fluid channels: two main channels (`BUNDLE` and `OUTER`) and one bypass channel (`BYPASS`), axially subdivided into 26 control volumes, 21 of them for the active fuel length of 1 m. The inner main channel contains the 8 inner fuel rods (`ROD1`) together with the central AIC absorber rod, whereas the outer 12 fuel rods (`ROD2`) are assigned to the outer main channel `OUTER`. No differentiation was made between the 2 fresh fuel rods and the 10 irradiated fuel rods in the outer ring. The bypass channel is necessary in case of a flow blockage of the main channels caused by relocation processes. Each control volume at the same elevation of both main channels as well as between inner channel and bypass are connected by cross flow junctions (objects `IN-OUTER` and `CROSSFLOW`).

The fluid channel `OUTER` is surrounded by an annular shroud structure, with 26 heat conduction objects (`BUNDLE-Wi`), one for each axial mesh. Each object is composed by three material zones, the first for the porous thoria (5 layers), the second for the porous zirconia (9 layers) and the third for the dense zirconia spray coating and the Inconel (2 layers). The zirconia coating on the inner side of the Inconel tube was taken into account in the heat conductivity of the third material zone. The heat conductivities of the coating and Inconel were averaged in such a way that for a given heat flux the surface temperatures are the same using the averaged conductivity or having modelled two separated material zones. .

The heat transfer coefficients in the gaps between the material layers are calculated by superimposing the conductive heat transfer coefficient, taking into account the varying gap width due to thermal expansion of the shroud layers, and the radiation heat transfer coefficient. In case of a closure of the gaps, a contact heat transfer coefficient of 1000 W/(m² K) is assumed.

The four stiffeners, not shown in the diagram, were modelled by 26 structures, which also consider the two Zircaloy spacer grids, under conservation of the surface and of the Zircaloy mass available for oxidation. The effect of the spacer grids is taken into account also by the local reduction of the flow area within the objects `BUNDLE` and `OUTER`. The two ultrasonic thermometers are not represented by heat structures.

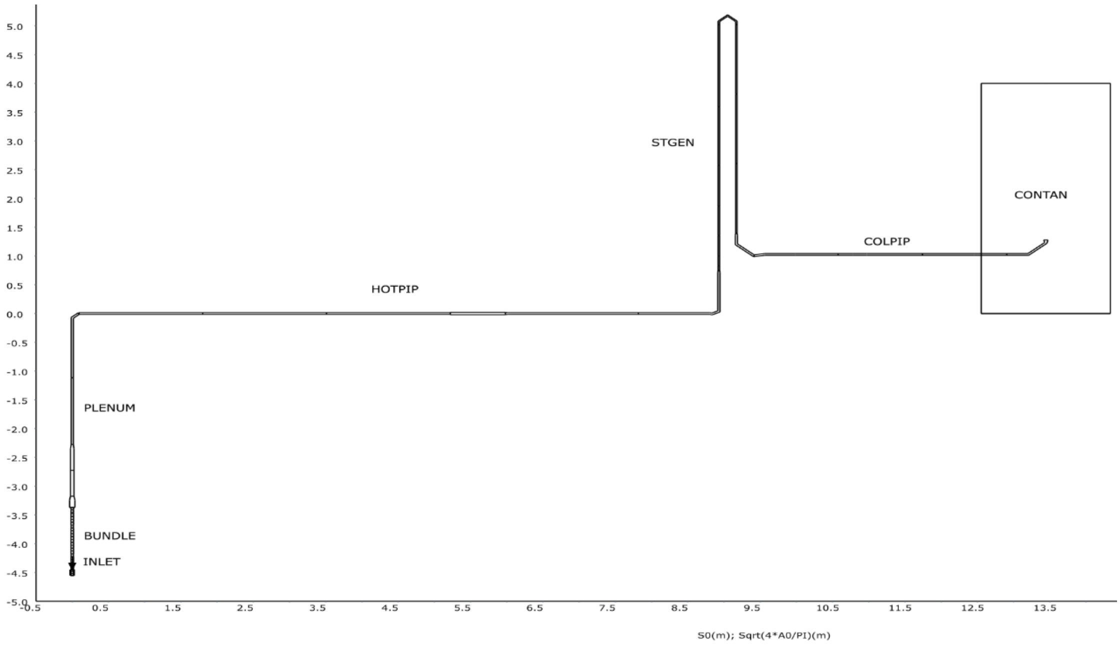

Fig. 5.29 ATHLET-CD Nodalisation for PHEBUS test FPT1 (circuit)

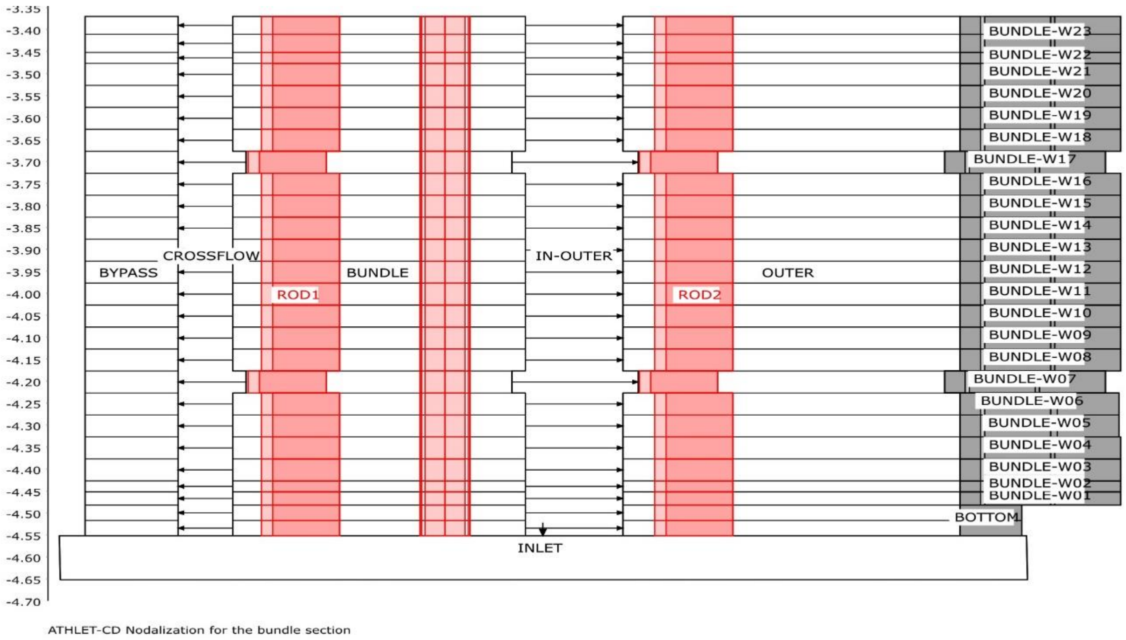

Fig. 5.30 ATHLET-CD Nodalisation for PHEBUS test FPT1 (bundle)

5.5.3.2 Model Options

The calculation starts from isothermal and adiabatic conditions for the bundle and the circuit with zero mass flow and power. The first hundred seconds of the transient were used to reach the initial conditions of the experiment. The following main initial and boundary conditions were specified:

- the bundle power, the axial and radial power profile as specified for ISP-46 /CLÉ 03/;
- the injected steam mass flow rate and the fluid temperature at the bundle entrance;
- a constant temperature (438 K) and heat transfer coefficient (10000 W/(m^2 K)) on the external surface of the shroud;
- a constant temperature of the unheated part of the upper plenum (438 K), of the upper part of the plenum and the hot leg (975 K) and of the steam generator and cold leg (425 K);
- a constant pressure (0.22 MPa) and temperature (420 K) as boundary conditions for the time-dependent object `CONTAN`;
- the initial fission product inventory of the following elements was taken as input from the final report /JAC 00/:
  Br, Kr, Rb, Sr, Zr, Mo, Tc, Rh, Ru, Y, Nb, La, Ce, Pr, Nd, Sm, Eu, Ag, Sb, Te, I, Xe, Cs, Ba;

fuel material: U, Pu, Np, Am, Cm;
absorber: Ag, In, Cd;
structure: Fe, Cr, Ni, Sn, Zr.

During the calculation of the transient the oxidation processes, including melt oxidation, are modelled using the correlations of Leistikow and Prater-Courtright (`IOXMOD`=3). The TESPA model with Rosinger correlation (1979) is applied for the simulation of the mechanical rod behaviour.

The dissolution of UO_2 by molten cladding material starts with the melting temperature of metallic zircaloy, which is set to 2030 K (β-Zr). This effect is modelled using a diffusion model with a parabolic rate equation by Hofmann. The dissolution phase ends when the maximum dissolution rate is reached and the candling of metallic melt starts. At that point the cladding temperature reaches the supposed failure temperature (2250 K or 2450 K, depending on the oxide layer thickness: less or greater than 0.3 mm).

The relocation or solidus temperature of UO_2 was set to 2573 K. The melting temperature of the absorber material was set to 1073 K and the failure of the absorber rod and guide tube to 1523 K.

Tab. 5.5 summarizes the main input options and model parameters used in the calculation.

Tab. 5.5 Main input parameters and modelling options for test PHÉBUS FPT-1

Parameter	**FPT-1**
Zr oxidation correlation – `IOXMOD`=3	Leistikow (T < 1800 K) Prater-Courtright (T > 1900 K)
Melting temperature of metallic cladding – `TAM`	2030 K
Lower clad failure temperature (low cladding oxidation) - `TALLOW`	2250 K
Upper clad failure temperature (high cladding oxidation) - `TALHIG`	2450 K
Minimum oxide layer thickness for upper failure temperature - `DDTAL`	0.3 mm
Maximum effective oxide layer thickness (bundle/shroud) - `ROXLIM`/`HROXLM`	1.0 m (recommended)

Upper limit of relative steam availability - `OXXLIM`	0.1
Relocation temperature for UO_2 ($T_{solidus}$) - `TCOMPM`	2600 K
Liquidus temperature for UO_2 – `TCOMPL`	2800 K
Melting temperature of absorber – `CRTVER`	1523 K
Temperature difference for refreezing (metallic/ceramic) - `DETSL`/`DTSLUO`	50 K
Metallic melt relocation velocity – `WSLMAX`	0.03 m/s
Ceramic melt relocation velocity – `WSLUO`	0.03 m/s
Absorber melt relocation velocity- `CRWSL`	0.06 m/s

5.5.4 Main Results

The main results of the post-test calculation of the degradation phase of the test FPT1 concerning thermal behaviour and relocation processes are presented in the Fig. 5.31 to Fig. 5.40.

The calculated temperatures are compared to the measured ones for elevations between 200 mm and 700 mm in Fig. 5.31 to Fig. 5.36. For each elevation, the calculated temperatures of the fuel in the inner ring, and of the shroud (1/4 depth) are shown, together with the corresponding measured values. The blue curves depict the corresponding results obtained with the previous release version 3.4.3. Due to the failure of the thermocouples at elevations 200 mm (Fig. 5.31) and 500 mm (Fig. 5.34), the experimental values are replaced by the measurements from the ultrasonic thermometers (TUS).

In general, there is a good agreement between calculated and measured values for the whole degradation phase, indicating a good description of the overall heat balance for the bundle. The ultrasonic thermometers (TUS) measured a lower temperature in the bundle than the thermocouples on the absorber rod and on the fuel rods. Therefore, the temperature indicated by the ultrasonic thermocouples is closer to the temperature of the inner surface of the thoria layer than to the fuel rod temperature.

The main heat conduction resistance is in the zirconia layer and in the two gaps. The relatively high conductivity of the thoria and of the Inconel keeps the temperature gradient in these two layers small. Considering that the exact thermocouple position can vary in the holes in the shroud and that the temperature gradient is very sharp in the zirconia layer, the agreement between calculation and measurement is rather good, with exception of the steep increase of the temperature at the elevation 200 mm at the begin of melt relocation (t~ 16200 s). This behaviour is not reproduced quantitatively accurately in the calculation, although an increase can still be observed making the qualitative prediction acceptable.

During the so-called calibration period (0 s-7900 s), the first cladding burst was calculated to occur at 5172 s, at the elevation 450 mm, due to internal over-pressure. The failure criterion applied was the occurrence of a maximum strain of 38 %. The cladding temperature in the middle of the bundle was calculated to be ~1085 K. Shortly thereafter the first release of fission products was predicted (~ 5800 s in the test).

The following pre-oxidation period started by increasing the nuclear power. The bundle cladding temperature increased up to ~1273 K, and Zircaloy oxidation with hydrogen generation was calculated to start at ~8100 s, nearly in the middle of the bundle. The calculated and the measured hydrogen generation rates are shown in Fig. 5.37. The control rod fails at a calculated time of ~10170 s in the upper part of the bundle, when the given failure temperature of the absorber rod and guide tube of 1523 K is reached. During the experiment, the control rod failure with the release of absorber material was first detected at ~9690 s. At that time the maximum temperature measured in the bundle was 1620 K.

This pre-oxidation period ended with the temperature escalations mainly in the upper part of the bundle, at about 11300 s. The beginning of the runaway oxidation, with a rapid increase of the bundle temperatures due to the Zircaloy reaction was well captured by the simulation. The diagrams of the temperature histories show a good agreement between the calculated and the measured time for the beginning of the runaway oxidation (Fig. 5.37). At this point the oxidation rate accelerates considerably, leading to a measured peak value of the H_2 generation rate of ~0.10 g/s at ~ 11700 s, which is overestimated by the simulation (Fig. 5.37). A better agreement considering the maximum hydrogen generation rate can be obtained with the Cathcart and Urbanic-Heidrick correlations (`IOXMOD`=2), though with a time delay concerning the onset point of the oxidation run-away.

Because of the high steam inlet mass flow rate, no steam starvation was observed. After the oxidation peak, a short cool down of the temperatures was observed, due to the almost complete oxidation of the metallic Zircaloy in the upper regions of the bundle and the heat losses through the shroud.

At the end of the degradation phase the calculated total mass of hydrogen released was ~104 g, which somewhat overestimates the measured value of 96 g. Considering the experimental uncertainties ±13 g the measured values envelope the simulated ones (Fig. 5.38).

The following heat-up period (14580-17039 s) was characterized by the increase of the nuclear power up to fuel liquefaction in order to produce extensive degradation of the bundle and additional fission product releases. During the experiment, first possible fuel movements were identified at ~15380 s at the elevation 300 mm, and fuel relocation was clearly detected at ~16000 s /JAC 00/. A second distinct fuel relocation phase was observed at ~16900 s. At the end of the degradation phase, a molten pool zone had formed in the lower part of the bundle, mainly between the elevations 153 mm and 236 mm.

In the calculation, melting and relocation of the fuel started in the inner ring at ~16643 s, beginning at the elevation 500 mm. Degradation and slumping of material were calculated to occur in both rod rings. However, the modelling of relocation does not take into account a radial spreading of molten material. During the relocation phase, a second smaller hydrogen generation peak has been calculated, due to melt and crust oxidation (Fig. 5.37).

About 2.11 kg of the bundle was calculated to melt (Fig. 5.39) and relocate during the degradation phase. In the experiment, the mass of molten pool was estimated to be around 2 kg.

The results obtained with the new version 3.5 are practically identical to those of the previous version, except for molten fuel mass, also with respect to the computational performance (Fig. 5.40).

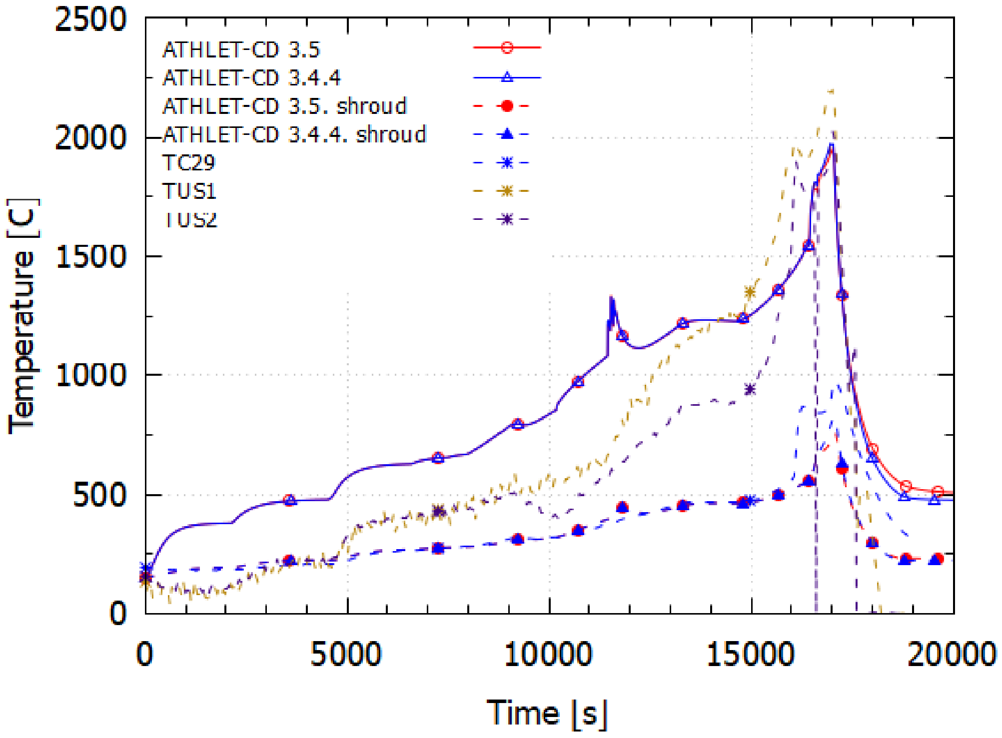

Fig. 5.31 FPT1 – Bundle temperatures at elevation 200 mm

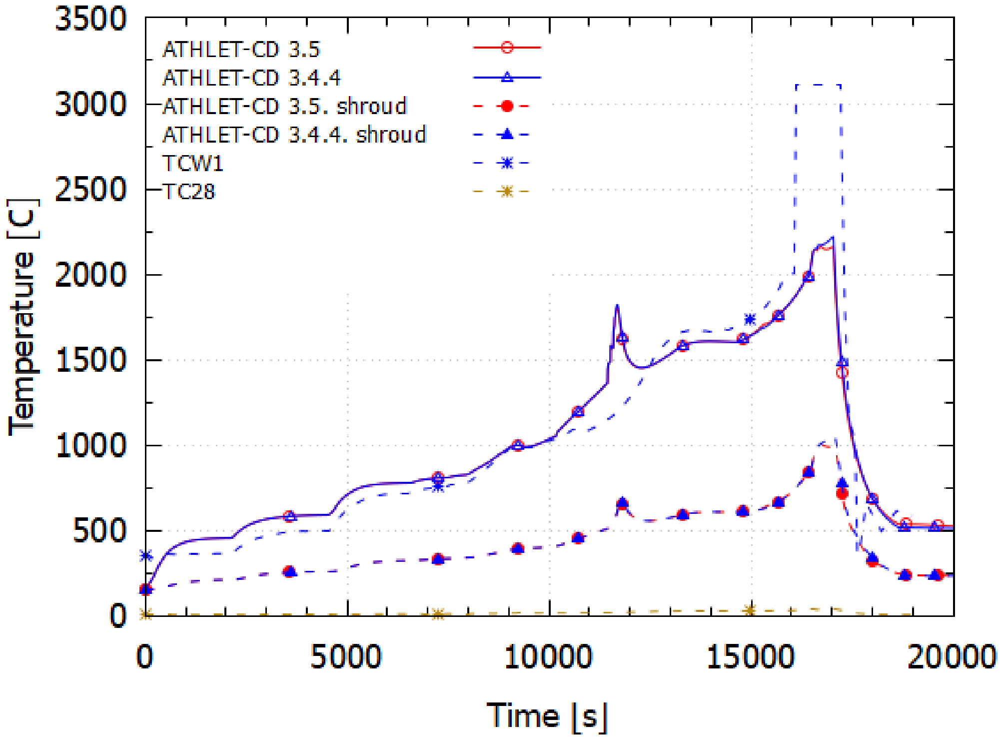

Fig. 5.32 FPT1 – Bundle temperatures at elevation 300 mm

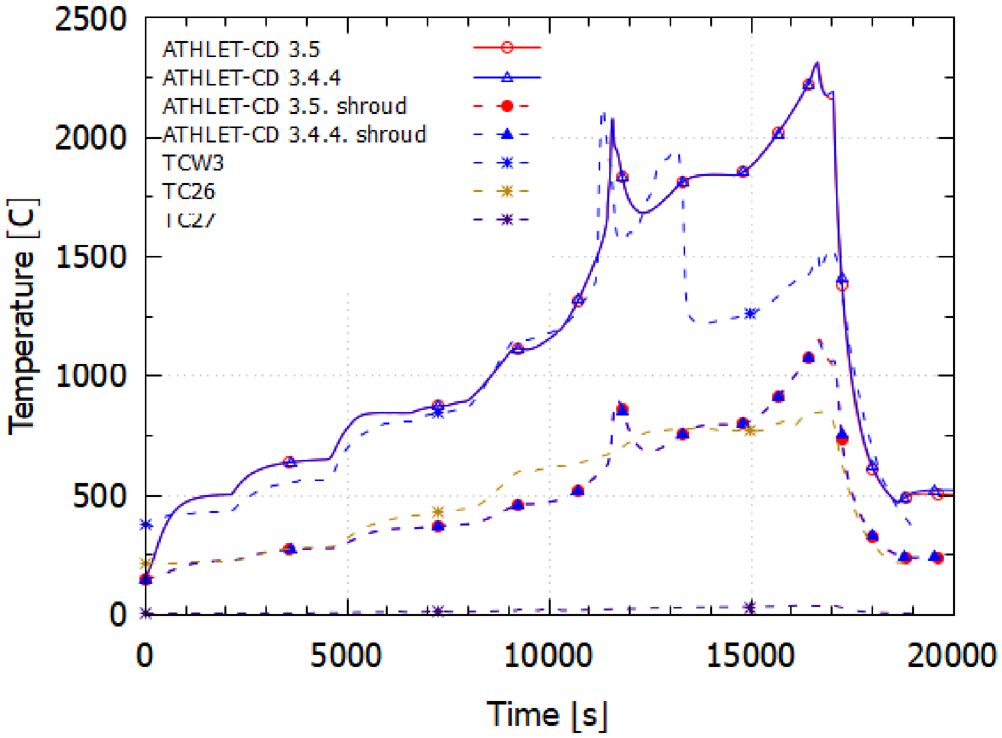

Fig. 5.33 **FPT1 –** Bundle temperatures at elevation 400 mm

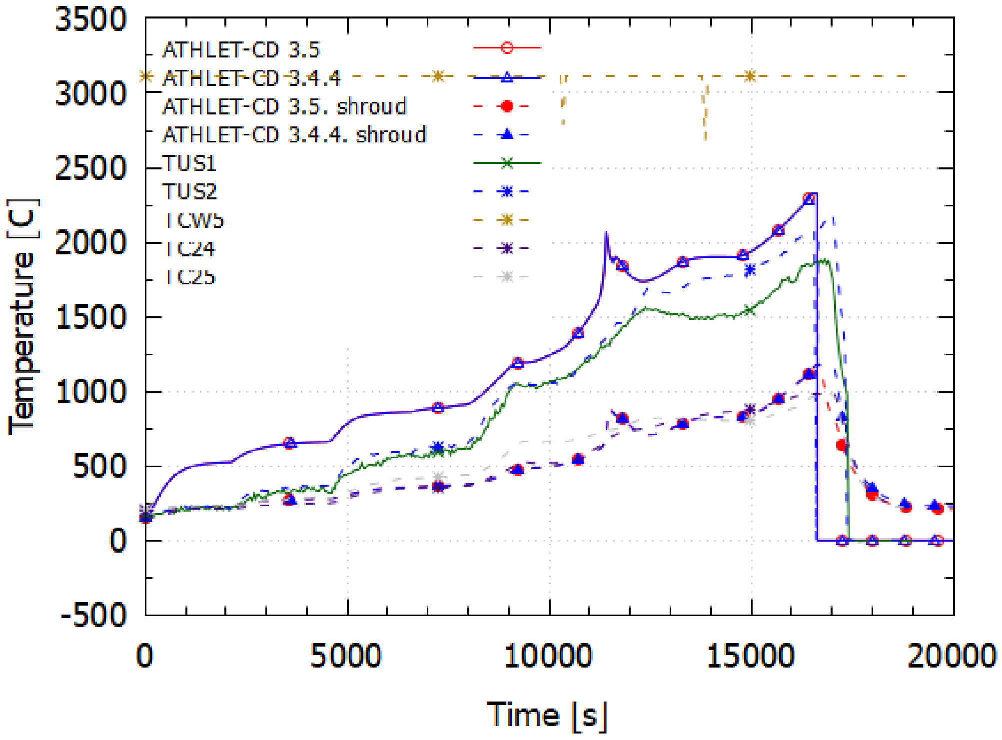

Fig. 5.34 FPT1 – Bundle temperatures at elevation 500 mm

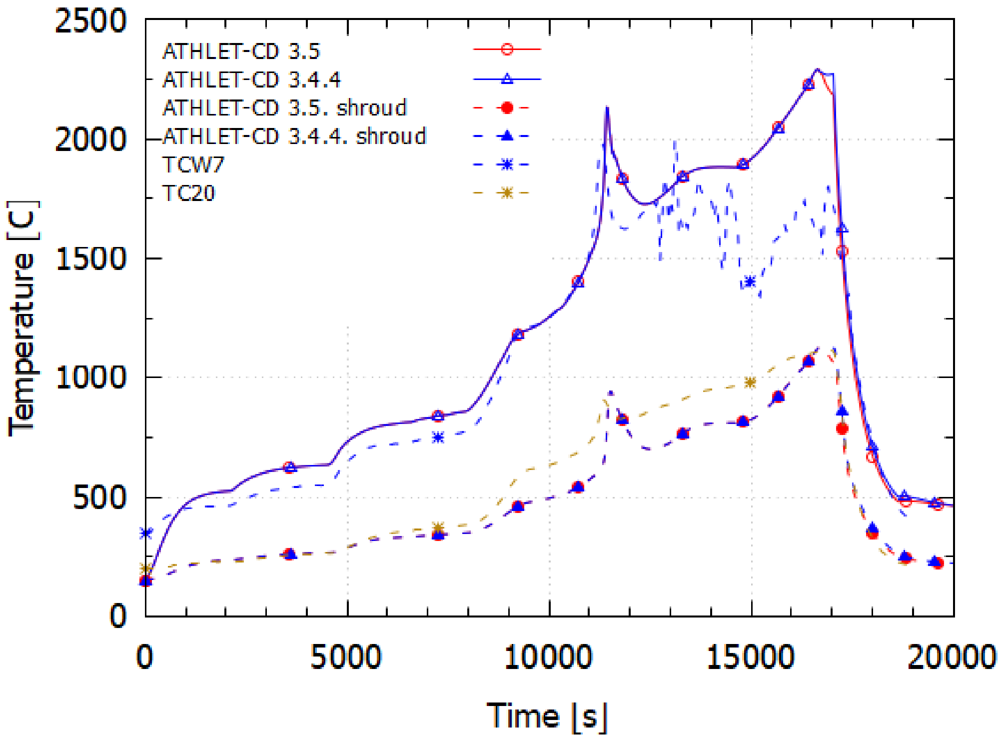

Fig. 5.35 FPT1 – Bundle temperatures at elevation 600 mm

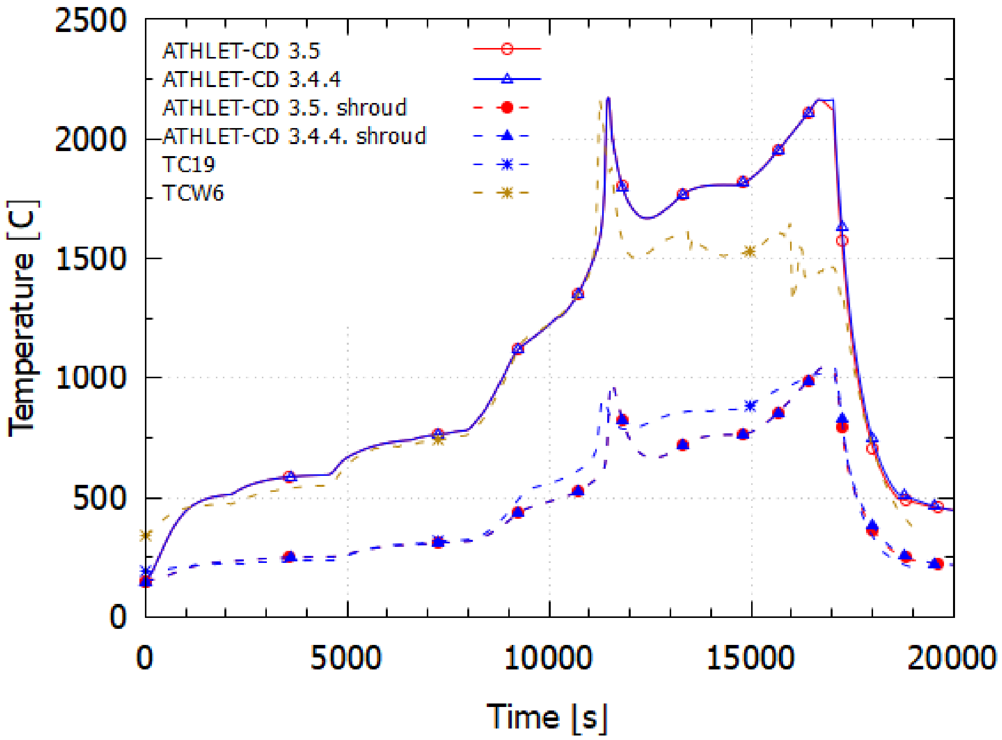

Fig. 5.36 FPT1 – Bundle temperatures at elevation 700 mm

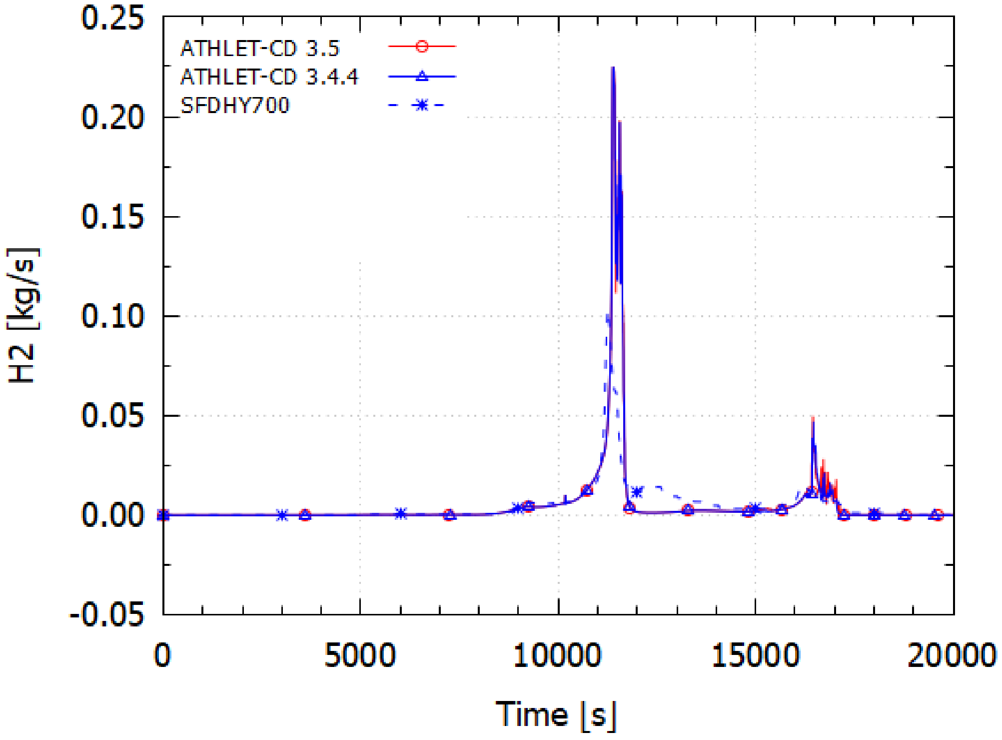

Fig. 5.37 FPT1 – Hydrogen generation rate

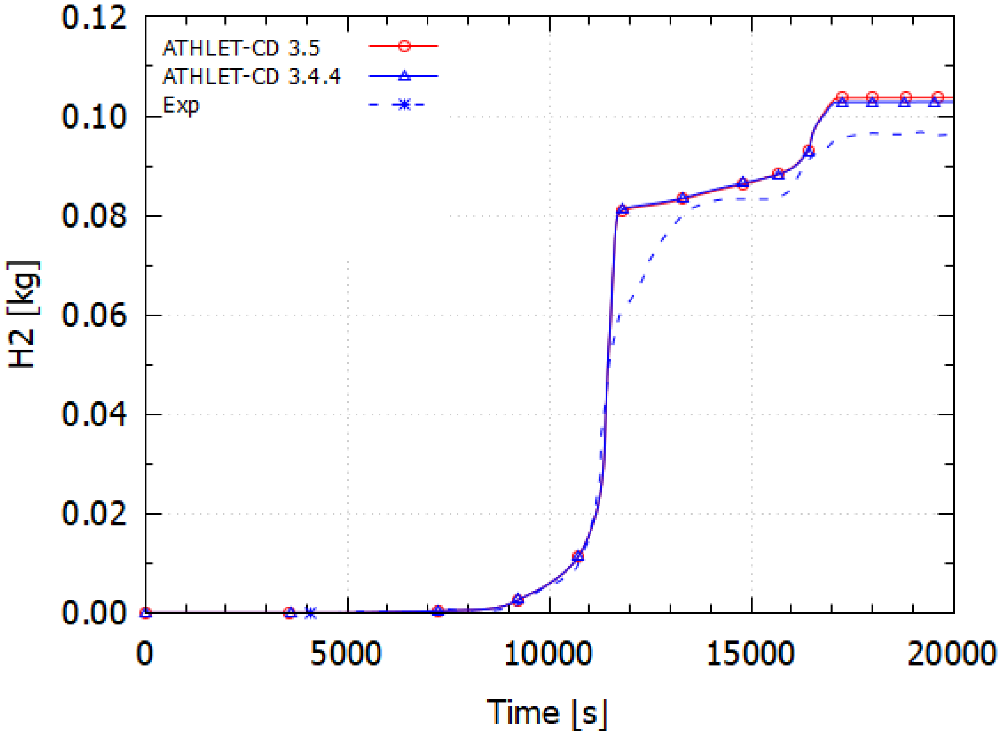

Fig. 5.38 FPT1 – Total hydrogen production

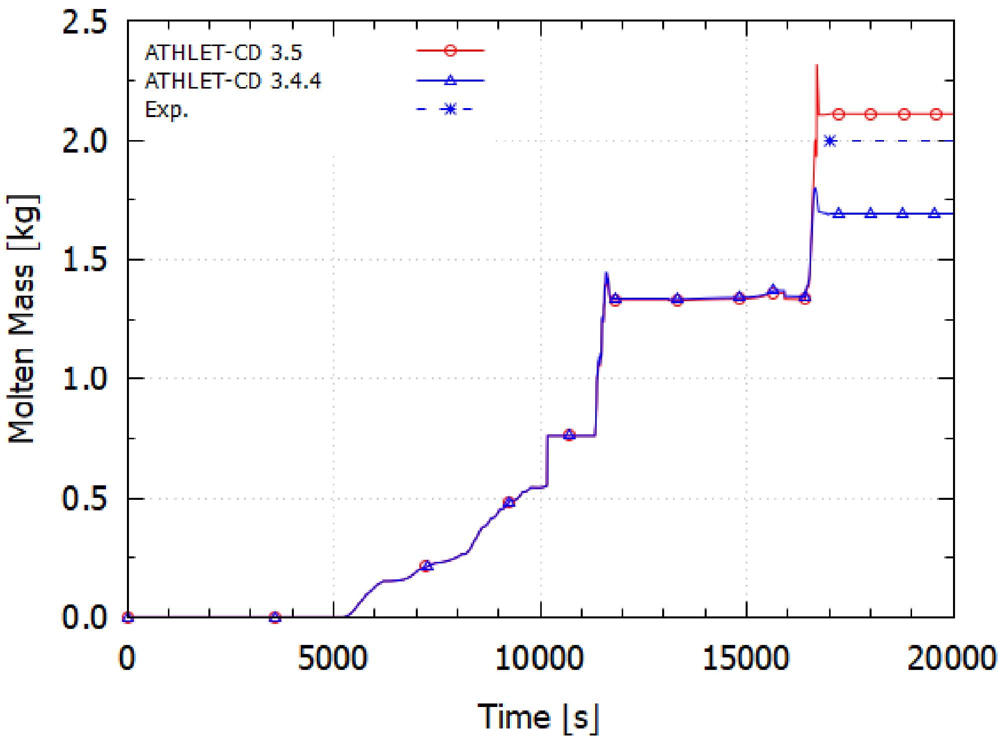

Fig. 5.39 FPT1 Molten mass

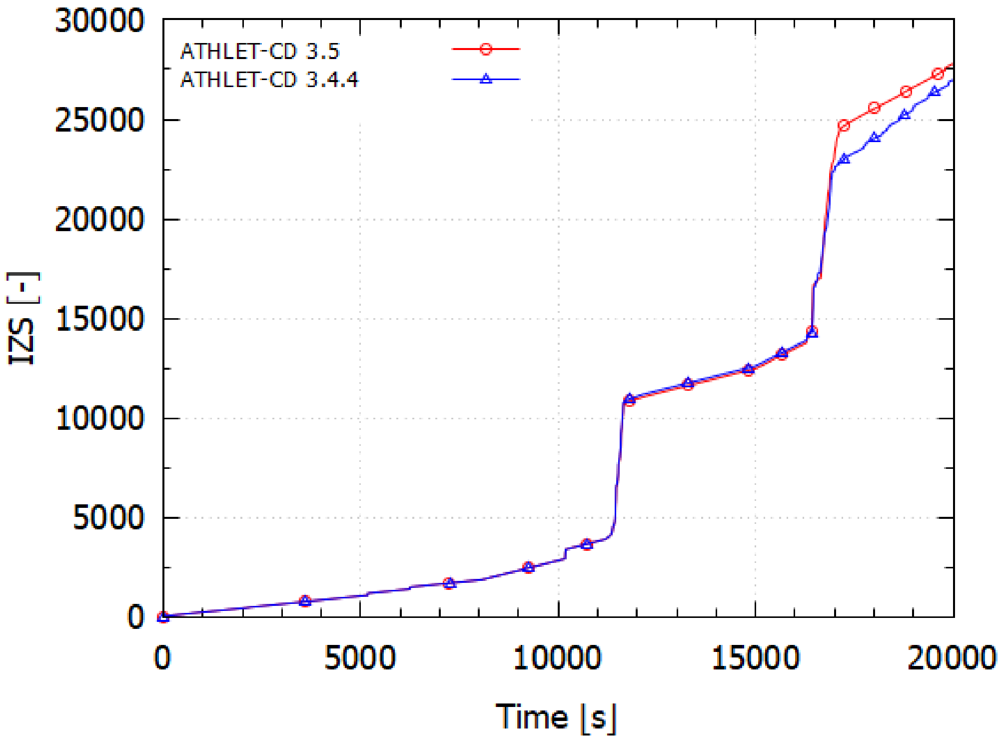

Fig. 5.40 FPT1 – Number of time steps and Jacobian calculations

5.5.5 Main Findings

The calculated results for the test FPT1 show good agreement with the experimental data regarding the thermal behaviour of the test bundle. However, the simulation of relocation processes with both code versions is still not fully satisfactory.

Several input parameters can influence the calculation of melt relocation. The most important of them seems to be the solidus temperature T_{sol} for UO_2 (input parameter `TCOMPM`). The lower the input value for T_{sol}, the earlier the start of relocation and the higher the amount of relocated mass at reactor shutdown. For the test FPT1, changes of 50 K in the solidus temperature may result in differences of about 20-25 % of the relocated fuel mass. Nevertheless, due to the minor differences in temperatures and the cliff-edge nature of melting of the nodes the estimated amount of melt is (though somewhat overestimated) in better agreement with the measured one compared to the previous version. This effect also explains the small differences in time step behaviour.

The liquidus temperature (input `TCOMPL`) also influences the start of the relocation process, but to a lesser extent. It affects mainly the ratio between crust and melt masses, and thus the formation and extension of the liquefied melt pool: the higher the liquidus temperature `TCOMPL`, the later the formation of the melt pool and the smaller the amount of melt mass. Additionally, higher liquidus temperatures lead to reduced melt oxidation, and to a shift of the mass accumulation toward lower bundle regions.

Another important parameter is the input value for the candling velocity of the ceramic melt (input `WSLUO`). This parameter influences not only the total amount of relocated mass, but mainly the axial mass distribution. The higher the candling velocity, the smaller the total amount of relocated mass, and the more the axial distribution is shifted towards the lower bundle regions. A similar effect can also be obtained with the variation of the melt viscosity.

Melt retention due to the spacer grids is not taken into account by the code, explaining some of the deviations.

5.6 PHÉBUS FPT-3

5.6.1 Facility Description

The facility description is given in chapter 5.5.1.

The test bundle consists of 20 Zircaloy-clad fuel rods (Fig. 5.41), out of which 18 are previously irradiated. In the central position a boron carbide (B_4C) control rod is found.

5.6.2 Test Conduct

Before the transient test phase, a re-irradiation phase was carried out in order to obtain a representative bundle fission product inventory by re-creating short lived fission products. This phase was followed by a transition phase, after that the experimental phase was performed starting with the bundle degradation phase and followed by a long-term phase for investigation of phenomena in the containment. As Fig. 5.43 shows, the core degradation phase can be divided into six phases: the calibration phase (till 7920 s) followed by the pre-oxidation (7920 s -8640 s) and the oxidation (8640 s -11100 s), the P4 power plateau (11100 s -15420 s), the heat-up phase (15420 s -17370 s), and finally the cool-down (starting at 17370 s).

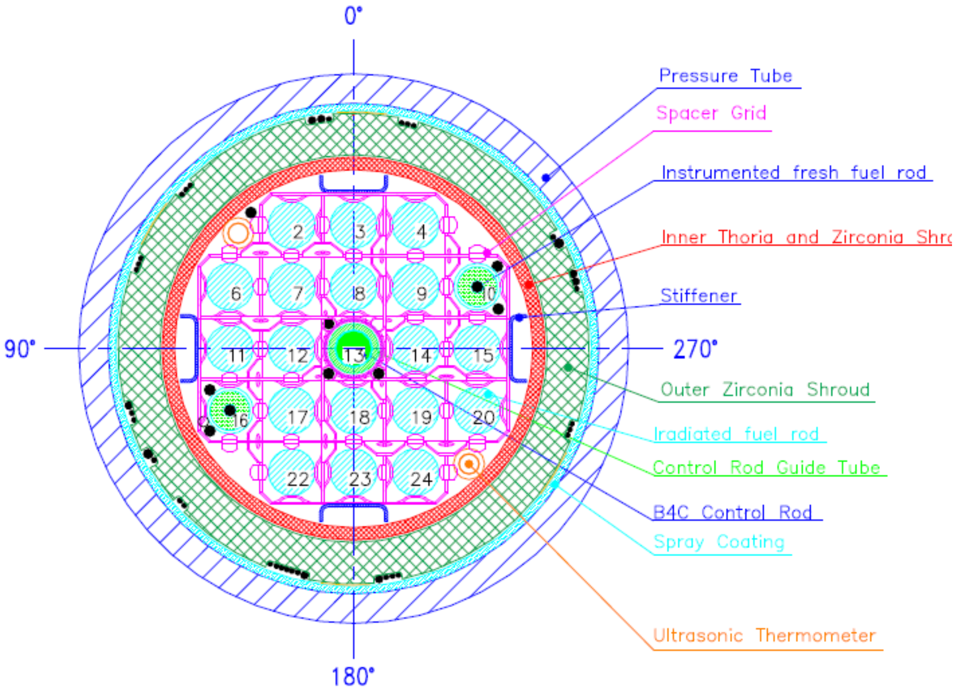

Fig. 5.41 Cross section of the test bundle

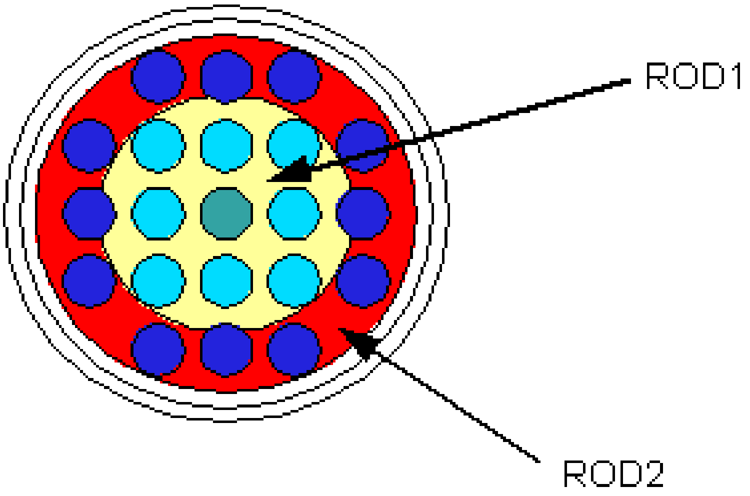

Fig. 5.42 Modelling approach of the test bundle

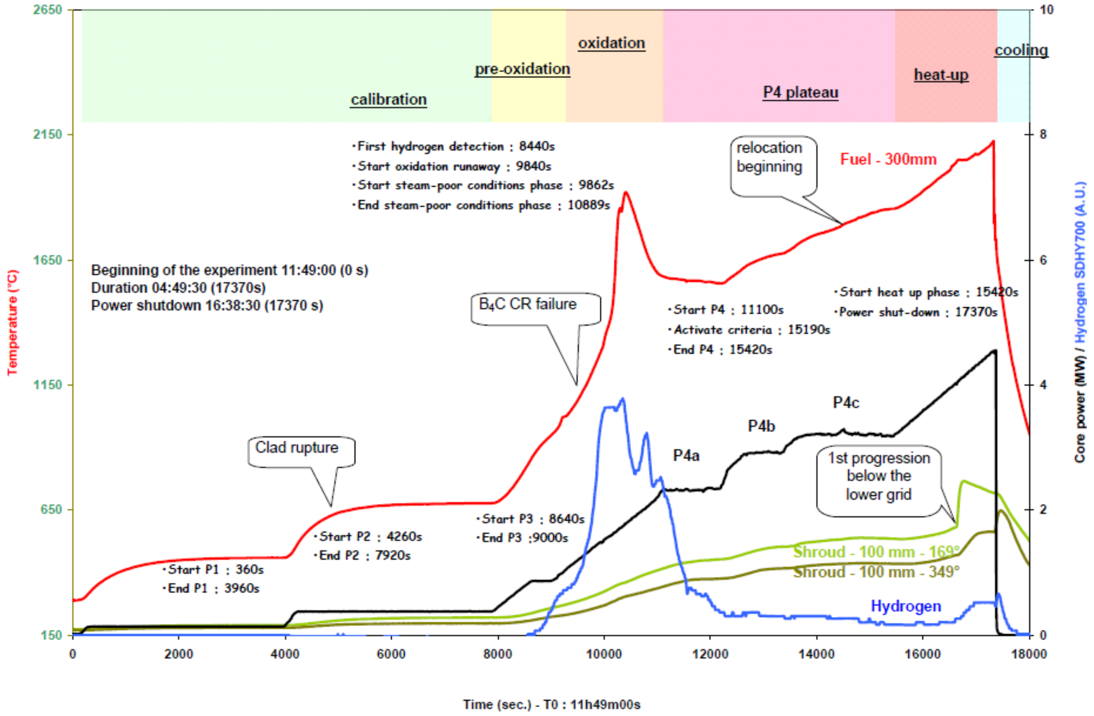

Fig. 5.43 FPT3 Chronology /PAY 10/

5.6.3 Input Dataset

5.6.3.1 Nodalisation

Fig. 5.44 shows the nodalisation of the primary circuit. The circuit nodalisation comprises the test bundle, the bypass (`BYPASS`), the plenum (`PLENUM`), the hot leg (`HOTPIP`), the steam generator (`STGEN`), the cold leg (`COLPIP`), and the containment (`CONTAN`). The test bundle of the Phébus facility is modelled by two concentric rings (`BUNDLE`, `OUTER`) with 26 axial nodes and with cross flow connections to allow flow deflection due to fuel rod deformation and blockage formation caused by refreezing of molten material. The implementation of a B4C absorber instead of AIC like in FPT-1 significantly influences the melting behaviour and its phenomena. The eight innermost fuel rods are situated within `ROD1`, while the outer twelve fuels are assigned to the object: `ROD2`, as shown in Fig. 5.42. Altogether the model consists of 13 TFOs including 110 CVs, 52 HCO with 98 HCVs, as well as 1 SAFT-Loop comprising of 4 TFOs.

5.6.3.2 Model Options

Fuel rod relocation has been simulated in rod-like geometry (candling model) assuming a constant relocation velocity. Radial melt spreading between core rings is not taken into account. The release of fission products is simulated with the help of the `NMODI` Option 3 (taking into account not only the temperatures, but the partial pressures of some elements as well). The transport of the FPs is calculated by SAFT, which is defined starting from the plenum, including the whole path up until the containment. The simulation time was 22500 s.

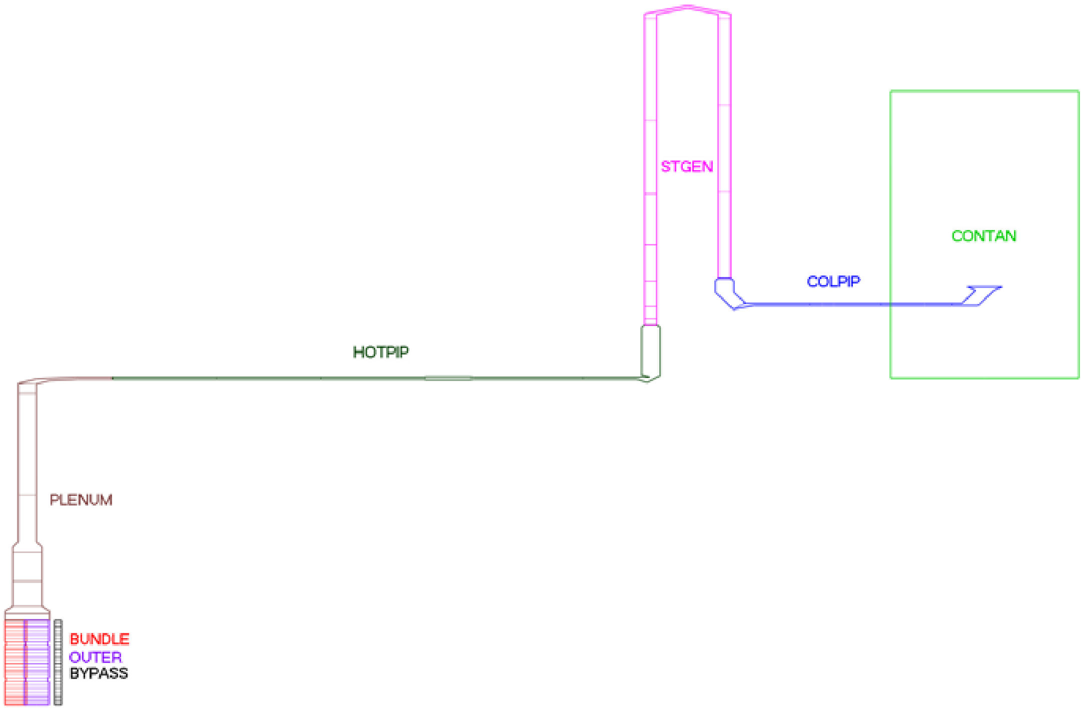

Fig. 5.44 ATHLET-CD model of the FPT-3 test

5.6.4 Main Results

There is no relevant difference between the simulated temperatures within the core region with the code versions ATHLET-CD 3.5 and 3.4. There are only small deviations between the two versions throughout the whole simulation time.

Fig. 5.45 to Fig. 5.48 depict the temperatures at different elevations within the bundle. The fuel and clad temperatures are both well predicted, though somewhat overestimated especially starting from 10000 s, by both code versions. Nevertheless, the qualitative progression of the heat-up is very well captured, and the simulated values are generally in good agreement with the measurements.

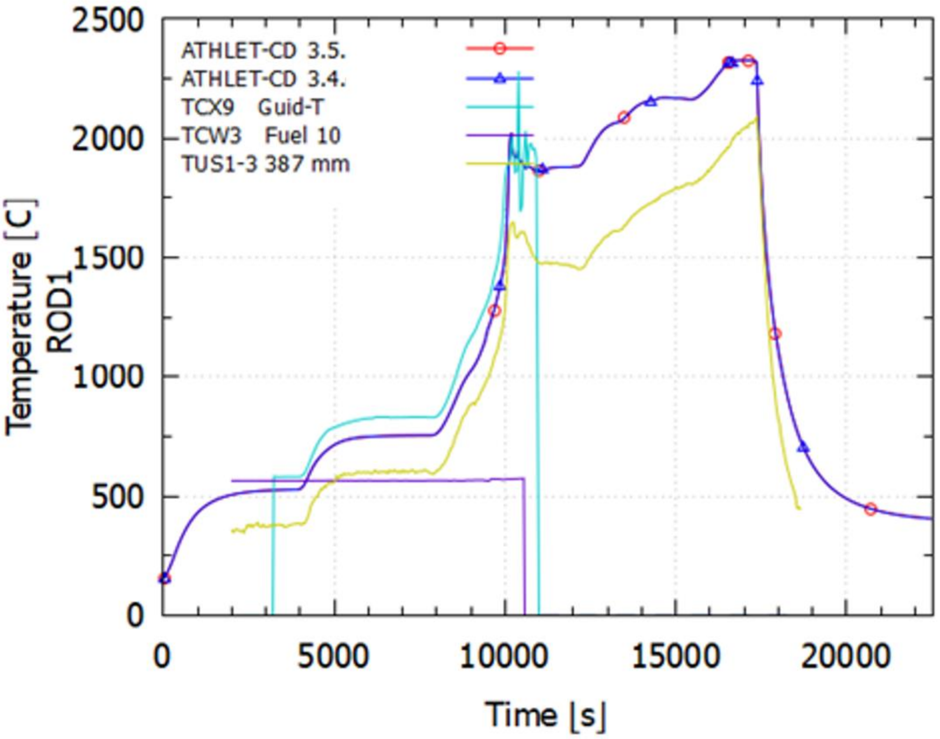

Fig. 5.45 Measured and calculated temperatures at 400 mm elevation with TCX9 guide tube temperature, TCW3 fuel temperature and TUS1-3 ultrasonic thermometer measurements

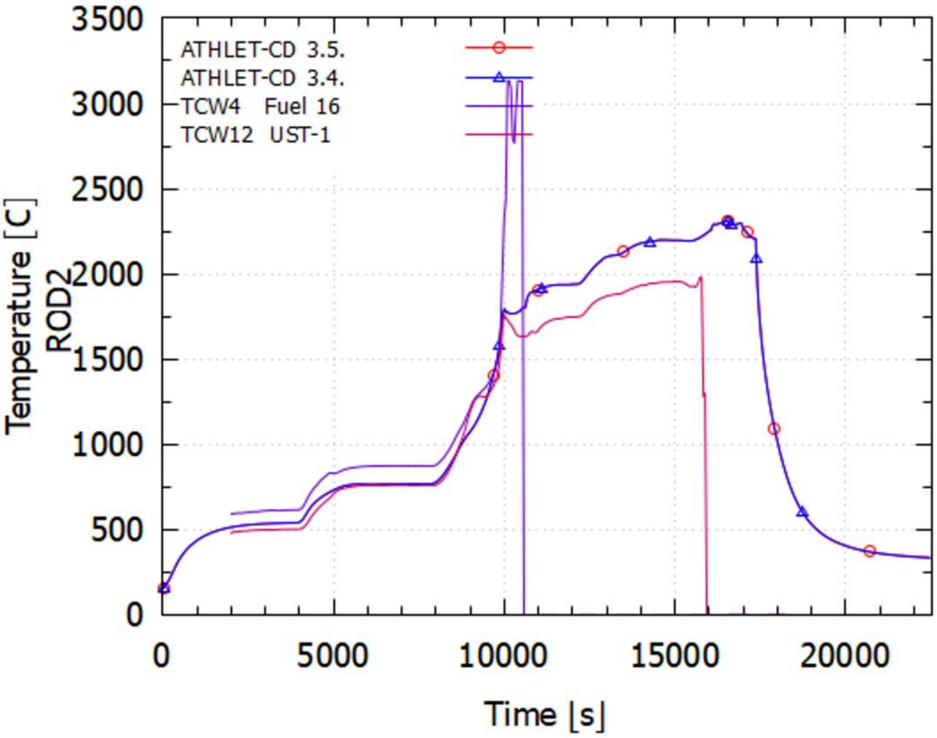

Fig. 5.46 Measured and calculated temperatures at 500 mm elevation with TCW4 fuel temperature and TCW12 ultrasonic thermometer measurements

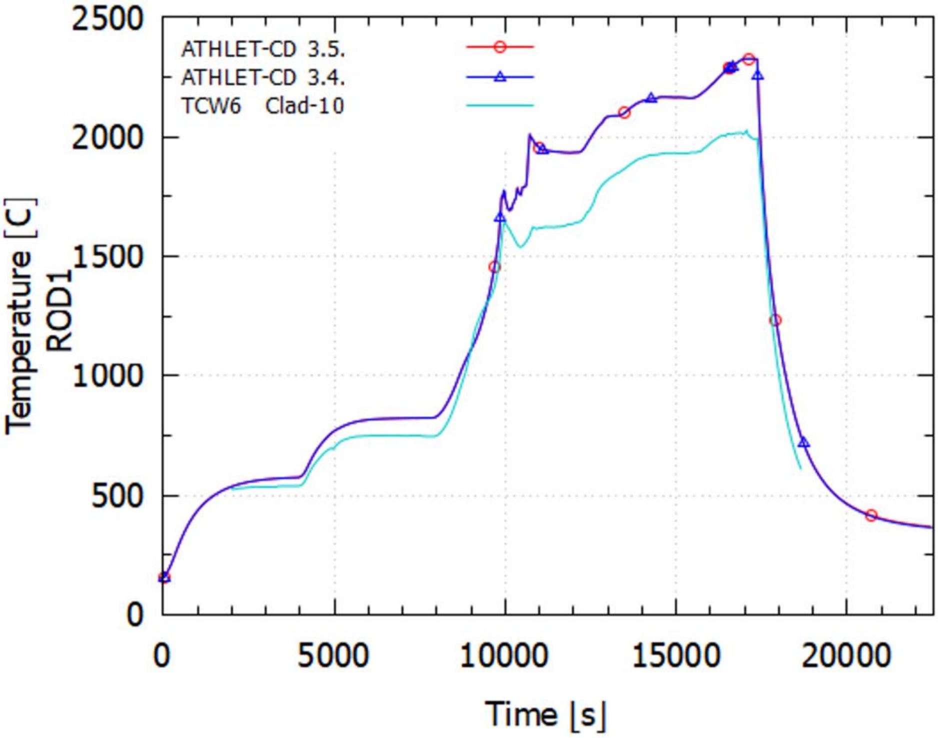

Fig. 5.47 Measured and calculated temperatures at 600 mm elevation with TCW5 cladding temperature measurement

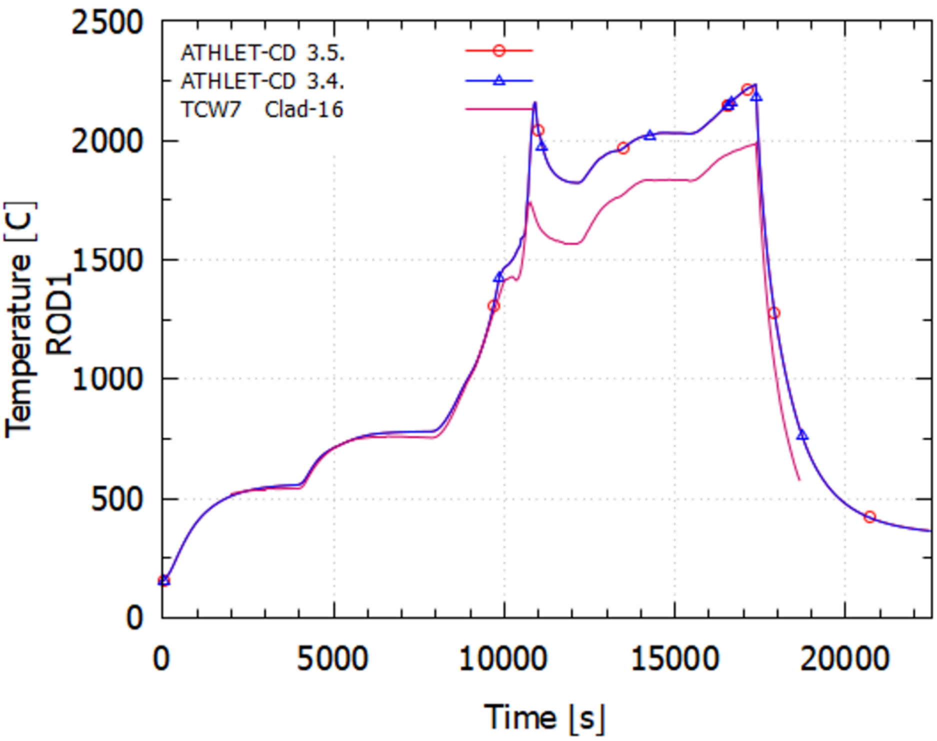

Fig. 5.48 Measured and calculated temperatures at 700 mm elevation with TCW8 cladding temperature measurement

Fig. 5.49 shows the hydrogen produced during the experiment. The majority of the hydrogen production takes place during the first oxidation period (~9800 s-~10900 s), and only a small fraction of the overall amount is generated during the second oxidation phase (~16000 s-~17000 s). This qualitative process is well captured by the simulations, though there are some quantitative deviations. The dynamics of the production is somewhat overestimated in the first oxidation period and greatly underestimated in the second. The underestimation of the second oxidation phase is due to the overestimation of the first, as the material oxidised during the second period in the experiment has been predicted to be oxidised during the first oxidation period. The experimental value of 60±3 mol is underestimated by the simulation. Nevertheless, considering the experimental uncertainties the cumulated value is only slightly below the measurements. On the other hand, it is enveloped by the SDHY700 and SDHY701 measurements, showing the significant uncertainties present in the measurements. Generally, it can be concluded that the prediction is acceptable.

The amount of molten mass in the experiments was ~1.6 kg, which is slightly overestimated by the calculated value of ~1.8 kg (Fig. 5.50).

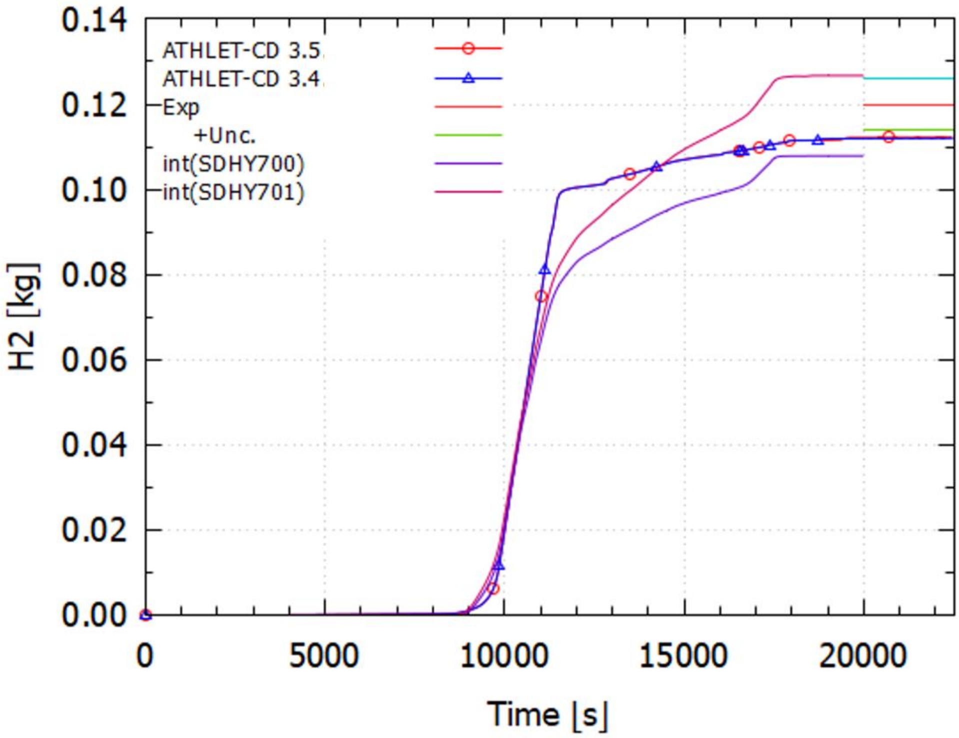

Fig. 5.49 Cumulated hydrogen production

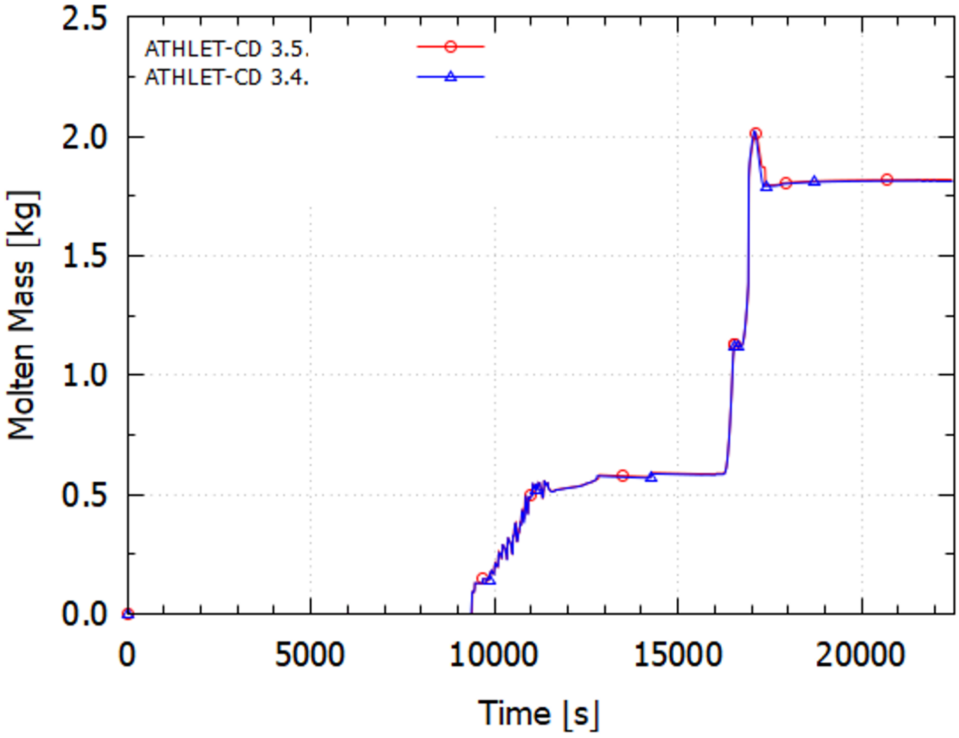

Fig. 5.50 Calculated molten masses

The release fraction of fission products from the core is depicted in Fig. 5.51 for iodine, Fig. 5.52 for caesium, Fig. 5.53 for xenon, and Fig. 5.54 for barium. Where available, the following diagrams include error bars corresponding to the experimental uncertainty (1 standard deviation). Both versions ATHLET-CD 3.5/3.4 show practically the same results, with no significant differences. The noble gases, such as Xe, are very well predicted, as well as the total amount of iodine, though the actual release dynamic is overestimated. As shown in the figures the bug in the dataset had practically no effect on the simulation of the fission product behaviour.

In the experiment about 9 % of the initial bundle inventory (%i.i.) of caesium was found to be deposited in the upper core region, i.e. trapped as Cs_2MoO_4 or Cs_2ZrO_3 in the higher parts of the bundle, yielding a total estimated caesium release of 73 %i.i. from the fuel. In the graph, the result labelled “Exp. Fuel” represents this fuel release calculated by multiplying the bundle release with the final fuel/bundle release ratio. Since the present simulation does not take deposition in the core region into consideration, the simulation results correspond more to this adjusted value, which is very well captured.

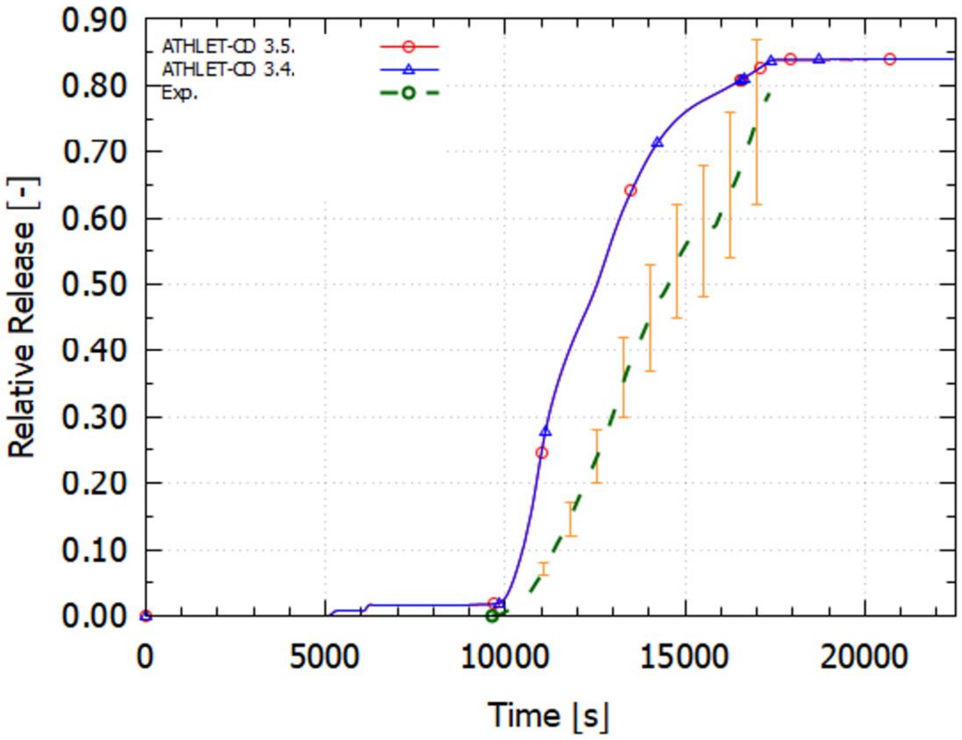

Fig. 5.51 Iodine release fraction from the core

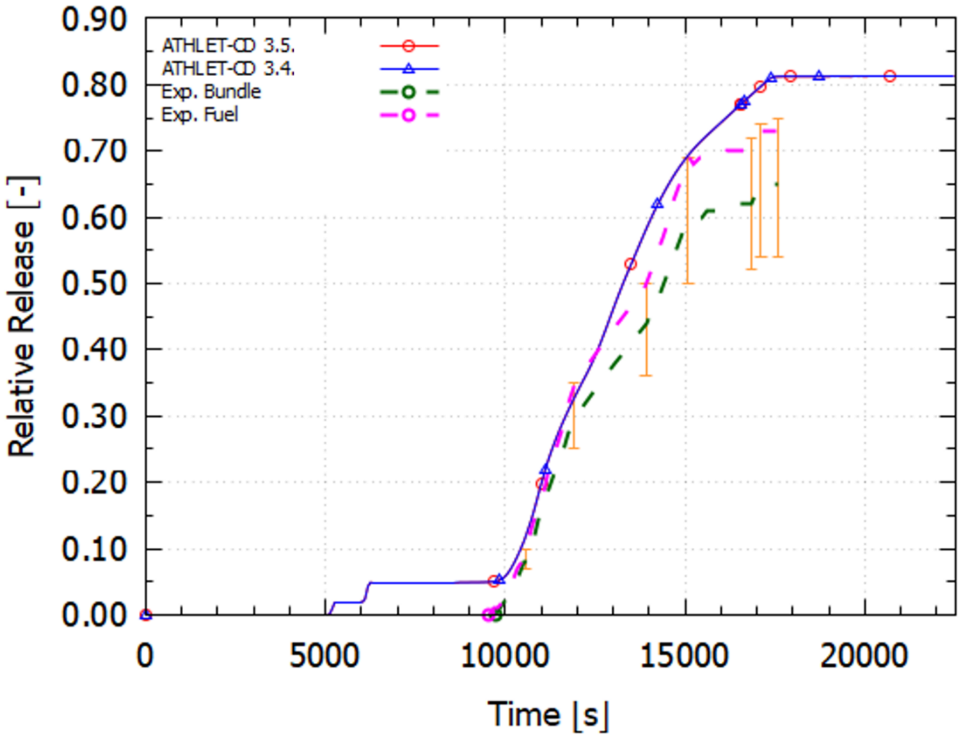

Fig. 5.52 Caesium release fraction from the core

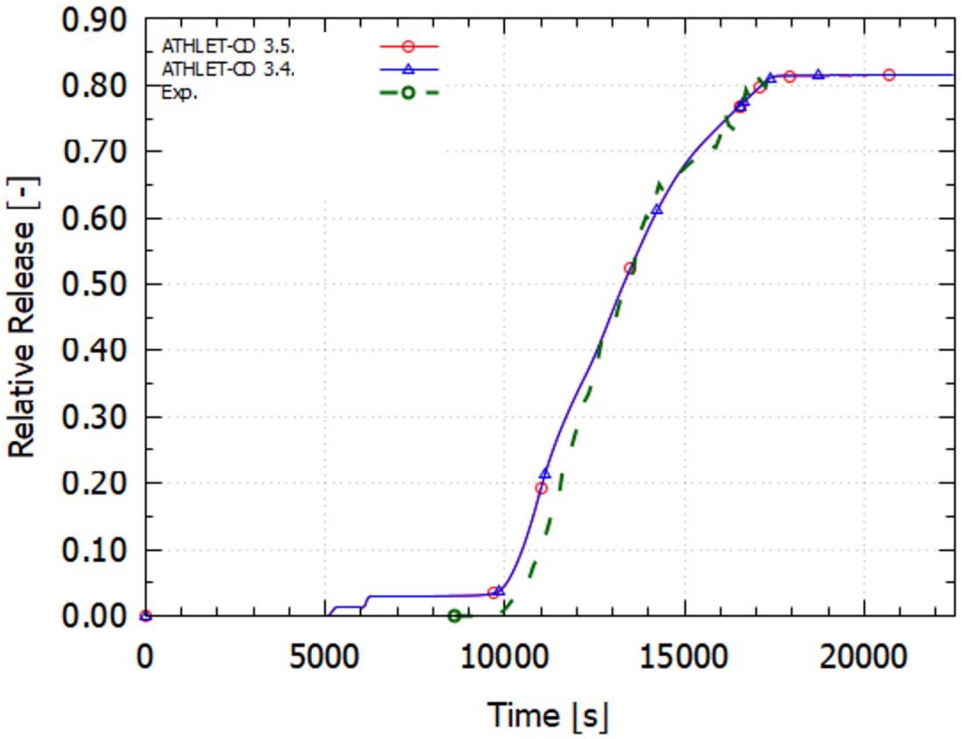

Fig. 5.53 Xenon release fraction from the core

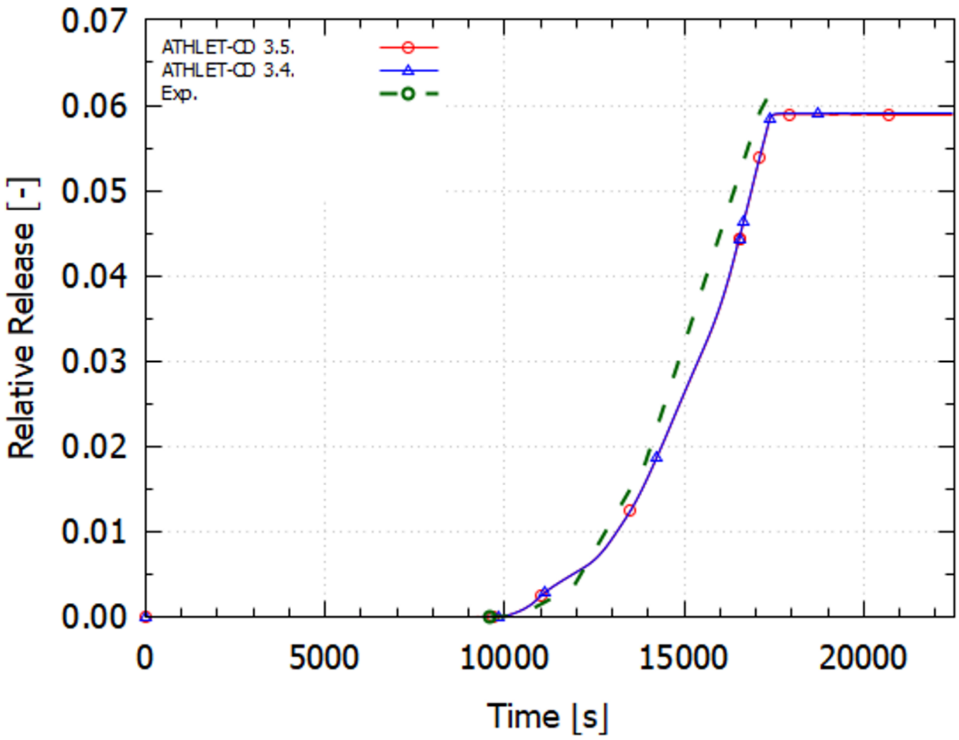

Fig. 5.54 Barium release fraction from the core

The release into the containment is shown in Fig. 5.55 for caesium, Fig. 5.56 for iodine, Fig. 5.57 for silver, Fig. 5.58 for tellurium, Fig. 5.59 for xenon and Fig. 5.60 for molybdenum. Where available, the diagrams include error bars corresponding to the experimental uncertainty (1 standard deviation). In case of all elements both versions predict practically the same values, which are in good agreement with the experiment In case of iodine and caesium the predictions are enveloped by the given experimental uncertainties. For other elements no such open information is available.

In what form iodine enters the containment is highly important. Contrary to previous tests, where iodine was almost entirely injected in an aerosol form, in the FPT-3 test 87,7 % of the iodine released into the containment was in gaseous form and only to a lesser extent in an aerosol from (12.3 %). This behaviour is not well captured by either versions, both predicting about 72 % of aerosol, and only 28 % gaseous iodine to enter the containment. On the other hand, previous versions predicted the iodine being almost only in aerosol form

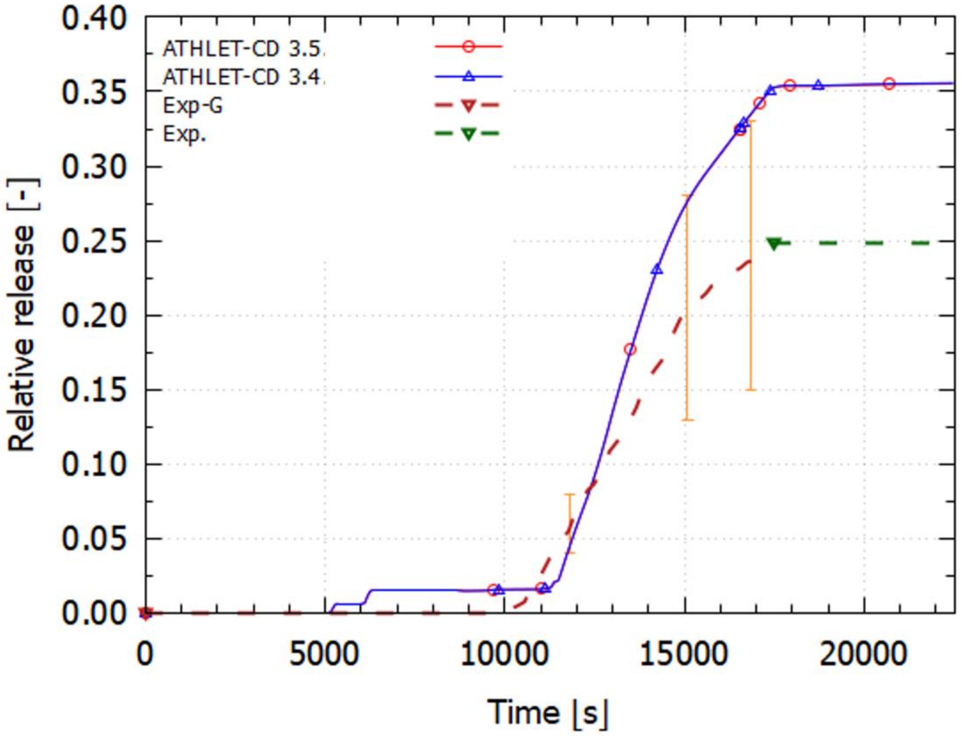

Fig. 5.55 Fraction of Cs mass released into the containment

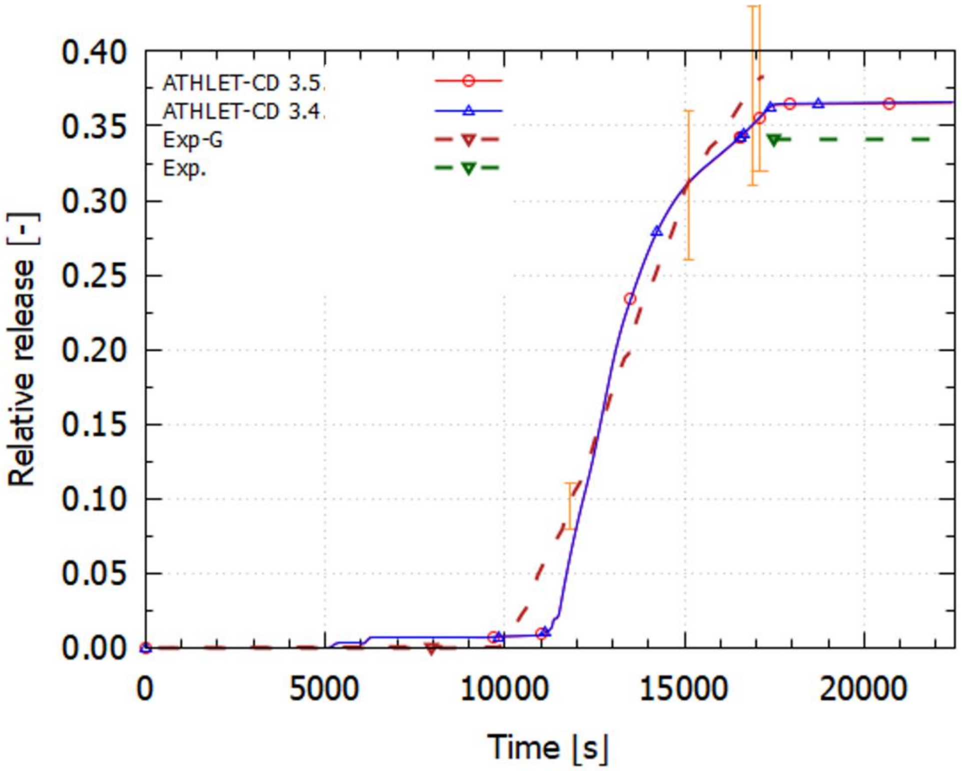

Fig. 5.56 Fraction of I mass released into the containment

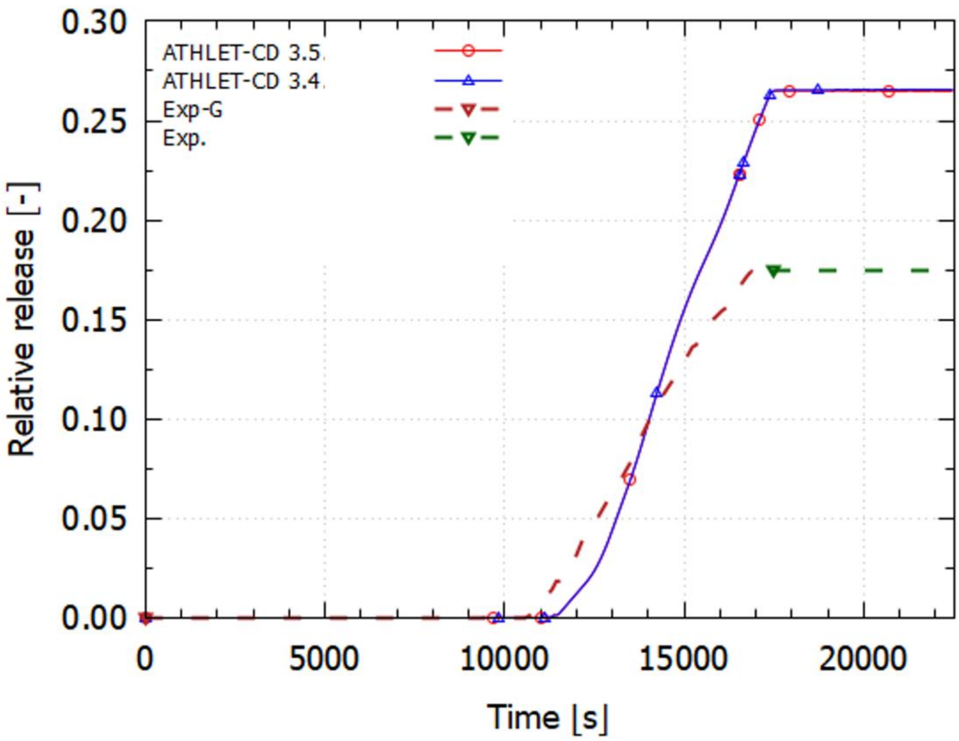

Fig. 5.57 Fraction of Ag mass released into the containment

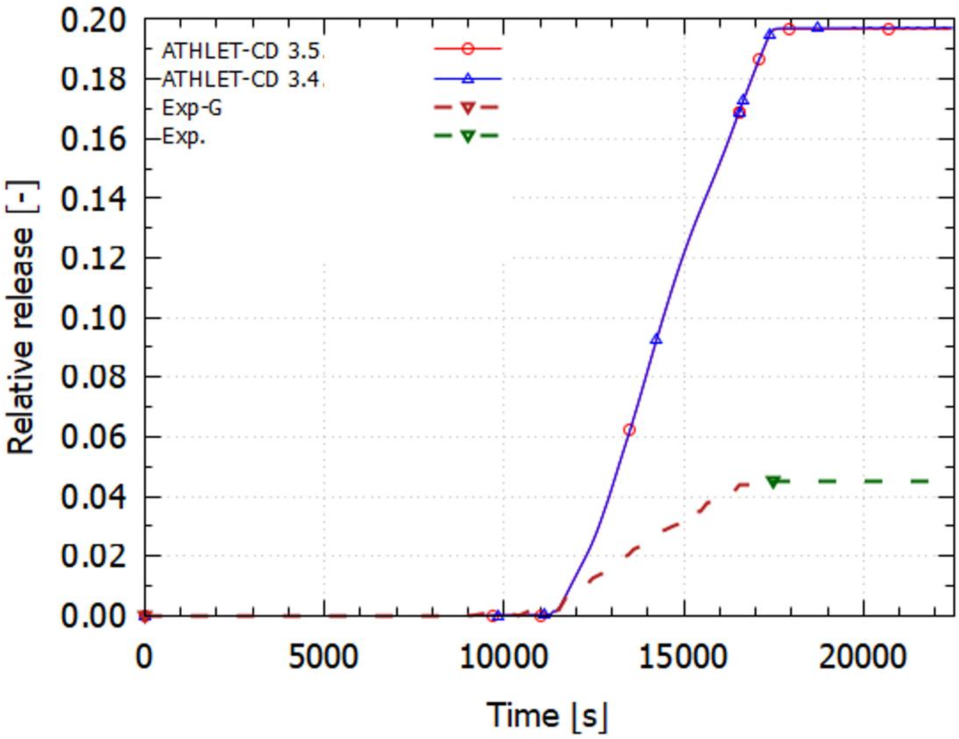

Fig. 5.58 Fraction of Te mass released into the containment

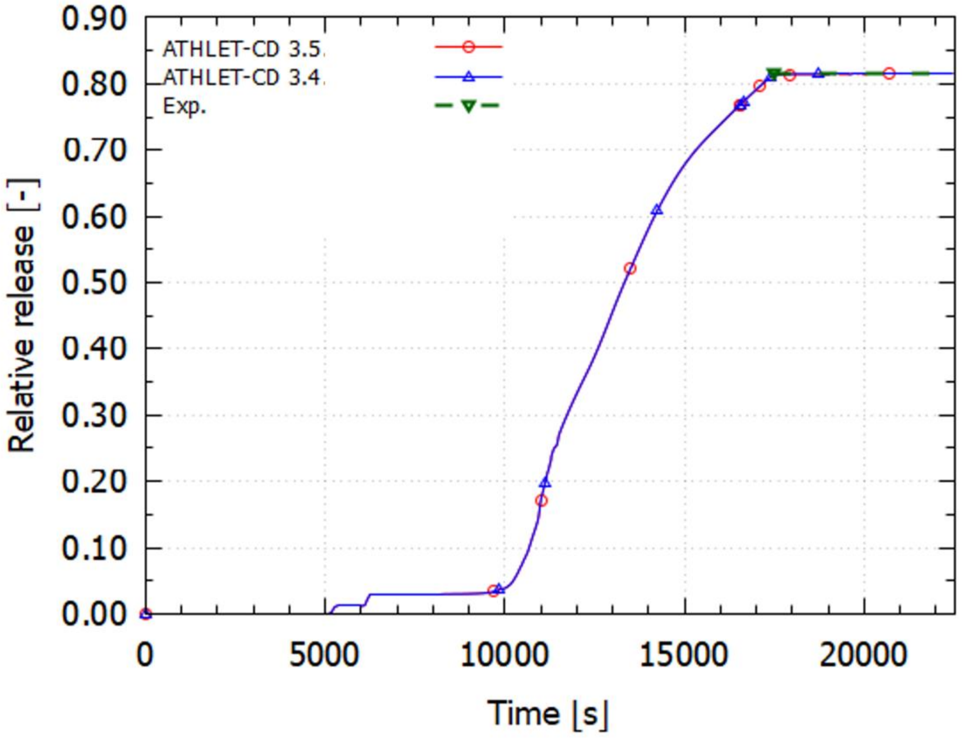

Fig. 5.59 Fraction of Xe mass released into the containment

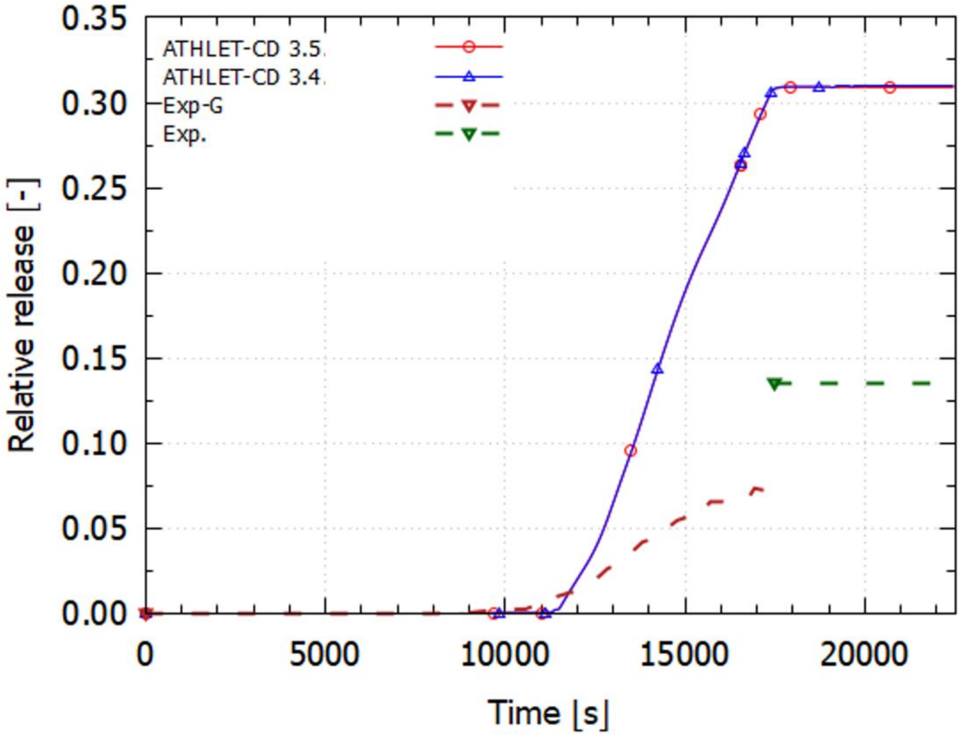

Fig. 5.60 Fraction of Mo mass released into the containment

The deposition of caesium und iodine (at 17370 s) alongside the circuit can be seen in Fig. 5.61 and Fig. 5.62. The vertical lines show the division between the segments alongside the cooling circuit: up to 3.472 m Plenum+Vertical line; 3.472 m-13.032 m Hot leg; 13.032 m-21.359 m Steam generator; starting from 21.35 m Cold leg. Both versions ATHLET-CD 3.5./3.4 predict very similar deposition. The predicted evolution of other elements is similar. A quantitative analysis of the deposition (where measurements are available), shows that on average the two versions perform similarly, and that overall results for deposition are satisfactory considering the uncertainties involved and the limitations in ATHLET-CD models.

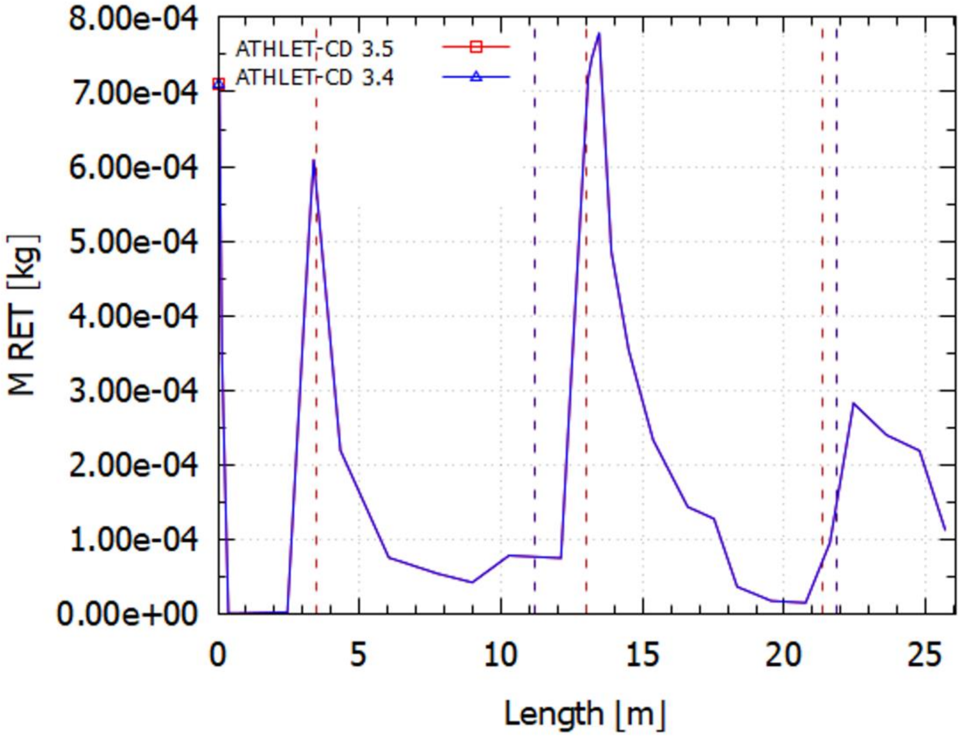

Fig. 5.61 Deposition of Cs (at 17370 s) in the circuit with vertical lines indicating release path up to the upper plenum, the hot leg, the steam generator entry, and steam generator exit into the cold leg

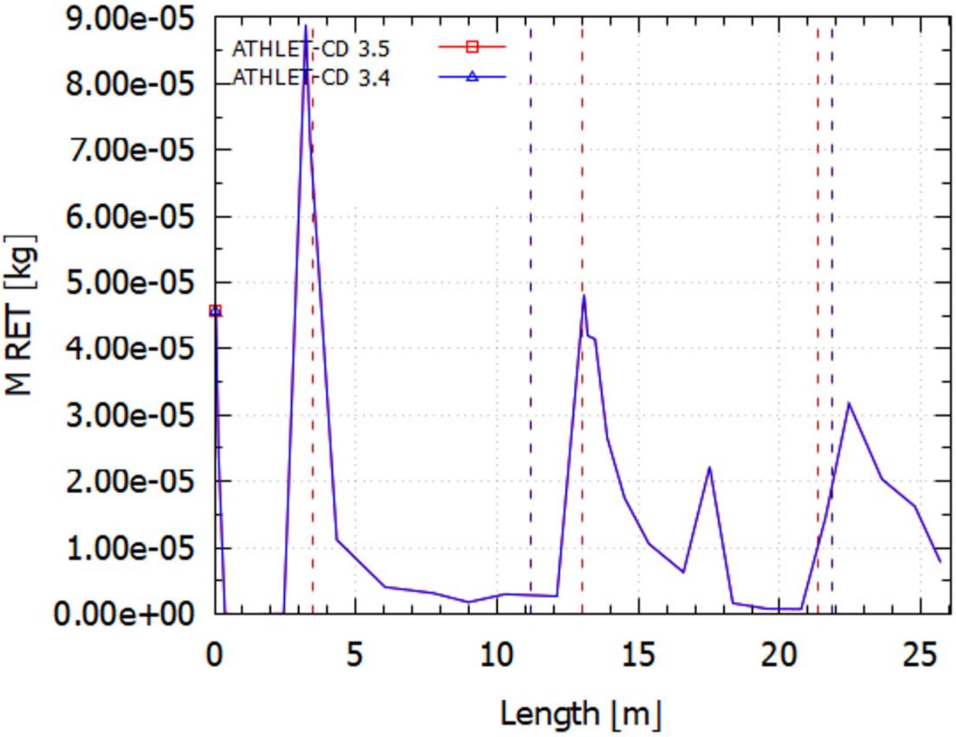

Fig. 5.62 Deposition of I (at 17370 s) in the circuit with vertical lines indicating release path up to the upper plenum, the hot leg, the steam generator entry, and steam generator exit into the cold leg

5.6.5 Main Findings

The main conclusions from the simulation of test PHÉBUS FPT-3 with ATHLET-CD 3.5 and 3.4 are the following. All versions are producing consistent results with the experiments and the deviations between the versions are minimal (practically non-existant). ATHLET-CD 3.5 reproduces all relevant figures of merit for the core degradation, hydrogen production, corium behaviour, fission product release and transport with at least satisfactory accuracy, given the uncertainties inherent both in the experiment and the ATHLET-CD modelling. Consequently, the validation of ATHLET-CD against test FPT-3 is judged to be successful, while there is still room for improvement both in ATHLET-CD models as well as the input deck.

5.7 QUENCH-16

5.7.1 Test Facility

The facility description is given in chapter 5.4.1.

In addition to the gas inflow line (steam and argon as carrier gas), there are lines at the bottom of the test area for the inflow of the quenching water and synthetic air (77 % N_2 + 23 % O_2).

5.7.2 Test Conduct

First, the rod bundle is electrically pre-heated with a power of 4.3 kW until reaching a maximal temperature of 873 K. Then, in order to initiate the pre-oxidation phase (0 s) from the overheated steam (3.4 g/s) and Argon (3 g/s) flow, the power is increased to 9.7 kW. It is followed by another power increase to 10.8 kW, and then to 11.3 kW, which heats the bundle up to 1300 K within approx. 2300 s, and reaching after another 4000 s a maximal temperature of 1428 K. The intermediate cooling phase is started by reducing the power to 3.9 kW (at 6301 s). The temperature decreases to approx. 1000 K, in order to ensure a low overheating due to the oxidation with air, as air introduction starts at 7300 s. The low air injection rate of 0.2 g/s, as well as the argon mass rate of 1 g/s (steam flow is stopped) lead to a slower heat-up, during which (at approx. 10350 s) the consumption of the whole oxygen inventory and the beginning of nitrogen reaction can be noticed.

When the maximum temperature of approx. 1873 K has been reached, quenching water injection (53 g/s) starts (after 11350 s). Due to an unexpected temperature escalation from the new steam oxidation, shroud failure occurs at a height of 1020 mm (~ 11380 s). This causes the quenching water to leak from the shroud (through the break) and delays the cooling of the bundle. After 11380 s, the thermocouples attached above the heated length also indicate rewetting in agreement with the measurement of the water level, so that the water injection is stopped after approx. 12050 s. At the end of the data recording, the electrical power is switched off.

The temperature excursion during quenching in the middle and upper bundle region reaches a maximum temperature of 2420 K; this leads to a significant hydrogen production during the flooding phase. In the metallographic examination of the bundle crosssections after the test, nitride layers are detected mostly in the bundle area between 350 mm and 550 mm; In addition, solidified melt has been relocated from higher levels (500 mm to 800 mm) and has accumulated in this bundle region.

5.7.3 Input Dataset

5.7.3.1 Nodalisation

Fig. 5.63 shows the reproduction of the QUENCH test facility in ATHLET-CD 3.5 for the current validation study. Due to the division of the core region into two parallel channels to avoid flow stagnation by blockage formation the input described in chapter 5.4.3.1 was updated and is described below.

The flow path is modelled by an inlet (`INPIPE`), the flow channel containing the bundle (`BUNDLE`) and the outlet (`OFFPIPE`). The bundle (`BUNDLE`) is divided into 20 axial cells – 10 of them belong to the heated region – which are connected via cross-connections to a bypass (`BYPASS`). `BYPASS`, which represents the region between the fuel rod simulators and the shroud, allows fluid to keep flowing if a blockage is formed (area ratio `BUNDLE` / `BYPASS` = 90 % / 10 %). The entire `BUNDLE` is divided from bottom to top into the following regions: 2 cells for the region below the ZrO_2-insulation (`SHROUD`) in which the copper electrode is located; 3 cells for the region above with the molybdenum electrode. In the heated region, the height of the cells was defined as 0.10 m according to the distances between the thermocouples (i.e., 10 cells). Above the heated region is the region surrounded by argon, in which the molybdenum electrode is located; this region is also divided into 3 cells. The molybdenum electrode goes up to the upper plenum, which has been divided into 2 cells. This axial division was defined identically for the flow channel, fuel rod simulators and HCOs to simulate the wall structures.

The overheated steam and argon (carrier gas) flow in at the lower end of the test facility via the `INPIPE` inlet. The synthetic air (77 % nitrogen, 23 % oxygen) and the water used to quench the bundle are injected directly into the `BUNDLE` a few centimetres above the outlet of the `INPIPE`. The steam that is not consumed during the oxidation, the remaining oxygen, nitrogen, argon and the hydrogen generated during the zirconium reaction are evacuated to the outside at the upper end of the test bundle (`OFFPIPE`). Inlet and outlet are surrounded by HCOs.

The bundle model takes into account the central unheated fuel rod simulator (`ROD1`), the inner ring with 8 fuel rod simulators (`ROD2`) and the outer ring with 12 fuel rod simulators (`ROD3`). The flow channel (`BUNDLE`) is surrounded by various HCOs. In the lower plenum region up to a height of 300 mm, the flow channel is bounded by the HCO `OUTERLP`. Above it and up to the upper plenum (included), the coolant tube is modelled by the HCOs `SHROUD` (up to +1.0 m) and `SHRTOP` (up to +1.30 m). The `SHROUD` structure is composed of 3 layers radially from the inside to the outside made of 3 materials: a layer of zircaloy (shroud) subdivided into 2 layers, the ZrO_2-insulation layer subdivided into 8 layers and a layer of Inconel subdivided into 2 layers (inner wall of the cooling jacket). The structure `SHRTOP` covers the region above the insulation in which argon is located during the experiment. `SHRTOP` is defined similarly to the `SHROUD` structure, with argon being modelled with a modified thermal conductivity to account for the existing convection (instead of the ZrO_2-insulation). The upper plenum is surrounded by the HCO `TOPHS`.

Outside the ZrO_2-insulation is represented the cooling jacket with argon in counterflow (`JACKETTUBE`), which is delimited by the outer wall made of steel (`OUTERWALL`). A further cooling channel (`TOPJACTUBE`) is located above it, through which cooling water flows, and which is bounded from the environment by the HCOs `OUTERTOP1` and `OUTERTOP2`.

The 5 spacers (`GRID1` to `5`) were also considered as HCOs. As well as the 4 corner rods (`RODA` and `RODB`).

In addition to the convective heat exchange, the energy transfer due to radiation is also taken into account. This takes place both from the fuel rods to the surrounding structures and between the structures.

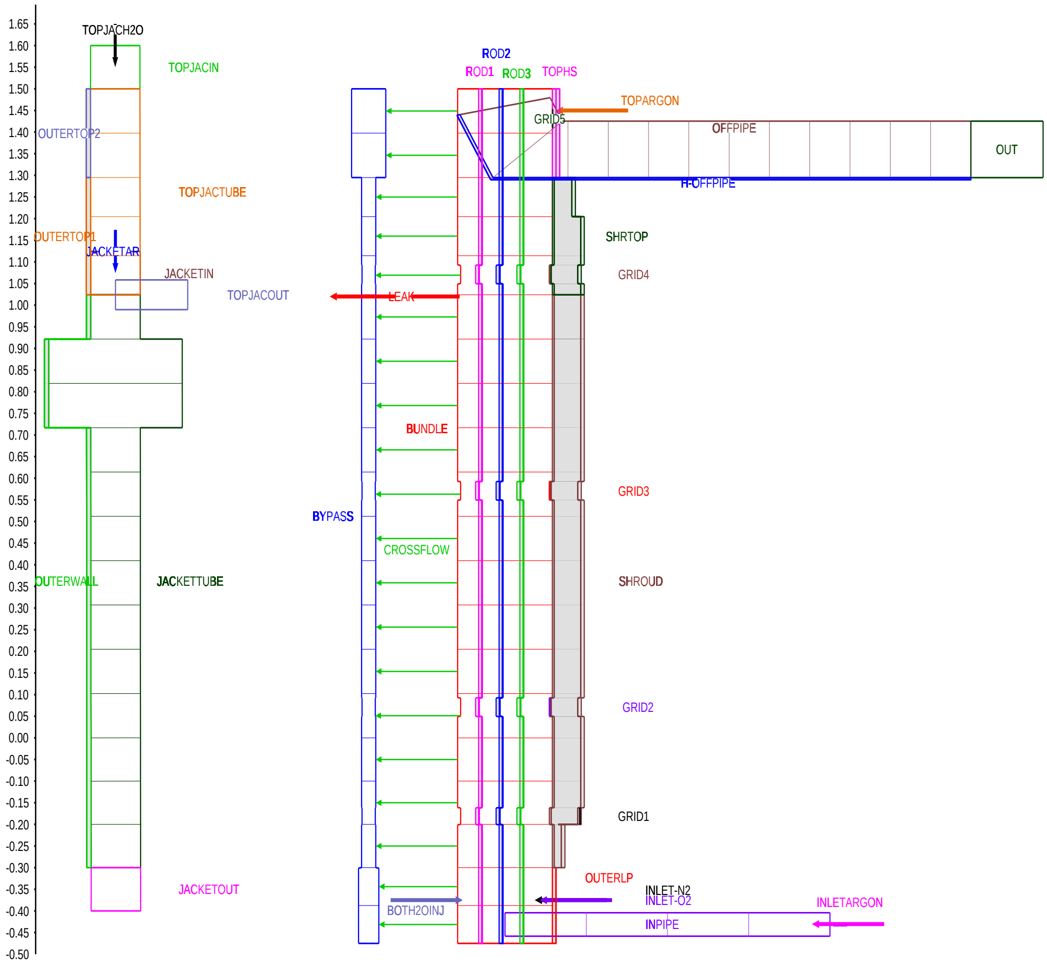

Fig. 5.63 Nodalisation of QUENCH-16

The initial and boundary conditions required for the calculation were determined from the existing measurement data. The electrical power input applied in the experiment was distributed over `ROD2` and `ROD3`. Losses are considered by setting the external resistance per rod `WHRES0` to 4.5 mΩ.

Mass flows of steam, argon and air supplied into the bundle were defined like described in the test conduct section. The steam supply is switched off as soon as the air supply (0.2 g/s) begins; the argon supply is reduced from 3.0 to 1.0 g/s at the beginning of the "air ingress" phase. The injection of quenching water (temperature of approx. 23 °C) at a rate of 53 g/s starts after 11350 s and lasts for approx. 700 s.

5.7.3.2 Model Options

In the present calculation, steam oxidation during the pre-oxidation phase was calculated with Cathcart (T<1773 K) and Prater-Courtright (T>1773 K) correlations (`IOXMOD` = 15). After reaching an oxide layer thickness of 150 µm, the transition from parabolic to linear oxidation rate is assumed (`ROXLIM` = $1.5 \cdot 10^{-4}$).

As for the air oxidation, the Steinbrück correlation (`IOXAIR` = 10) has been selected. However, in order to avoid an excessive increase in shroud temperatures due to air oxidation, the oxidation rate calculated for the shroud is reduced by factor `FLIMOH` = 0.1. Air oxidation of corner rods (`RODA` and `RODB`) is also reduced by factor `FLIMOH` = 0.05. Moreover, no air oxidation of the spacer grids is assumed.

In order to maintain the sharp rise in temperature observed in the experiment even after oxygen is fully consumed, the Hollands model for nitride formation has been selected (`INITN2` = 1).

In order to correctly predict the progress of the water level after the Shroud failure, and thus, the associated loss of water in the bundle after approx. 11380 s, a leak was defined at the rupture elevation (1020 mm), through which the injected water can flow out.

5.7.4 Main Results

Fig. 5.64 presents cladding temperatures of fuel rod simulators from experimental data (recorded by thermocouples TFS 20/9, TFS 18/11 and TFS 171/3) at three elevations: 550 mm, 750 mm and 950 mm. These thermocouples are in the upper half of the heated region of the rod bundle (heated region: from 0 mm to 1024 mm). These measured temperatures are compared with the temperatures calculated with the previous and current version of the code, ATHLET-CD 3.5 and 3.4, in the middle ring of the test bundle (`ROD2`) at the same elevations. A light overestimation of the temperatures by ATHLET-CD is noted. Results from both codes versions are almost identical during the whole sequence.

Fig. 5.65 presents the accumulated mass of generated hydrogen. ATHLET-CD 3.5 and 3.4 predicts the same amount of hydrogen until the start of quenching phase. After the quenching, ATHLET-CD 3.5 predicts a bit more hydrogen than ATHLET-CD 3.4. However, while both versions slightly underestimate the hydrogen amount until the quenching in comparison to the experiment, they present a significant underestimation of the hydrogen production during the quenching. This large difference can be explained by the fact that the reoxidation of nitride, as well as the oxidation of the melt and of the outer wall of shroud were not considered in the simulation.

Fig. 5.66 presents the accumulated mass of metallic melt calculated by ATHLET-CD 3.5 and 3.4. Results differ slightly with a higher value after quenching calculated by 3.5.

The oxide layer thickness distribution of the oxide layer over the length of `ROD2` at t = 7000 s and after the quenching is shown on Fig. 5.67, for ATHLET-CD 3.5 and ATHLET-CD 3.4. After the quenching, the predicted oxide layer between 750 mm and about 1300mm is slightly thinner with ATHLET-CD 3.5 than with ATHLET-CD 3.4.

Fig. 5.67 also shows the thickness of the nitride layer after the quenching. The profiles obtained with ATHLET-CD 3.5 and ATHLET-CD 3.4 are pratically the same. Since the simulation takes into account the reoxidation of nitride occurring during the quenching only quite simple, it is not reasonable to compare the calculated nitride layer profile with the experimental data.

To check the consumption of oxygen and nitrogen (from the injected air), mass flow rates of oxygen and nitrogen flowing out of the bundle are compared to the mass flows recorded during the experiment, namely during the air ingress phase. Fig. 5.68 and Fig. 5.69 show the mass flow rates of oxygen and nitrogen at the outlet of the bundle. A good agreement between simulations and experiment can be observed during the whole air ingress phase. ATHLET-CD also seems to capture the small flow peak of oxygen at the time of quenching. However, the peak mass flow rate of nitrogen at the time of quenching is still overestimated for both code versions.

Fig. 5.70 gives an overview of the number of time steps during the whole calculation with ATHLET-CD 3.5 and ATHLET-CD 3.4. ATHLET-CD 3.5 shows a noticeable increase of time steps during the quenching phase (again). This is a known consequence for such highly transient processes and the increase is still acceptable. However, this shows that numerical efficiency and robustness of quenching models need further improvement.

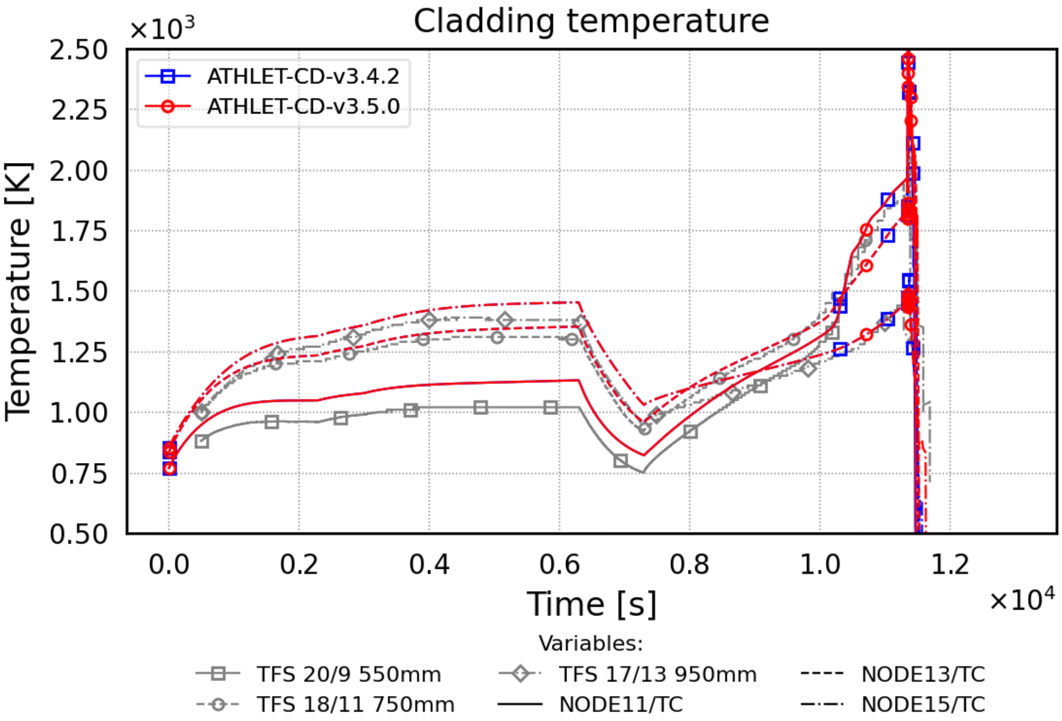

Fig. 5.64 Fuel rod temperature vs. time at three elevations: 550, 750 and 950 mm

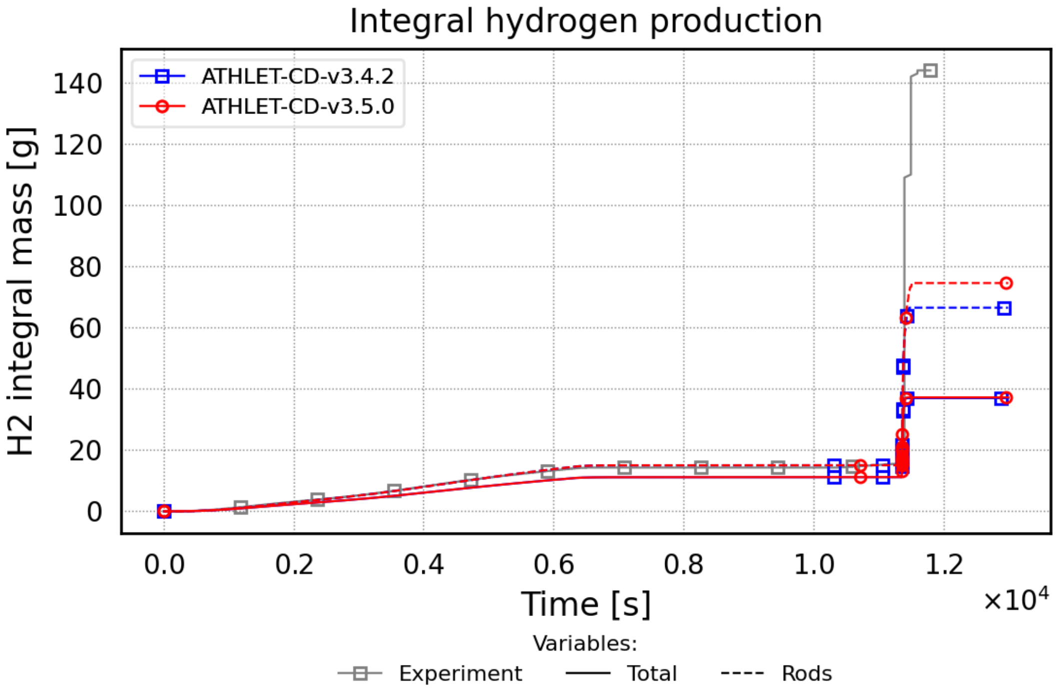

Fig. 5.65 Accumulated mass of generated hydrogen during the test

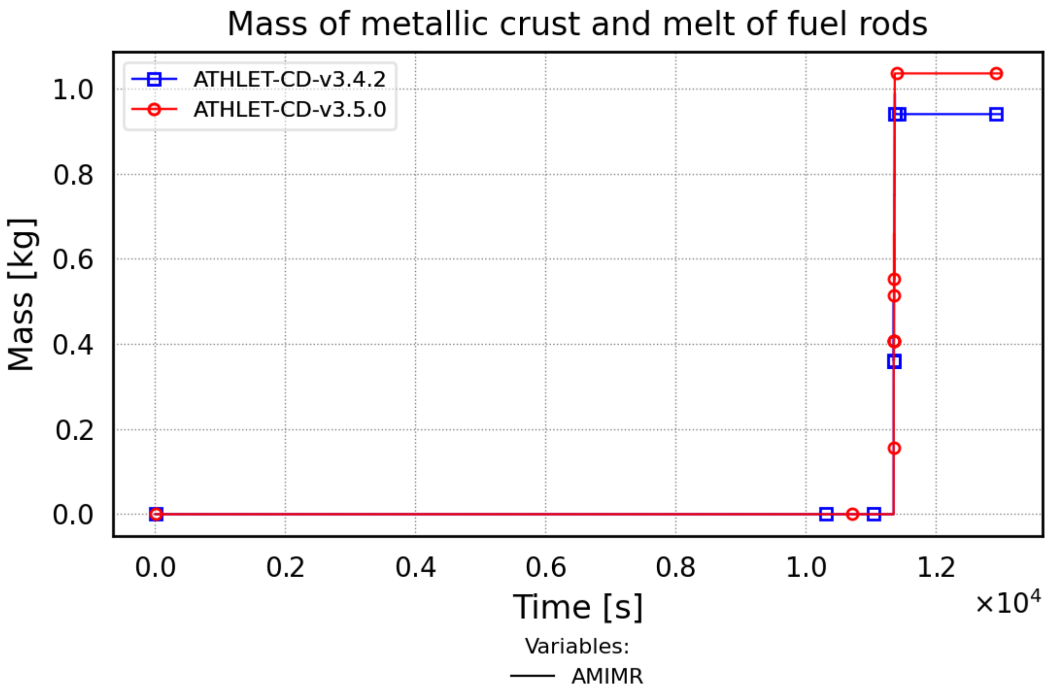

Fig. 5.66 Accumulated mass of metallic melt during the simulation

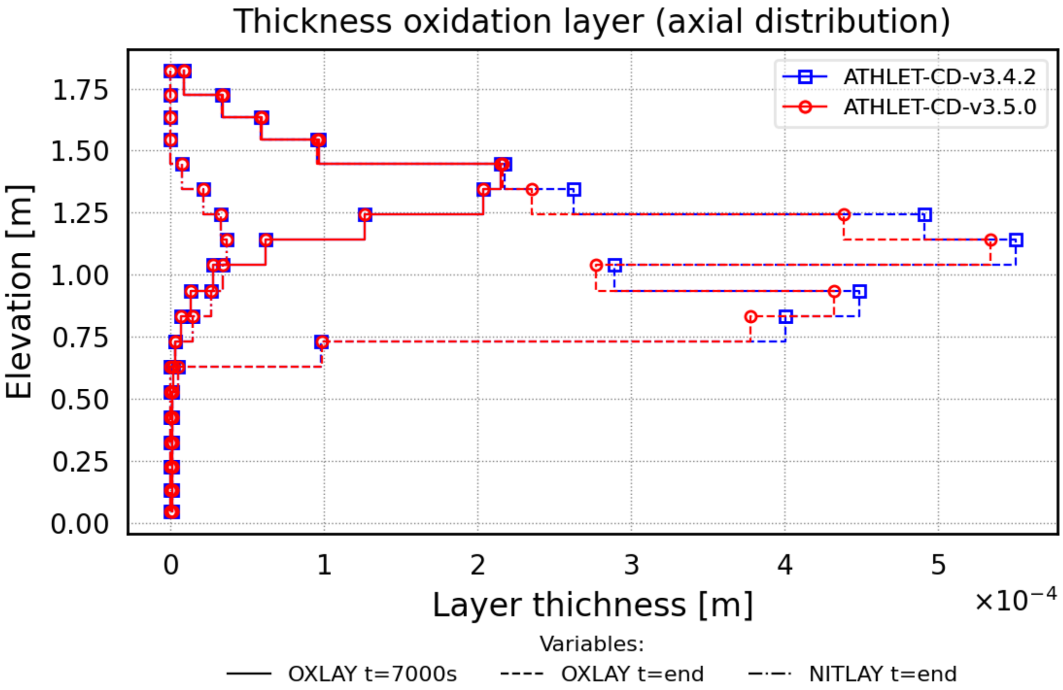

Fig. 5.67 Axial profile of oxide and nitride layer thicknesses: before air ingress (t=7000s) and at the end of the quenching (t=end)

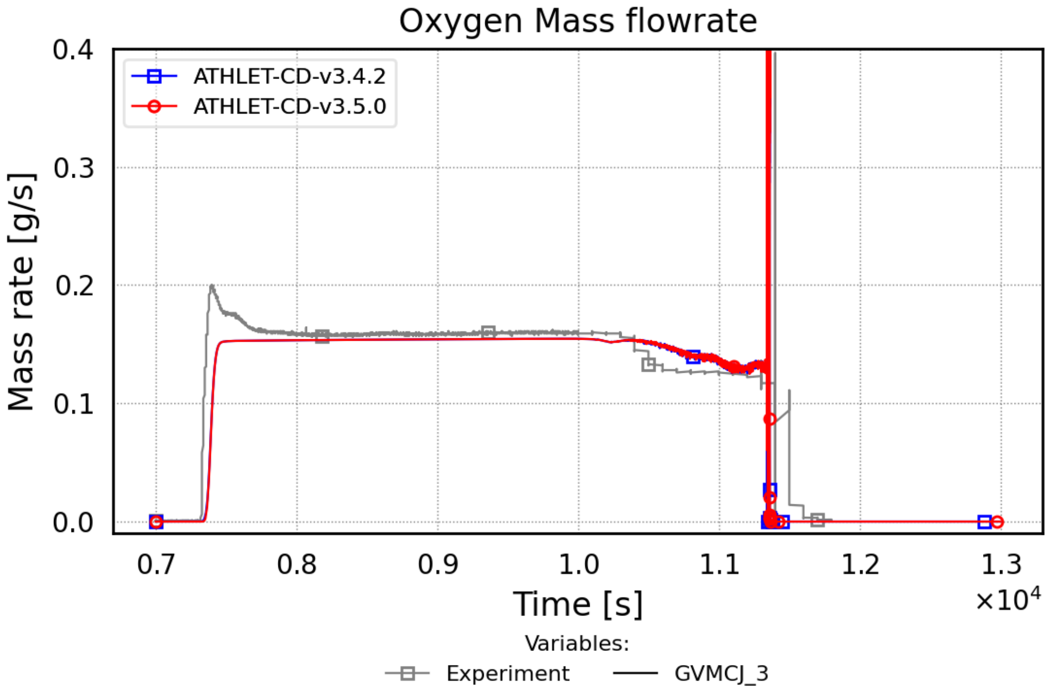

Fig. 5.68 Mass flow rate of oxygen at the bundle outlet

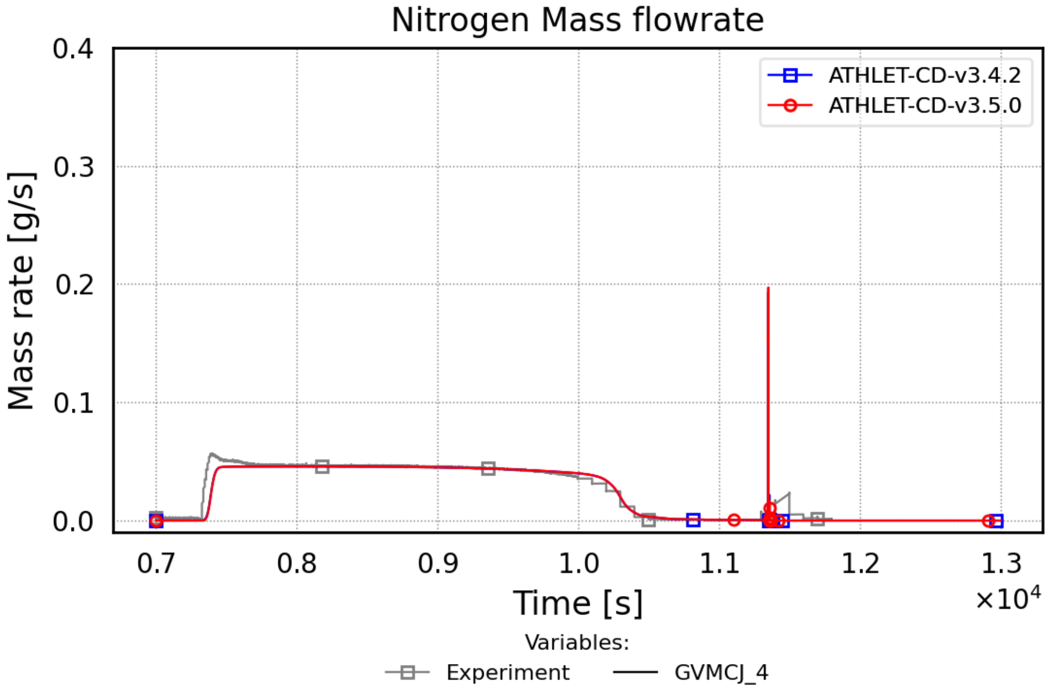

Fig. 5.69 Mass flow rate of nitrogen at the bundle outlet

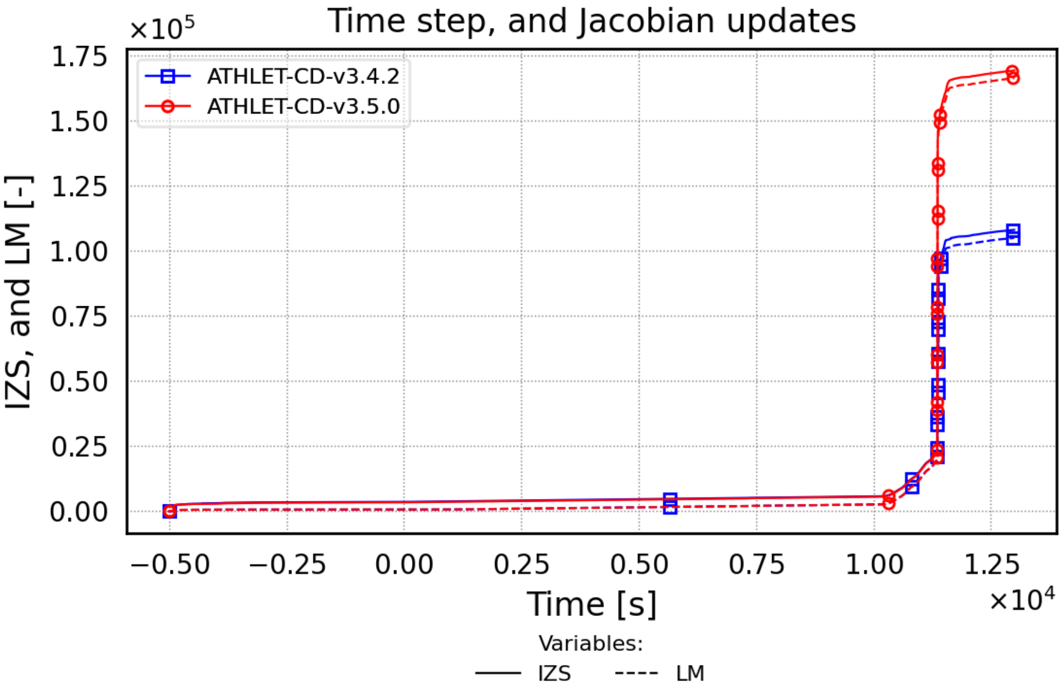

Fig. 5.70 Number of time steps of ATHLET-CD 3.5 and 3.4

5.7.5 Main Findings

The main outcome from this study is that ATHLET-CD 3.5 captures relevant phenomena like air oxidation and the subsequent temperature increase and the quenching process still reasonably well. The reduced numerical performance for this case is acceptable. Consequently, ATHLET-CD has been successfully validated against QUENCH-16.

5.8 QUENCH-18

5.8.1 Test Facility

The facility description is given in chapter 5.4.1. The test bundle configuration for QUENCH-18 is presented in Fig. 5.71.

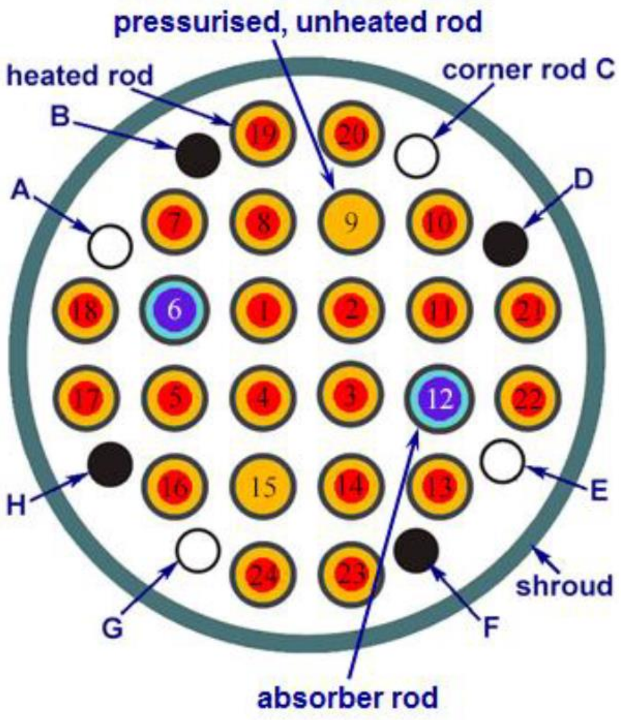

Fig. 5.71 Sectional view of the QUENCH-18 test bundle

5.8.2 Test Conduct

First, the rod bundle is pre-heated by a power of 4.1 kW until reaching a temperature of approx. 900 K, while argon and overheated steam are injected, both at 3.3 g/s. Then, in order to initiate the pre-oxidation phase (0 s) from the overheated steam and argon flow, the power is increased to 9.1 kW. First failure of the cladding of the pressurized rods #9 and #15 (on Fig. 5.71) occurs at 1035 K and 1045 K, respectively. After 4000 s, a maximum temperature of approximately 1400 K is reached at bundle elevation 950 mm. During this pre-oxidation phase, a total amount of generated hydrogen of 11.5 g was recorded.

The intermediate cooling phase is started by reducing the power to 3.8 kW (at 6309 s), the maximum rod temperature decreases to approximately 1080 K, in order to ensure a low overheating due to the oxidation with air, as air introduction starts at 7537 s. Steam and argon mass rates are also reduced to 0.3 g/s and 1.0 g/s, respectively. Power is still held at 3.8 kW as the air ingress phase starts with a mass flow of 0.2 g/s.

As temperature increases, the oxygen consumption rate grows after 9000 s. At 10530 s, AIC-rod failure occurs for the first time, releasing aerosols. The maximum cladding tube temperature is at approximately 1350 K. Steam consumption starts increasing after 10550 s, releasing hydrogen. An accelerated heating of the bundle is observed at elevation 550 mm. nitrogen consumption starts after 10660 s. Massive cladding tube failure occurs, melt from absorber rods relocates. At 11000 s, steam is fully consumed. After 11253 s, argon begins to ingress into the bundle region due to shroud failure. During this air ingress phase, approx. 45 g of hydrogen was released; approx. 100 g of oxygen and 120 g of nitrogen were consumed.

The quenching phase starts at 12329 s by injecting 50 g/s water (after a quick (4 s) water injection in order to fill the base of the bundle) into the bundle, which is still maintained at a constant power of 3.8 kW; air and steam supply are switched off. Temperature excursion was measured in the middle and upper bundle zone with a maximum temperature of approximately 2450 K. Whereas quenching is fast in the middle zone of the bundle, the cooling appears to be delayed in the upper zone. The bundle was fully quenched within approximately 800 s. During this flooding phase, approximately 238 g of hydrogen were produced. In addition, over 54 g of nitrogen were released due to re-oxidation of nitride.

5.8.3 Input Dataset

5.8.3.1 Nodalisation

Fig. 5.72 shows the modelling of the QUENCH test facility in AC² for the current validation study.

The flow path is modelled by an inlet (`INPIPE`), the flow channel containing the bundle (`BUNDLE`) and the outlet (`OFFPIPE`). The bundle (`BUNDLE`) is divided into 20 axial cells – 10 of them are in the heated region, which are connected via cross-connections to a bypass (`BYPASS`). `BYPASS`, which represents the region between the fuel rod simulators and the shroud, allows fluid to keep flowing if a blockage is formed (area ratio `BUNDLE` / `BYPASS` = 90 % / 10 %). The entire `BUNDLE` is divided from bottom to top into the following regions: 2 cells for the region below the ZrO_2-insulation (`SHROUD`) in which the copper electrode is located; 3 cells for the region above with the molybdenum electrode; in the heated region, the height of the cells was defined as 0.10 m according to the distances between the thermocouples (i.e., 10 cells). Above the heated region is the zone surrounded by argon, in which the molybdenum electrode is located; this region is also divided into 3 cells. The molybdenum electrode goes up to the upper plenum, which has been divided into 2 cells. This axial division was defined identically for the flow channel, fuel rod simulators and HCOs to simulate the wall structures.

The overheated steam and argon flow in at the lower end of the test facility via the INPIPE inlet. The synthetic air (80% nitrogen, 20% oxygen) and the water used to quench the bundle are injected directly into the lowest cell of BUNDLE. The steam that is not consumed during the oxidation, the remaining oxygen, nitrogen, argon and the hydrogen generated during the zirconium reaction are evacuated to the outside at the upper end of the test bundle (`OFFPIPE`). Inlet and outlet are surrounded by HCOs.

As shown in Fig. 5.73, the bundle model takes into account the 4 central heated fuel rod simulators (`ROD1`), the 4 heated fuel rod simulators with the 2 absorber rods in the middle ring (`ROD2`), the 2 unheated rods that are also under higher internal pressure (`ROD3`) and the 12 rods of the outer ring (`ROD4`). The 4 corner rods A, C, E and G on Fig. 5.71 are represented by HCO `RODA`, while the HCO `RODB` represents the corner rods B, D, F and H. In order to take also into simulate the pulling-out of the corner rod H before the start of the quenching phase, the `RODB` object is considered to be no longer present at the beginning of the water supply by using the CREEPING option `IMOD` = 4 (GCSM signal controlled shutdown) and is therefore no longer available for the oxidation.

The flow channel (`BUNDLE`) is surrounded by the HCO `SHROUD`. This is defined in 3 layers, i.e., radially from the inside to the outside: Zr (Shroud), the insulation (ZrO_2 fiber) and the inner wall of the cooling jacket (Inconel). The TFO `JACKETTUBE` connects the HCOs `SHROUD` and `OUTERWALL` in the region up to the upper end of the heated zone. The TFO-chain `TOPJACIN` - `TOPJACTUBE` – `TOPJACOUT`, lying just above `JACKETTUBE`, is water-cooled (Fill `TOPJACH2O`).

The 5 spacer grids (`GRID1` to `5`) were also taken into account as thermal structures, whereby the material properties of Inconel were defined for `GRID1`; The HCO’s `GRID2` to `GRID5`, on the other hand, are made of zirconium and contribute to the oxidation with steam. However, they were not taken into account for air oxidation.

In addition to the convective heat exchange, the energy transfer due to radiation is also taken into account. This takes place both from the fuel rods to the neighbouring structure `SHROUD` and between the structures `SHROUD` – `OUTERWALL`.

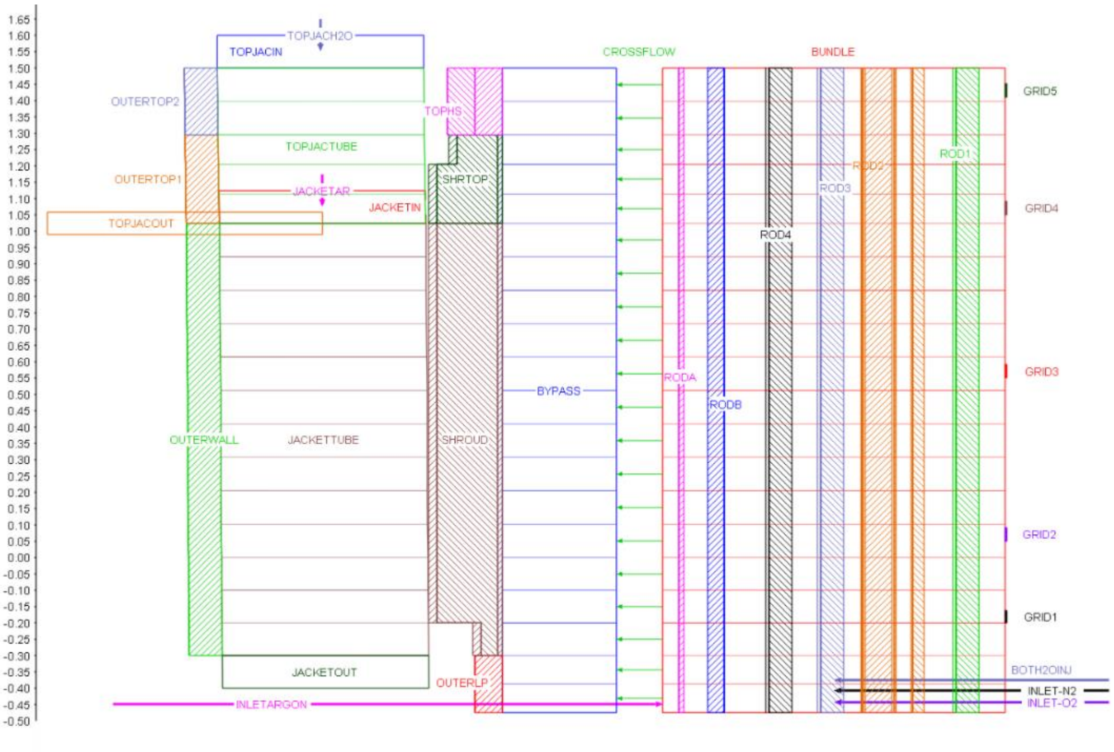

Fig. 5.72 Nodalisation of QUENCH-18

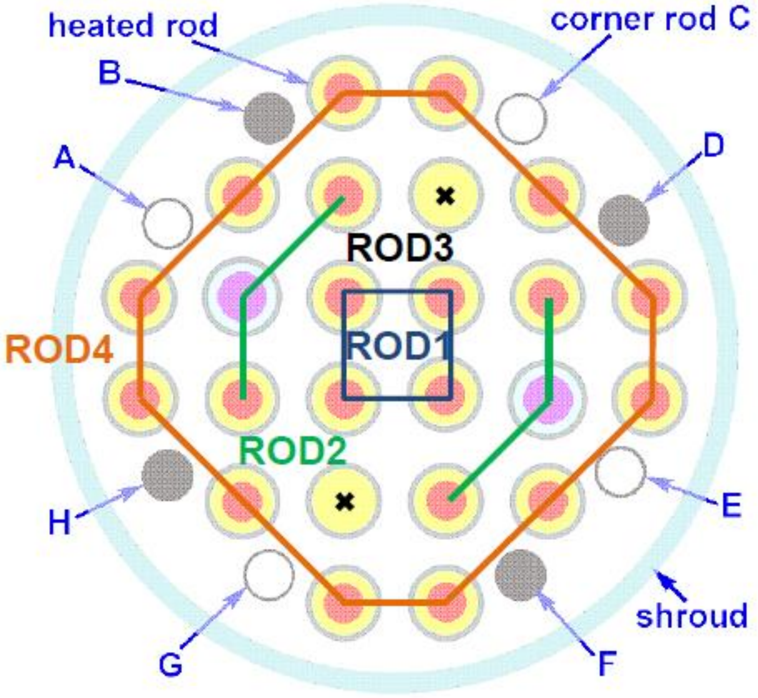

Fig. 5.73 Sectional view of the representation of the rod bundle

The initial and boundary conditions required for the calculation were determined from the existing measurement data. The electrical power input applied in the experiment was distributed over `ROD1`, `ROD2` and `ROD4`. Losses are considered by setting the external resistance per rod `WHRES0` to 3.5 mΩ.

Before the start of the air supply, the steam and argon injection rates were reduced to 0.3 g/s and 1.0 g/s, respectively, in order to yield the desired slow temperature increase and reach the expected starvation conditions. Shortly after the detection of the aerosols from absorber failure, the quenching phase begins at 12329 s by the start of water injection (temperature 22 °C). The temperature of the steam and argon injection used in the calculation is selected according to the measured gas temperature in the experiment.

5.8.3.2 Model Options

The existing physical properties for Zr are considered to be sufficiently accurate also for M5®. Besides, when selecting the correlations for the reactions of the cladding material with steam or air, it is assumed that the oxidation behaviour of M5® does not differ significantly from that of pure zirconium. The Cathcart-Prater / Courtright correlation for the simulation of the steam oxidation of the cladding material (`IOXMOD` = 15) was selected in this current calculation according to the simulation of the QUENCH-16 experiment. Regarding air oxidation, the transition from the NUREG2 to the NUREG1 correlation was selected (`IOXAIR` = 4), unlike in the QUENCH-16 calculation, where the Steinbrück correlation was chosen.

The measurement data show the start of temperature escalation in the “Air Ingress” phase at an elevation of 550 mm – 650 mm. This behaviour can be correctly captured in the calculation by reducing the oxidation rate by factor `FLIMOH` = 0.1 for the shroud. Air oxidation of corner rods (`RODA` and `RODB`) is also reduced by factor `FLIMOH` = 0.05. Moreover, no air oxidation of the spacer grids is assumed.

The Hollands correlation (`INITN2` = 1) was used for the nitrogen reaction that begins after the oxygen is consumed and leads to the formation of a nitride layer. A factor `FLIMNIT` = 0.25 was set (higher than in QUENCH-16 simulation, where `FLIMNIT` = 0.15).

The release of aerosols that begins after the failure of the AIC absorber rods and their transport to the outlet pipe are not taken into account in the present simulation.

5.8.4 Main Results

Fig. 5.74 presents cladding temperatures of fuel rod simulators from experimental data (recorded by thermocouples TFS 11/9, TFS 1/11 and TFS 1/13) at three elevations: 550 mm, 750 mm and 950 mm. These thermocouples that are in the upper half of the heated region of the rod bundle (from 0 mm to 1024 mm) provide clear measures, useful for the present study. These measured temperatures are compared with the temperatures calculated with the current and previous versions of the code, ATHLET-CD 3.5 and ATHLET-CD 3.4, in the middle ring of the test bundle (`ROD2`) at the same elevations. A small overestimation of the temperature of ATHLET-CD 3.5 and ATHLET-CD 3.4 is observed as well as some opposite behaviour at different elevations especially during air ingress. The temperature excursion during the quenching is well captured by both code versions.

Fig. 5.75 presents the accumulated mass of generated hydrogen. ATHLET-CD 3.5 and 3.4 predict nearly the same amount of hydrogen until quenching. After the quenching, ATHLET-CD 3.5 calculates slightly less hydrogen than ATHLET-CD 3.4, but this change is not significant. While both versions predict the hydrogen amount until the quenching in comparison to the experiment quite closely, they present a significant underestimation of the hydrogen production during the quenching. This large difference can be explained by the fact that the reoxidation of nitrides, as well as the oxidation of the melt and of the outer wall of shroud were not considered in the simulation.

Fig. 5.76 presents the accumulated mass of metallic melt calculated by ATHLET-CD 3.5 and ATHLET-CD 3.4. Results are basically the same, and reasonable.

The oxide layer thickness distribution of the oxide layer over the length of `ROD2` at t = 8000 s, and after the quenching, is shown on Fig. 5.77 for ATHLET-CD 3.5 and ATHLET-CD 3.4. Notably, the thickness along `ROD2` has an irregular profile after flooding for both code versions. After the quenching, oxide layer thicknesses are very similar as well, with ATHLET-CD 3.4 mostly predicting slightly thicker layers. The most noticeable deviation is at the bundle outlet around 1.3 m. Fig. 5.77 is also shows the thickness of the nitride layer after the quenching. The profiles obtained with ATHLET-CD 3.5 and ATHLET-CD 3.4 are almost identical. Since the simulation does not consider the reoxidation of nitride occurring during the quenching, it is not reasonable to compare the calculated nitride layer profile with the experimental data.

In order to check the consumption of oxygen and nitrogen (from the injected air), mass rates of oxygen and nitrogen flowing out of the bundle are compared to the mass flows recorded during the experiment, namely during the air ingress phase. As evident from Fig. 5.78 for nitrogen and Fig. 5.79 for oxygen, there is a good agreement between simulations and experiment for outlet mass flows during the whole air ingress phase. However, the abrupt increase of oxygen and nitrogen mass flow rate after the start of quenching could not be captured by both code versions. This is probably partly due to the fact that nitride reoxidation is not considered in the simulation.

Fig. 5.80 gives an overview of the number of time steps during the whole calculation with ATHLET-CD 3.5 and ATHLET-CD 3.4, without any relevant differences.

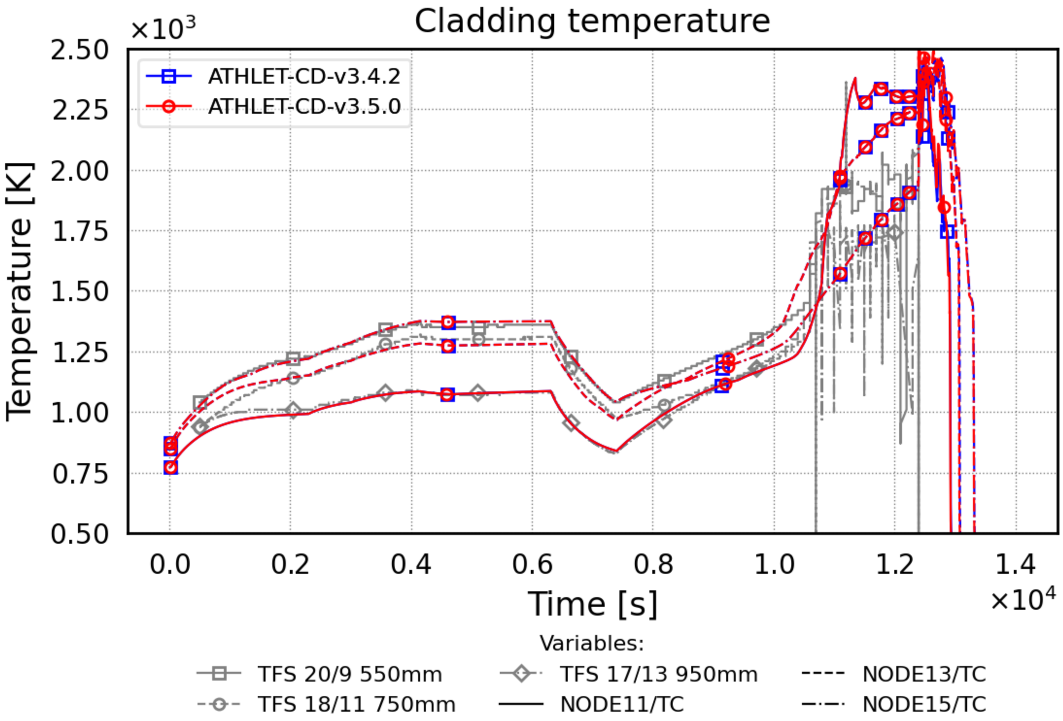

Fig. 5.74 Fuel rod temperature vs. time at three elevations: 550, 750 and 950 mm

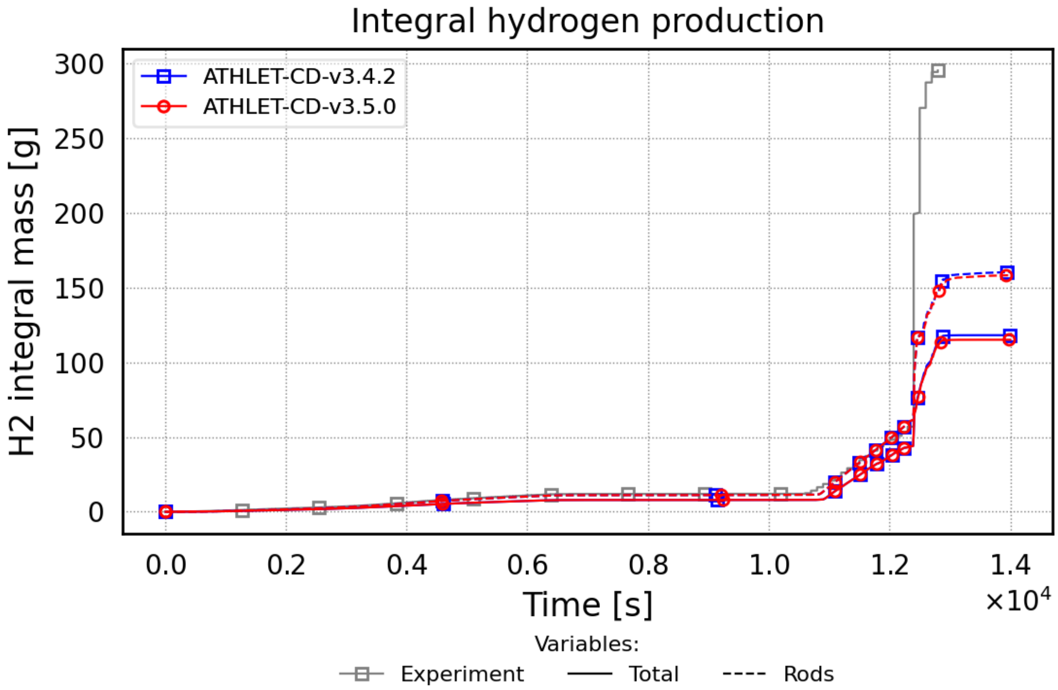

Fig. 5.75 Accumulated mass of generated hydrogen during the test

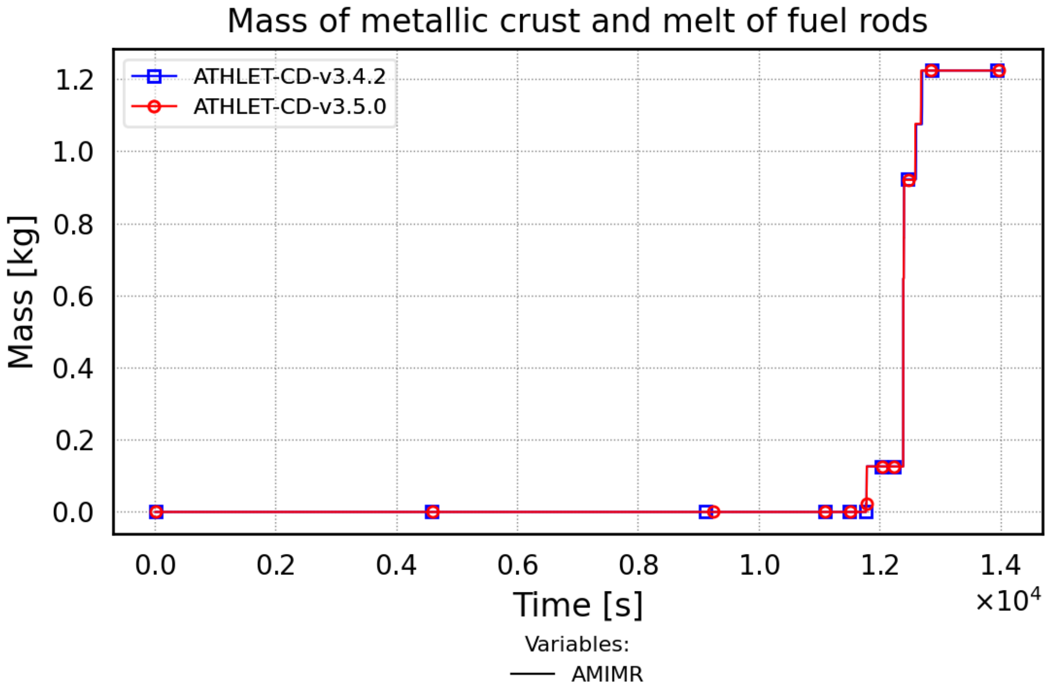

Fig. 5.76 Accumulated mass of metallic melt during the simulation

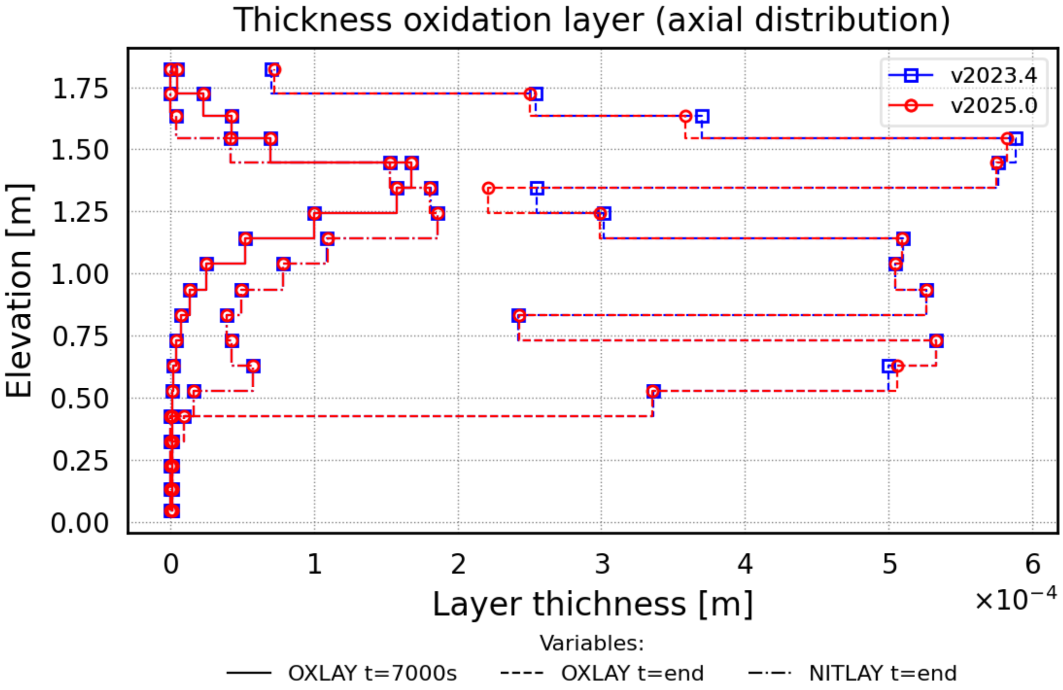

Fig. 5.77 Axial profile of oxide and nitride layer thicknesses: at the beginning of air ingress (t=8000s) and at the end of the quenching (t=end)

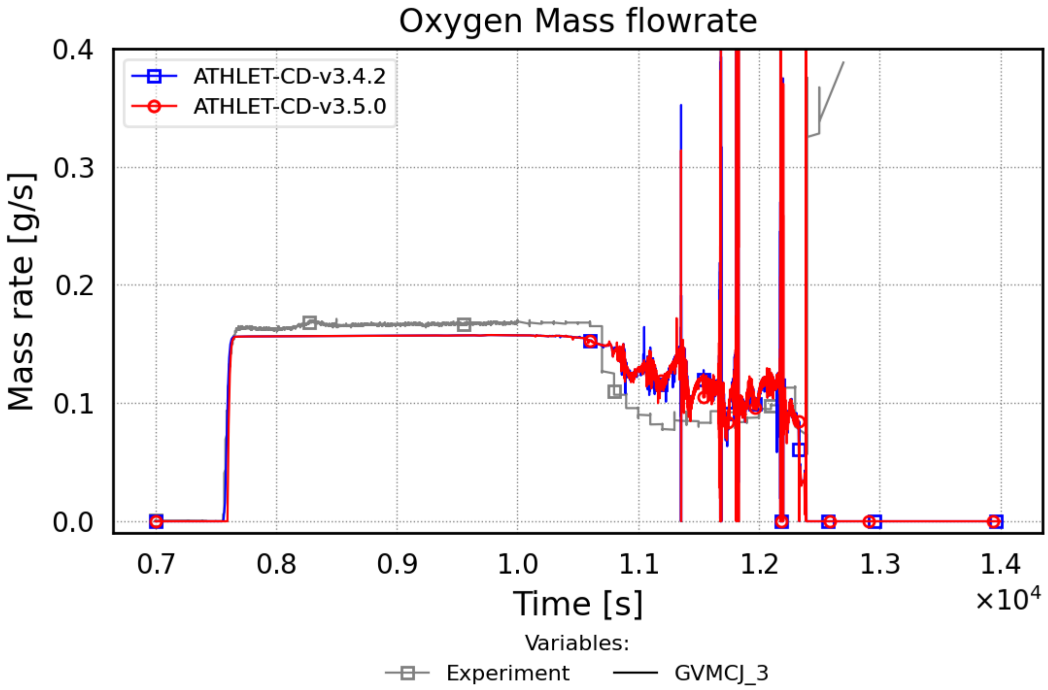

Fig. 5.78 Mass flow rate of oxygen at the bundle outlet

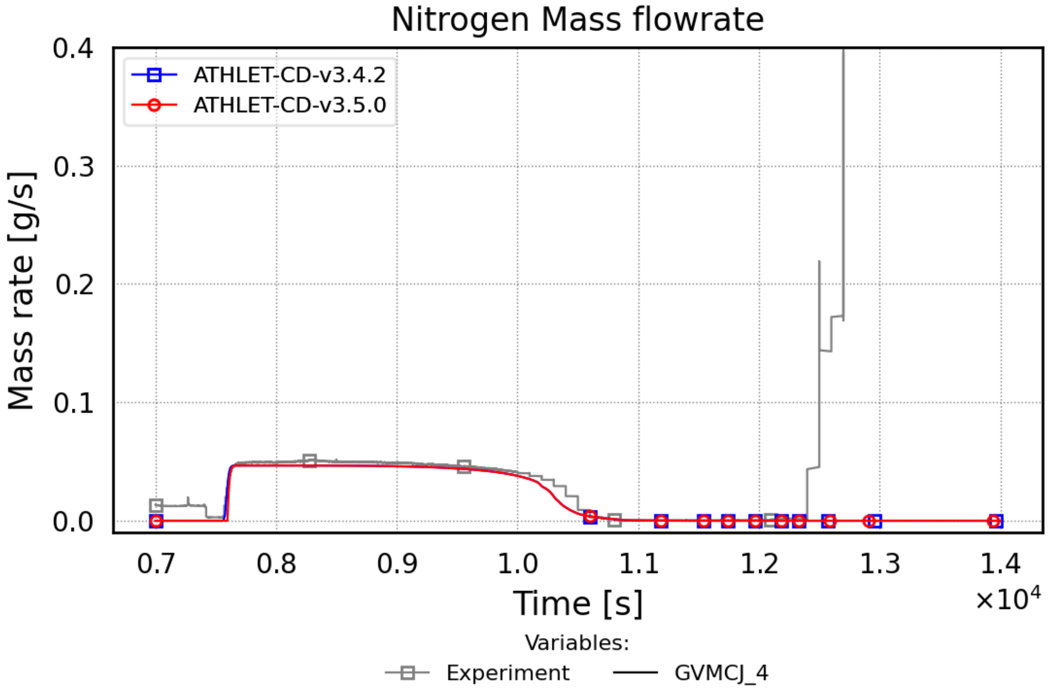

Fig. 5.79 Mass flow rate of nitrogen at the bundle outlet

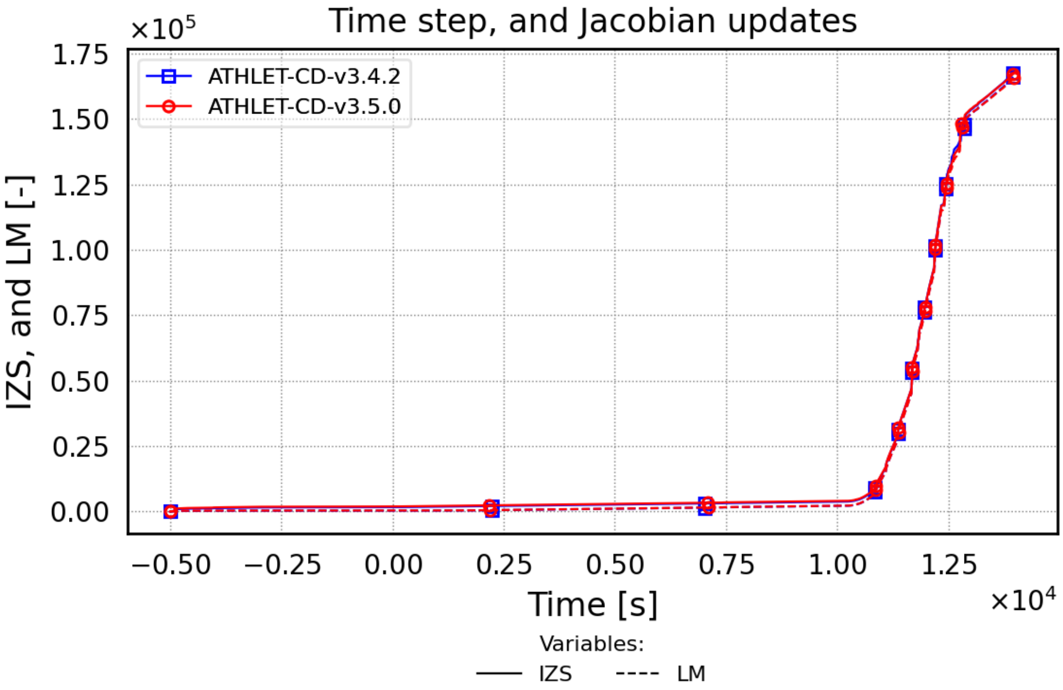

Fig. 5.80 Number of time steps of ATHLET-CD 3.5.0 and 3.4.3

5.8.5 Main Findings

The quenching process is captured reasonably well in both code versions. The numerical performance during quenching is not fully convincing, showing that numerical stability improvements for that challenging process should be sought.

The other phenomena like air oxidation and the subsequent temperature increase are still well captured, remaining deviations can large be explained by (unavoidable) differences between facility and simulation model. Overall, the validation of ATHLET-CD against QUENCH-18 was successful.

5.9 LIVE L-10 and L-11

5.9.1 Test Facility

In frame of the LIVE program performed by KIT (Karlsruhe Institute of Technology) the transient molten corium behaviour in a large-scale 3D lower head model has been experimentally investigated under different cooling conditions /GAU 11/, /PAN 18/. The experiment is focusing on crust formation, the heat flux distribution along the vessel wall and melt temperature evolution.

The scheme of LIVE 3D facility is shown in Fig. 5.81. The test vessel with the inner diameter of 1 m and a wall thickness of about 25 mm simulates the hemispherical lower plenum of a reactor pressure vessel of a PWR in 1:5 scale. The test vessel material is stainless steel. The test vessel is enclosed with a second vessel to represent a cooling channel to investigate the influence of different external cooling conditions on the melt pool behaviour. Cooling air or water flows in at the bottom and flows out via a side outlet at the top of the cooling vessel. The cooling vessel is enclosed with an insulation layer. The melt surface can be either maintained as free surface by covering the test vessel with an insulation lid or cooled with a water-cooled lid. The lid has several openings for the instrumentations and two opening to allow pouring of the melt centrally or close to the side wall.

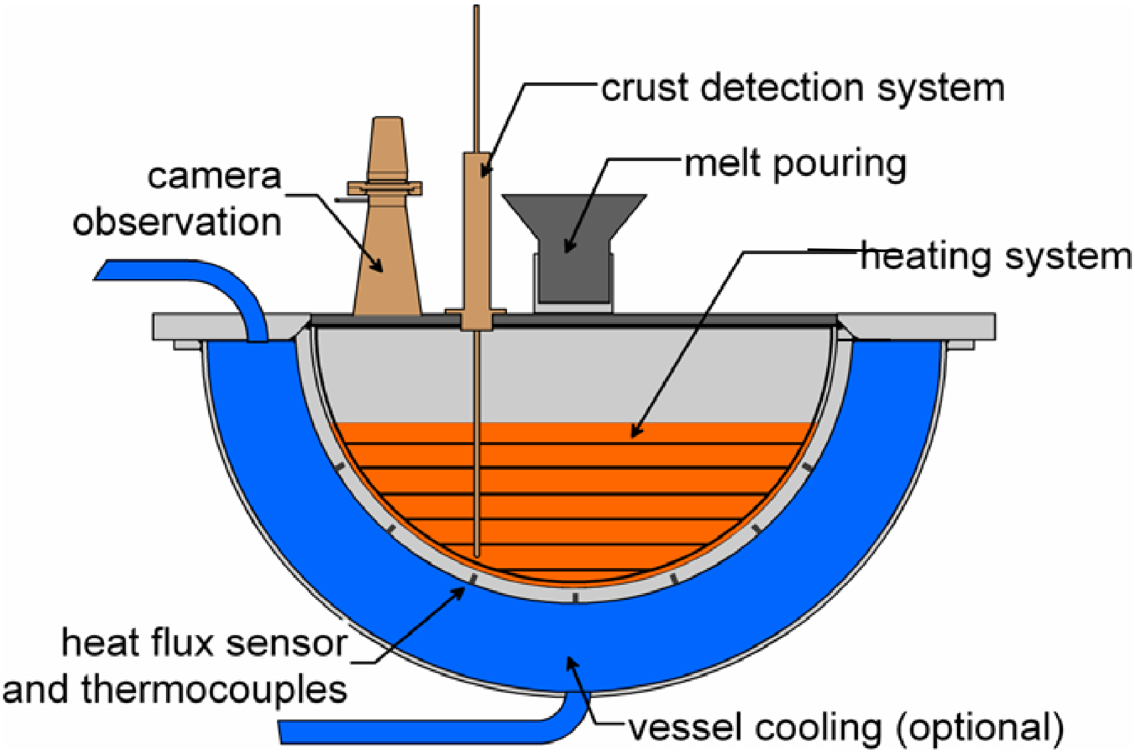

Fig. 5.81 Scheme of the LIVE facility /GAU 11/

A volumetric heating system has been implemented to model the decay power (Fig. 5.82). It consists of horizontal electrical heating coils, which can be controlled individually to realize homogenous power generation in the melt pool. The maximum homogenous heat generation is 29 kW. The liquid simulant melt is prepared in an external heating furnace, which can tilt and pour the liquid melt into the test vessel. After one test the liquid melt can be extracted back to the heating furnace and the 3D post-test crust profile can be determined.

Fig. 5.82 Test vessel with the volumetric heating system /GAU 11/

In the LIVE experiment the corium melt was substituted by a composition of sodium nitrate $NaNO_3$ and potassium nitrate KNO_3. The mixture allows a safe technical handling, because as a substitute for the oxidic part of corium of the mixture shows comparable physical properties as well as thermodynamic and thermal hydraulic behaviour at melt temperatures in the range around 300 °C. The mixture consists of 80 mol-% KNO_3 and 20 mol-% $NaNO_3$ and has a maximum temperature difference between solidus and liquidus of approximately 60 K. This melt composition can be used in the range of 284 °C (liquidus temperature) and 370 °C (chemical dissociation). The phase diagram of the mixture is shown in Fig. 5.83.

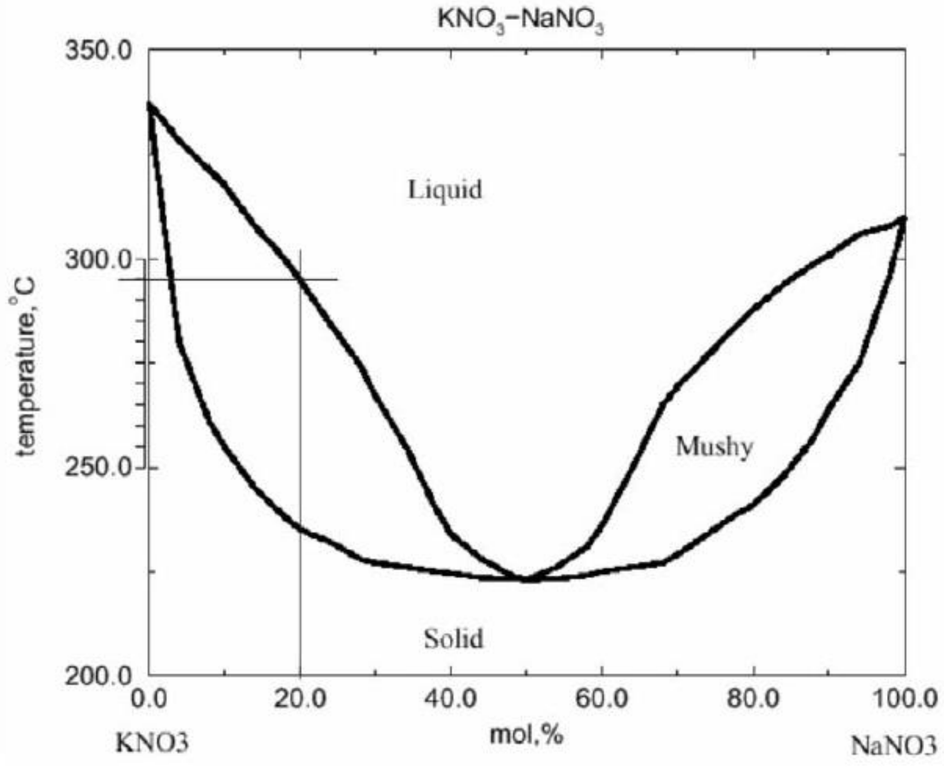

Fig. 5.83 Phase-diagram of the used KNO_3 – $NaNO_3$ mixture /GAU 11/

The LIVE-3D test vessel is extensively instrumented: the 3D melt temperature and 3D heat flux distributions can be determined with 80 melt thermocouples (MT) in the bulk melt, 26 pairs of thermocouples on inner and outer surface on the vessel wall and 7 thermocouple trees (CT) mounted perpendicularly to the wall in the wall boundary area (Fig. 5.84). The crust temperatures are important parameters for the determination of the boundary position of the melt/crust interface. Besides, two video cameras are installed for the observation of melt pouring process and one IR camera records the turbulent pattern on the melt surface. A more detailed description of the instrumentation is given in /GAU 11/.

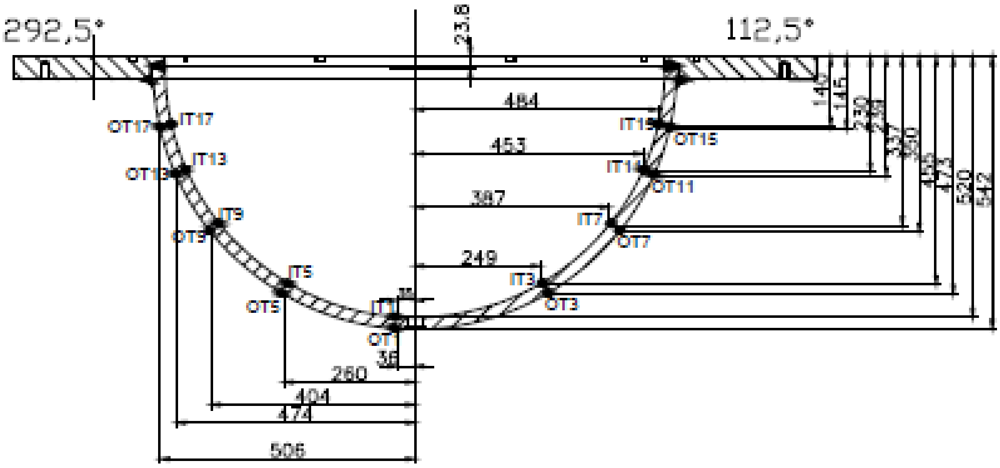

Fig. 5.84 The positions of the wall temperature measurements /GAU 11/

5.9.2 Test Conducts

Two LIVE tests with similar test conditions except the external cooling are studied: LIVE-L10 and LIVE-L11. There are following similar test conditions in L10 and L11 tests:

- Melt pool height: 410 mm
- Heating plateaus (Fig. 5.82): The heat input was volumetric. Five heating plateaus in the order of 21 kW, 16.4 kW, 9 KW, 16.4 kW-II, 21 kW-II were performed in L11 and in L10 after the second melt pouring. Each heating plateau had reached thermodynamic steady state before the power was switched to the next one. The last heating plateau was terminated by melt extraction.
- Upper boundary: the test vessel was covered with an insulation lid.

- Initial cooling water temperature: cooling vessel was filled with cooling water at ambient temperature.

The progressions of melt temperature at three heights in the bulk melt are illustrated in Fig. 5.85. The radial position of the measurements is 174 mm from the vessel central axis. The total heating power inputs in L11 were identical to the heating powers after the second melt pour in L10.

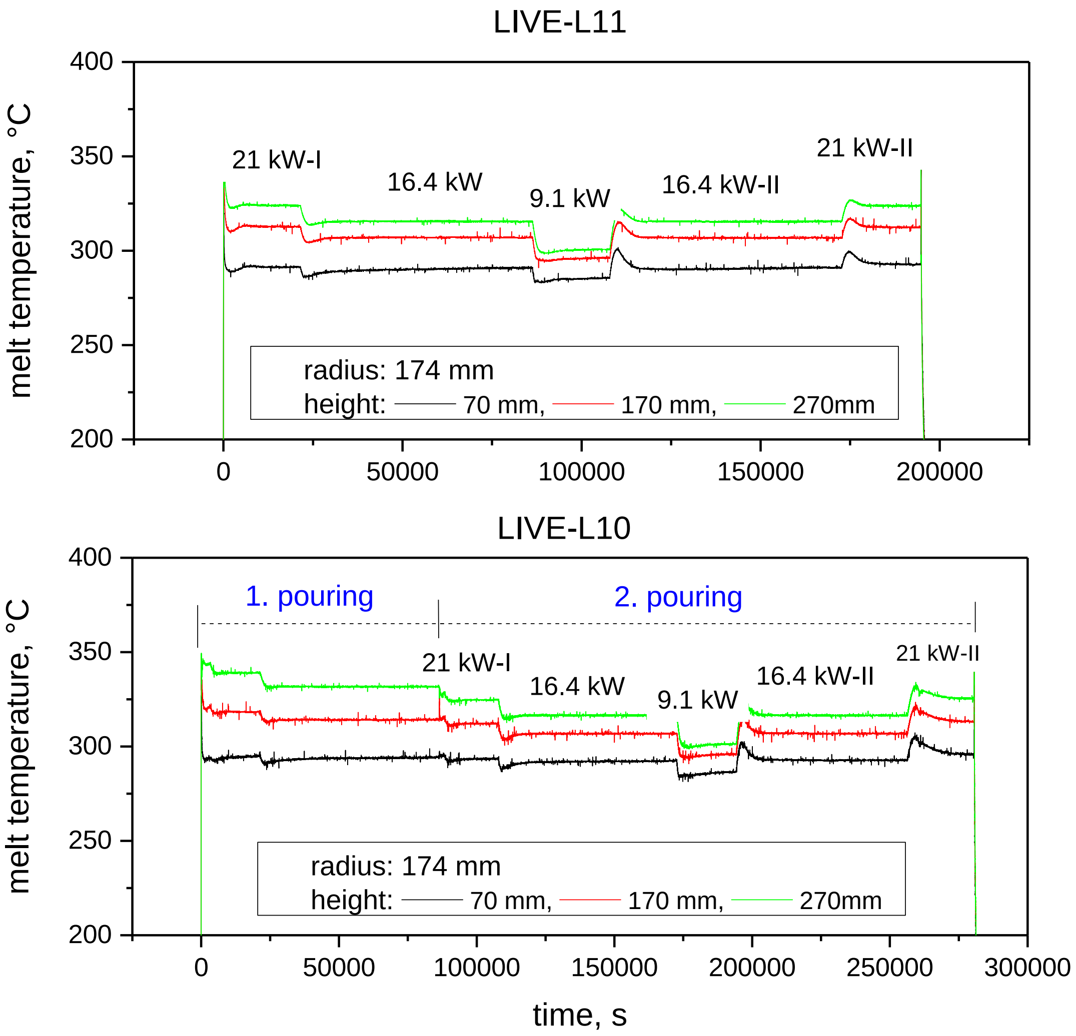

Fig. 5.85 Temperature progression during the test period in LIVE-L11 (top) and LIVE-L10 (bottom)

The difference between the two tests was the external cooling condition during the test. In LIVE-L10, cooling water with a 1.3 kg/s flow rate was maintained during the whole test period, so that the water outlet temperature was only several K above the inlet temperature. In contrast, in LIVE-L11 the cooling water outlet temperature reached boiling temperature after an initial period. The evaporation of water was compensated with a very low and non-continuous inlet flow in order to maintain the water level constant. Another difference between the two tests is that there are two melt pours in LIVE-L10 test, and after the second pour, the melt in L10 has the same pool height and heating power as in L11 test. Therefore, this discussion focuses on the LIVE-10 test in the region after the second pouring.

Tab. 5.6 Properties of the simulant in LIVE-10 and LIVE-11

80 mol% KNO_3 – 20 mol% $NaNO_3$	**Solid**	**Liquid**
Mol weight [g/mol]	97.88	97.88
Particle density [g/cm^3]	2.1 -2.26	284 °C: 1.914; 340 °C: 1.873
Transition temperature, [℃]	104.8	284.4
Transition enthalpy, [J/g]	65.7	161.69
Heat capacity, [J/g/℃]	$0.9474 + 0.00113 \cdot T$ ($119\ °C < T < 182\ °C$)	$1.2475 + 2.8E\text{-}4 \cdot T$ ($300\ °C < T < 400\ °C$)
Thermal conductivity [W/(mK)]	0.4 – 0.6	0.42 -0.46
Viscosity [Pa s x10^3]		280 °C: 3.772; 350 °C: 2.508

5.9.3 Input Description

The calculations have been performed using stand-alone simulations with the AIDA module of ATHLET-CD 3.5 (AC^2 2025). Similar to the experiment a fully hemispherical lower plenum has been modelled with a radius of 0.4966 m and a wall thickness of 0.025 mm. To modelling the two-dimensional heat conduction in the wall it has been divided into 60 axial nodes (along the wall) which have been split with 10 radial layers. Regarding of previous calculations, the carbon steel model of AIDA with built in tables has been chosen among the three available wall materials to modelling the temperature dependent wall properties.

The stand-alone calculation of AIDA requires to define the corium properties in the input dataset. The corium pool has been modelled homogeneous similar to the experiment.

The material properties have been defined according to the experimental data (see Tab. 5.6). Not all of the material properties of the simulant are exactly described in the experiment documentation or have been measured during the experiment. In these cases, an average value considering the experience from previous calculations has been defined. The most important material properties defined in the AIDA module part of the input data set are summarized in Tab. 5.7. Preliminary sensitivity studies showed that the definition of the transition temperature has a significant influence on melt temperature and crust formation. For the present calculation, the default option (mean value of the solidus and liquidus temperatures) was chosen.

Tab. 5.7 Corium properties in the AIDA calculation

Material properties in AIDA	
Solidus temperature [K]	497
Liquidus temperature [K]	557
Transition temperature, [K]	527
Density, [kg/m^3]	1915
Heat capacity, [J/kg/K]	1461
Thermal conductivity [W/(mK)]	0.5
Kinematic viscosity [m^2/s]	1.33×10^{-6}

The insulated top cooling condition has been modelled with a heuristically defined small heat transfer coefficient (`HTCUP`=0.1 W/m²/K) in AIDA. The heat transfer between melt and crust (upwards and sidewards) has been calculated with the correlation of Reineke according to previous investigations /HOL 15/. To achieve a heat transfer distribution, which is typical for the modelled hemispherical geometry, a shape factor of 2.0 has been defined /AUS 19/.

The external vessel cooling has been modelled in both cases with a constant, user defined HTC value. The external cooling conditions are:

- LIVE-L10: 1000 W/m^2/K by a constant mass flow of 1.3 kg/s,
- LIVE-L11: 10000 W/m^2/K by a transient mass flow, based on evaporation.

During the simulation, the volumetric heat has been defined as a boundary condition using the measured values.

5.9.4 Main Results

The calculations, ATHLET-CD 3.4 and ATHLET-CD 3.5 both, have been performed on a standard GRS PC with INTEL ® CORE™ i7-7700 processors at 3.60 GHz under the 64-bit operating system Windows 10 Enterprise. With the new code version, the required, already short CPU-min of 1.4 reduced on about 0.45 CPU-min for the total simulation time of 55 hours.

Fig. 5.86 and Fig. 5.89 show the resulting averaged melt temperatures in simulation compared to the experimental result and to the previous calculations (ATHLET-CD 3.4) for L10 and L11, respectively. The temperature distributions reflected the five heat stages. The calculation results agree with the experimental result, particularly during the third heat stages in case of L11 and in the first and fifth stages in L10 case. In the second stage the temperatures are slightly underestimated in L10 case. In L11 the temperatures in first and second case are slightly overestimated. The new results are slightly different from the previous one (ATHLET-CD 3.4) which is mainly because of updates of the heat transfer calculation and the selected default melt interface temperature (in the previous version it was lower than the recommended value). In case of L10 the new results are generally closer to the experimental values. In case of L11 the overall deviation is about the same.

One of the reasons of the minor deviations is that the stand-alone AIDA module does not consider the temperature dependence of the material properties. Hence, these are given as a constant value in the input data. According of the results the material properties used describe the material well at 295 °C. The comparison of the current code version with the previous version shows very well that the recent improvements in AIDA do not have a significant impact on the homogeneous pool modelling.

The measured and predicted inner and outer wall temperatures for L10 test are given in Fig. 5.87 and Fig. 5.88. The comparison is based on the measurement data given in /PAN 18/. Both the calculated inner and outer wall temperatures agree well with the experimental results. The small differences can be an artefact of the assumption of a well-mixed homogeneous molten pool with one average temperature in the calculation. The aforementioned shape-factor to consider the hemispherical lower head compensates for this assumption only to a certain degree. Therefore, the best agreement can be observed about at the upper half of the molten pool (about 50 degrees at inner wall and about 60 degrees at outer wall). Furthermore, the correlation chosen to calculate the heat transfer, the non-exactly defined material properties, particularly enthalpy difference and heat capacity, have an effect of the heat transfer and crust formation calculations.

The measured and calculated outer and inner wall temperature of L11 test are shown in Fig. 5.90 and Fig. 5.91. The inner wall temperatures are in good agreement. However, the same discrepancy can be observed as in the L10 calculations. The upper region is slightly underestimated while the lower region is overestimated. The simulation results at 76.5° (relative to the focal point horizon of the test facility, see also Fig. 5.83) are already lower than at position of 65.5°. This is likely an effect of the upper boundary condition and the axial heat transfer towards non-wetted wall parts.

The calculated outer wall temperatures show more discrepancies compared to the measurement values in the water heating-up phase. During the test, the water is being heated up and evaporates, therefore after a heating-up phase, the complete cooling channel reached saturation temperature. In the AIDA simulation the channel geometry is modelled only in a very simply way with a constant cross section along the wall and the initial water temperature is set close to the saturation temperature. As a consequence, in the AIDA simulation the water reaches much earlier the saturation temperature. A more realistic modelling of the external cooling channel needs to perform a coupled simulation with the thermohydraulic module ATHLET.

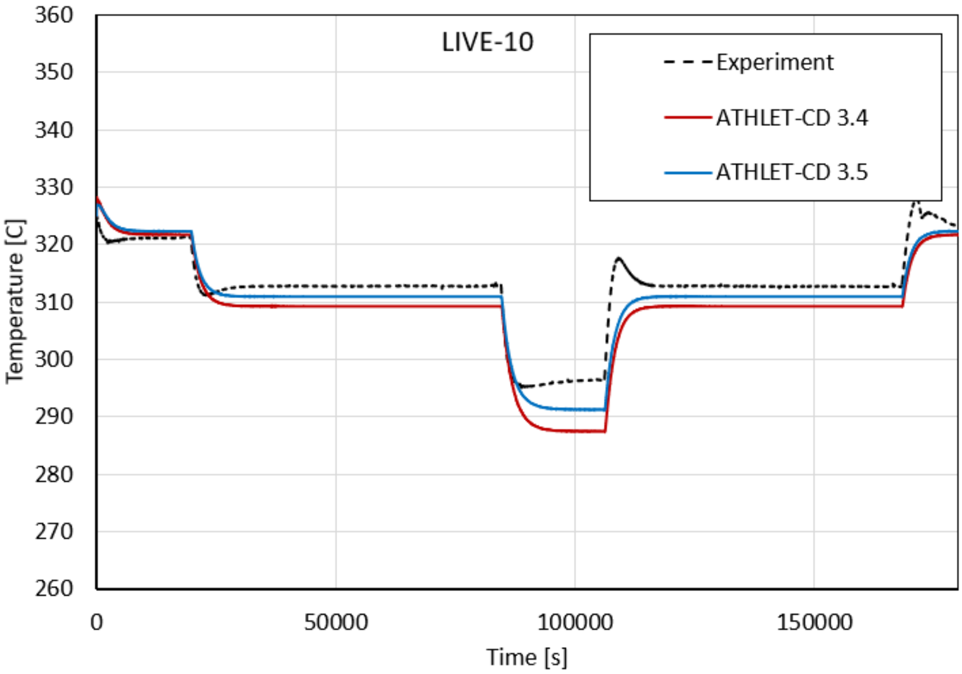

Fig. 5.86 Melt temperature evolution in L10 test and in ATHLET-CD simulations (3.4 and 3.5)

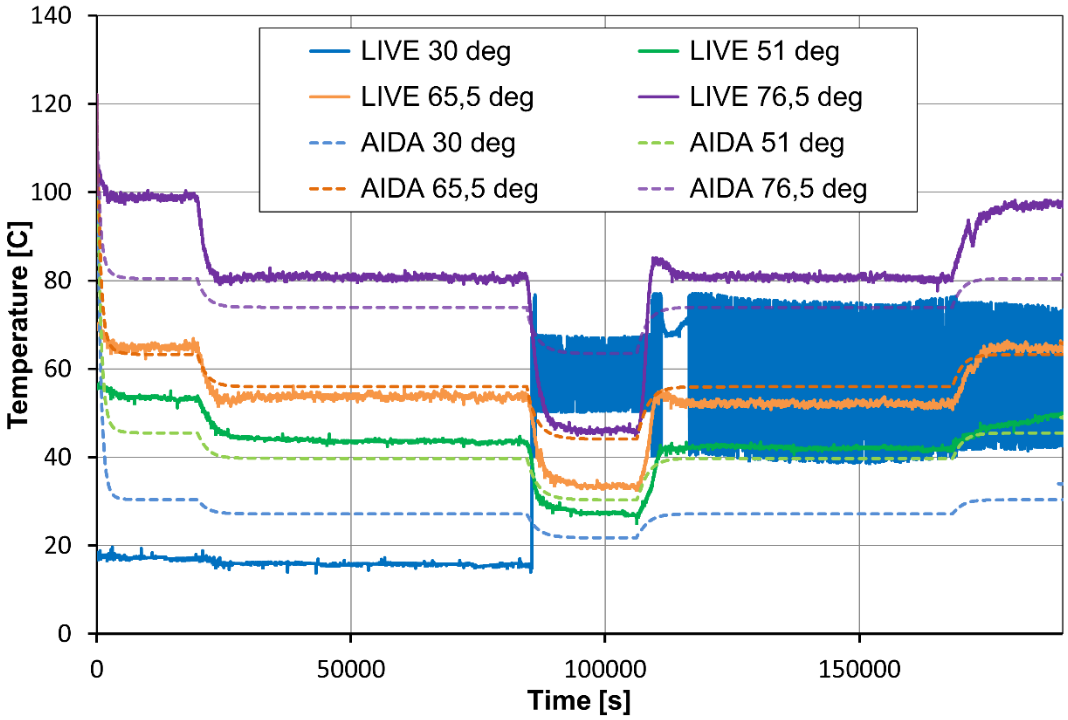

Fig. 5.87 Inner wall temperature evolution at different positions in L10 test and the AIDA (ATHLET-CD 3.5) simulation

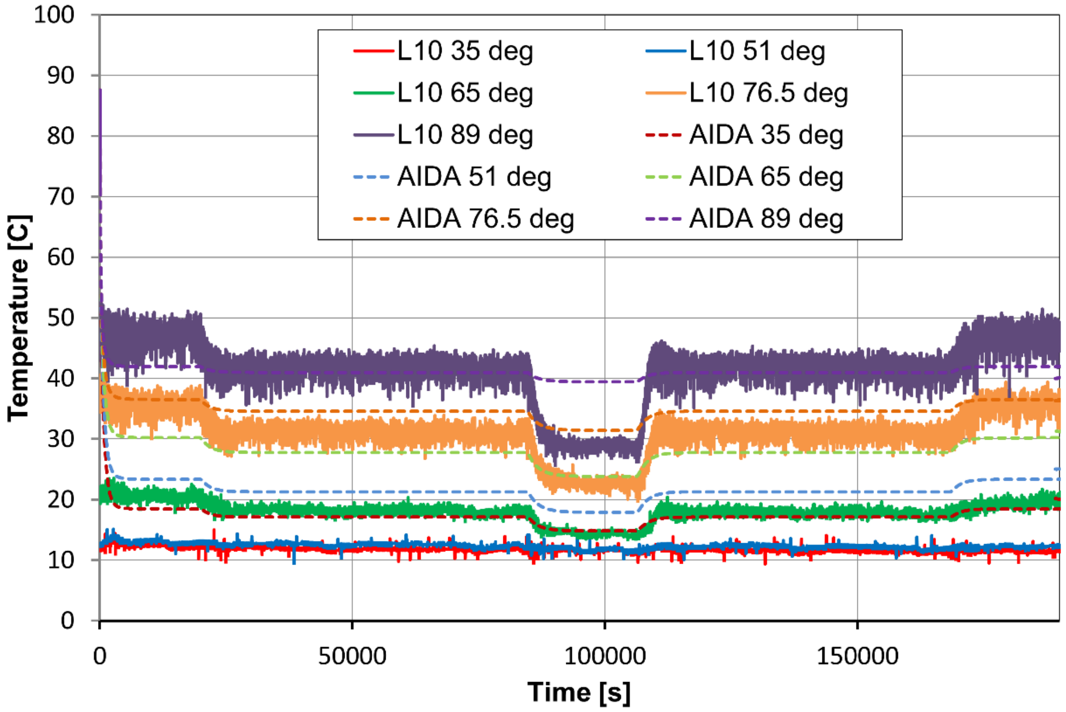

Fig. 5.88 Outer wall temperature evolution at different positions in L10 test and in AIDA (ATHLET-CD 3.5) simulation

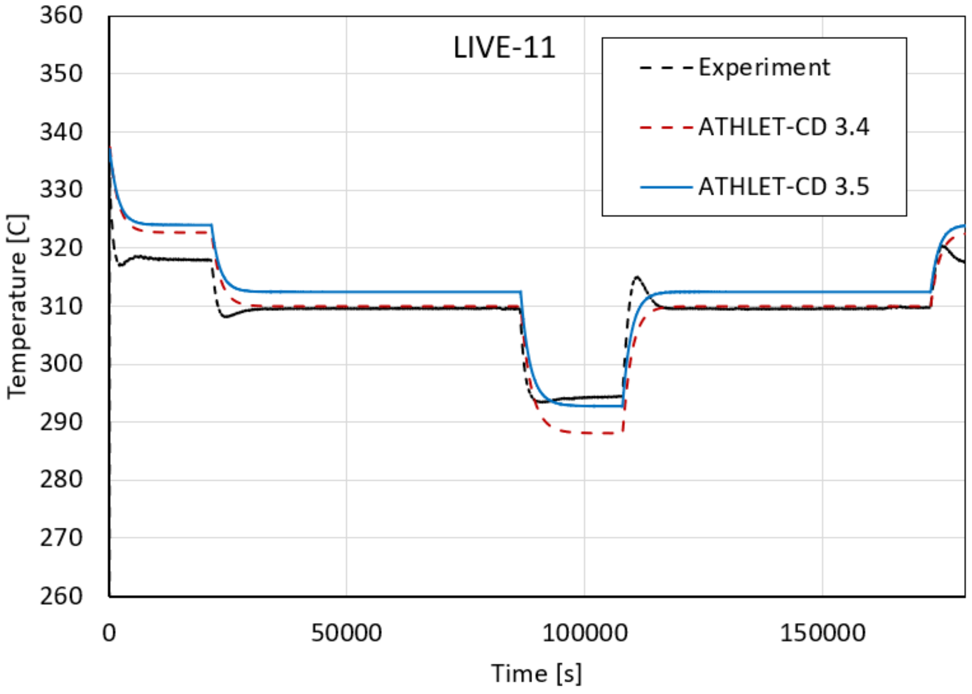

Fig. 5.89 Melt temperature evolution in L11 test and in ATHLET-CD simulations (3.4 and 3.5)

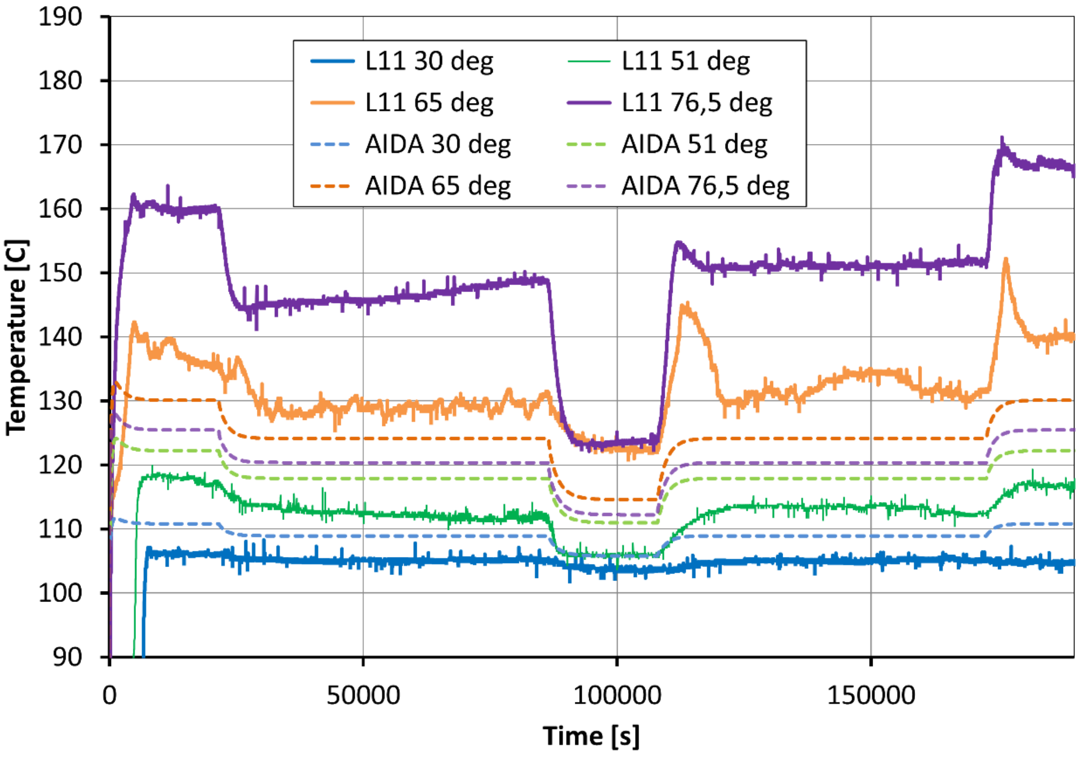

Fig. 5.90 Inner wall temperature evolution at different positions in L11 test and the AIDA (ATHLET-CD 3.5) simulation

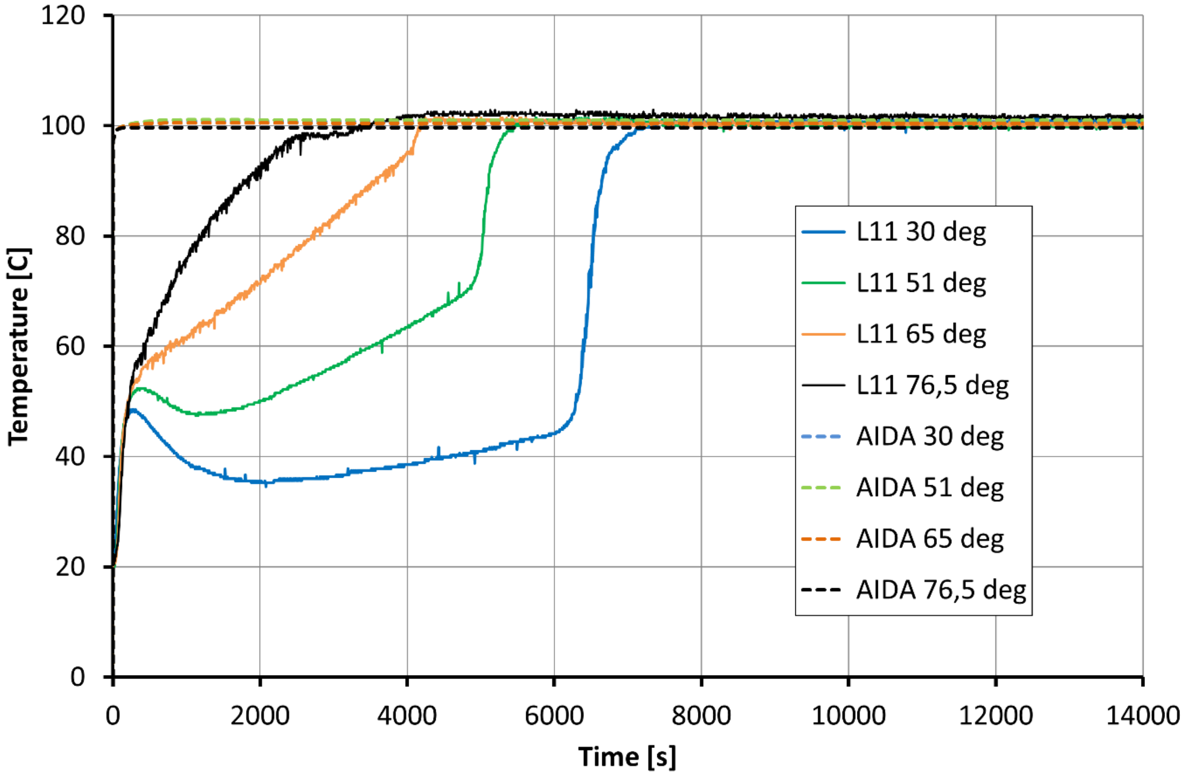

Fig. 5.91 Outer wall temperature evolution at different positions in L11 test and in AIDA (ATHLET-CD 3.5) simulation

Fig. 5.92 shows the calculated and the measured crust thickness of the L10 test. The simulation results agree well with experimental results. In the present cases AIDA slightly overestimate the crust formation at all position. Since crust formation strongly depends on the material properties and the heat transfer calculation, the minor deviations are likely the result of the aforementioned simplifications in AIDA. Another possible reason could be a slight difference between the location of the measurement-sensors and the simulation results. In addition, the calculation is based on averaged values, as opposed to point based sensor data.

The evolution of the crust formation in L11 test and the corresponding simulation with the new code version is shown in Fig. 5.93. Qualitatively the simulation results agree well with the experimental results. However, the AIDA calculations underestimate the crust thickness especially in the lower region. In the upper region (67.5 degree) the results are in good agreement. The likely reason for this is the simplification in the outer heat transfer modelling since that has a strong influence on crust formation. The choice of a different Nusselt correlation could improve the results, but this has been not changed because of a better comparison with the calculations of the L10 tests.

The comparison of the crust thickness calculation within the two code versions with experimental results are shown in Fig. 5.94. Generally, the simulation results are in good agreement with the experimental results in case of LIVE-10. The current version is slightly closer to experimental data than the previous version at all heating stages. In the case of LIVE-11, both versions underestimate the crust thickness; however, the new calculation predicts nearly double the crust thickness. The main reason for this is the inadequate modelling of the multiphase phenomena in external cooling.

Further comparison of the calculated results with the two code versions have been made regarding of the wand temperatures. Fig. 5.95 and Fig. 5.96 show the measured and calculated wall temperatures at 51 degree (ca. at the middle height) in case of LIVE-10 and LIVE-11 respectively. In the case of LIVE-10, both versions show generally good agreement with the experimental results. In stages one and two, the previous code version is closer to the experimental data, whereas in stage three the new code version shows better agreement. In the case of LIVE-11, both calculations slightly overestimate the experimental results; however, the new code version is closer to the measurements. The inner wall temperature calculation is strongly connected to the crust formation calculation (see previous paragraph) and more likely a result of the previous modelling simplifications. To improve the simulation results, more realistic modeling of external cooling is necessary in boiling cases.

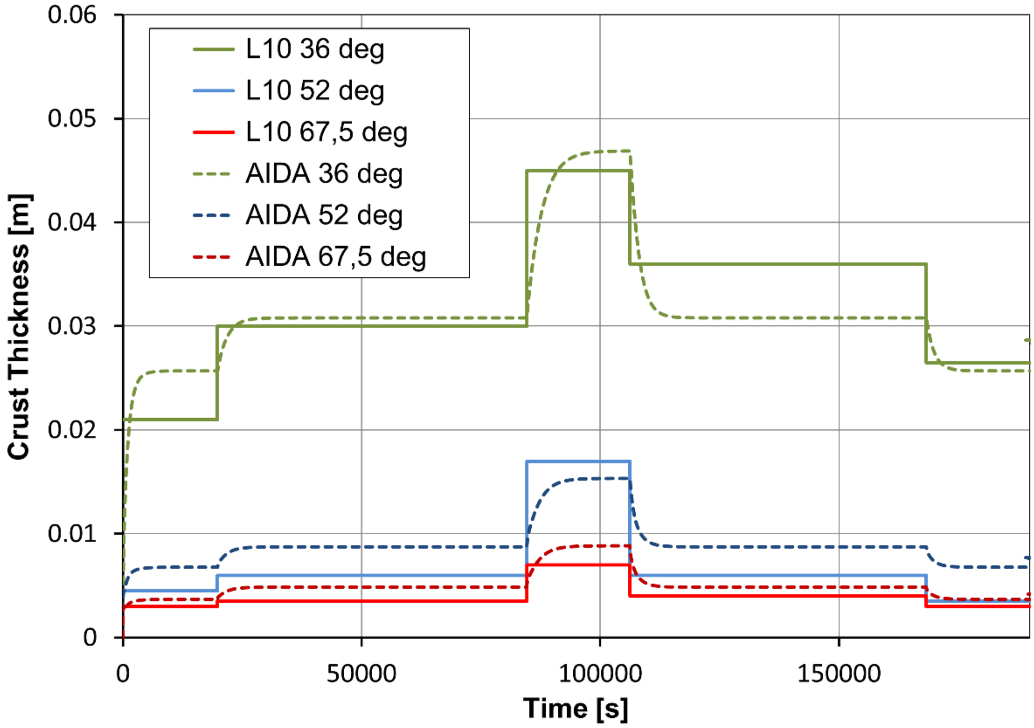

Fig. 5.92 Crust thickness evolution along the wall in L10 test and in AIDA (ATHLET-CD 3.5) simulation at different positions

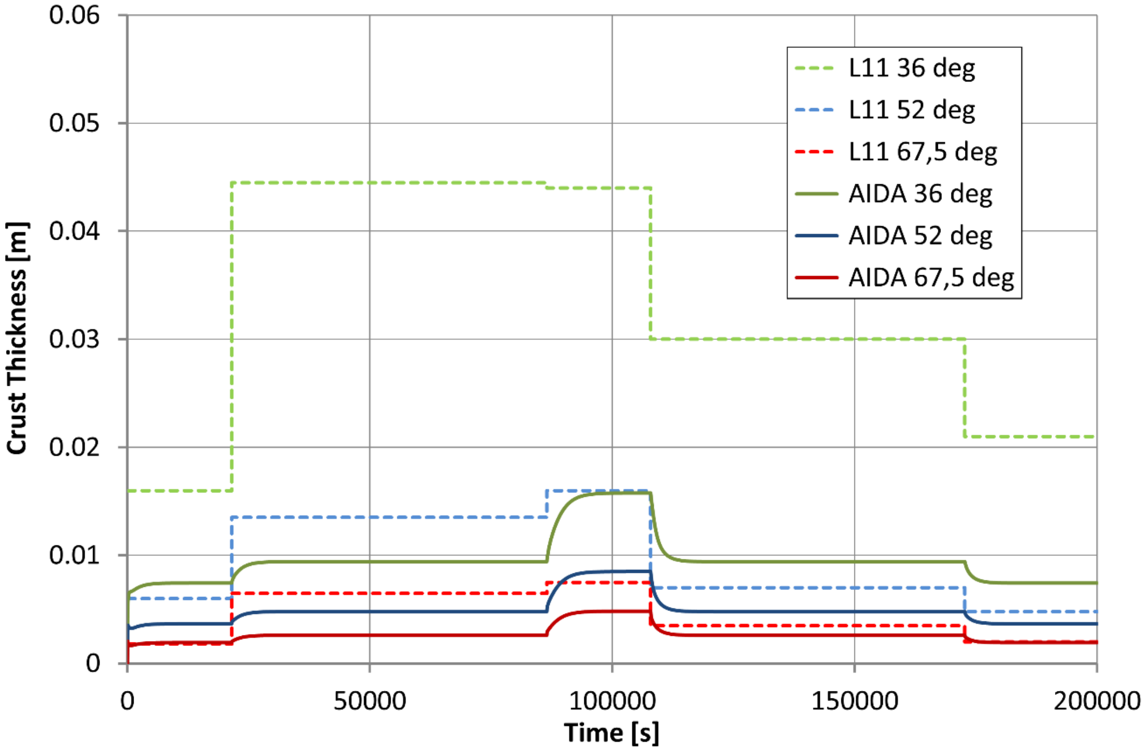

Fig. 5.93 Crust thickness evolution along the wall in L11 test and in AIDA ATHLET-CD 3.5) simulation at different positions

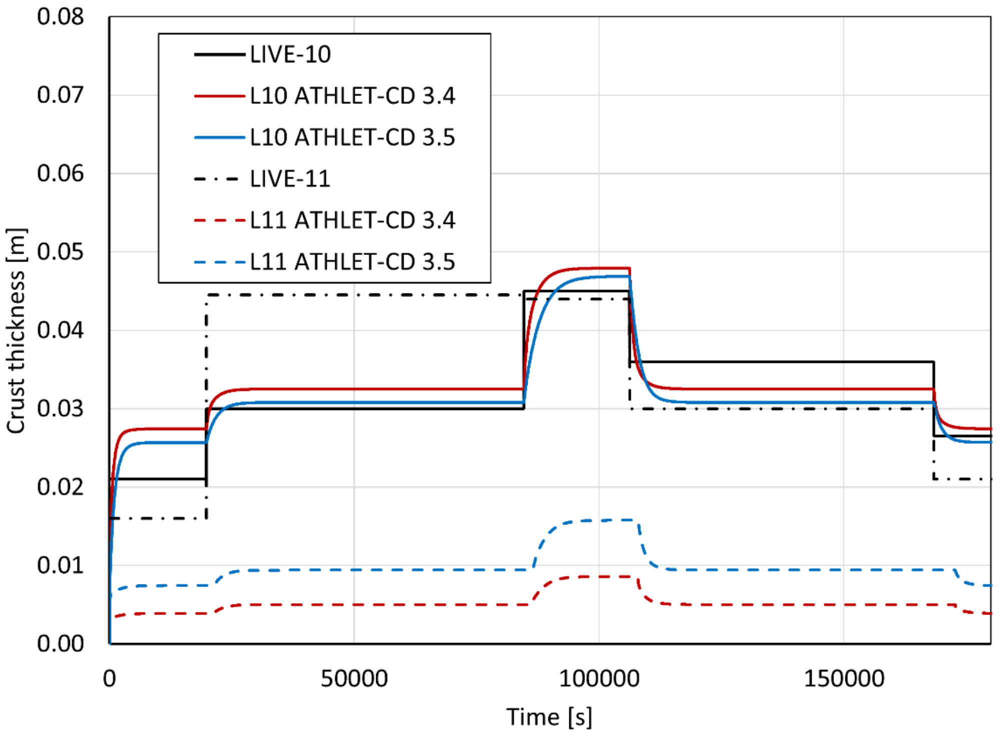

Fig. 5.94 Crust thickness at 36 degree in LIVE-10, LIVE-11 experiments and ATHLET-CD simulations (3.4 and 3.5).

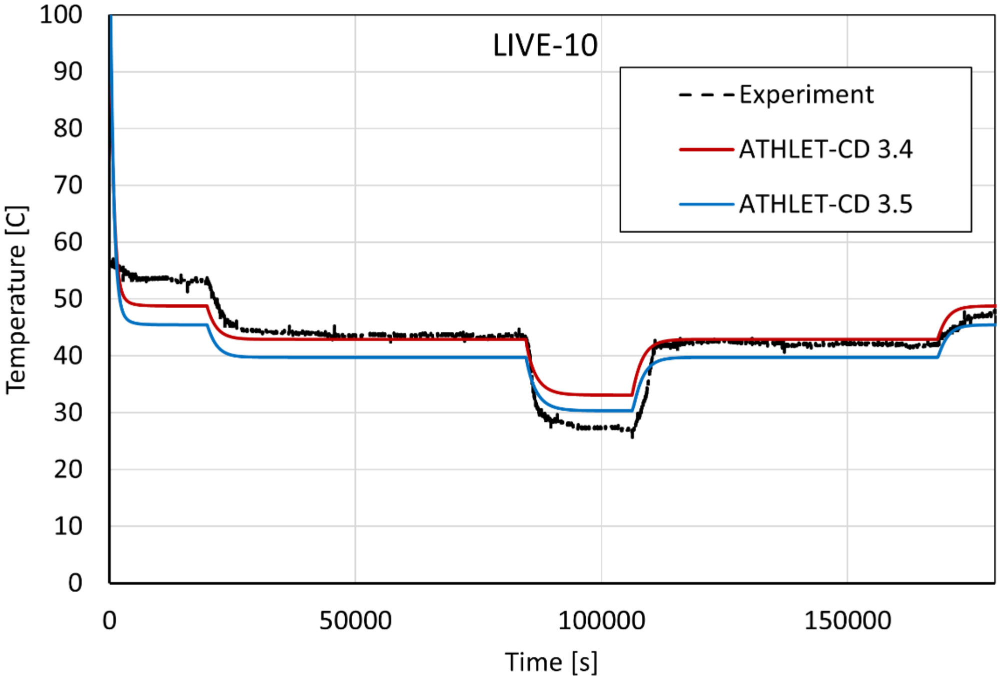

Fig. 5.95 Wall temperature evolution at 51 degree in LIVE-10 experiment and ATHLET-CD simulations (3.4 and 3.5).

.

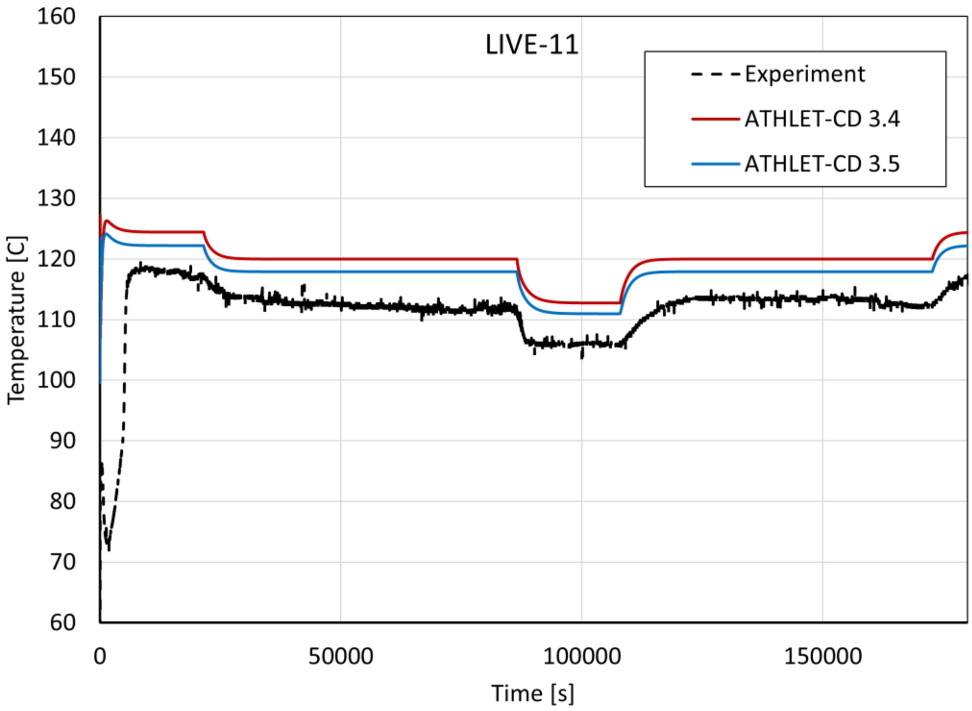

Fig. 5.96 Wall temperature evolution at 51 degree in LIVE-11 experiment and ATHLET-CD simulations (3.4 and 3.5).

5.9.5 Main Findings

Generally, the comparison results show, that the stand-alone module AIDA calculates the temperatures and the crust formations well in case of a homogeneous volumetric heated pool. Further improvements of the results are possible after an extensive sensitivity study regarding the not-exactly defined material properties in the experiment. Moreover, the results shows that the simplified modelling of the external cooling gives a realistic result in case of a continuously cooled channel. The modelling of boiling conditions in the external cooling channel needs the knowledge of the HTC value. Alternatively, the extended coupled method for AIDA is required to get more realistic results. The extended coupling with an ATHLET thermohydraulic model is already implemented in AC^2, however further investigations regarding the ATHLET modelling of the complex thermohydraulic phenomena in the cooling channel are still ongoing.

5.10 LIVE L-1, L-4, and L-6

A standard PC (64-bit Windows 10 Enterprise operating system) with an INTEL® CORE™ i7-1185H processor was used for the validation calculation. The simulations performed (LIVE-L1, -L4, and -L6) were run with AIDA in standalone mode. The CPU time required for all tests was in the single-digit minute range, with a maximum simulation time step of 1 second.

The numerical results of ATHLET-CD 3.4 and 3.5 show a high degree of consistency for the LIVE-L1 and LIVE-L4 tests. The melt pool temperature is slightly lower (less than 2 %) in ATHLET-CD 3.5 compared to the previous version, which result, a slightly greater crust thickness in the new results. The minor updates in the pool and crust heat balance calculations are the source of these slight differences.

The modified configuration of the test setup in the LIVE-L6 experiment, in which the additionally introduced copper plate has a significant influence on the convection behaviour of the melt used in the calotte, contributes significantly to the deviation between the experimental and simulated values. The influence of the copper plate cannot be described by the existing AIDA modelling options.

Other factors influencing the quality of the simulation results are the lack of consideration of the temperature dependence of the material data in AIDA and the simplified assumption of a well-mixed, homogeneous melt. The simplified approach of a constant temperature and a constant heat transfer profile along the calotte was also assumed for the cooling medium of the outer wall (air/water). Moreover, there is a lack of material property data from the experiment. These data have been defined using predicted mean values and based on previous experience.

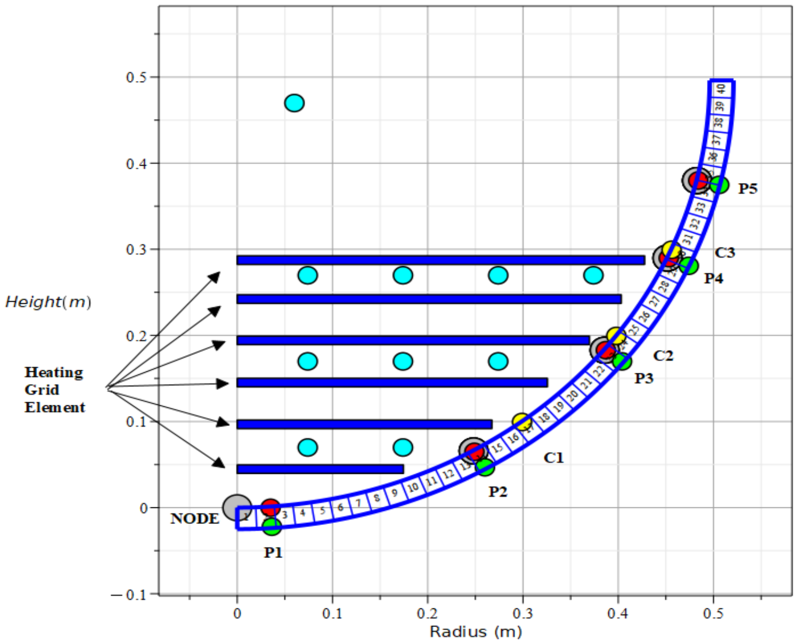

Fig. 5.97 LIVE instrumentation and AIDA parameterization

Tab. 5.8 Sensor types

	Sensor
🟢	OT: Temperature of the vessel outer surface (P1 – P5)
🔴	IT: Temperature of the vessel inner surface (P1 – P5)
🟡	CT: Crust temperature (C1 -C3)
🔵	MT: Melt temperature (MT1 to MT36 inside the melt, MT37 above the melt)
⚪	HF: Heat Flux through vessel wall

5.10.1 LIVE-1

For the comparative calculation, the period between the completion of the melt mixture filling of the vessel and the end of the LIVE-L1 experiment was considered. The experimentally determined fill level of 0.31 m in the calotte shows that the uppermost measuring point for internal and external temperature is above the melt level, so that the greatest deviation between the experimentally determined and simulated AIDA data is to be expected for this measuring point. The power fluctuation observed in the first 10,000 s across all heating stages is due to insufficient measurement data acquisition within this period. The mean (MEAN), maximum (MAX), and minimum (MIN) melting temperatures were determined considering the experimentally determined data from the 36 sensors. Under the given LIVE-L1 boundary conditions and power input, the melting temperature calculated with ATHLET-CD 3.4 and ATHLET-CD 3.5 lies between the measured mean and maximum melting temperatures. The crust thickness profiles calculated by AIDA show a direct dependence between the available power input and the melt temperature. The melt height of 0.4 m determined by AIDA is above the experimentally determined height of 0.31 m, so that constant values for the variables QCW (heat flux between the crust and the inner wall), QMC (heat flux between the melt and the crust), TCRO (crust temperature), THCR (crust thickness) could be determined.

Configuration

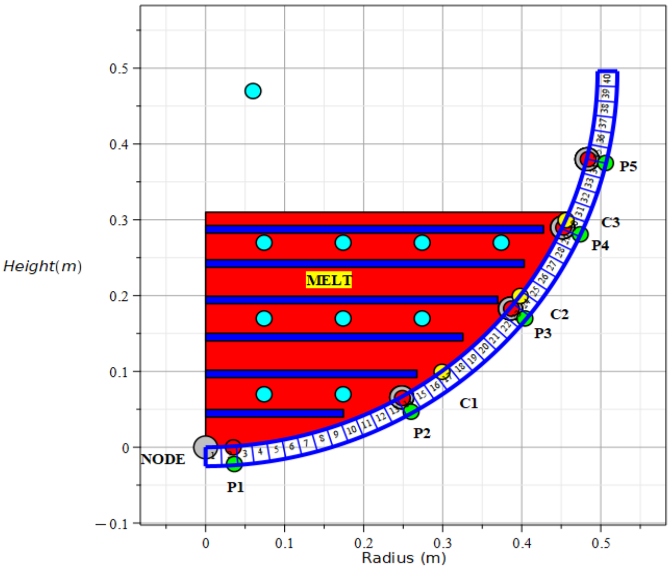

Fig. 5.98 LIVE-L1 melt configuration

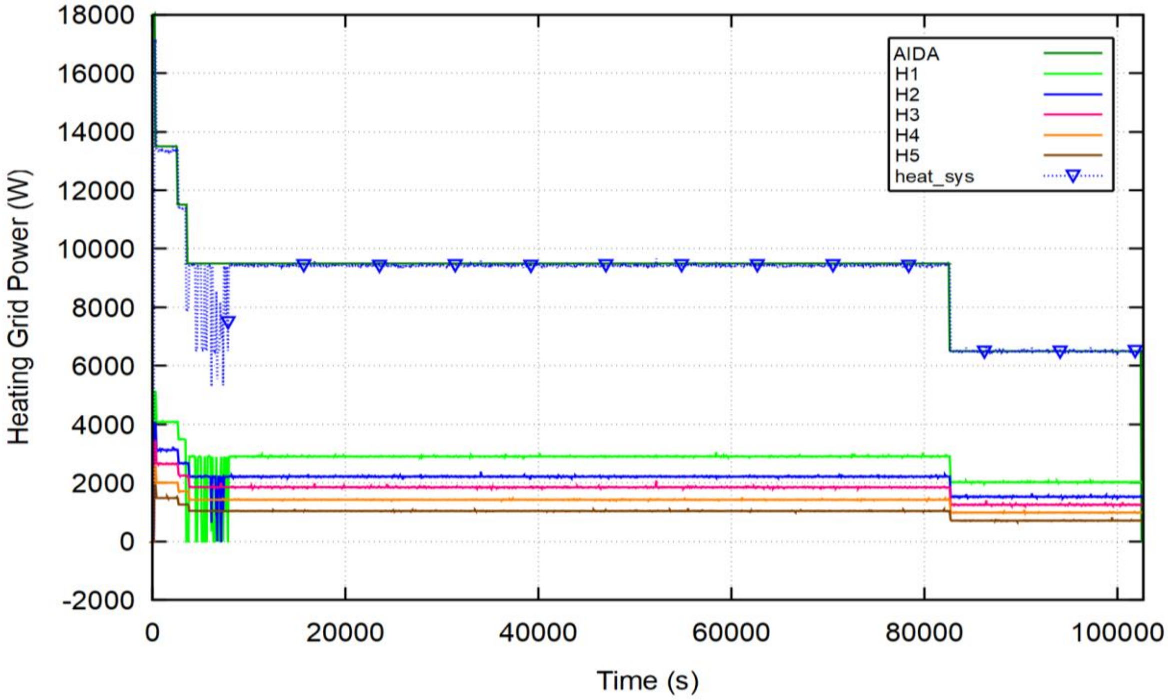

Fig. 5.99 Applied heating power

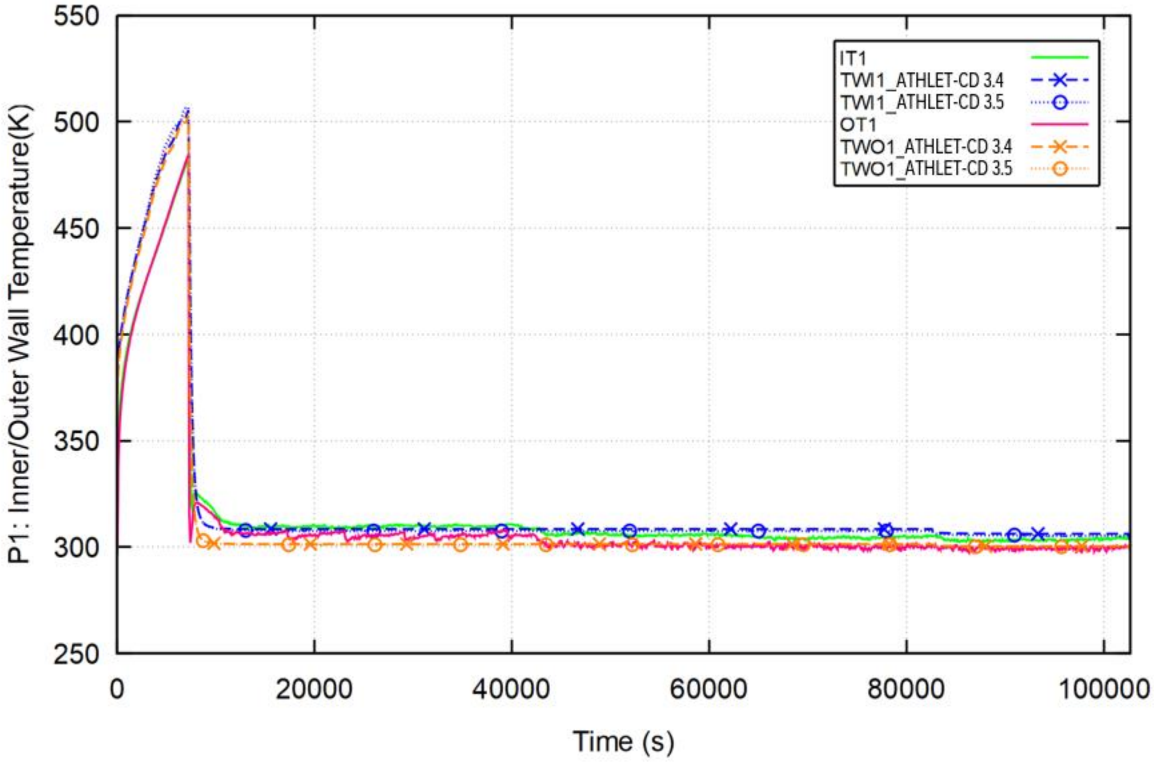

Fig. 5.100 Inner and outer wall temperature at measuring point IT1/OT1

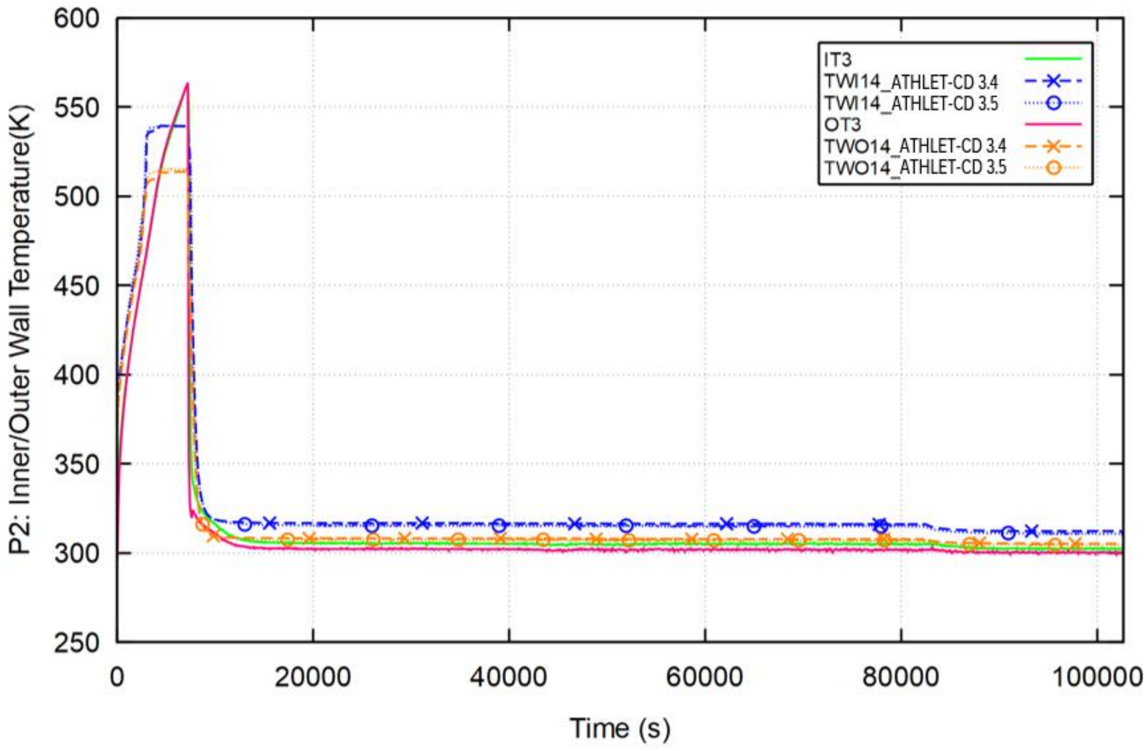

Fig. 5.101 Inner and outer wall temperature at measuring point IT3/OT3

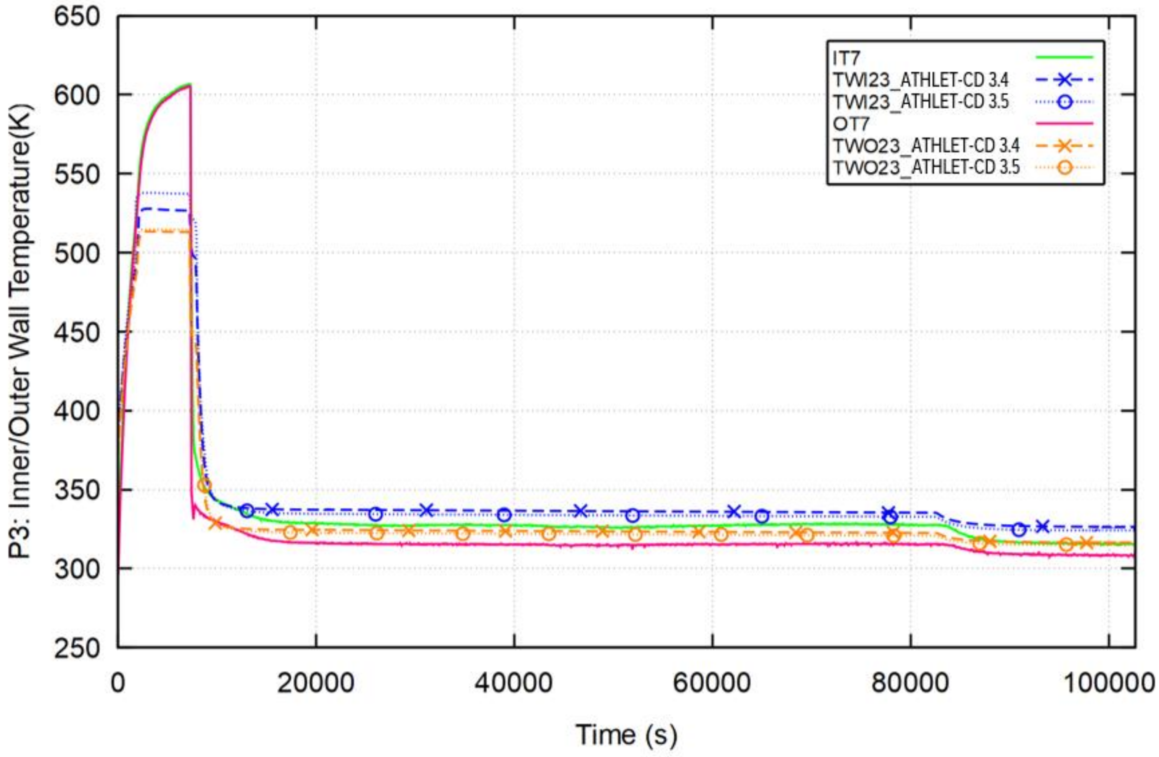

Fig. 5.102 Internal and external wall temperature at measuring point IT7/OT7

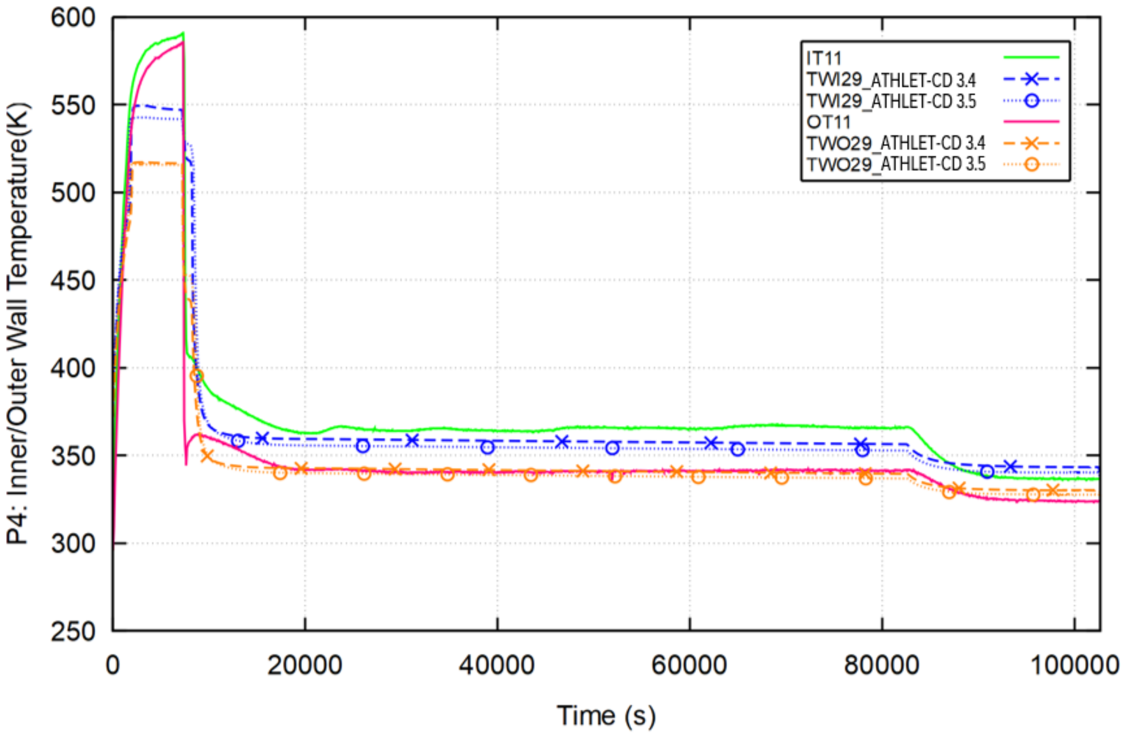

Fig. 5.103 Inner and outer wall temperature at measuring point IT11/OT11

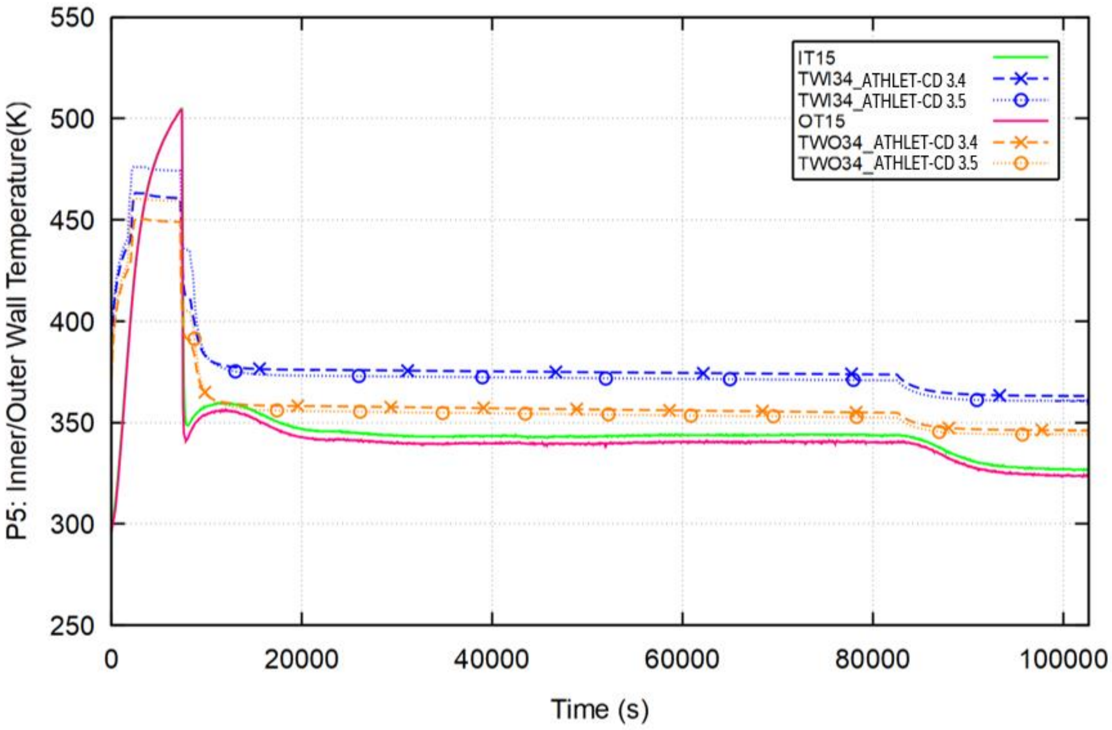

Fig. 5.104 Inner and outer wall temperature at measuring point IT15/OT15

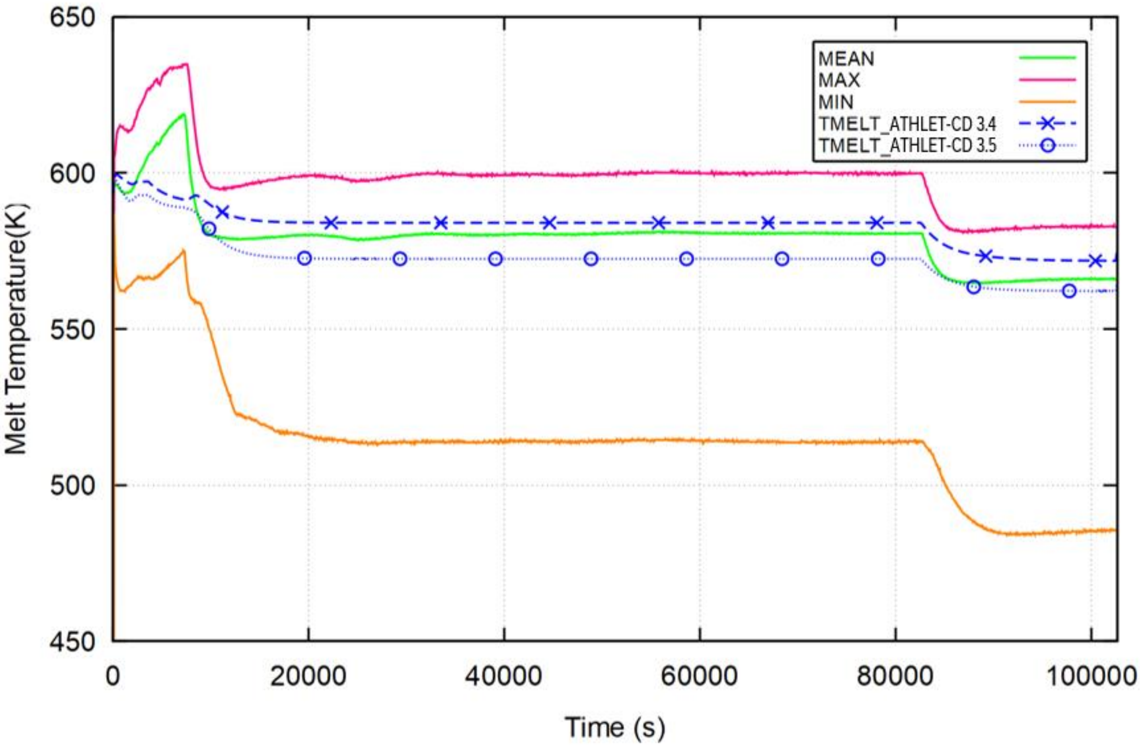

Fig. 5.105 Melt temperature

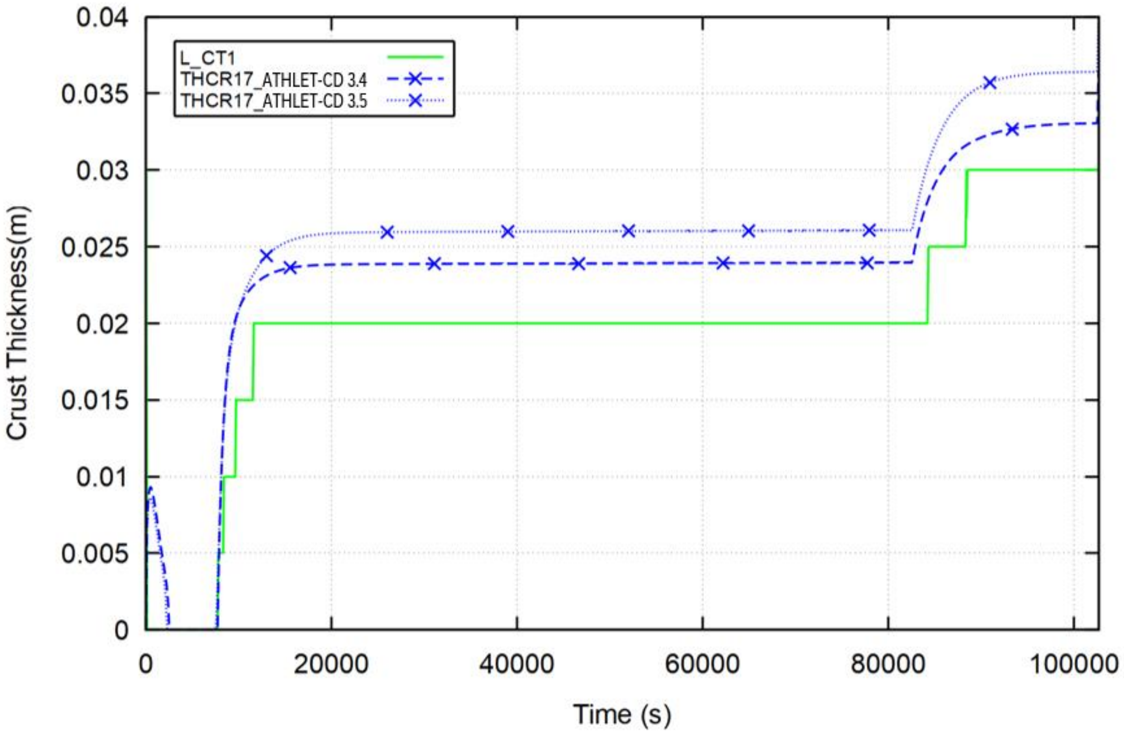

Fig. 5.106 Crust thickness at measuring point C1

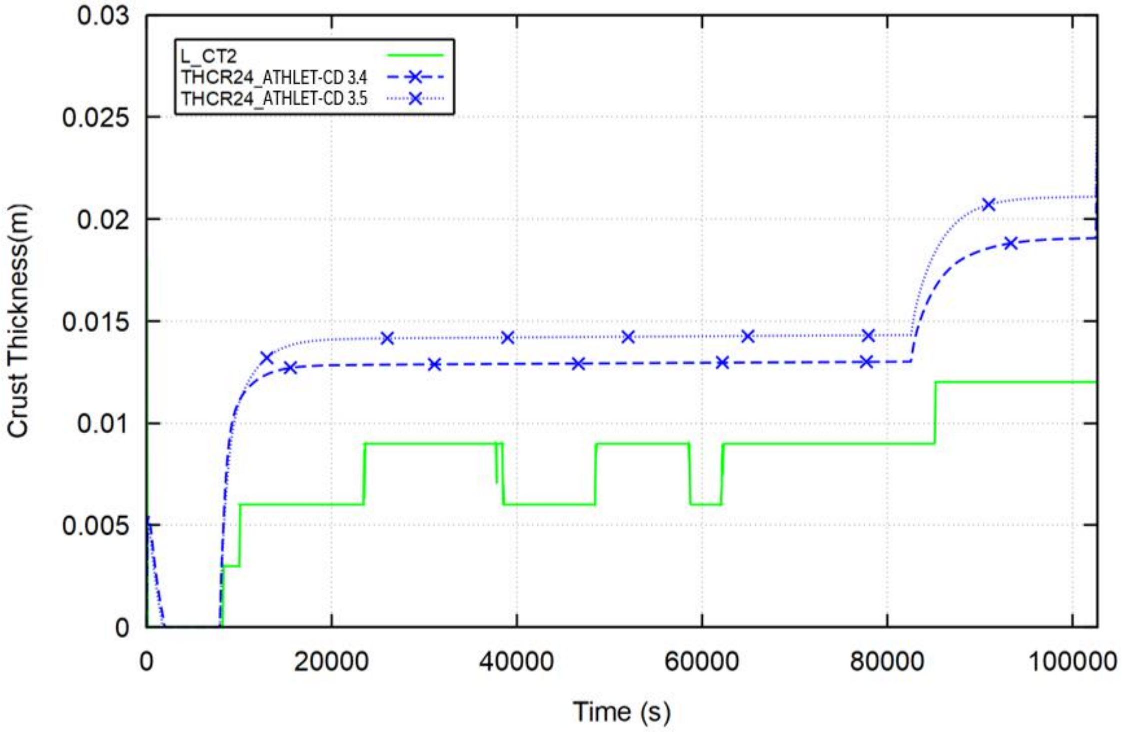

Fig. 5.107 Crust thickness at measuring point C2

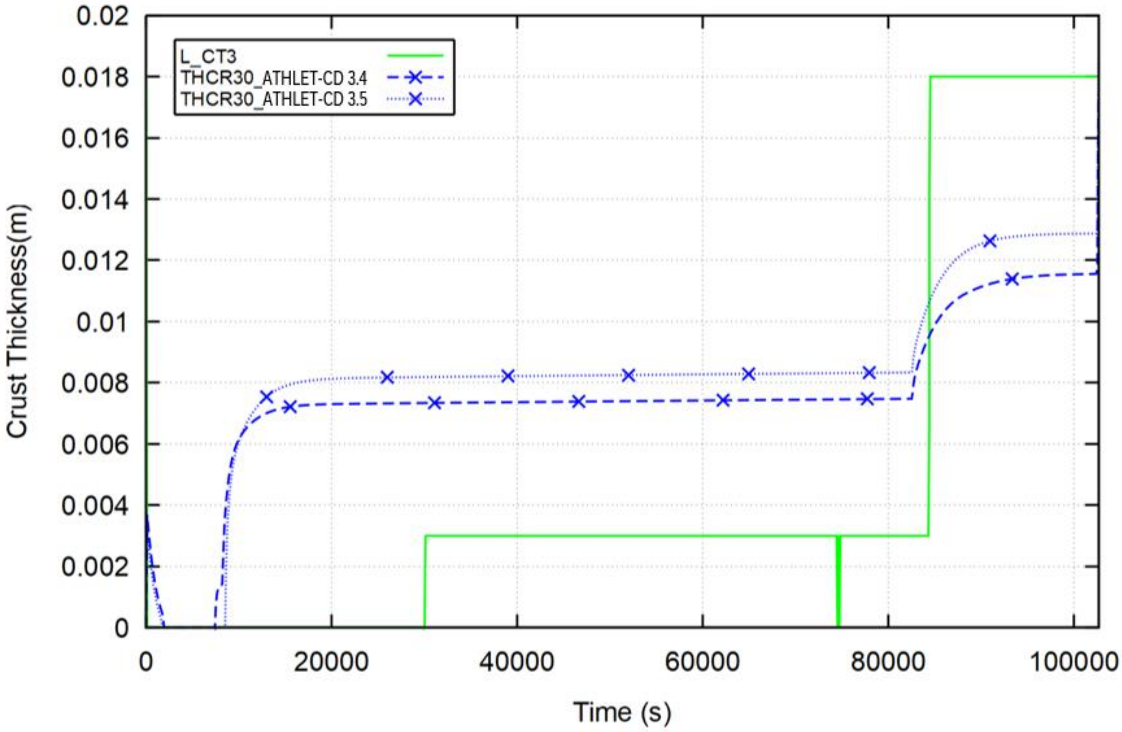

Fig. 5.108 Crust thickness at measuring point C3

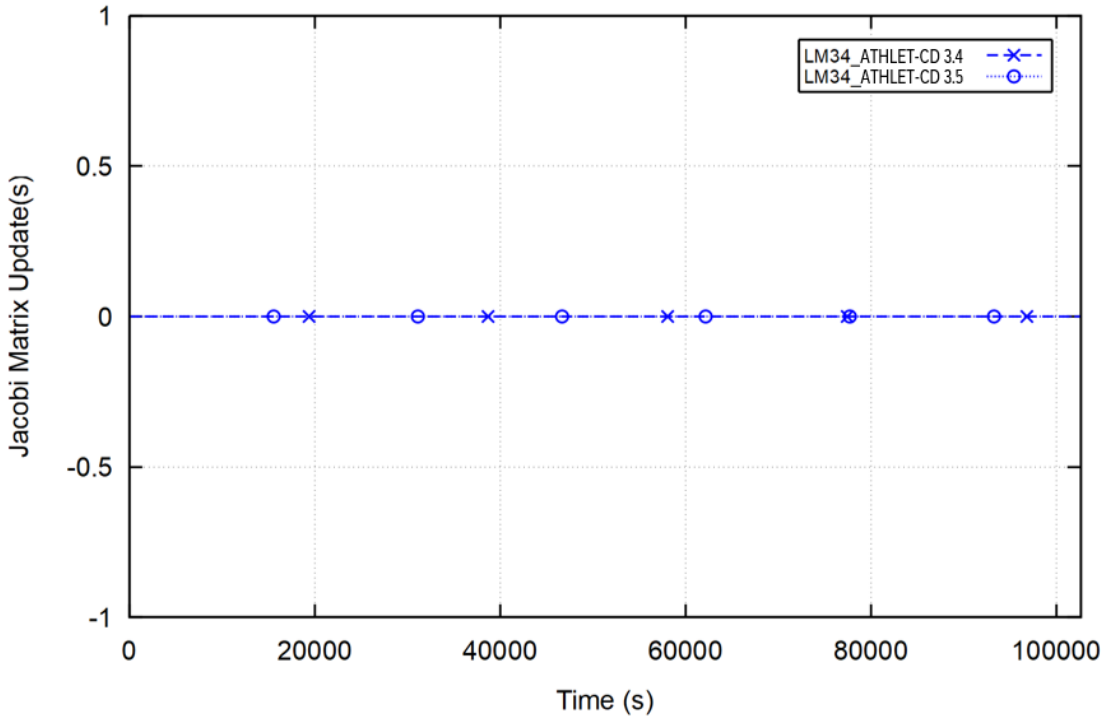

Fig. 5.109 Jacobi matrix update

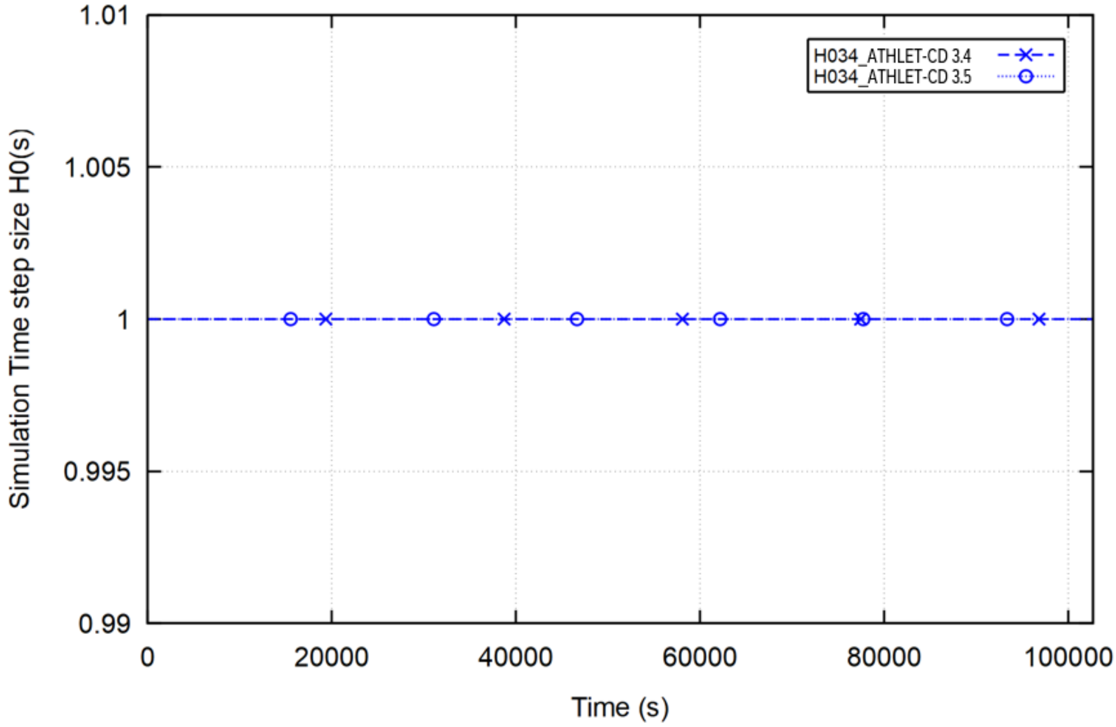

Fig. 5.110 Time step size

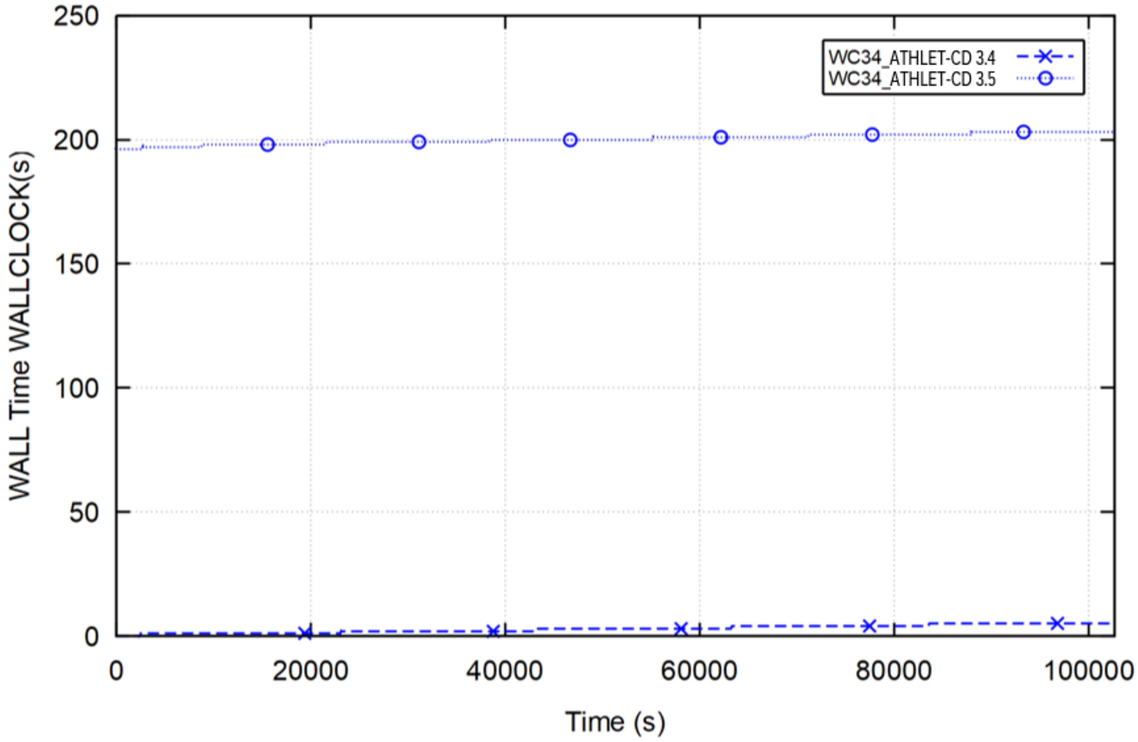

Fig. 5.111 WALLCLOCK

5.10.2 LIVE-L4

Compared to LIVE-L1, a larger mass (392 kg) of the melt mixture was used in the LIVE-L4 experiment in the test vessel, which also increased the resulting level height from 310 mm (LIVE-L1) to 435 mm. In addition, the initial temperature of the melt in the LIVE-L4 experiment was 7 K higher, and the outer wall of the vessel was cooled by a continuous water mass flow of 1.3 kg/s over the entire test period of 195221 s.

Over the five heating stages, the initial power of 18 kW was first reduced in two stages to 10 kW and 5 kW in 5 phases and then increased again in the 10 kW and 18 kW stages. During the first 18 kW phase, the melting temperature determined by AIDA with both code versions (ATHLET-CD 3.4 and ATHLET-CD 3.5) is slightly above of the maximum value measured experimentally. In the following 10 kW, 5 kW, and 10 kW phases, the melting temperature determined by the calculations lies between the maximum and average experimentally measured temperatures and rises to the maximum value in the second 18 kW phase.

The simulation of crust growth is reproduced identically in both ATHLET-CD versions. The largest deviation between the calculated and experimentally determined crust thickness is observed during the 5 kW phase. The largest deviation between the experimentally and numerically determined wall temperature occurs at measuring point P2, where both the inner and outer wall temperatures are above the measured values. For the other measuring points (P1, P3, P4, and P5), the calculated inner wall temperature TWI is largely between the experimentally determined inner and outer wall temperatures at these points. The outer wall temperature at all measuring points (P1 - P5) is above the experimentally determined measured value.

Configuration

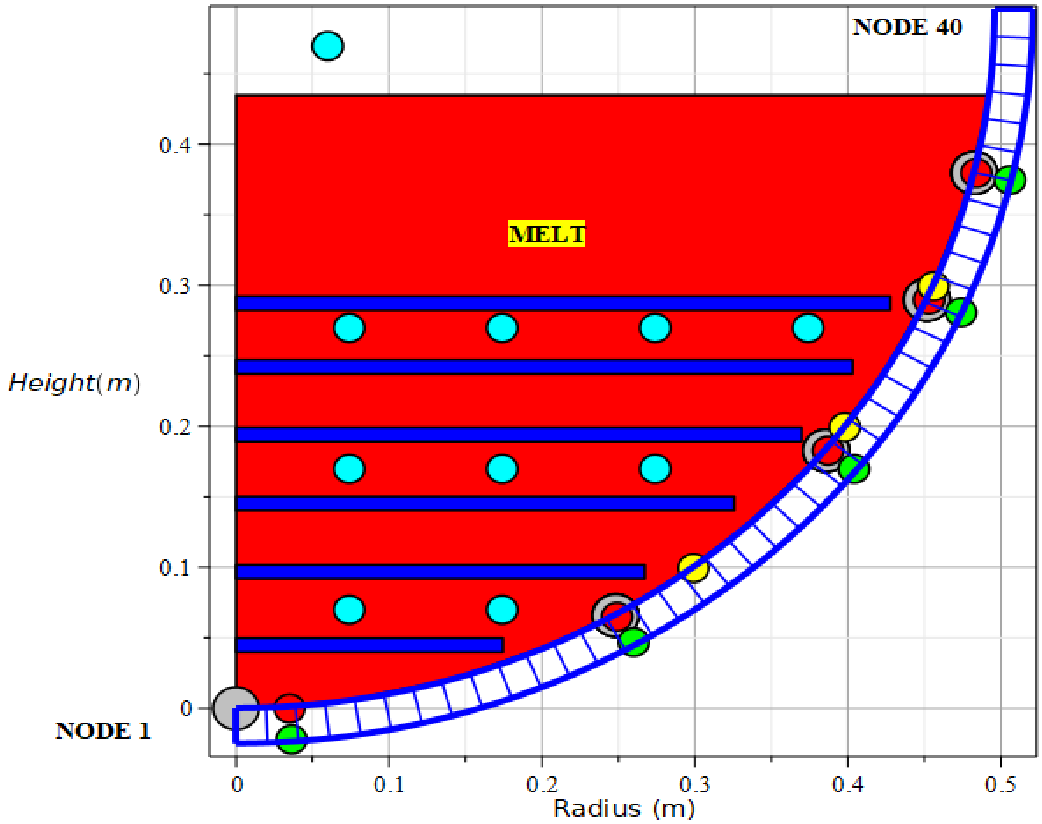

Fig. 5.112 LIVE-L4 configuration

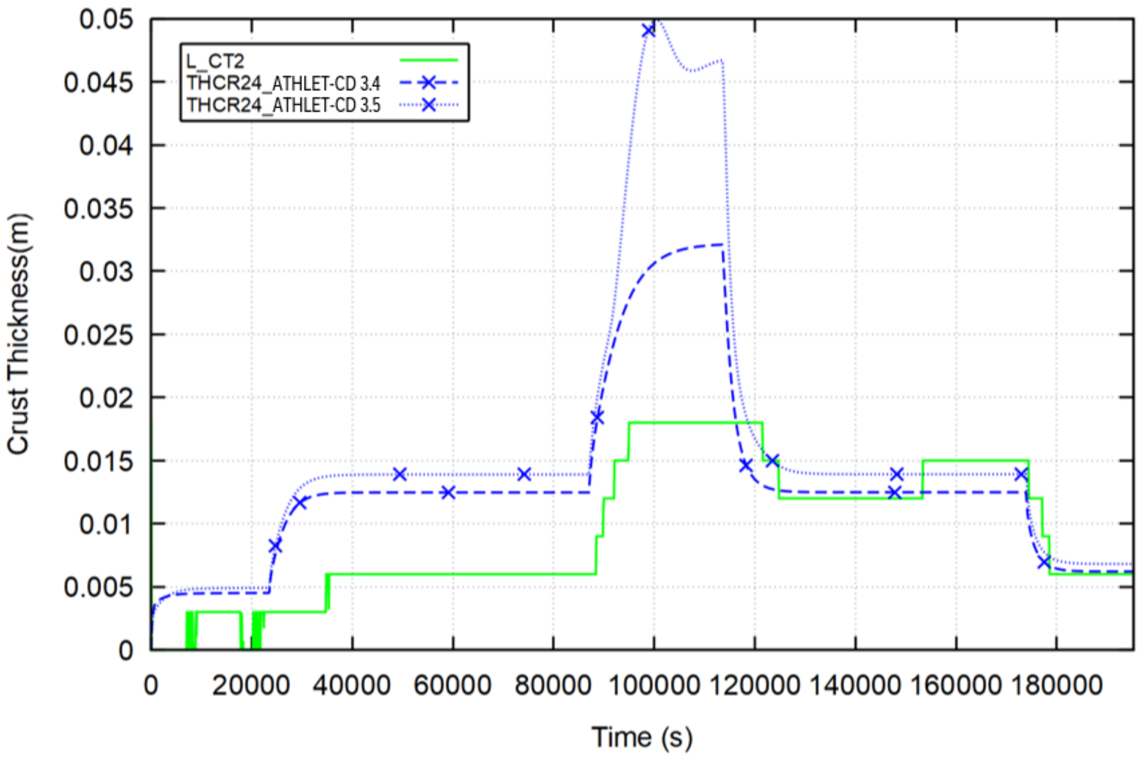

Fig. 5.113 Crust thickness at measuring point CT2

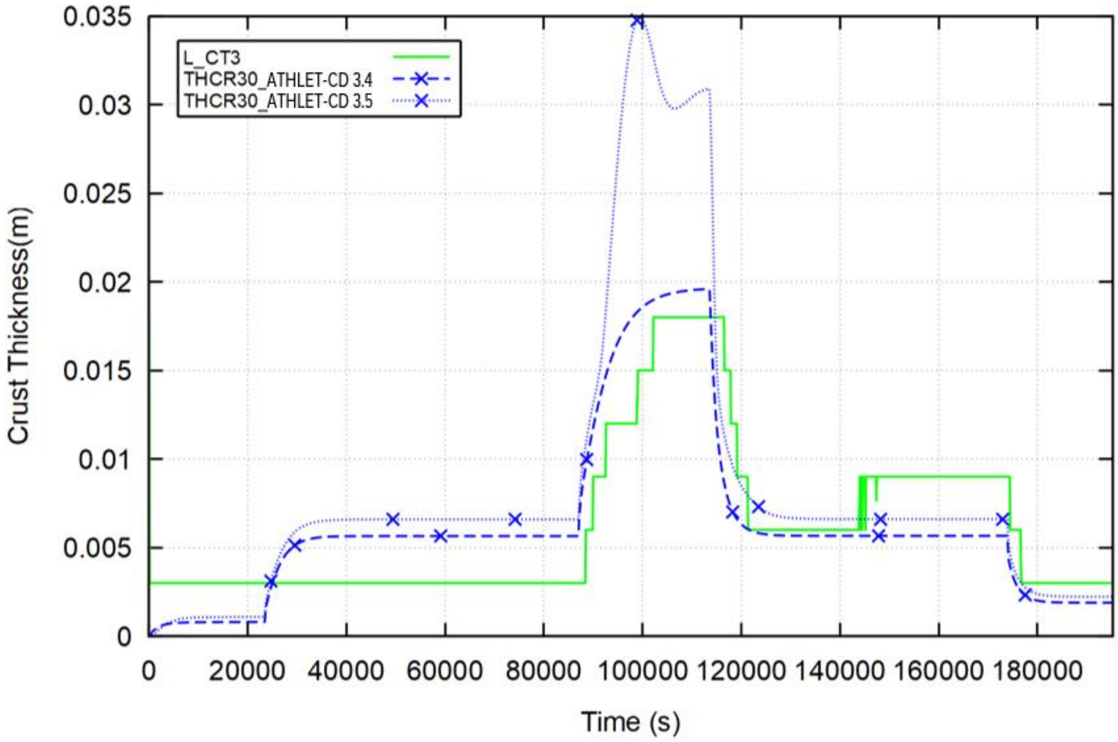

Fig. 5.114 Crust thickness at measuring point CT3

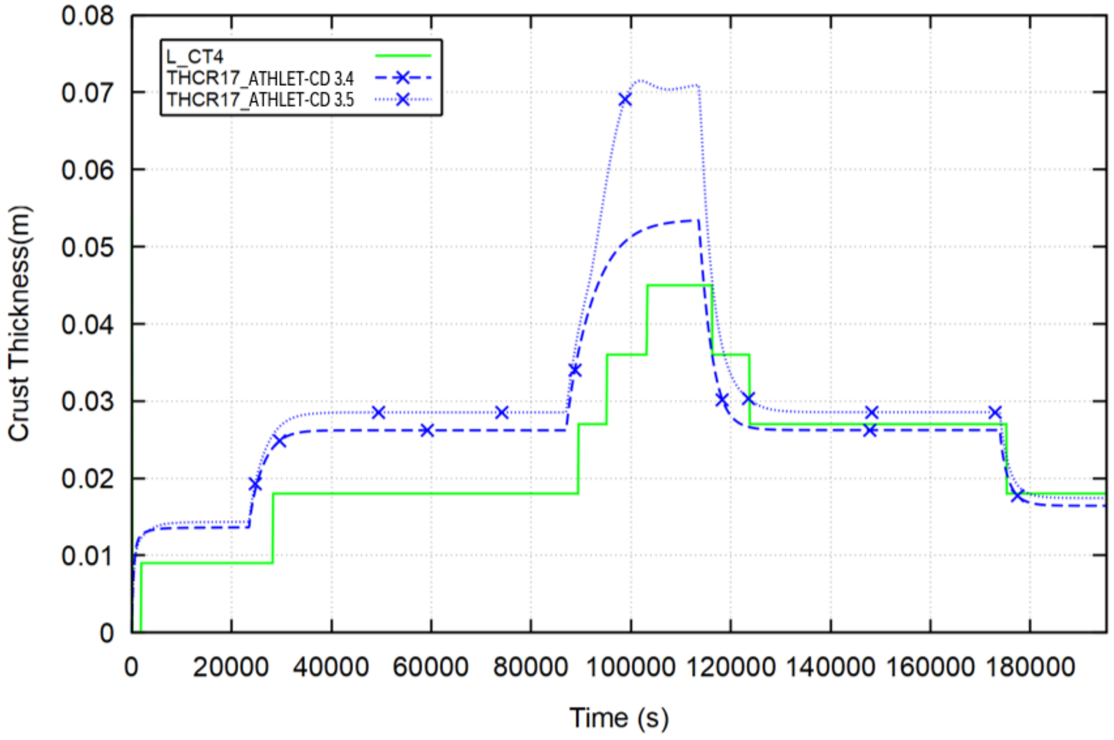

Fig. 5.115 Crust thickness at measuring point CT4

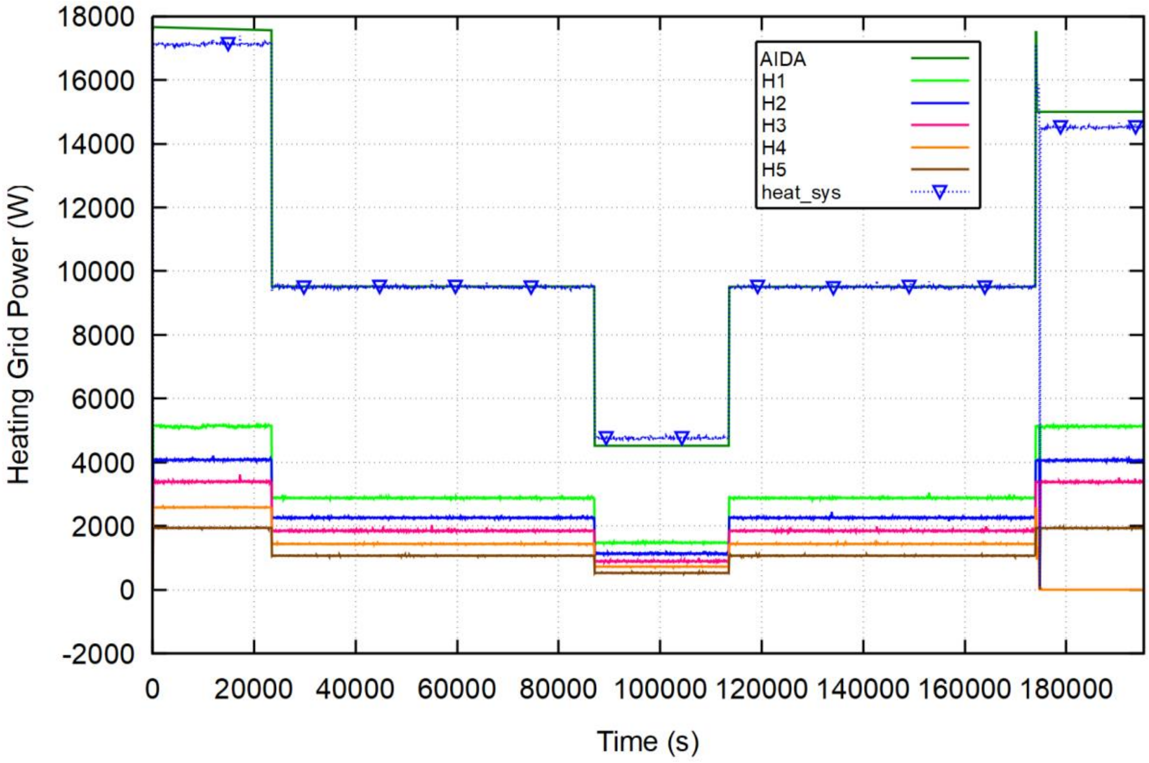

Fig. 5.116 Heating power supplied

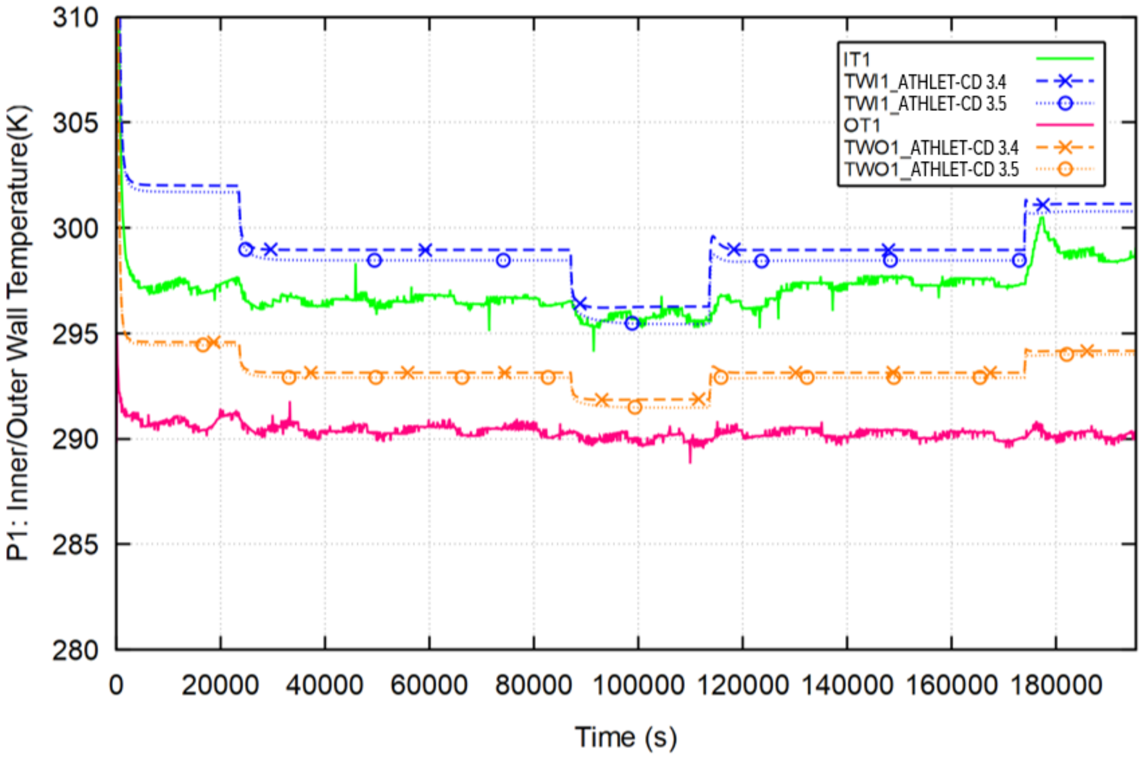

Fig. 5.117 Inner and outer wall temperature at measuring point IT1/OT1

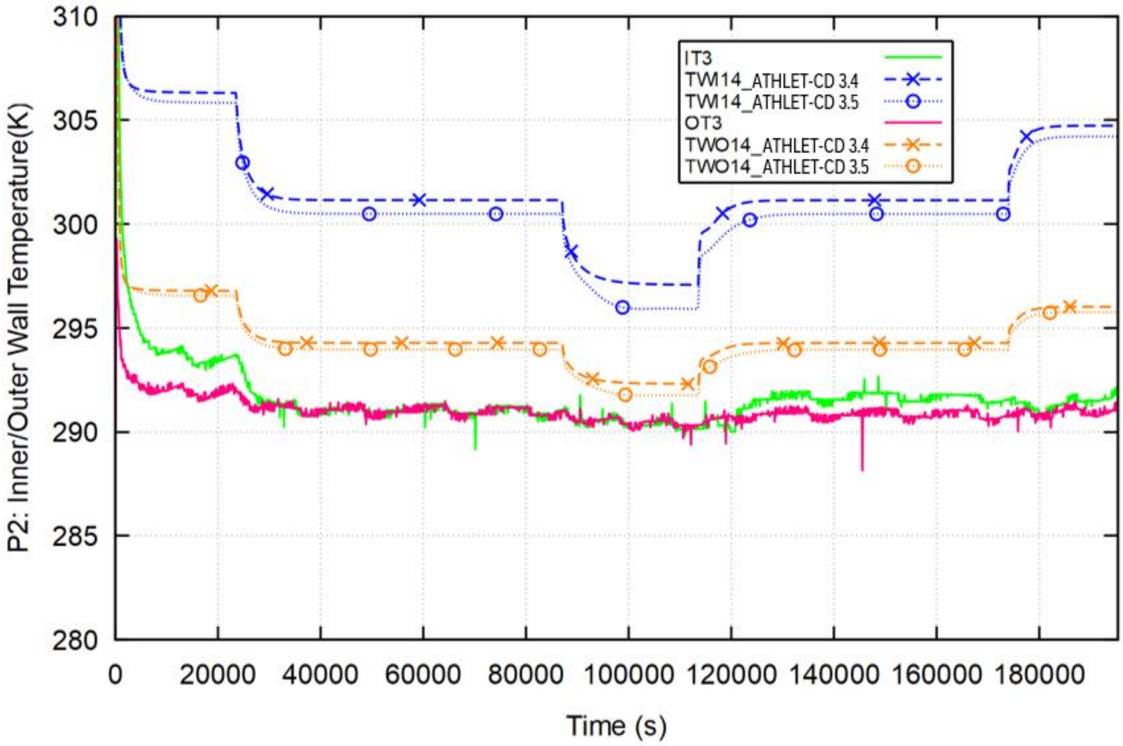

Fig. 5.118 Inner and outer wall temperature at measuring point IT3/OT3

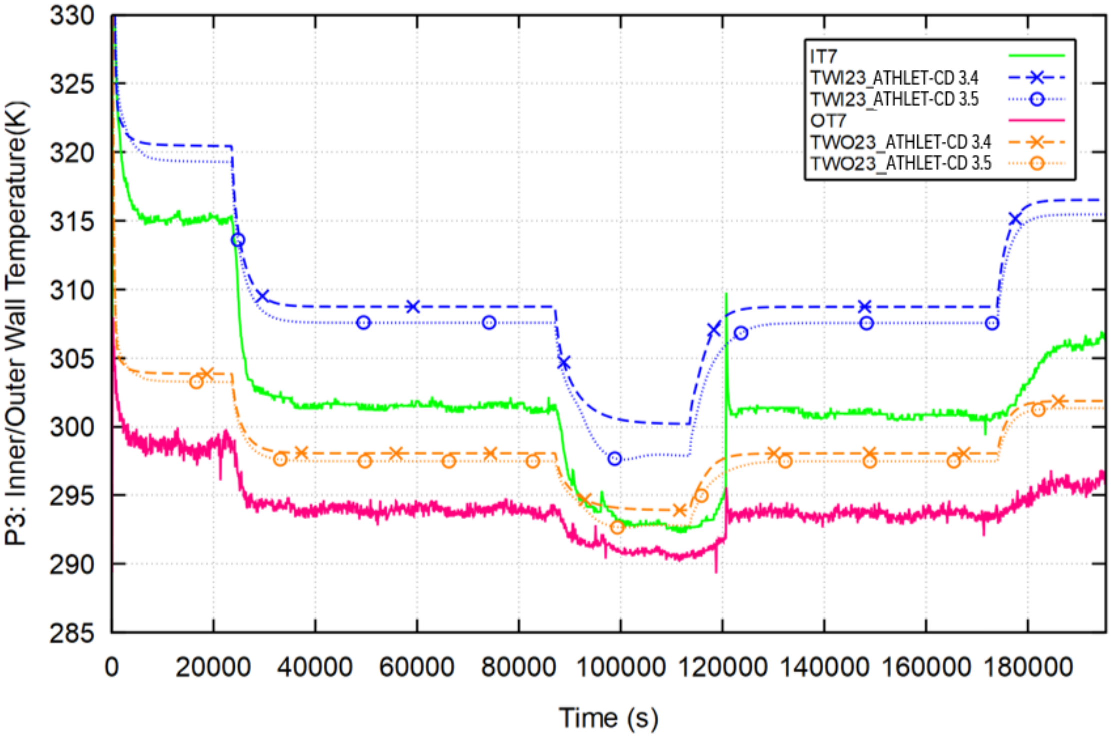

Fig. 5.119 Inner and outer wall temperature at measuring point IT7/OT7

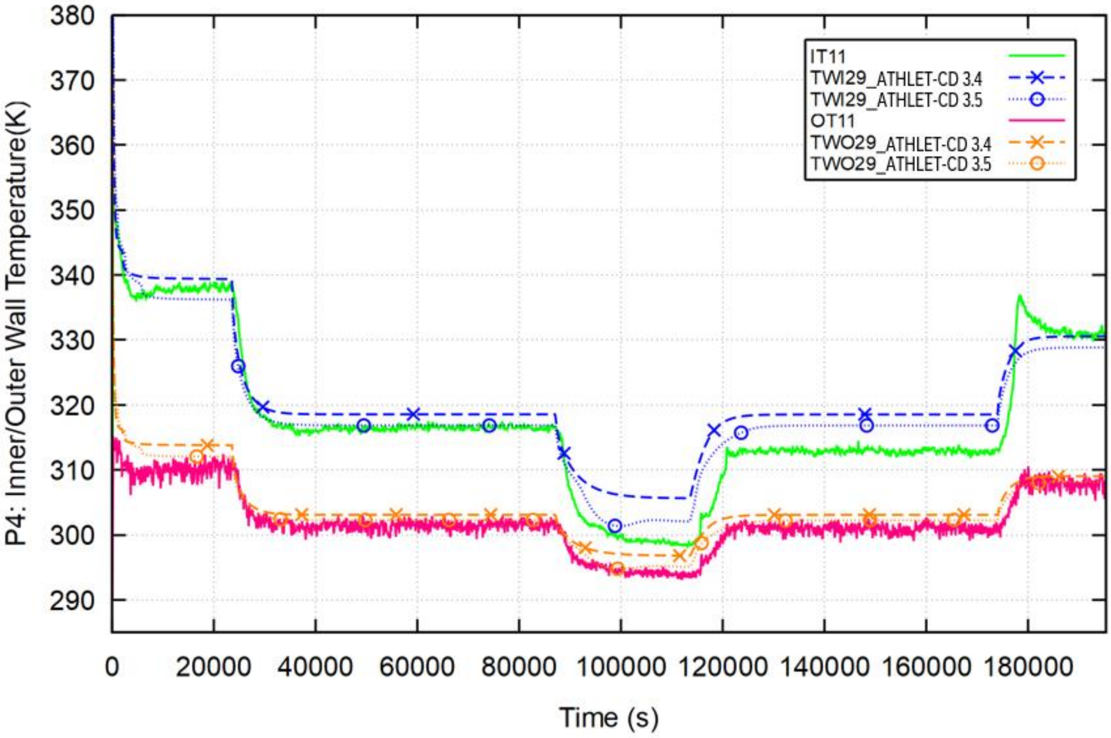

Fig. 5.120 Inner and outer wall temperature at measuring point IT11/OT11

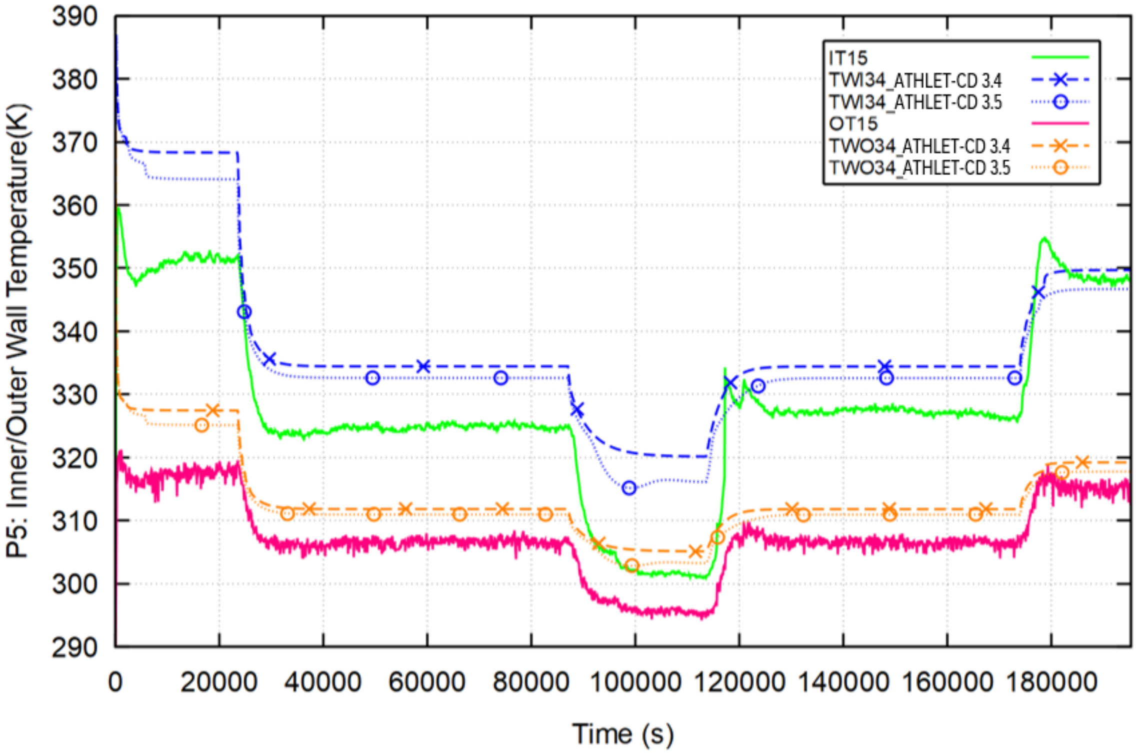

Fig. 5.121 Inner and outer wall temperature at measuring point IT15/OT15

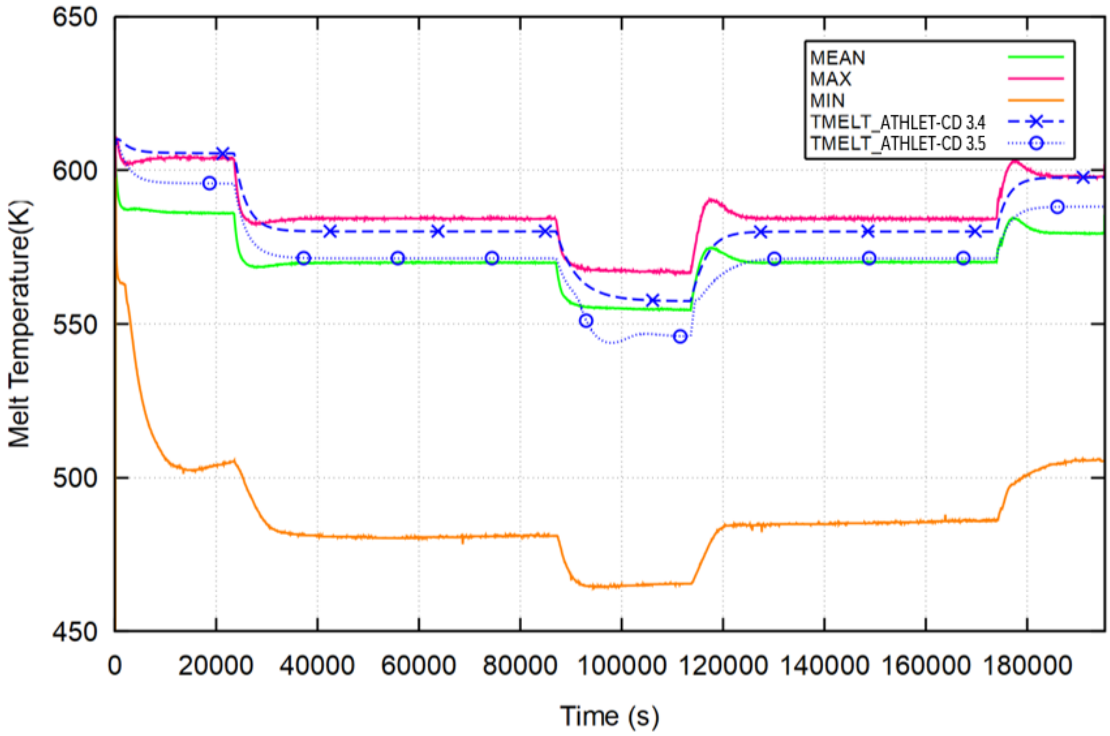

Fig. 5.122 Melt temperature

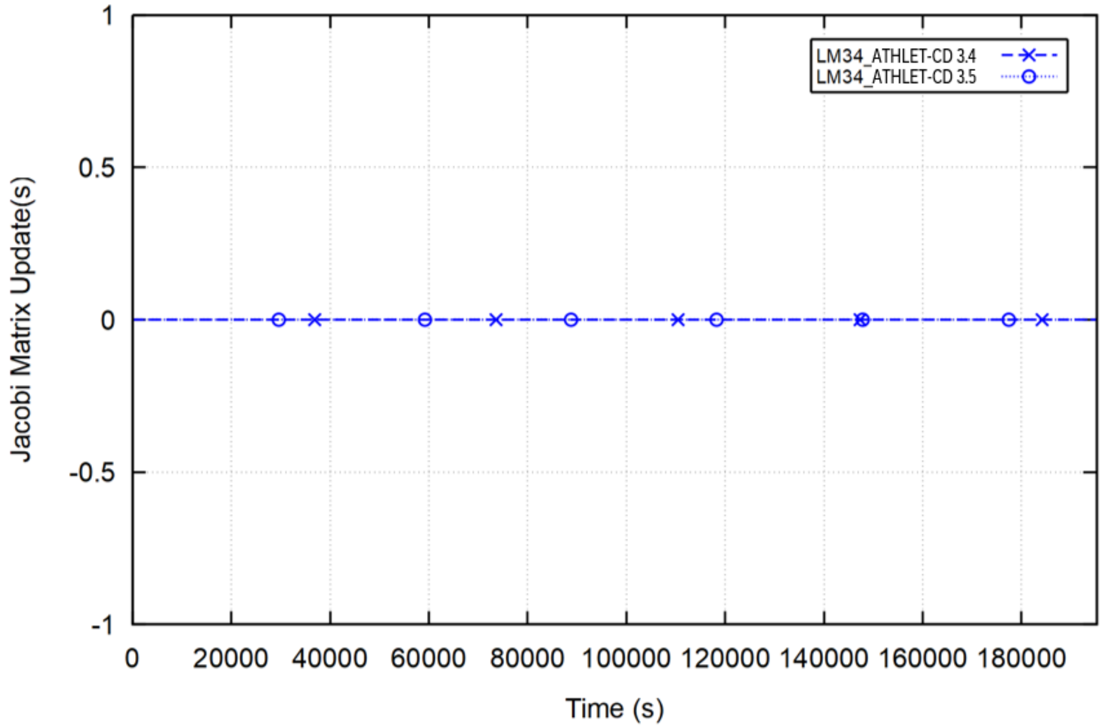

Fig. 5.123 Jacobi matrix update

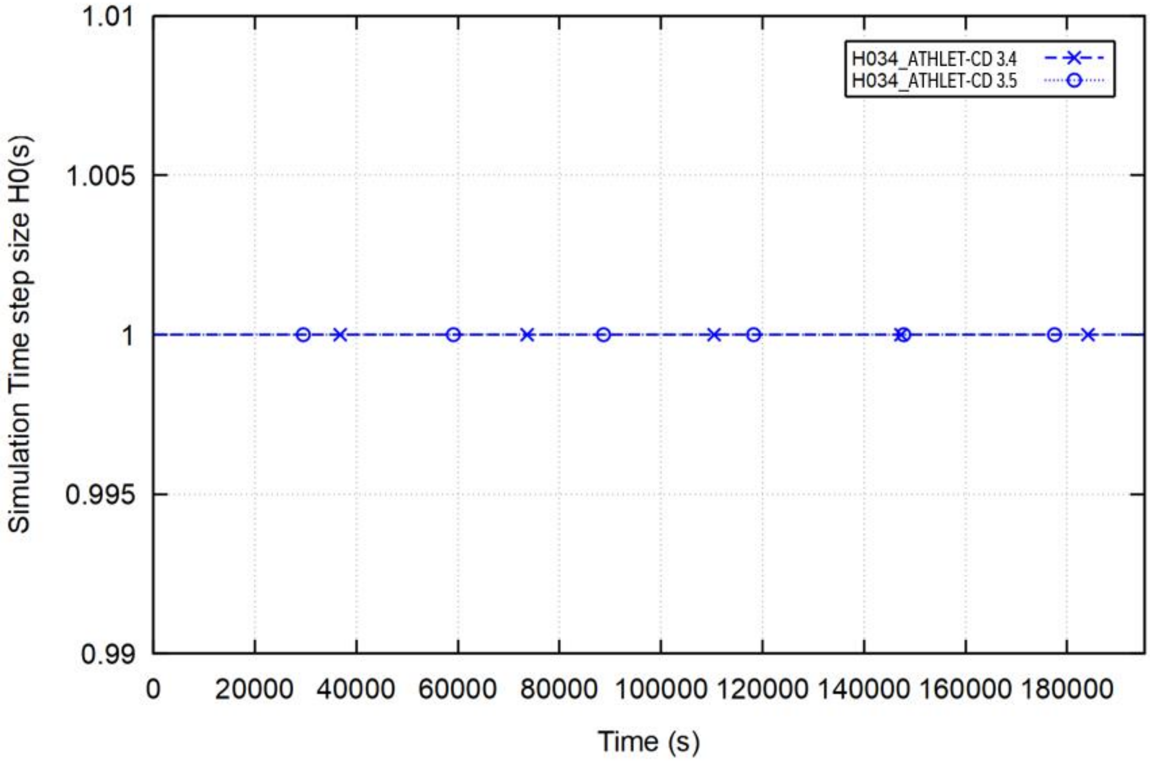

Fig. 5.124 Time step size

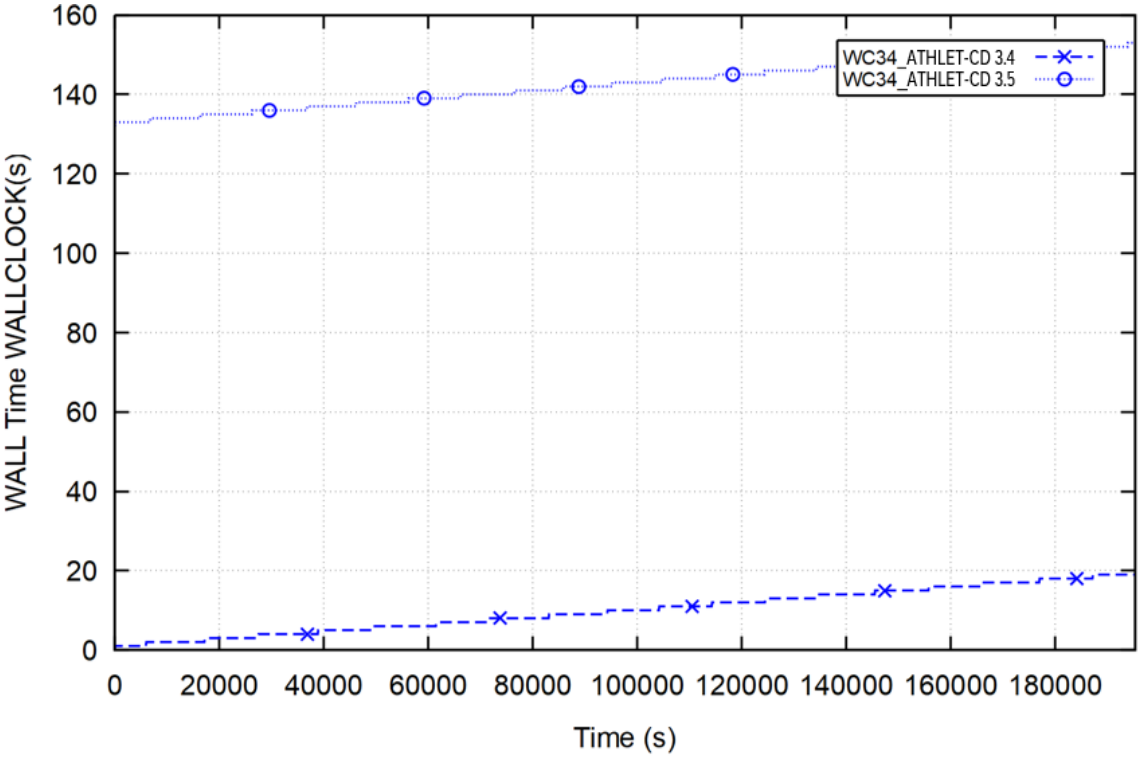

Fig. 5.125 WALLCLOCK

5.10.3 LIVE-L6

The melt mass of 392 kg used in the LIVE-L6 experiment is of the same order of magnitude as the mass used in the LIVE-L4 experiment. While in the LIVE-L4 experiment, the melt was able to form convection over the entire height range of 435 mm, in the LIVE-L6 experiment an additional 2 mm thick copper plate was inserted into the melt volume at a height of 333 mm to simulate a superimposed liquid metal layer.

However, the copper plate used does not reach the copper melting temperature during LIVE-L6, so that the melt introduced is separated convectively into an upper and lower region. Compared to the LIVE-L4 experiment, the initial temperature of the melt in LIVE-L6 was 2 K higher. The temporal course of the heating power supplied during the LIVE-L6 experiment was also modified compared to LIVE-L4. A slight deviation between the temperatures determined by versions ATHLET-CD 3.4 and 3.5 was observed at the simulated melting temperature. A deviation between the two code versions can also be seen for the inner and outer wall temperatures in a form, comparable to the melting temperature.

Configuration

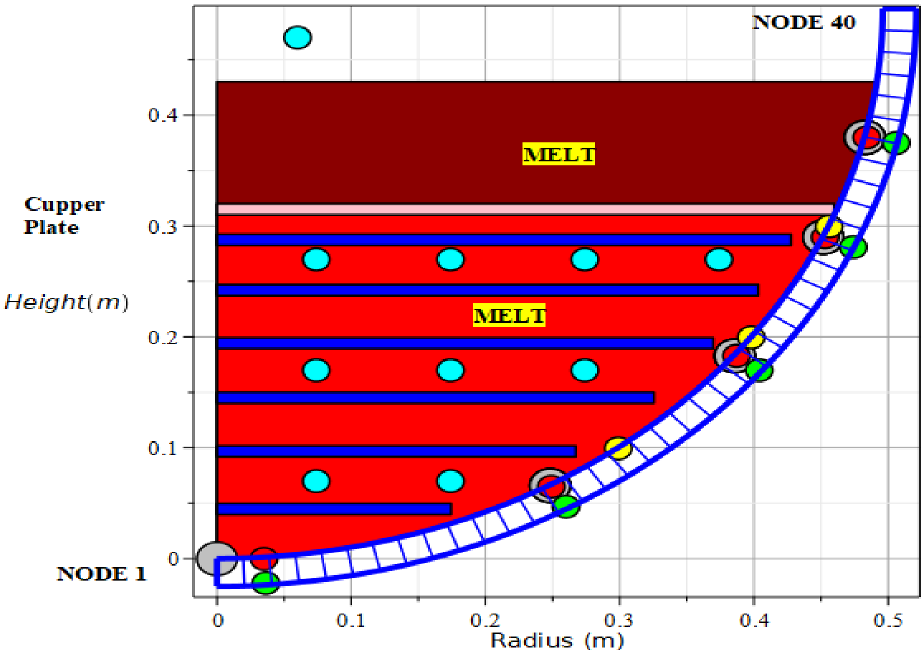

Fig. 5.126 LIVE-L6 experimental configuration

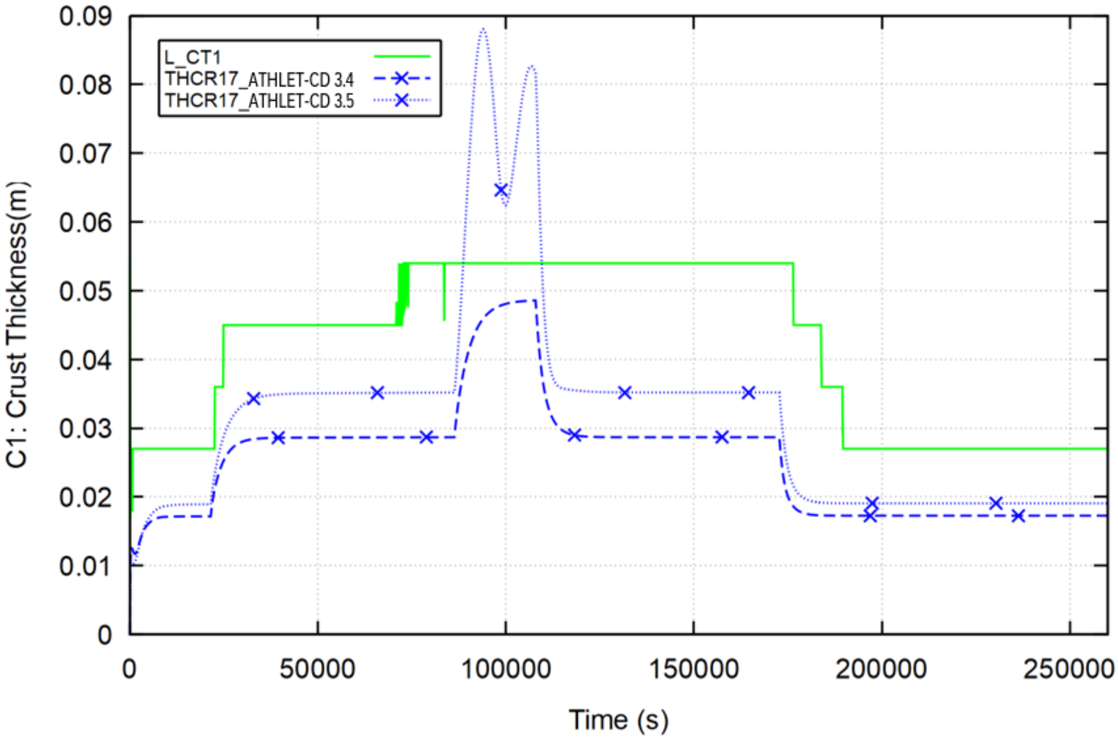

Fig. 5.127 Crust thickness at measuring point CT1

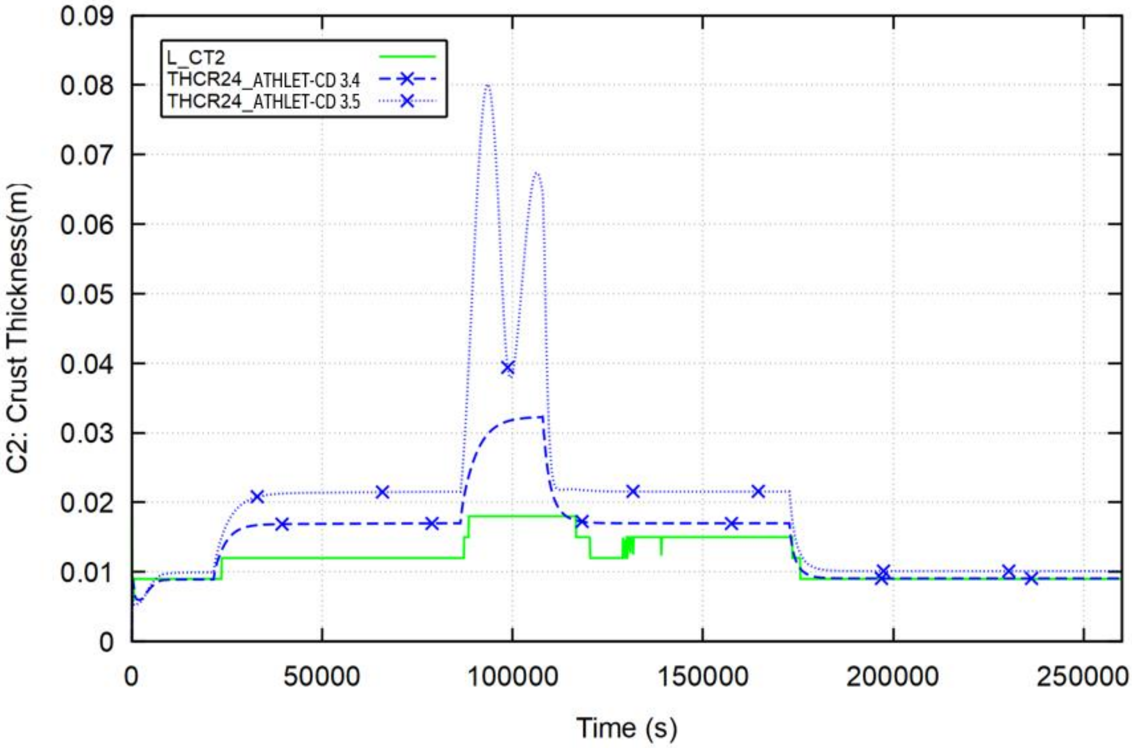

Fig. 5.128 Crust thickness at measuring point CT2

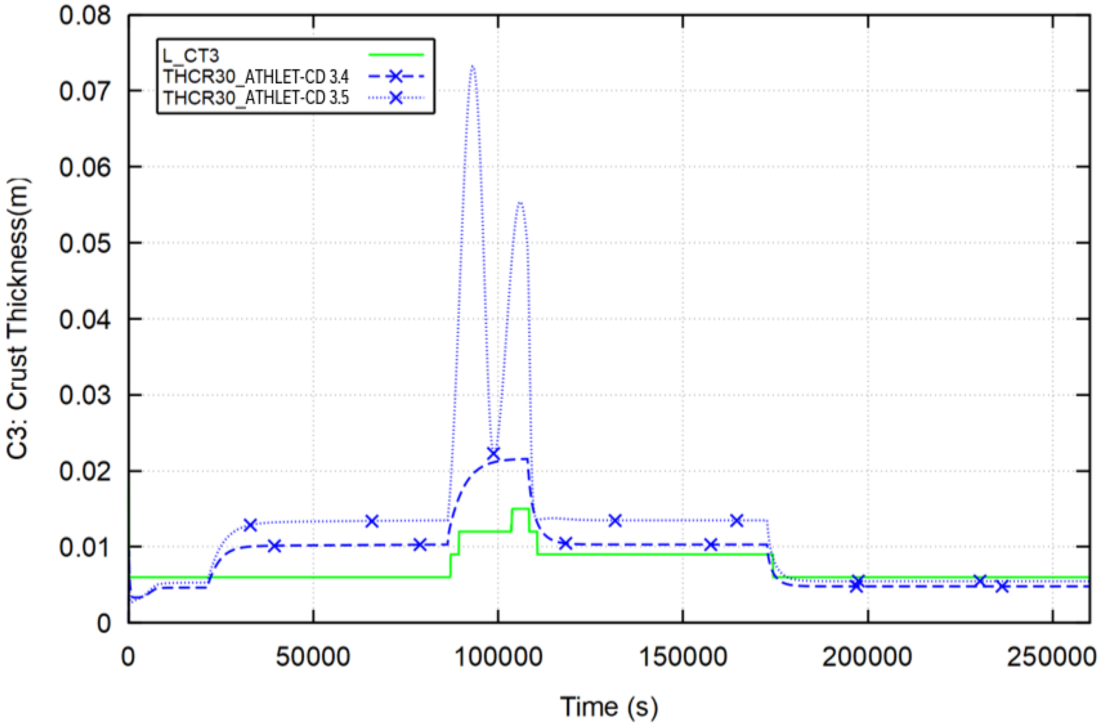

Fig. 5.129 Crust thickness at measuring point CT3

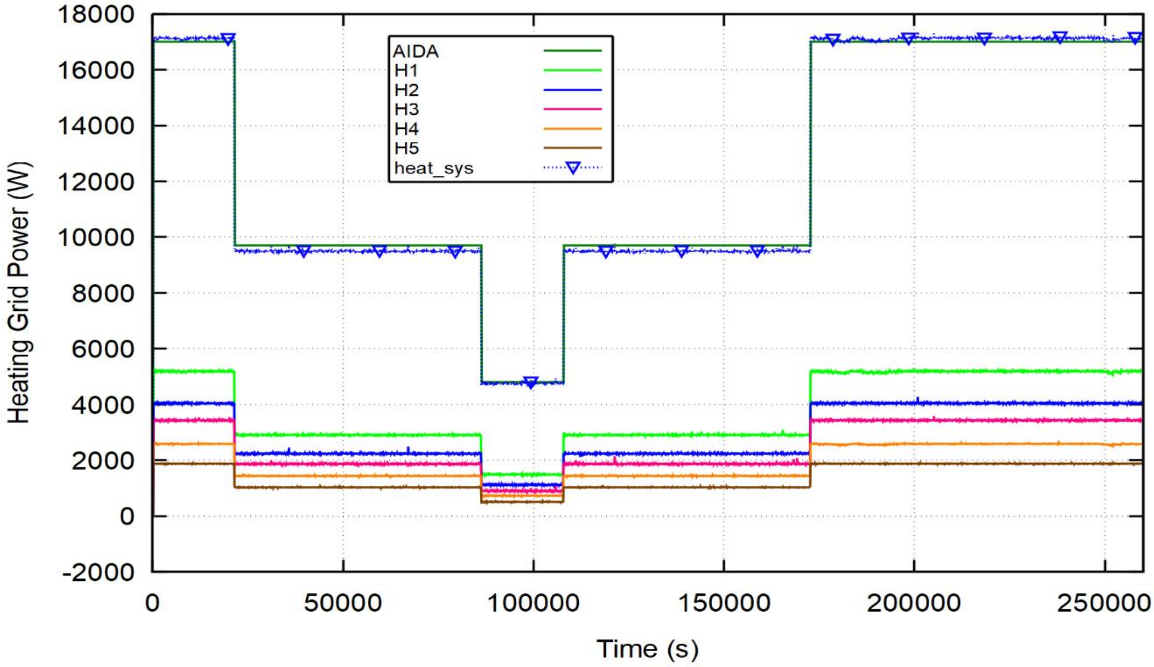

Fig. 5.130 Heating power supplied

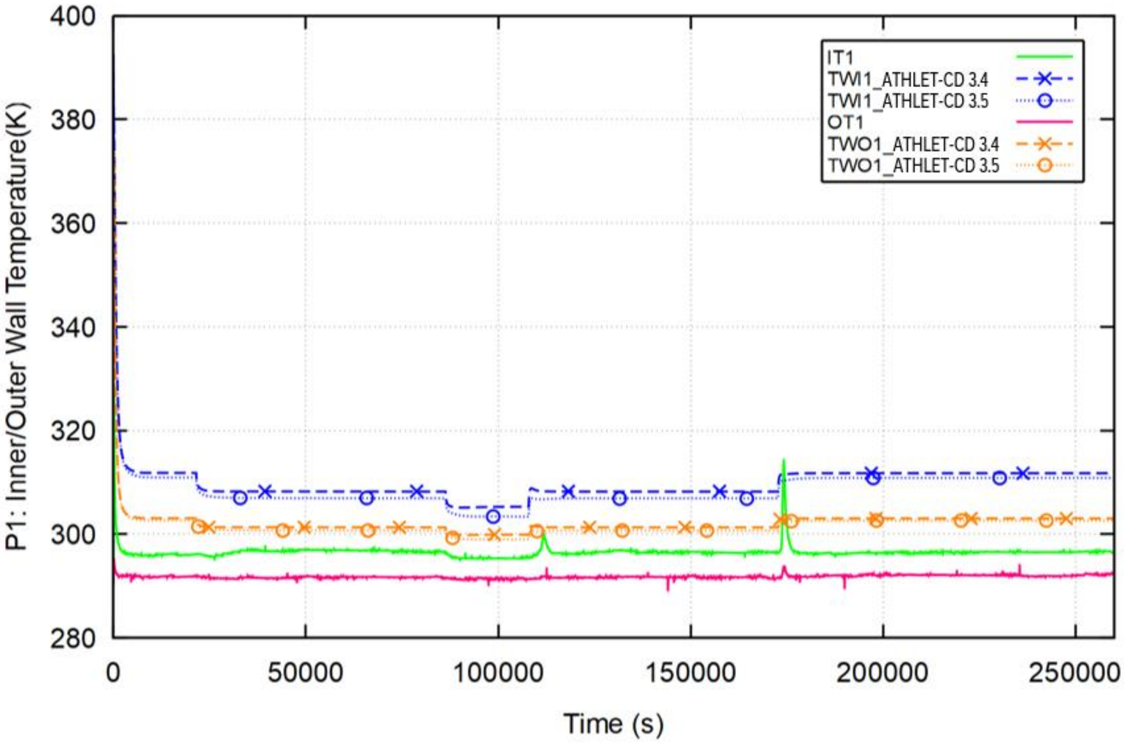

Fig. 5.131 Inner and outer wall temperature at measuring point IT1/OT1

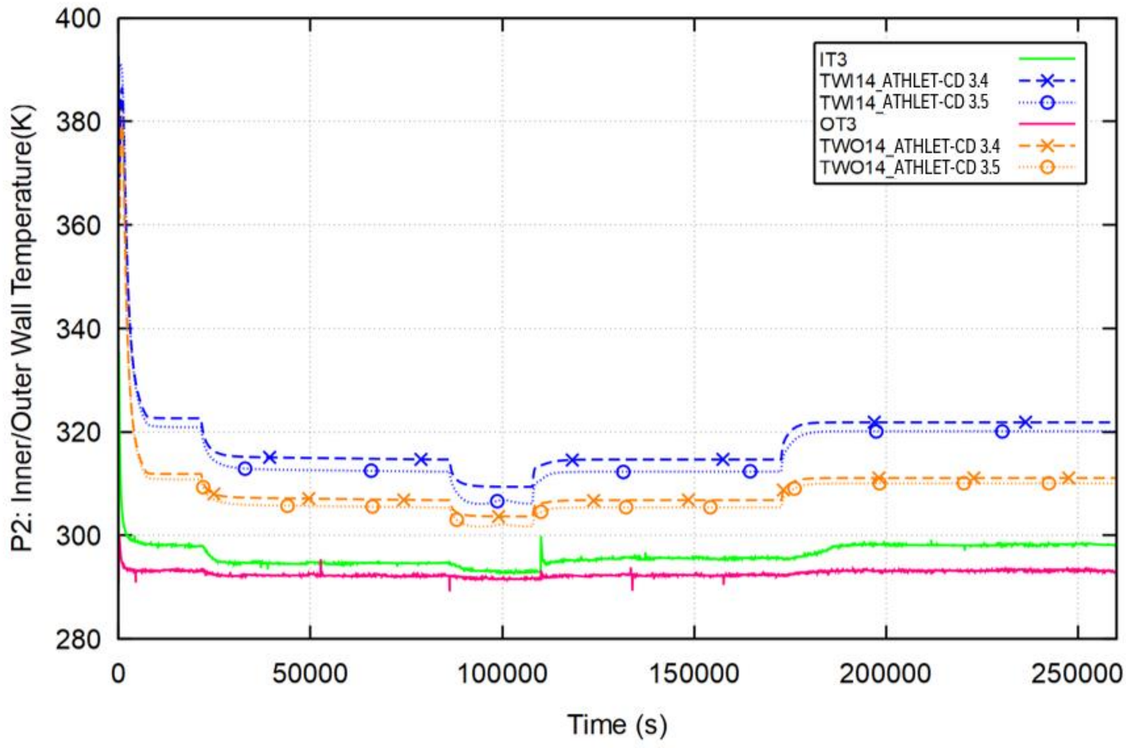

Fig. 5.132 Inner and outer wall temperature at measuring point IT3/OT3

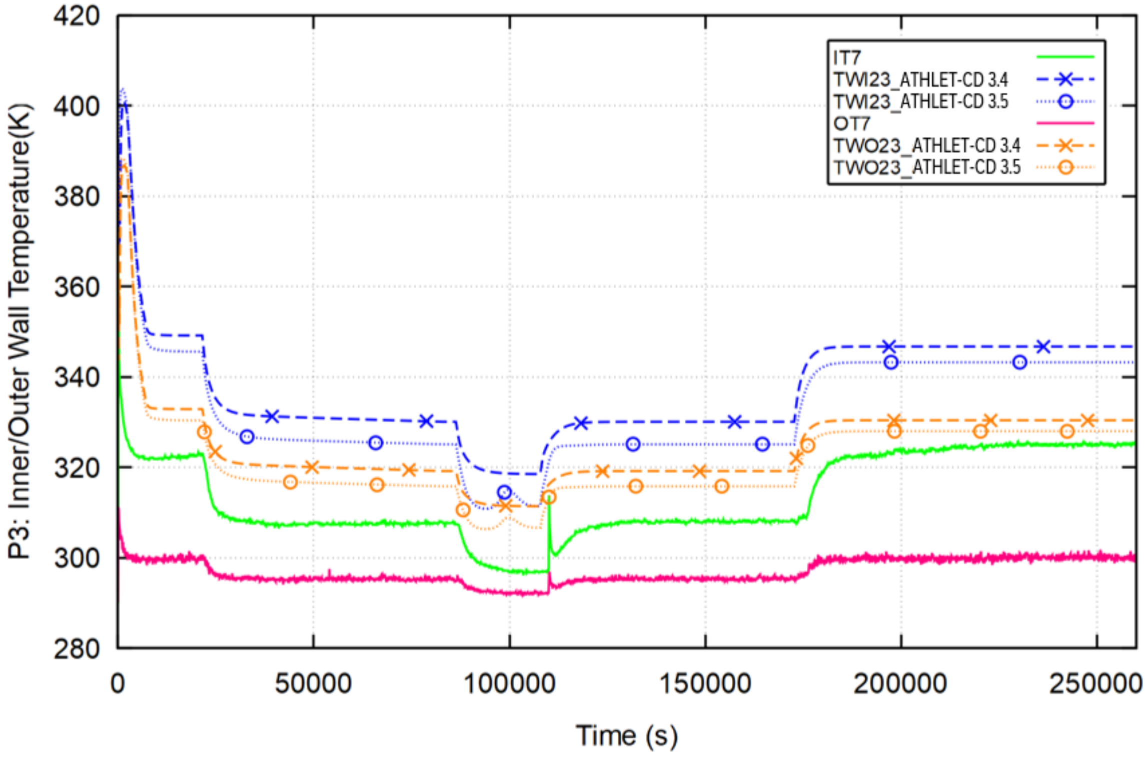

Fig. 5.133 Inner and outer wall temperature at measuring point IT7/OT7

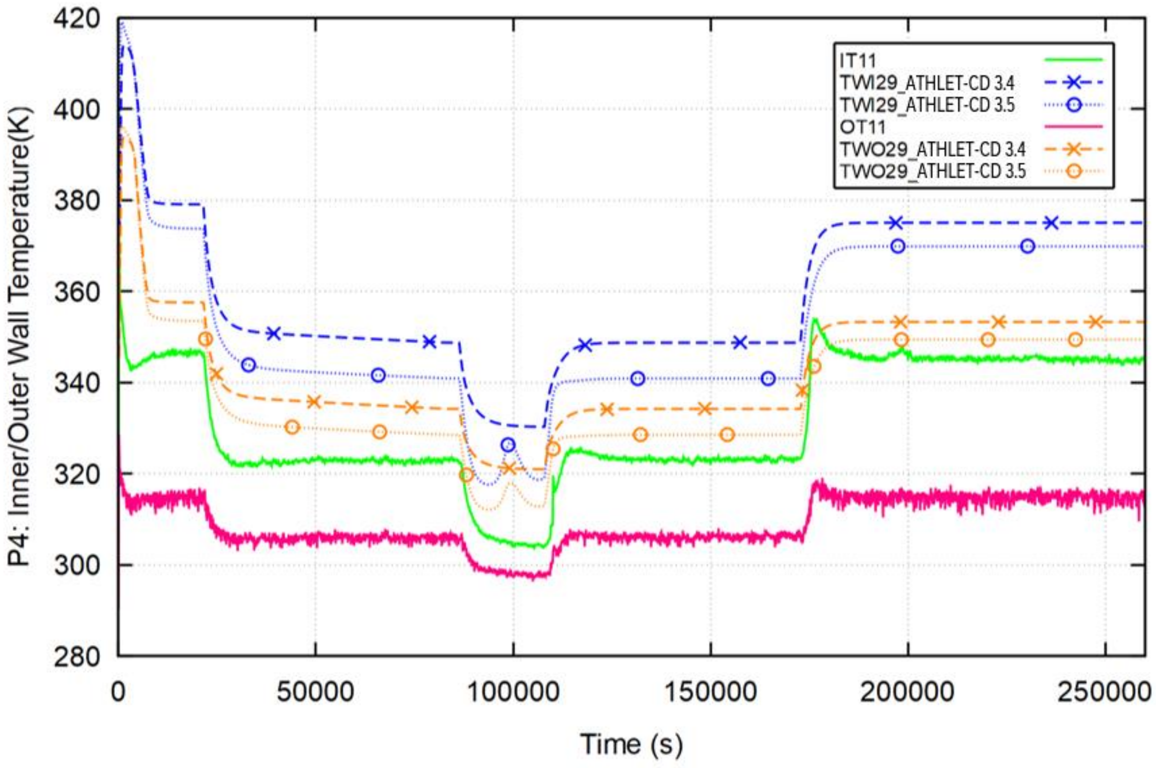

Fig. 5.134 Inner and outer wall temperature at measuring point IT11/OT11

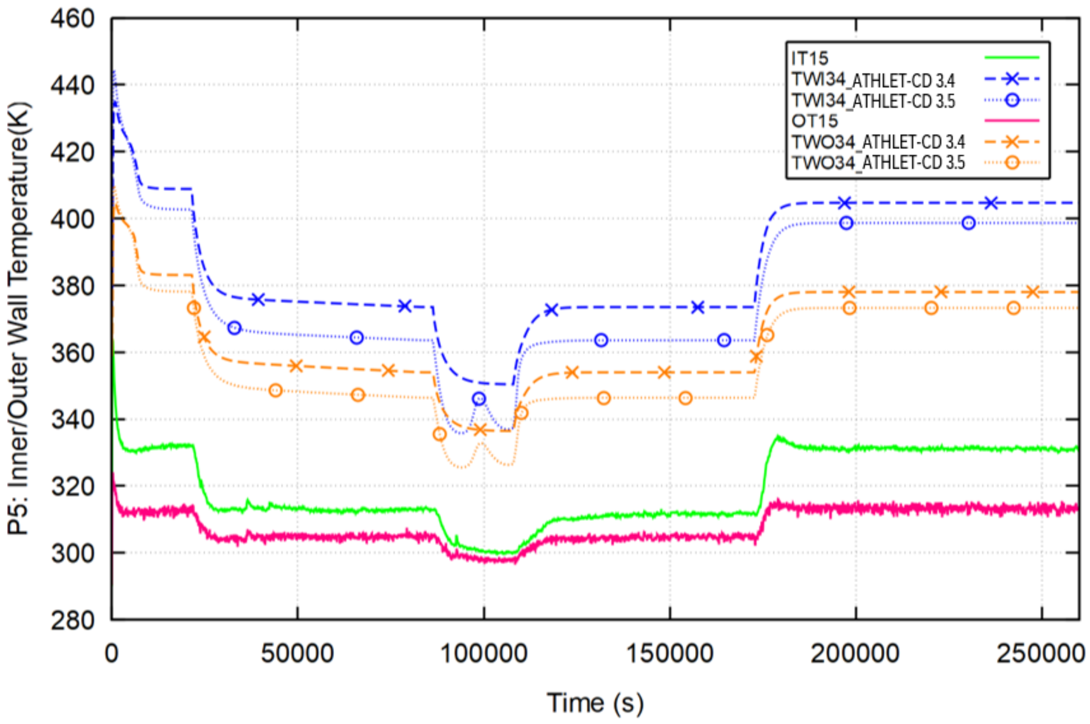

Fig. 5.135 Inner and outer wall temperature at measuring point IT15/OT15

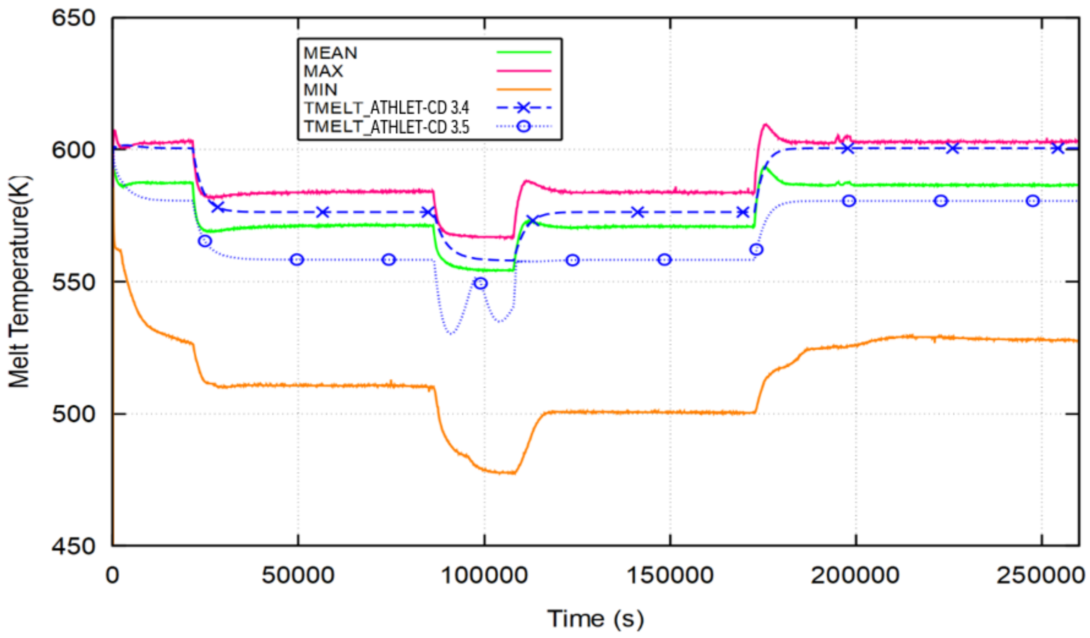

Fig. 5.136 Melting temperature

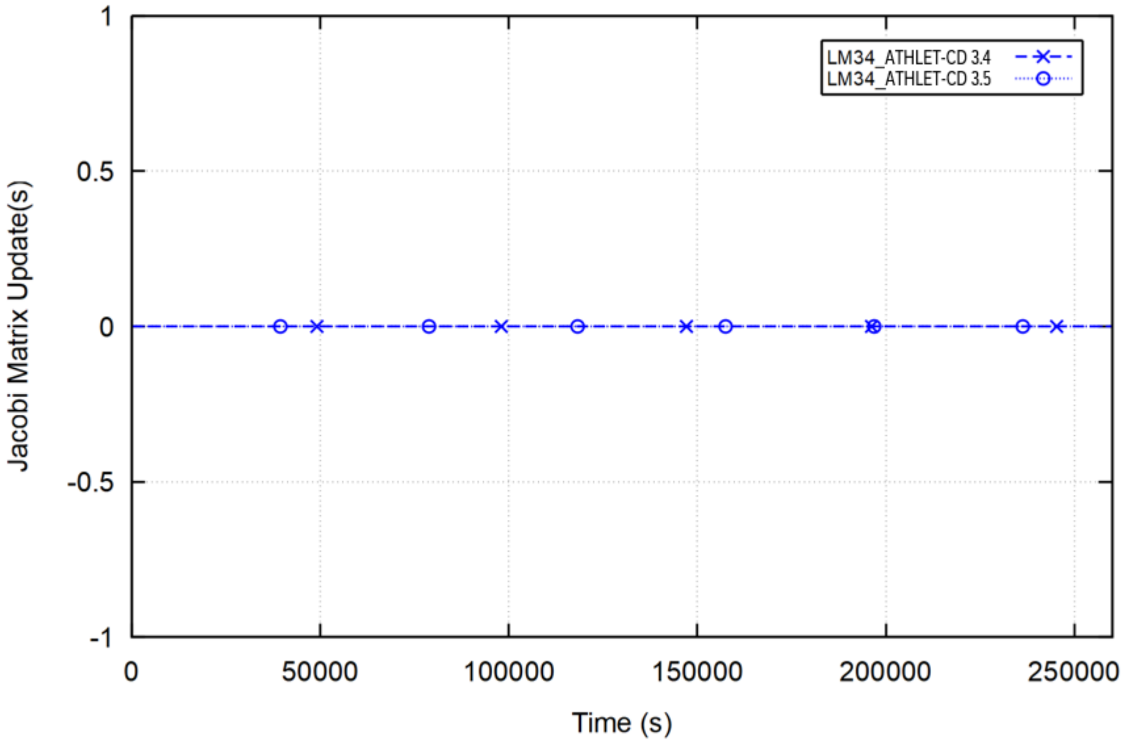

Fig. 5.137 Jacobian matrix update

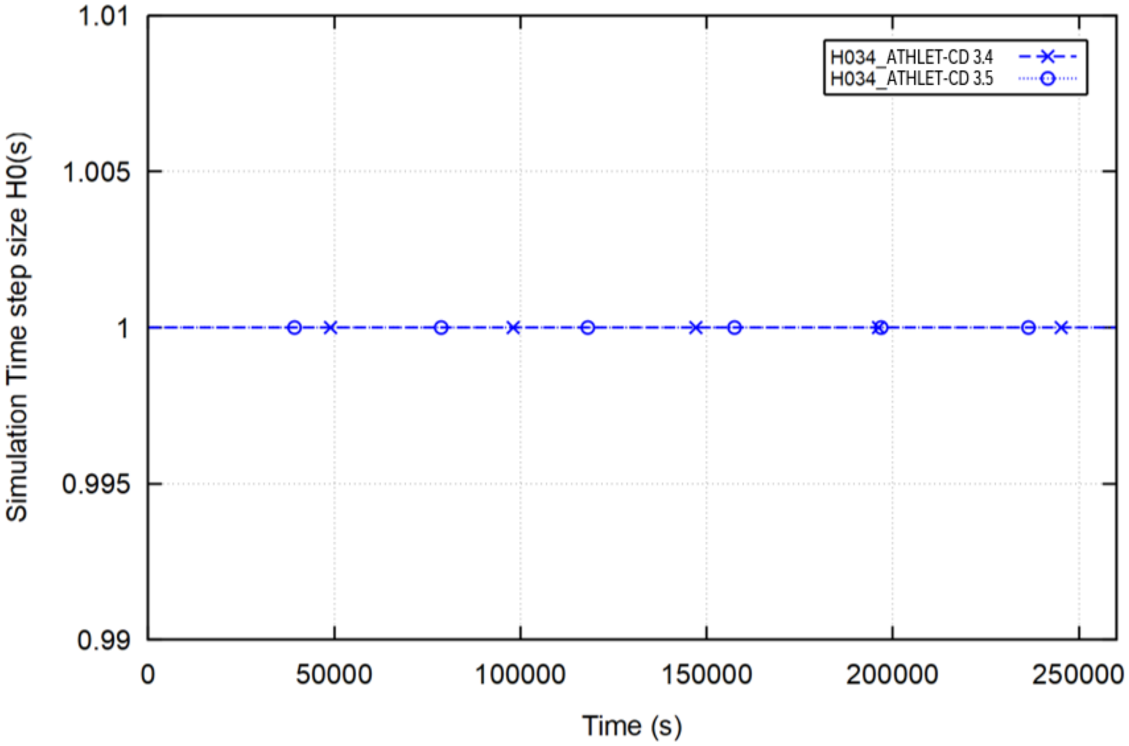

Fig. 5.138 Time step size

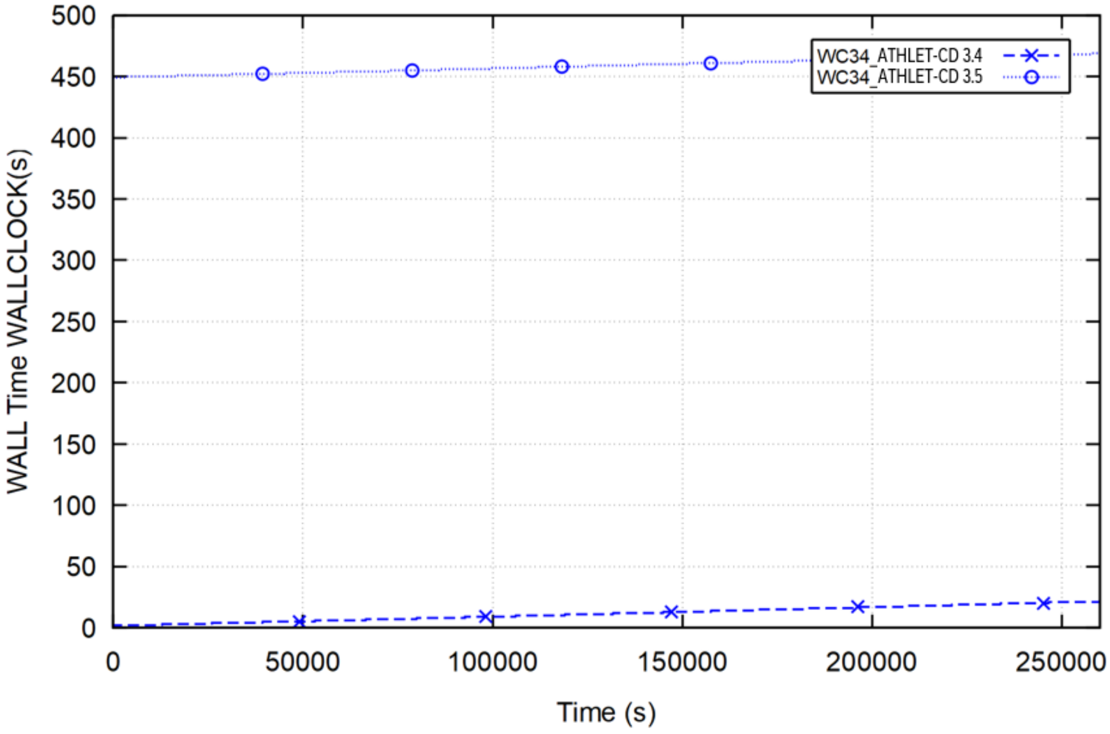

Fig. 5.139 WALLCLOCK

5.11 The TMI-2 Accident

5.11.1 Accident Progression

The analysis and evaluation of the accident at Three Mile Island Unit 2 (TMI-2) in 1979 /EPRI 80/, /TOL 88/, /WOL 94/ have been a challenge to all computer codes aiming to simulate severe accidents. It provides not only an opportunity to compare calculations with an event in a real power plant, but it also demonstrates the importance of reliable thermal-hydraulic models. The accident has been thoroughly analysed in the frame of international activities /TMI 92/, /WOL 94/ and served as a basis for a recent code benchmark activity organized by the Nuclear Energy Agency (NEA) of the OECD /NEA 15a/.

Since the beginning of the ATHLET-CD code development, calculations of the TMI-2 accident progression have been performed to validate the different code modules and their interactions as well as to evaluate the code capabilities and needs for improvements and further developments.

In terms of thermal-hydraulics, the TMI-2 accident was basically a small break loss of coolant accident (SBLOCA). The transient evolution up to the melt relocation into the lower plenum can be divided in three phases /BRO 89/:

- Phase 1 (loss of coolant): from 0 to 100 min
- Phase 2 (initial core damage): from 100 to 174 min
- Phase 3 (degraded core damage): from 174 to 224 min

The accident was initiated by loss of feedwater to the steam generators. The resulting increase of the pressure in the primary system caused the pilot-operated relief valve (PORV) on the pressurizer to open and the reactor to scram. As the primary pressure decreased, the PORV failed to close. Due to the high pressurizer liquid level, the reactor operators reduced the emergency core cooling injection. With the decreasing coolant inventory in the primary system, the void fraction increased sufficiently to cause strong vibrations due to cavitation in the reactor coolant pumps. At about 73 min after PORV opening, both pumps in the B-loop were switched off but the forced two-phase flow through the reactor core was enough to prevent core heat-up. At about 100 min, the A-loop pumps were also switched off, leading to a strong steam/water separation within the primary system, and the liquid from the top of the reactor vessel and from the hot legs settled down into the reactor vessel.

Afterwards, the liquid level in the reactor vessel decreased continuously. Core exposure began shortly after 110 min and the temperatures at the top of the core started to increase. Significant increase in the containment radiation levels at about 139 min indicated the occurrence of cladding failure and release of gaseous fission products. At about the same time, the operators manually closed the block valve upstream of the faulty PORV.

Despite the temporary termination of the coolant loss, core temperatures continued to increase. Between 150 min and 174 min, the primary pressure increased noticeably, indicating a strong oxidation of the Zircaloy cladding at temperatures above 1500 K, producing significant quantities of hydrogen and heating the core above the melt temperatures of control rods and fuel rod claddings. Further core degradation processes during this phase include the UO_2 dissolution by the molten Zr and the relocation of the molten material downwards to freeze and eventually block the coolant flow channels near the steam/coolant interface, estimated to be at 1 m above the bottom of the active core /BRO 89/. At the end of this phase, it is estimated that approximately 300 kg of hydrogen has been generated /KUA 89/.

With the activation of the coolant pump in loop 2B at 174 min, approximately 28 m^3 of water have been injected into the reactor vessel. Due to the strong oxidation of the metallic Zircaloy remaining in the upper half of the core, the primary pressure increased considerably. Fuel fragmentation and the formation of a debris bed is believed to have occurred during this period. Afterwards, core liquid level decreased again, and the core heat-up continued. It is estimated that about 150 kg hydrogen has been produced additionally during this phase.

At 200 min, the high-pressure injection (HPI) system was actuated, injecting emergency coolant for the next 17 min. At the end of this phase, a region of consolidated core materials has been formed at the bottom of the core, and the reactor vessel was nearly full of liquid. A considerable amount of water that filled the reactor vessel came from the drainage of the pressurizer coolant as the primary pressure decreased. The debris bed in the upper core regions is estimated to have been quenched, while melt material inside the consolidated core region continued to heat up.

The relocation of about 20 to 25 tons of molten corium into the lower plenum of the reactor pressure vessel occurred 224 min after reactor scram. One possible mechanism was the rupture of the crust encasing the molten pool in the consolidated core region due to the short primary side depressurization following the re-opening of the pressurizer block valve at 220 min /BRO 89/. Debris relocation was completed in approximately 2 min. The observed primary pressure increase between 224 min and 240 min indicates a significant heat transfer and steam generation within the lower head in this period. The restart of the HPI injection assured the coolability of the degraded core.

5.11.2 Input Dataset

The ATHLET-CD input dataset used for the validation of new code versions is strongly based on the dataset used for the benchmark exercise organized by the OECD/NEA /NEA 15a/, /NEA 15b/. The adopted nodalisation is shown in Fig. 5.141. It consists of the reactor pressure vessel (RPV), the two coolant loops A and B with the once-through steam generators, four cold legs with main coolant pumps, four high pressure injection lines connected to the cold legs and one let-down in loop A1, as well as the pressurizer with the surge line connected to the hot leg of loop A, heaters, spray line and the pilot operated relief valve (PORV).

The RPV comprises the downcomer, lower and upper plenum, upper head, the core region and the core bypass. The vent valves between downcomer and upper plenum are modelled as check valves.

The core region of the input data set used in the previous validation calculations was changed:

The core is modelled by five concentric rings with 22 axial nodes (20 within the active core region) and with cross flow connections to allow flow deflection due to fuel rod deformation and blockage formation caused by refreezing of molten materials. The four inner core rings include fuel and AIC control rods. The fifth channel contains no rods and is defined to avoid a complete core flow blockage in case of strong melt relocation and represents the area between the core barrel and the outermost fuel assemblies. The core rings no longer consist of an equal number of fuel assemblies per ring. This way, the rings contain more fuel assemblies with similar decay powers, therefore the averaging effect of the ring nodalization is smaller. The created new core nodalization is visible in Fig. 5.140.

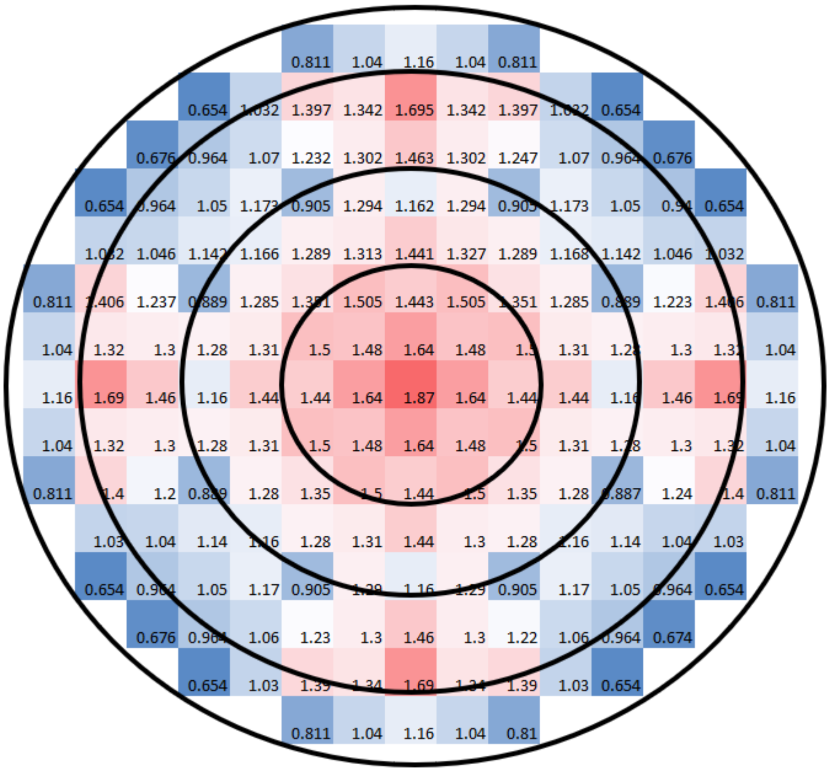

Fig. 5.140 Core nodalization of TMI based on power peaking factors at the hottest elevation.

With this, the rings contain the following number of fuel assemblies:

- Ring1: 21
- Ring2: 44
- Ring3: 68
- Ring4: 44

Some core melt parameters were also changed. The used parameters are listed in Tab.. Also, the model “QUENCHCORE” that is based on the quenching model of ATHLET was removed from the input deck. With the improvement of ATHLET heat transfer models, the QUENCHCORE model was no longer needed to simulate the quenching processes adequately, and also, because some flaws in the QUENCHCORE model were found that lead to inaccurate results, if the core is quenched more than once.

The simplified model of the secondary system consists of two components (loop A and B) simulating the riser with 16 axial volumes and the steam dome of the steam generators, as well as the boundary conditions for feedwater injection and steam outlet flow, simulated by fill components. In total, the nodalisation comprises 62 TFOs and 35 HCOs, with 282 control volumes and 403 flow paths, as well as 154 heat slabs (not including fuel and control rod components) for the modelling of the RPV and pipe walls. The geometrical data, material properties, axial and radial core power distribution and boundary conditions (secondary pressure, auxiliary feedwater flow rates, make-up and letdown flow rates) are based on contents of TMI-2 reports /GOL 86/, /MCC 87/.

For this calculation the ATHLET-CD modules ATHLET (thermal-hydraulics), ECORE (core degradation), OREST/FIPISO (nuclide properties and decay heat calculation) and FIPREM (release of fission products and structure materials) have been applied. Melt behaviour in the lower plenum after relocation at 224 min can be simulated either with the AIDA or with the LHEAD module.

The system thermal-hydraulics is simulated with the six-equation model in ATHLET (fully separated balance equations for liquid and vapor), complemented by an additional mass conservation equation for hydrogen as a non-condensable gas, except for the pressurizer and for the steam generator secondary side, where the five-equation approach (one mixture momentum equation) together with the mixture level tracking model was used.

The dedicated T-Junction model has been applied to the connection between surge line and pressurizer as well as between pressurizer and PORV line. The quench front model, which considers both top and bottom reflooding, has been applied for all rod components. Break mass flow rates are calculated with the CDR1D discharge model.

The main input data relevant for core degradation are summarized in Tab.. Fuel rod relocation is simulated in rod-like geometry (candling model) assuming a constant relocation velocity of 3.1 cm/s for metallic and melt ceramic melt. Radial melt spreading outside a core ring is not taken into account. The start of melt relocation into the lower plenum is defined as a GCSM time switch.

Changes since version 3.4:

- Drift model at the top and bottom of the fuel assemblies was changed to 2 instead 1, which is dedicated to be used in vertical bundles.

Tab. 5.9 ATHLET-CD code parameters relevant to core degradation

Parameter	Input	Unit	Value
Start of fuel dissolution by Zirconium	TAM	K	2250
Clad failure temperature (δ_{ox} < 0.3 mm)	TALLOW	K	2300
Clad failure temperature (δ_{ox} > 0.3 mm)	TALHIG	K	2500
Start of ceramic fuel and Zirconia melting	TCOMPM	K	2500
Melt temperature of absorber material	CRTAM	K	1073
Correlation for cladding oxidation	IOXM	-	2
Candling velocity for metallic melt	WSL	m/s	0.031
Candling velocity for ceramic melt	WSLUO	m/s	0. 031
Ratio wetted perimeter / clad perimeter	BUSL, BUSLUO, CRBUSL	-	0.05

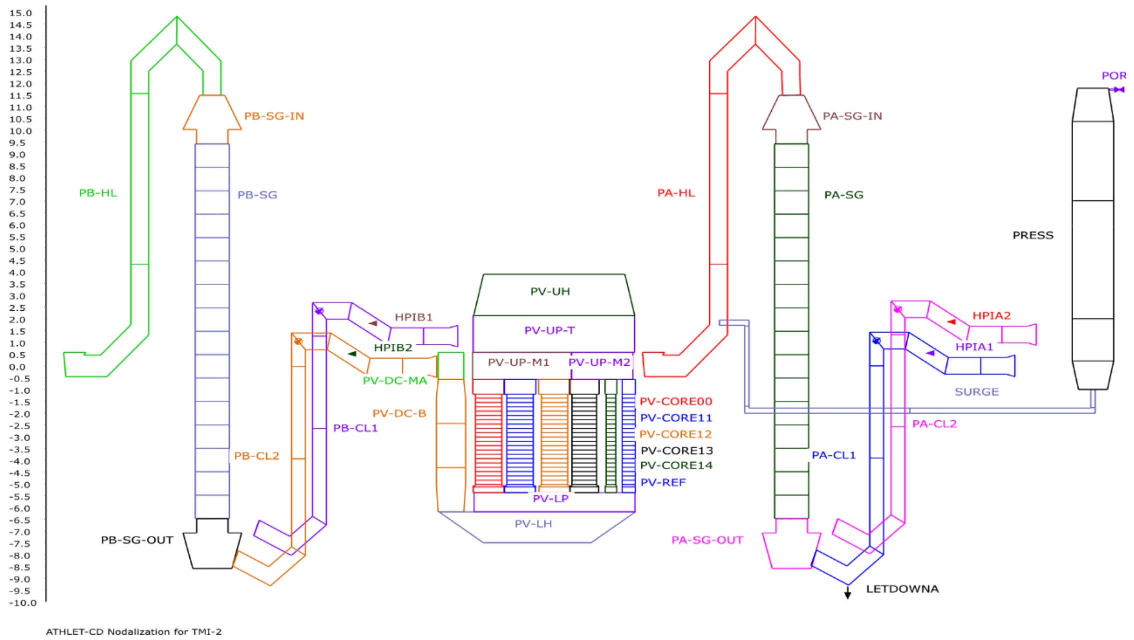

Fig. 5.141 ATHLET-CD nodalisation scheme for TMI-2 (primary circuit)

5.11.3 Main Results

The aim of this calculation is mainly to assess the core degradation models of different ATHLET-CD versions as well as the quenching during the pump B restart (174 min). Therefore, special attention has been given to the time from 100 to 224 min, i.e. the accident phases 2 and 3 up to the time of core slumping into the lower plenum. Phase 1 is a conventional small break transient. The objective of its simulation is to provide as far as possible a correct prediction of the water and energy distribution in the system at time 100 min, when the coolant pumps in loop A have been stopped. For comparison, results of ATHLET-CD 3.4.3 are also shown besides the results of ATHLET-CD 3.5.

Fig. 5.142 compares the calculated and the measured primary pressures. All curves agree well up to around 150 minutes. After the closing of the PORV block valve at 139 min (Fig. 5.143), the primary pressure increases again. The gradient of pressurization becomes even steeper with the start of oxidation excursion at about 155 min. Small differences occur between 150 minutes and 174 minutes, when the pump B2 transient starts. Pressure rises qualitatively similarly to the measured pressure with ATHLET-CD 3.5, however, the pressure increase starts a bit later than during the TMI-2 accident. In all the ATHLET-CD simulations the pump transient is followed by a pressure peak, overshooting the measured values. Shortly after the peak the pressure falls close to the real values. ATHLET-CD 3.5 underpredicts the pressure after the fall, but increases gradually to real values, while ATHLET-CD 3.4.3 reaches the real values directly after the peak, but gradually increases the pressure thus overpredicting the pressure at around 190 min.

After 190 min, the primary pressure decreases due to the twice short openings of the relief block valve (Fig. 5.143) and due to the steam condensation by the HP injection (60 kg/s) into the cold legs. The pressure evolution follows the real pressure evolution up until the melt relocation to the lower plenum. With the melt relocation into the lower plenum and the resulting steam generation, the primary pressure increases to a similar pressure, however, with a little delay and slightly differently in the different versions. The evolution of pressure after melt relocation to lower plenum is different to the measured values. This difference is most likely caused by the absence of fragmentation and debris bed modelling in ATHLET-CD.

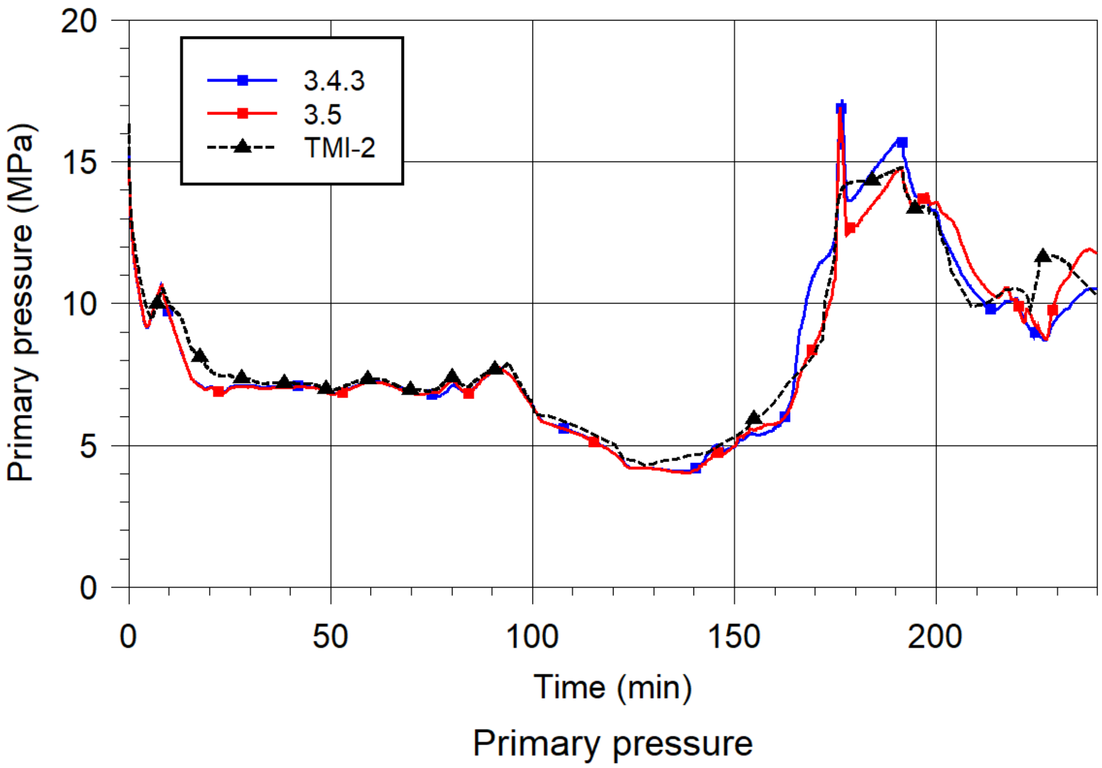

Fig. 5.142 Primary pressure calculated with ATHLET-CD 3.5.0 and 3.4.3 compared to measured data

Fig. 5.143 shows the calculated PORV outlet mass flow rates in comparison with best-estimate values presented in /NOM 87/. A good prediction of the coolant inventory in primary system is essential to reproduce adequately the sequence of events during the core degradation phase. As recommended in the ATHLET user's manual, the connection between PORV line and pressurizer is defined as a horizontal junction. The application of the T-Junction model to this junction does not affect considerably the calculated amount of entrained liquid towards the PORV. At around 195 min a large flow rate through the PORV outlet can be seen in the simulations, similarly to the measured values. The mass flow rate overestimation at around 230 min is smaller with ATHLET 3.5 is mostly originating from the larger pressure build up after melt relocation to the lower plenum.

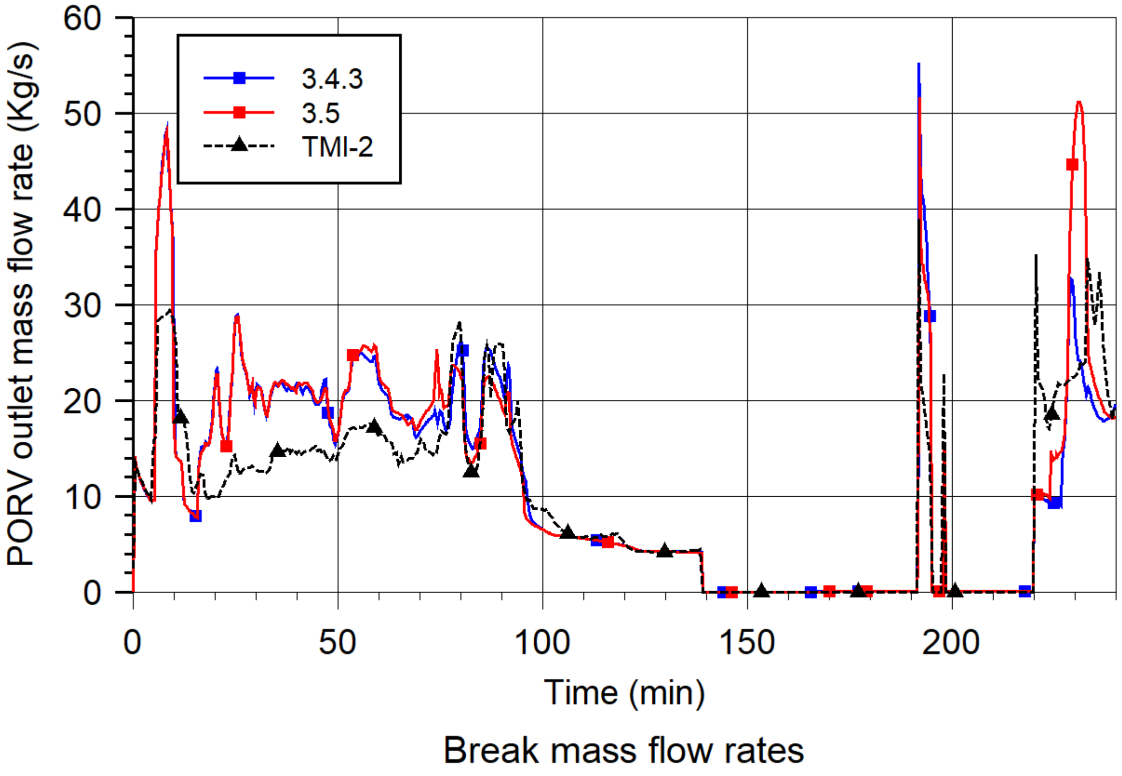

Fig. 5.143 Break mass flow rates calculated with ATHLET-CD 3.5.0 and 3.4.3 compared to measured/estimated data

In Fig. 5.144 the calculated mixture and collapsed levels in the pressurizer are compared with the signal of the level measurement. This signal is however affected with large uncertainties due to the operation beyond design limits. The calculated mixture and collapsed levels are equal as long as the pressurizer block valve is closed. The results indicate that the pressurizer behaviour and the sealing effect of the surge line are satisfactorily reproduced. The contribution of the pressurizer coolant to the core reflooding after 200 min was also captured by the code, however, with a bit of overestimation.

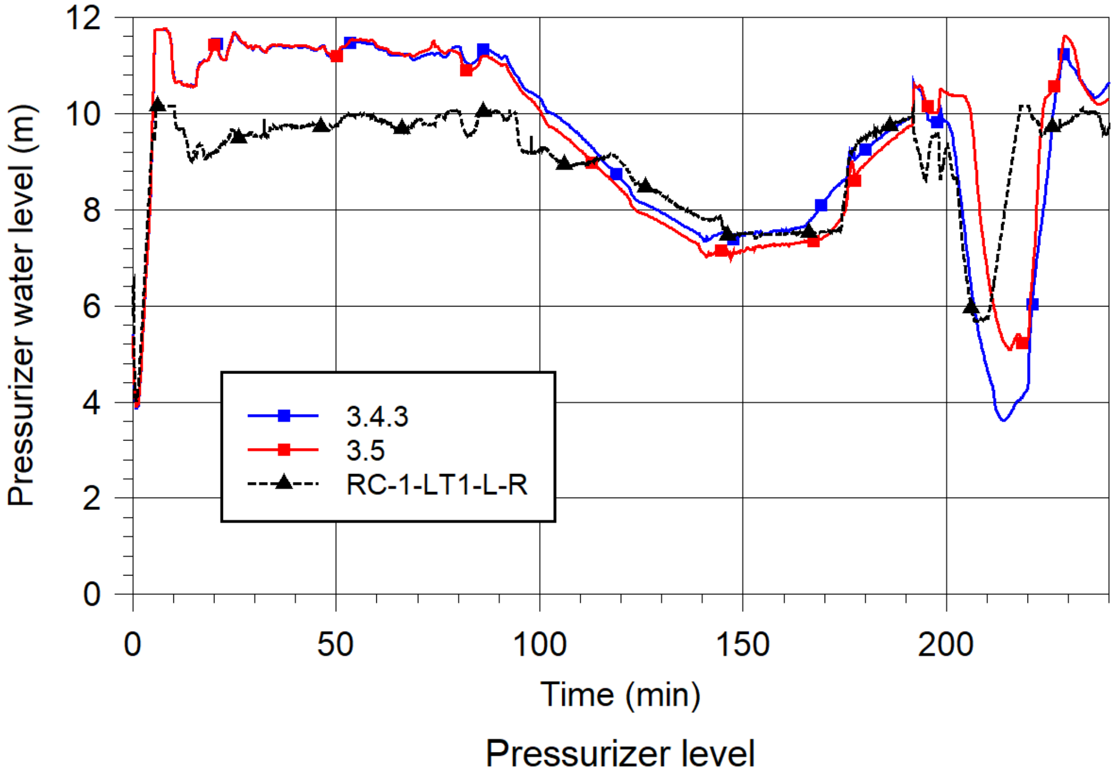

Fig. 5.144 Pressurizer level calculated with ATHLET-CD 3.5.0 and 3.4.3 compared to measured/estimated data

The collapsed levels in the core channels and reflector bypass are depicted in Fig. 5.145 to Fig. 5.146. After the pump stop at 100 min, the two-phase mixture collapses and the coolant is accumulated in the lower plenum and in the lower core region. Continuous loss of coolant results in a slow level decrease up to 170 min. The pump restart at 174 min leads to a sharp level rise, more pronounced in the outer rings than in the inner rings. Afterwards, the core dries out again. At time 200 min core reflooding starts due to the high-pressure injection. As measured data values are missing, here only the comparison of the simulations with different ATHLET-CD versions is shown.

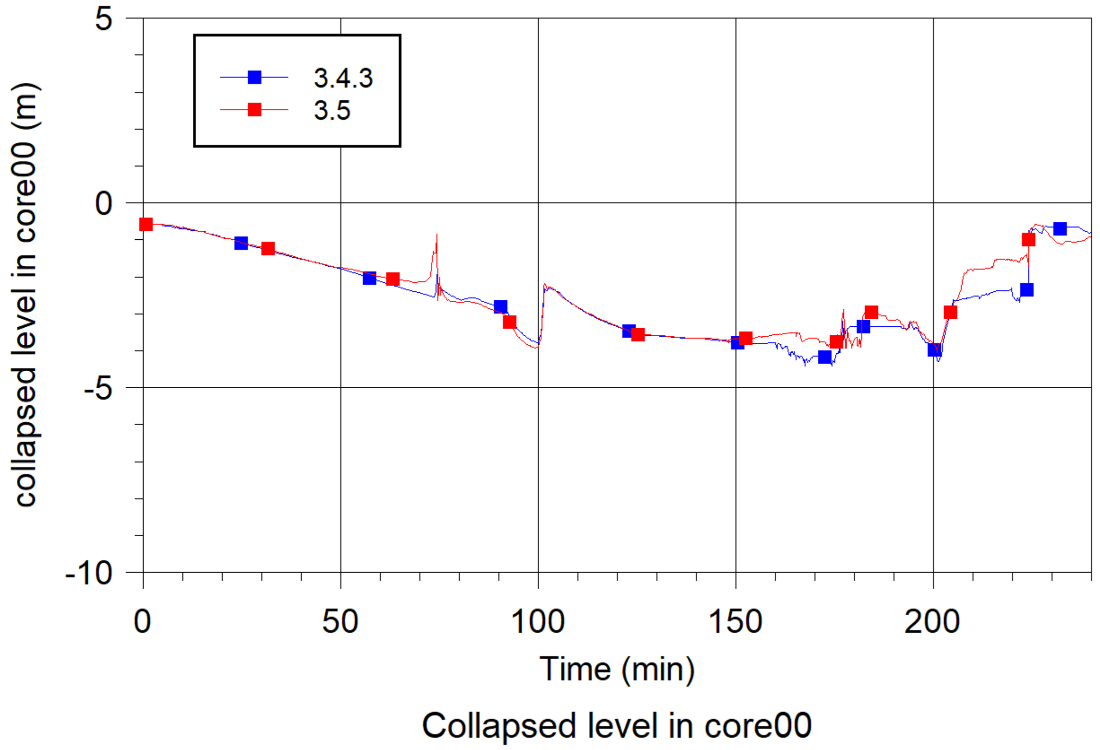

Fig. 5.145 Core collapsed levels calculated with ATHLET-CD versions 3.5.0 and 3.4.3

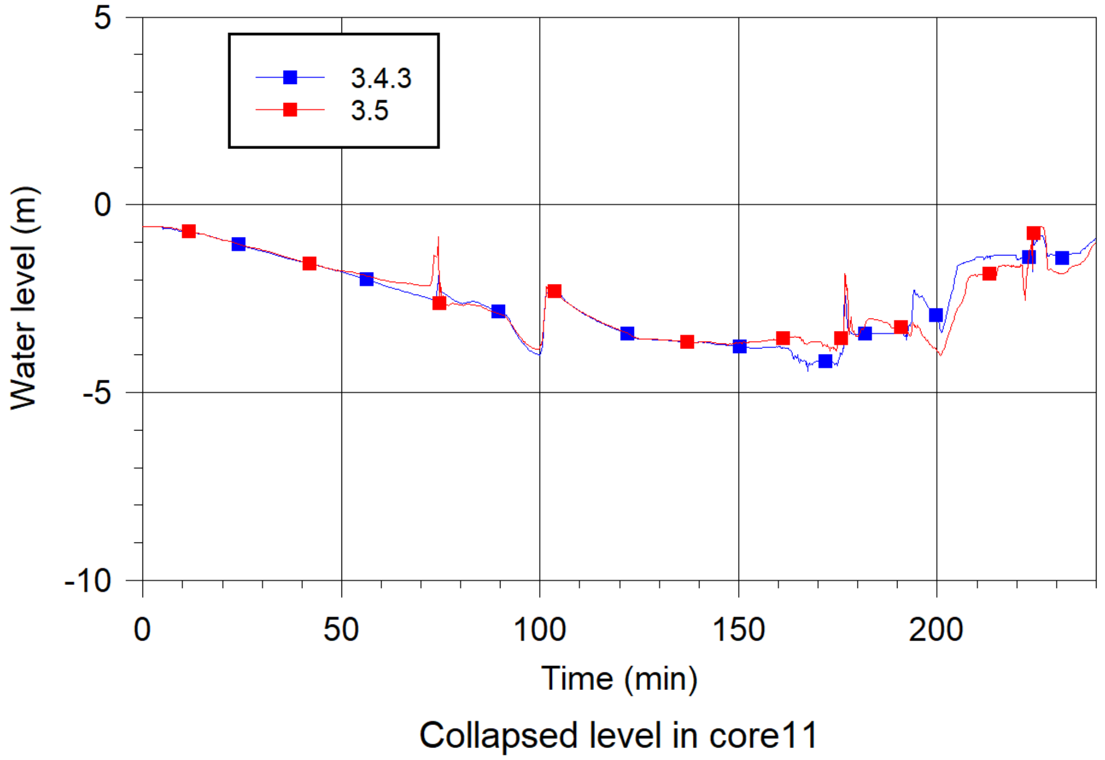

Fig. 5.146 Core collapsed levels calculated with ATHLET-CD versions 3.5.0 and 3.4.3

The hydrogen generation is shown in Fig. 5.147. The beginning of the oxidation at about 135 min agrees well with the pressure stabilization at this time, short before the pressurizer valve has been closed (139 min). The calculated start of oxidation excursion, at about 155 min, is slightly later than the estimated time point given in /TOL 88/. From the plant data a total mass of about 300 kg has been estimated before the quench phase, and 400 to 500 kg after it /KUA 89/. The calculations predict 280 kg before pump transient and around 310 kg at the end of phase 3. The calculated amount of hydrogen production during the quench seems to be underestimated, also according to experimental findings like in the QUENCH tests. During the first opening of the pressurizer block valve at time 192 min, about 30 kg of hydrogen are released to the containment. Hydrogen generation during the relocation of melt into the lower plenum is not taken into account due to lack of available models in ATHLET-CD. The absence of the oxidation of the unoxidized material during relocation of melt to the lower plenum can explain the 100-200 kg less produced H_2 mass compared to the estimated real values.

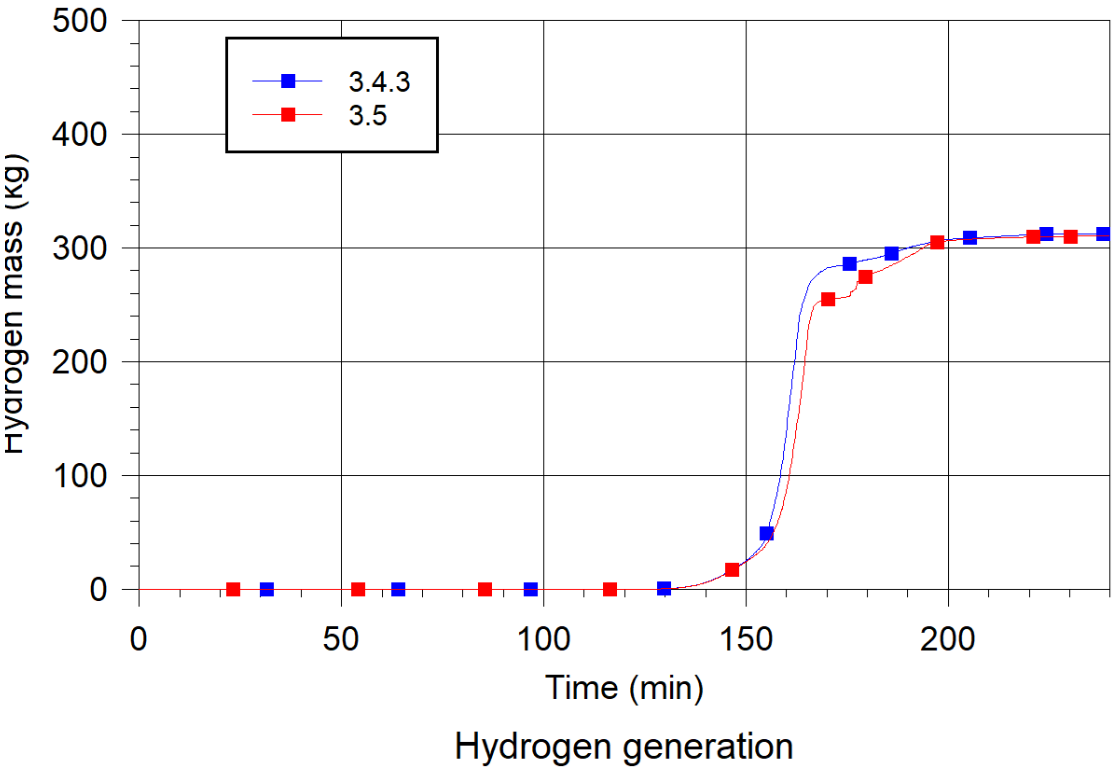

Fig. 5.147 Hydrogen generation calculated with ATHLET-CD 3.5.0 and 3.4.3

Fig. 5.148 to Fig. 5.151 depict the fuel rod temperatures in the innermost core ring (ROD1) at different elevations. After trip of the pumps in loop A and inception of core dry-out at approximately 105 min, the core temperatures above the water surface steady increase continuously. In the upper core regions, temperature escalation due to oxidation starts shortly before 155 min, until the failure criteria are reached, leading to melt formation and relocation. During the first quenching phase (pump restart) the upper core regions are refilled with water. Due to melt relocation and flow channel blockage, temperatures in the lower, central core region increase. The molten material is cooled mainly from the top. Quenching of this region is enhanced after the start of the high-pressure injection at 200 min. Here again, no measured data is available, therefore only comparison of the simulation results of different ATHLET-CD versions are shown. Larger differences can be seen between the versions, however, because the integral values are similar in all the calculations it only shows that the performed bugfixes and smaller developments can have a larger impact on local parameters.

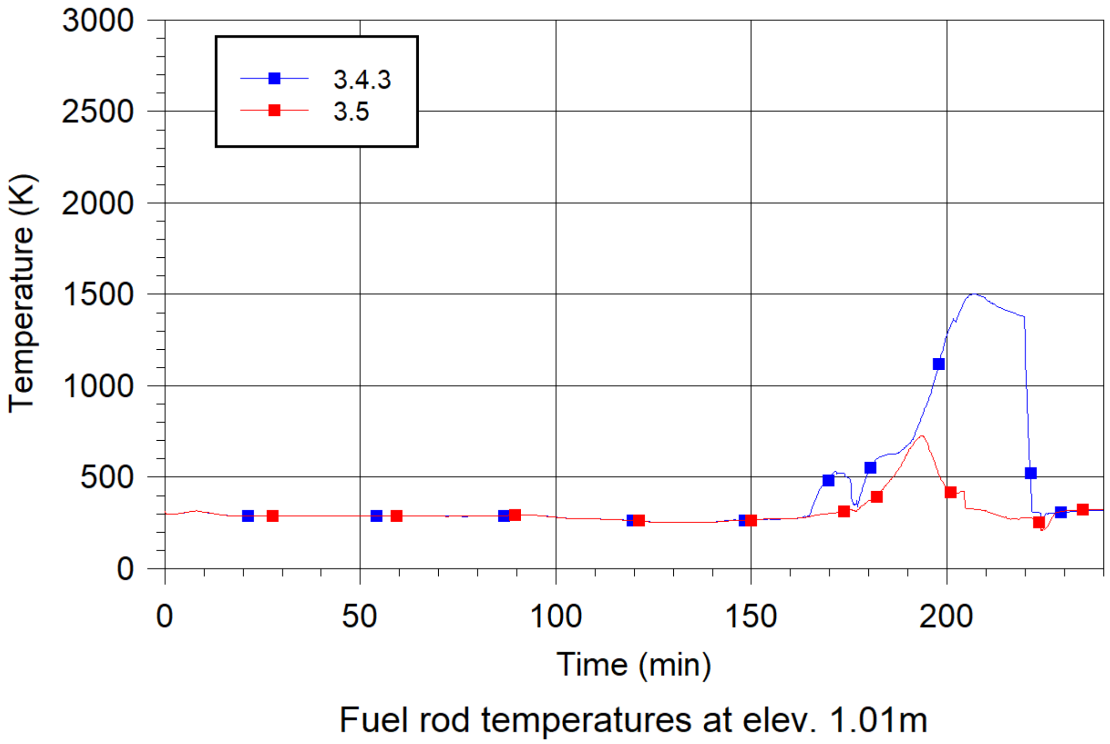

Fig. 5.148 Fuel rod temperatures – innermost ring (ROD1) calculated with ATHLET-CD versions 3.5 and 3.4.3

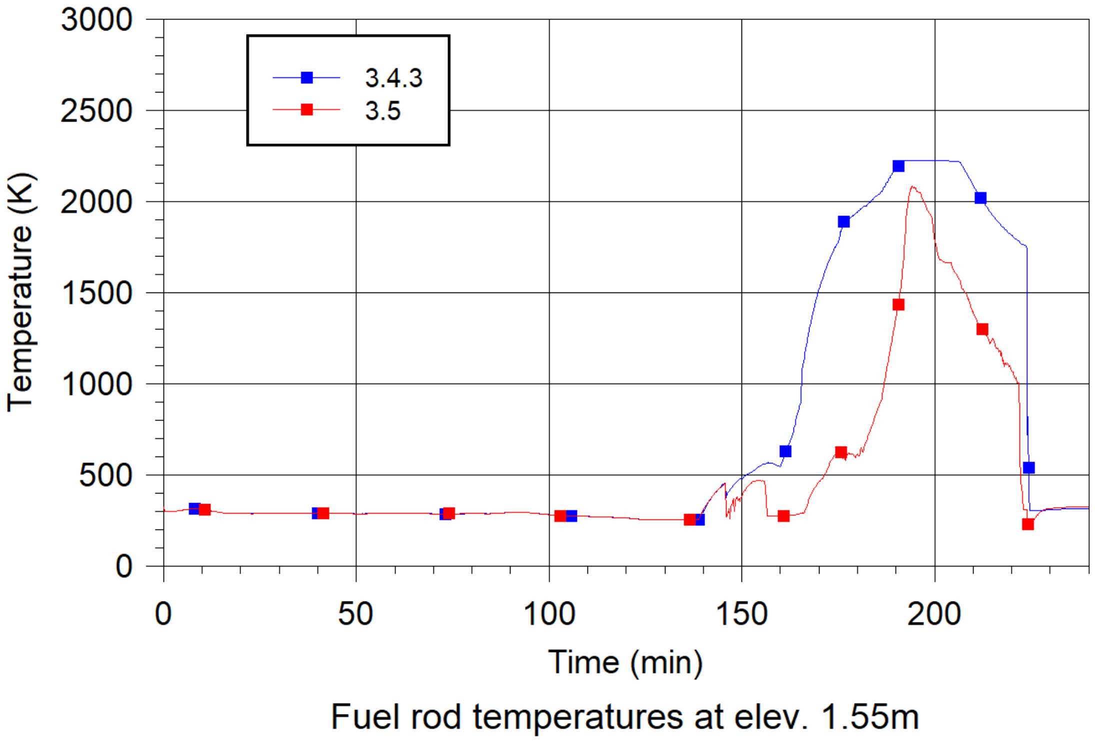

Fig. 5.149 Fuel rod temperatures – innermost ring (ROD1) calculated with ATHLET-CD versions 3.5 and 3.4.3

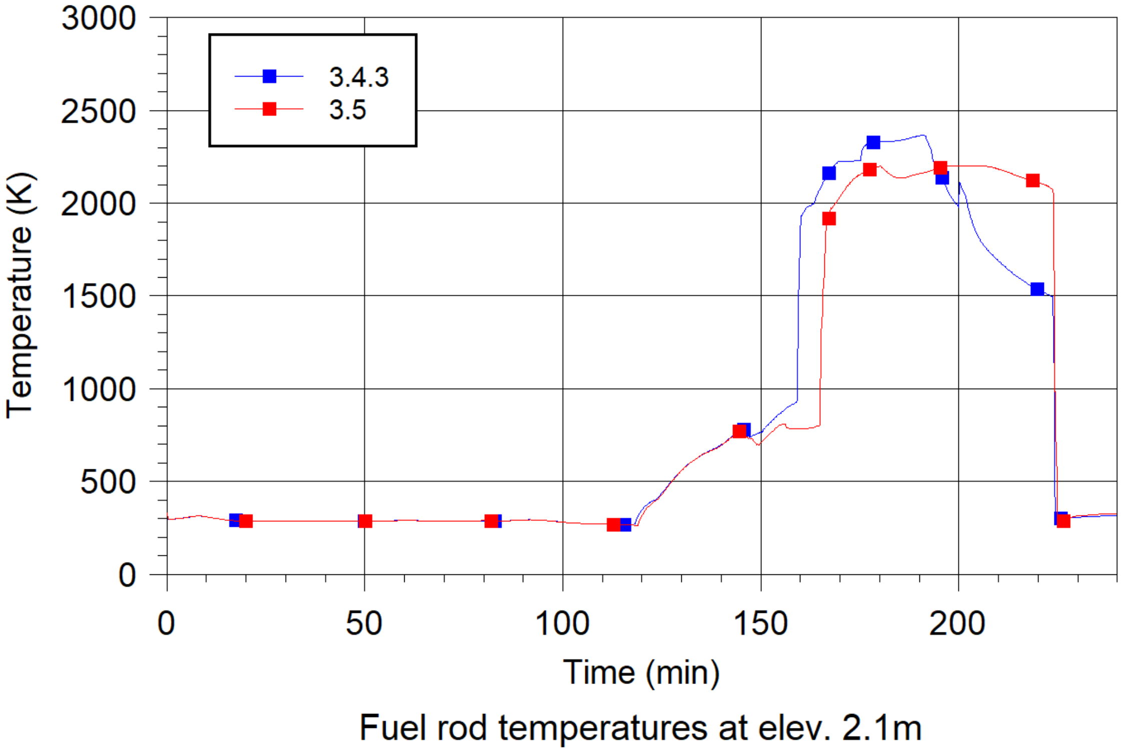

Fig. 5.150 Fuel rod temperatures – innermost ring (ROD1) calculated with ATHLET-CD versions 3.5 and 3.4.3

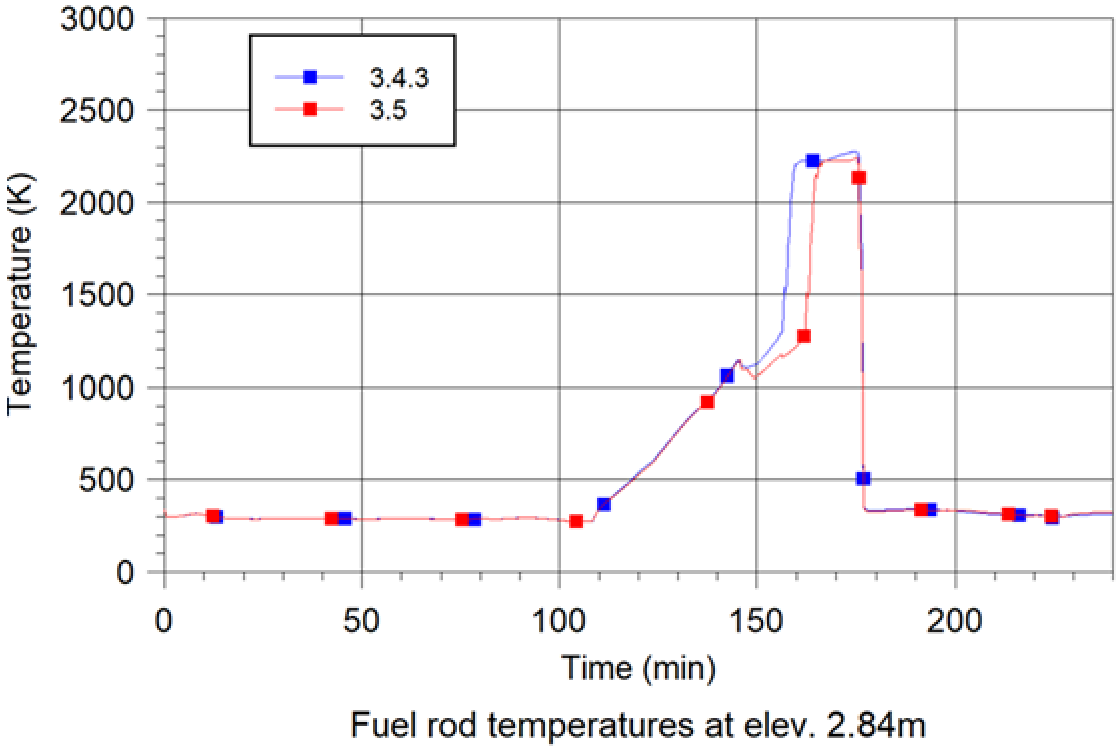

Fig. 5.151 Fuel rod temperatures – innermost ring (ROD1) calculated with ATHLET-CD versions 3.5 and 3.4.3

The melt and crust masses are shown in Fig. 5.152 to Fig. 5.155. The metallic melt consists of molten cladding and dissolved fuel, and candles down after clad failure. The ceramic melt includes molten fuel and molten zirconia from the oxidized cladding that relocate after reaching the rod failure temperature and complete melting. The metallic melting and crust formation starts at 155 min. Ceramic melting starts at around 172 min. Core refilling during pump transient is not enough to cool down liquid melt completely. Here again, no measured data is available, therefore only comparison of the simulation results of different ATHLET-CD versions are shown.

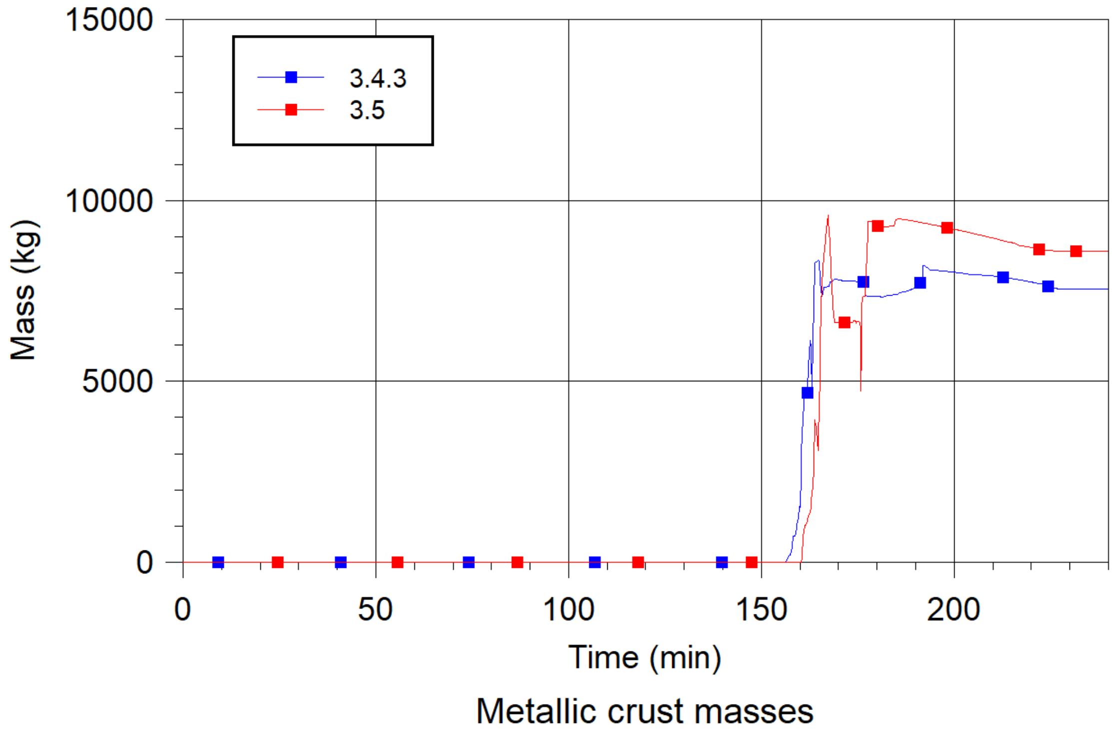

Fig. 5.152 Metallic melt and crust masses of fuel rods calculated with ATHLET-CD versions 3.4.3 and 3.5

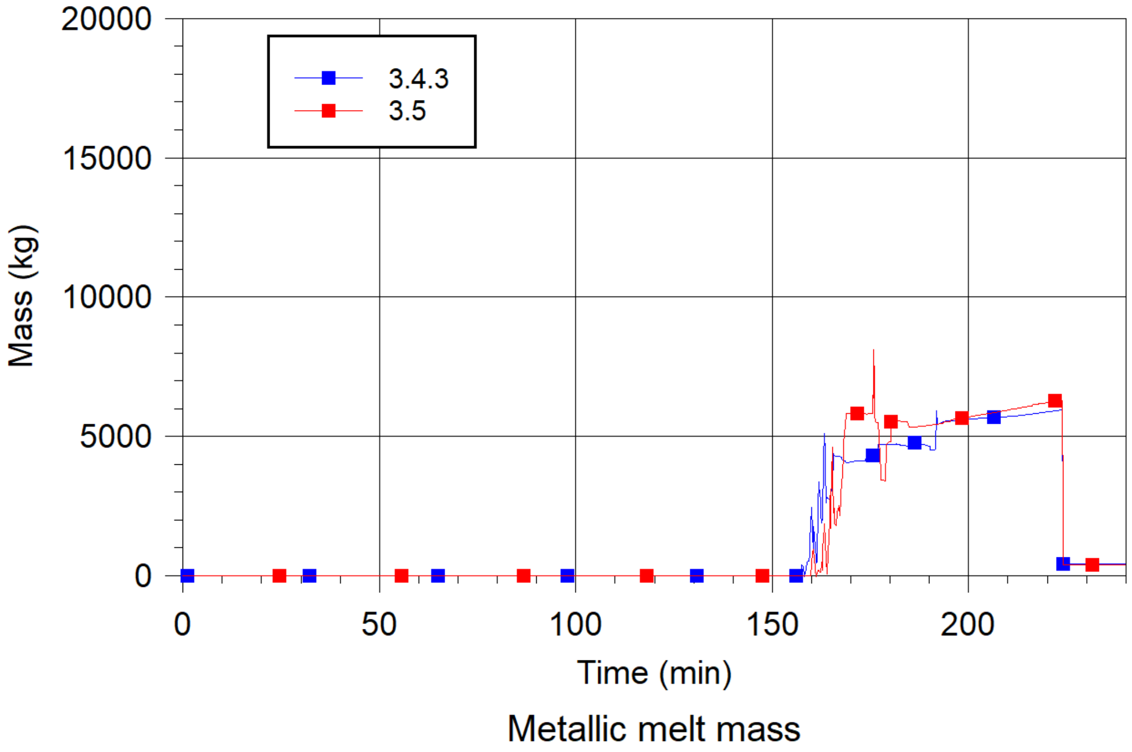

Fig. 5.153 Metallic melt and crust masses of fuel rods calculated with ATHLET-CD versions 3.4.3 and 3.5

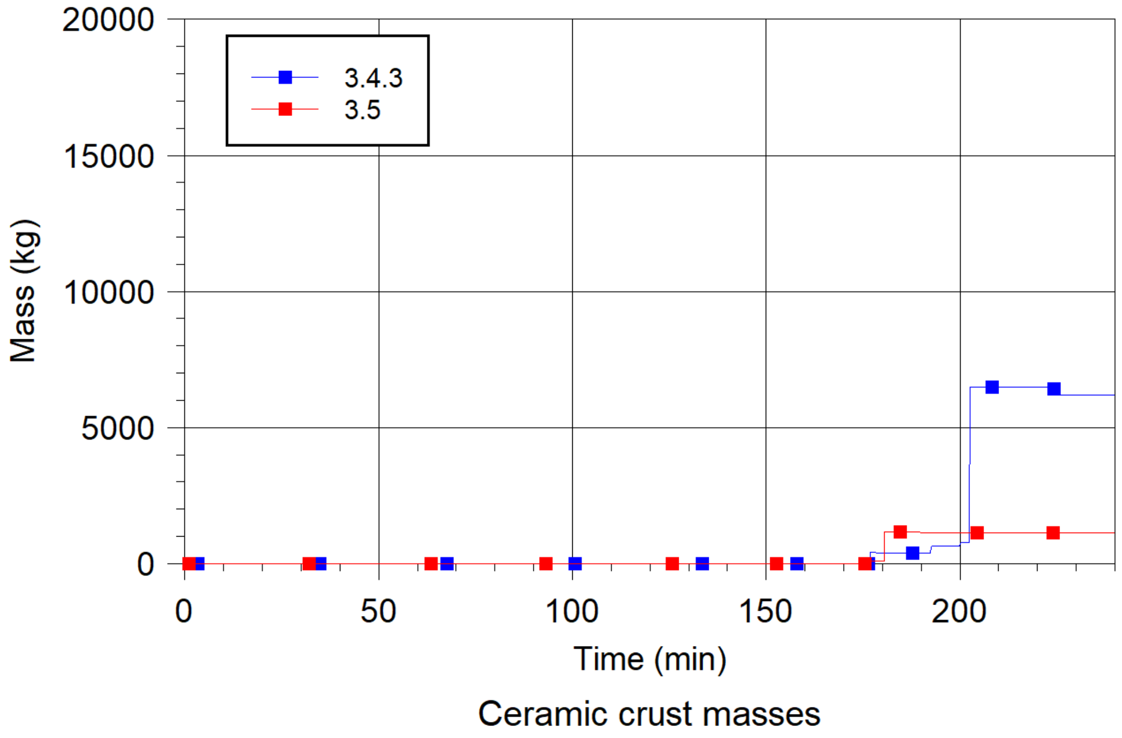

Fig. 5.154 Metallic melt and crust masses of fuel rods calculated with ATHLET-CD versions 3.4.3 and 3.5

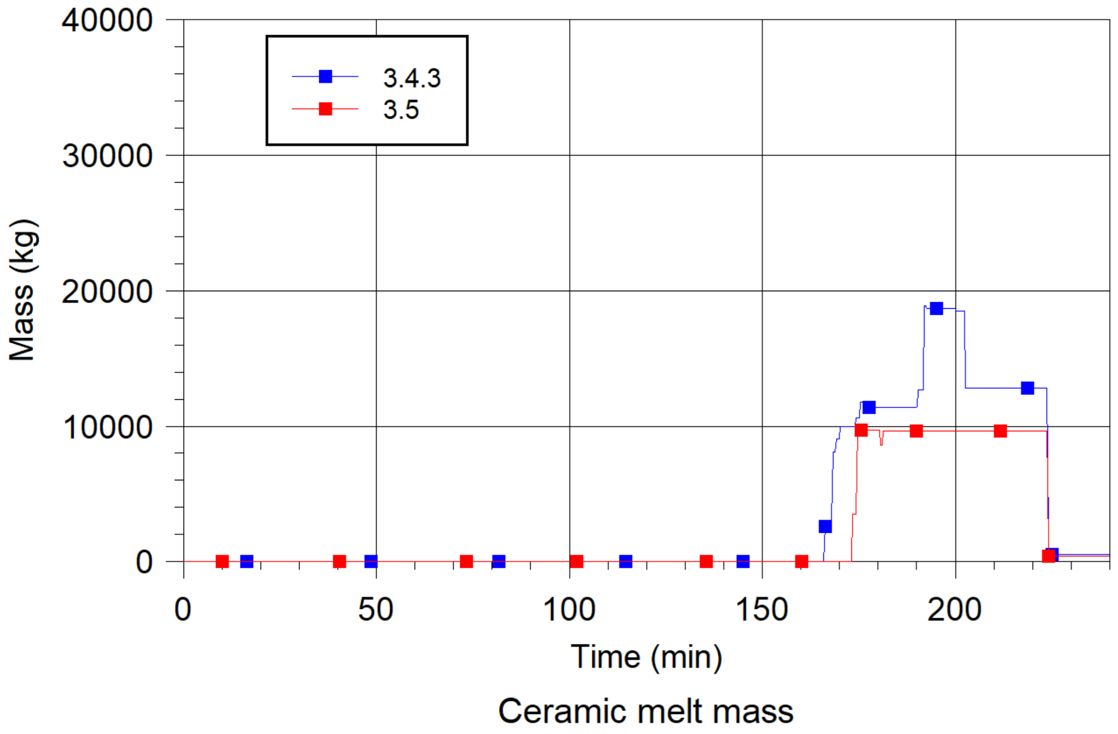

Fig. 5.155 Metallic melt and crust masses of fuel rods calculated with ATHLET-CD versions 3.4.3 and 3.5

At the end of phase 3 liquid melt is relocated into the lower plenum (Fig. 5.156). The calculated values for the relocated masses are between 16 t with 3.5 and 19 t with 3.4.3. Both results reproduce the real data realistically. Note that the results have some uncertainty depending on where the boundary of the lower plenum is defined (and therefore what part of the relocated material is counted to “relocated to lower plenum” and which part is still part of the “core-bypass” region).

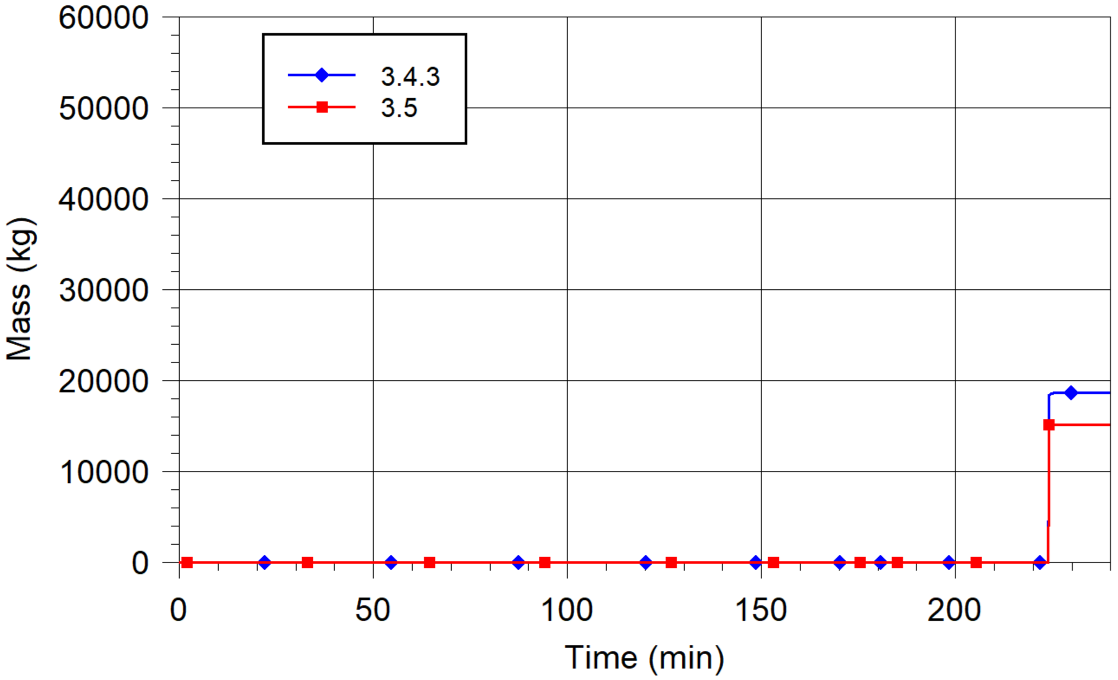

Fig. 5.156 Total relocated mass to lower plenum with ATHLET-CD versions 3.4.3, 3.5

The thermal-hydraulic behaviour in the simulation with ATHLET-CD 3.5 is illustrated in Fig. 5.157 to Fig. 5.160, with the spatial distribution of the water in the primary coolant system and the core status (rod temperatures and relocation profiles) for the time points 174 min and 210 min. The colour scale for water distribution goes from blue (only water) to white (no water) and for the rod temperatures from dark blue (0 K) to light yellow (2500 K). The core status is represented by the four concentric rings of fuel elements, from the central (`ROD1`) to the outer ring (`ROD4`), together with the corresponding groups of control rods.

At the time of pump restart a clear separation of water and steam/hydrogen exists. The water level in the core is about 1.5 m and in equilibrium with the level in the downcomer (Fig. 5.157). Loop A (pressurizer loop) is nearly empty, only about 4000 kg remained in the loop seal. The letdown is connected to the loop seal of this loop (cold leg A1), while the make-up flow feeds into loop B (cold leg B1) between pump and pressure vessel. At this time only control rod melting occurs in all the channels (Fig. 5.158). This melt relocates later to lower core regions, leading to a partial flow channel blockage. The fuel rods do not melt significantly, yet.

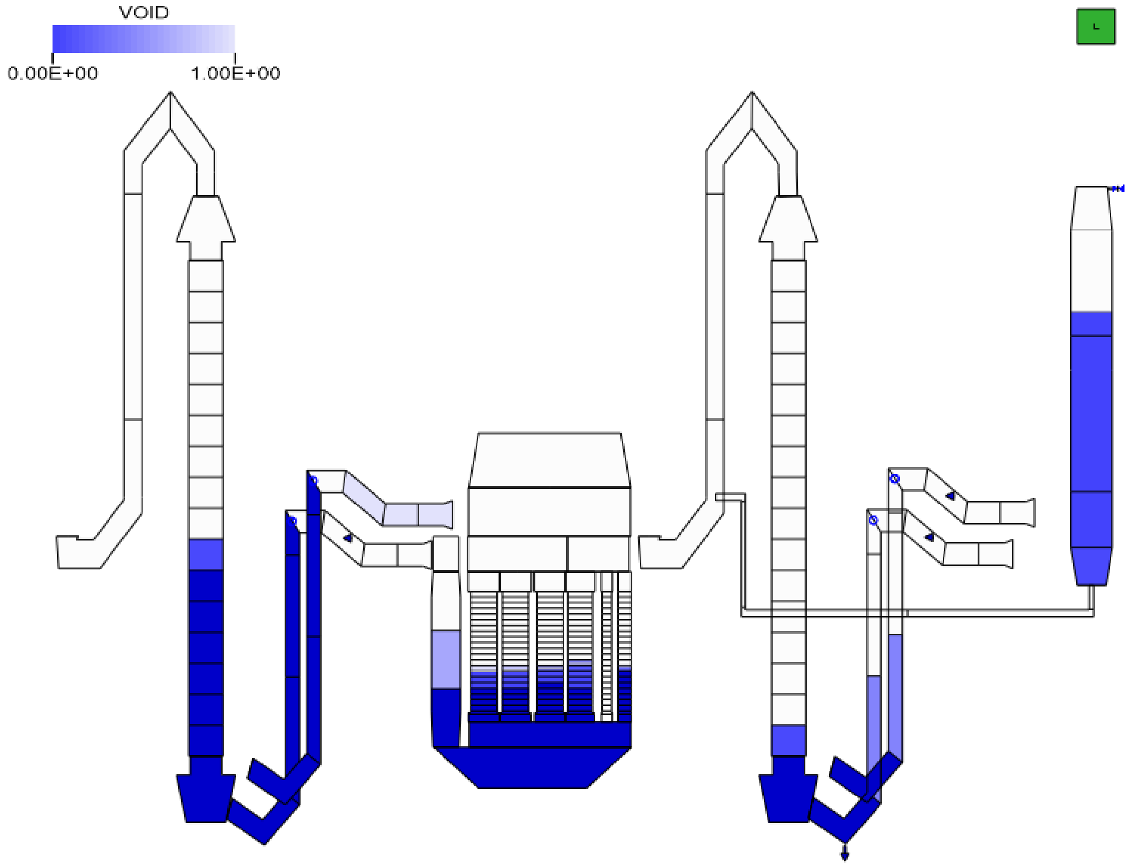

Fig. 5.157 TMI-2 - Plant status at time 174 min – Void fraction in the primary circuit

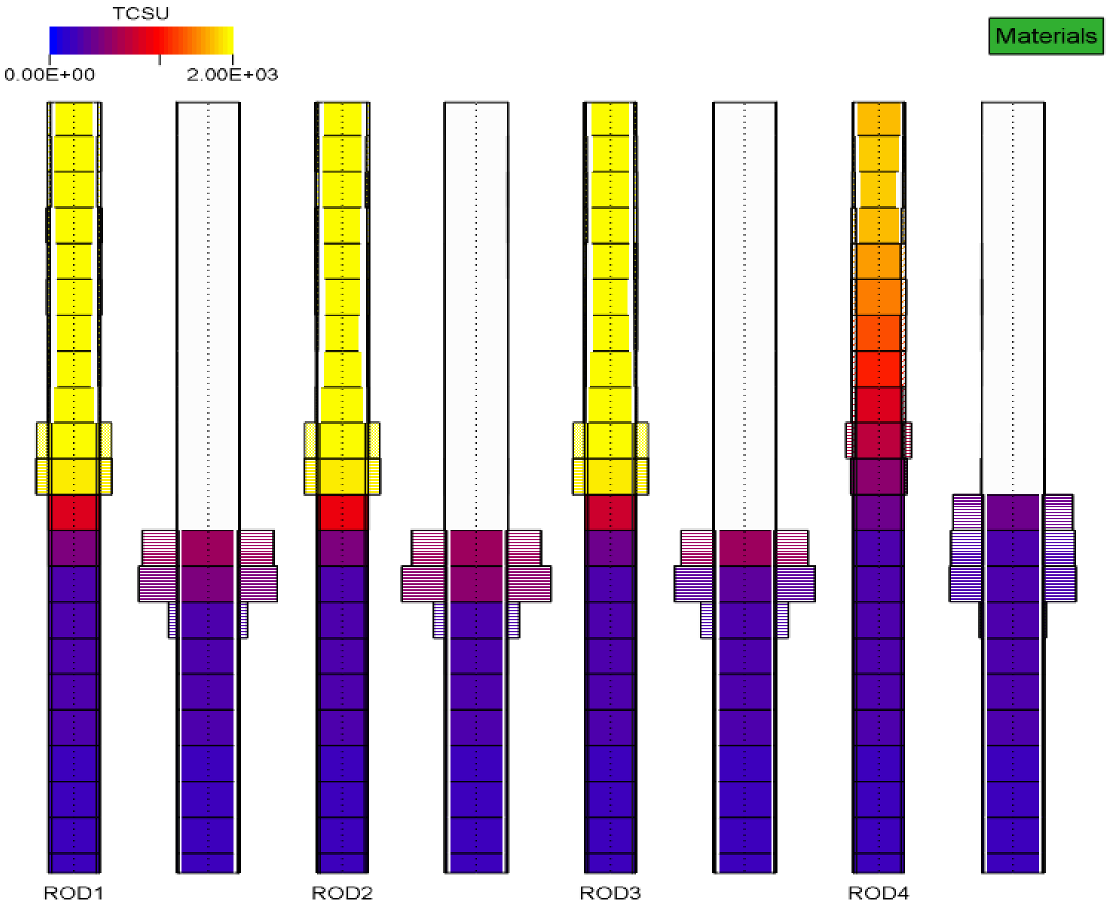

Fig. 5.158 TMI-2 - Plant status at time 174 min – Material distribution and cladding temperatures in the core

With the pump restart, coolant water penetrates the core region mainly through the outer channels and through the core bypass (Fig. 5.159). In this phase, the melt pool could only by cooled from the sides, leading to the formation of a crust of refrozen material, which in turn acts as an additional resistance to further melt quenching. At about 178 min the core water level is high enough to allow water flow into the cavity, partly from the core bypass and upper plenum, partly due to cross flow from the outer core rings. This water flow quenches then the melt pool from the top. After the pump transient the core dries out again. During this phase, molten material relocates into lower core elevations.

With the start of the high-pressure injection the reactor core refills. Core debris accumulates mainly in the lower, central core regions. The total mass of molten materials at this time point (210 min) amounts to around 35 t (Fig. 5.160).

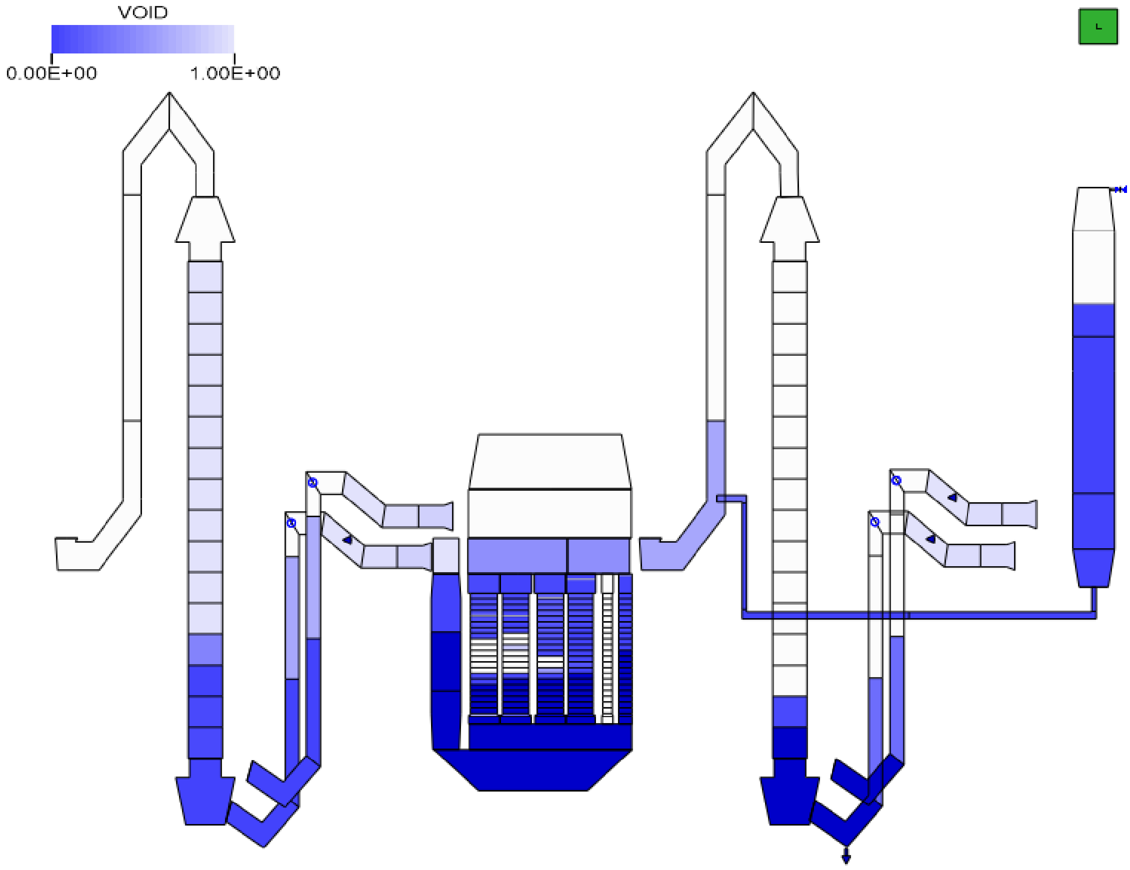

Fig. 5.159 TMI-2 - Plant status at time 210 min – Void fraction in the primary circuit

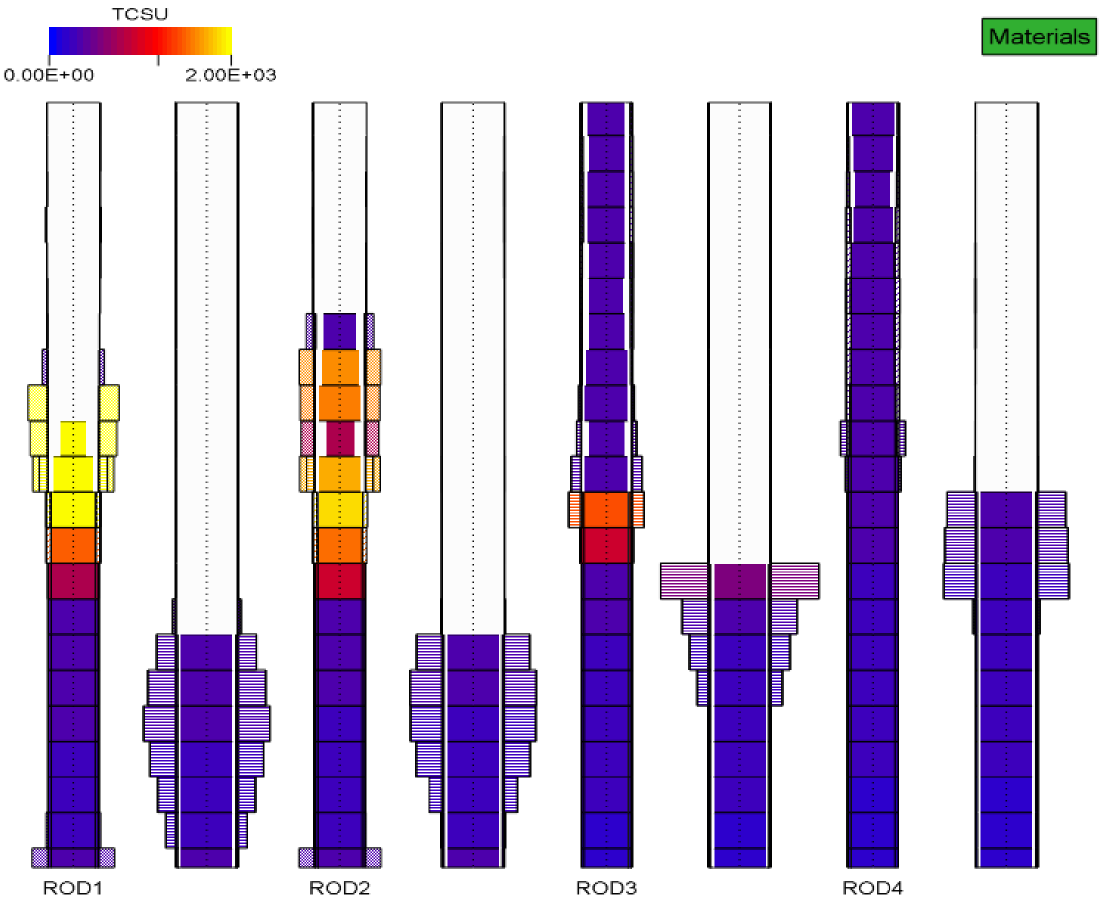

Fig. 5.160 TMI-2 - Plant status at time 210 min – Material distribution and cladding temperatures in the core

This calculation has been performed on a standard GRS PC with INTEL ® CORE ™ i7-7700 processors at 3.60 GHz under the 64-bit operating system Windows 10 Enterprise. It took about 240 min to simulate the first 4 h of the accident with 3.5, which is slower than the 200 minutes with 3.4.3. Note, that the calculation speed depends on multiple factors, so this is just an indication and it not a final conclusion about the performance of the version.

The capabilities of the code ATHLET-CD are demonstrated with this calculation. The first three phases before core slump into the lower plenum were successfully simulated in a reasonable computing time. The calculated pressure history after pump trip, during the pump restart and until core slump is in good agreement with the measured data. The calculated hydrogen generation before the pump restart is in accordance with the deduced value. Contrary to estimates based on the system behaviour, only a relatively small increase of hydrogen production was calculated during the quench phase. The debris bed and melt pool formation may be underestimated due to the lack of a model for embrittlement and relocation of solid fuel fragments. Further model improvements regarding the quenching of degraded core material and the fracture and relocation of solid fuel rods, as well as the consideration of radial melt spreading are necessary to further improve the simulation. No significant differences can be seen between the results in the simulations with 3.4.3 and with 3.5.

6 Summary and overall validation status

This report has briefly summarized the approach to the validation of ATHLET-CD 3.5.0 for application to safety analyses of nuclear facilities and in particular LWR NPP. The overall validation approach for ATHLET-CD 3.5.0 is firmly grounded in international good practice and used well-balanced validation matrices of suitable integral test as well as separate test facilities for PWR, BWR and VVER reactor designs, and the two severe accidents in Three-Mile-Island in 1979 as well as Fukushima-Daiichi in 2011. References to relevant validation calculations with ATHLET-CD going back to the initial release version are given. These demonstrate the overall comprehensive validation status of the code for LWR NPP related scenarios and phenomena. In addition, further validation activities relating spent fuel pools are reported. This is complemented by validation of the coupling of ATHLET-CD to COCOSYS as the code package AC^2.

Exemplary validation calculations demonstrate the quality of the current release version ATHLET 3.5.0 for 13 experiments and one NPP, covering integral test as well as the whole range of phenomena occurring in the plant accident (TMI-2). Moreover, the range of tests presented in this report addresses are large subset of models in ATHLET-CD including the thermal-hydraulic models in ATHLET and most models needed for safety analyses of LWR NPP. The results show that ATHLET-CD 3.5.0 has been successfully validated in all presented cases.

The validation report has also summarized the quality assurance process for the ongoing and systematic validation of ATHLET-CD, which is part of the overall quality assurance processes of GRS for the verification and validation of ATHLET in line with IAEA SSG-2, Rev. 1 /IAEA 19/. This includes important advice and guidance for organisations wanting to perform external validation of ATHLET-CD.

Overall, the available information from validation calculations performed for the release of ATHLET-CD 3.5.0 and the validation status previously reached for ATHLET-CD 3.4.3 allow the following conclusions:

- ATHLET-CD has been successfully validated for safety analyses of LWR reactor designs.
- ATHLET-CD validation has been successfully extended to spent fuel pool applications.

- The validation of ATHLET-CD shows for many cases a better and more stable performance during reflooding of an overheated and (partially) degraded core.
- The model basis for core degradation/melting, oxidation (steam and air ingress), fission product release and transport was validated and shows reasonable predictions in comparison to the measured data for several applications.
- The late phase model AIDA was successfully validated against two cases with different external flooding.
- The simulation of the accident in TMI-2 was successfully performed and the results show in general good agreement to the plant observations.

7 References

/ADR 92/ Adroguer, B., Commande, A., Rongier, C., Mulet, M.: International Standard Problem ISP-28 PHEBUS-SFD B9+ Experiment on the Degradation of a PWR Core Type. Report NEA/CSNI/R(92)17, December 1992.

/ARN 23/ Arndt, S., Band, S., Beck, S., Eschricht, D., Iliev, D., Nowack, H., Reinke, N., Spengler, C., Klein-Heßling, W., Sonnenkalb, M., Weber, G.: COCOSYS 3.2.0 User Manual. Gesellschaft für Anlagen- und Reaktorsicherheit (GRS) gGmbH (GRS), GRS-P-3 / Vol. 1, 2023.

/ASN 17/ ASN: Qualification des outils de calcul scientifique utilisés dans la démonstration de sûreté nucleaire - 1re barrière, Réalisé conjointement avec IRSN. Guide No 28, 20 p., 25. June 2017.

/AUS 10/ Austregesilo, H., Bals, C., Erdmann, W., Horche, W., Krzykacz-Hausmann, B., Pointner, W., Schöffel, P. J., Skorek, T., Weber, S., Wielenberg, A.: Validierung des Rechenprogrammsystems ATHLET / ATHLET-CD, Abschlussbericht. Gesellschaft für Anlagen- und Reaktorsicherheit (GRS) gGmbH (GRS), GRS-Bericht, GRS-A-3522, 557 p., April 2010.

/AUS 19/ Austregesilo, H., Bals, C., Hollands, T., Lovasz, L., Köllein, C., Luther, W., Pandazis, P., Schubert, J.-D., Tiborcz, L., Weber, S.: ATHLET-CD 3.2-User's Manual. Ed.: Gesellschaft für Anlagen- und Reaktorsicherheit (GRS) gGmbH (GRS), GRS-P-4/Vol. 1, 2019.

/BAL 91/ Ball, A., Trambauer, K.: OECD-CSNI International Standard Problem No. 28 - Post test calculations for PHEBUS SFD Test B9+ with ATHLET-CD. GRS-A-, No. 1801, July 1991.

/BAL 17/ Bals, C.: Nachrechnung des Experiments CORA-W2 mit ATHLET-CD 3.1A. Gesellschaft für Anlagen- und Reaktorsicherheit (GRS) gGmbH (GRS), Technische Notiz, TN-MIS-17/2, August 2017.

/BAN 18/ Band, S., Richter, C., Sogalla, M., Sonnenkalb, M.: Unfallablauf- und Quelltermanalysen zu den Ereignissen in Fukushima im Rahmen des OECD/NEA BSAF-Projektes Phase II. Gesellschaft für Anlagen- und

Reaktorsicherheit (GRS) gGmbH (GRS), GRS-Bericht, GRS-485, ISBN 978-3-946607-69-4: Köln, 2018.

/BMUB 15/ Sicherheitsanforderungen an Kernkraftwerke vom 22. November 2012 (SiAnf) as amended 3. März 2015 - Neufassung (BAnz AT 30.03.2015 B2).

/BRO 89/ Broughton, J. M., Kuan, P., Petti, D. A., Tolman, E. L.: A Scenario of the Three Mile Island Unit 2 Accident. Nuclear Technology 87, pp. 34-53, August 1989.

/CLÉ 03/ Clément, B., Haste, T.: Comparison Report on International Standard Problem ISP-46 (PHEBUS FPT1). IRSN, Note Technique Semar 03/021: Cadarache, France, 2003.

/CSN 98/ Consejo de Seguridad Nuclear (CSN): Garantía de calidad de las aplicaciones informáticas relacionadas con la seguridad de las instalaciones nucleares. Guía de Seguridad, No. 10.9, 14 p., 8. October 1998.

/CSNI 89/ Committee on the Safety of Nuclear Installations (CSNI): Thermohydraulics of Emergency Core Cooling in Light Water Reactors, A State-of-the-Art Report by a Group of Experts of the NEA Committee on the Safety of Nuclear Installations. OECD Nuclear Energy Agency (NEA), CSNI Report, No. 161, 1989.

/DRA 05/ Drath, T., Kleinhietpaß, I. D., Unger, H. E., Koch, M. K.: Simulation des TMI-2-Unfalls mit dem Programmsystem ATHLET-CD (Teil 2). Ruhr-Universität Bochum (RUB), LEE-26, June 2005.

/DRA 06/ Drath, T., Hollands, T., Kleinhietpaß, I. D., Wagner, H.-J., Koch, M. K.: Simulation der Bündelversuche QUENCH-07 und -08 mit ATHLET-CD 2.0A/1.1L. Ruhr-Universität Bochum (RUB), LEE-40, July 2006.

/DRA 07/ Drath, T., Hollands, T., Wagner, H.-J., Koch, M. K.: Nachrechnung des "In-Pile"-Versuchs PHEBUS FPT-3 mit ATHLET-CD 2.1A und Bewertung der B_4C-Modellbasis. Ruhr-Universität Bochum (RUB), LEE-43, March 2007.

/EPRI 80/ Electric Power Research Institute (EPRI): Analysis of Three Mile Island-Unit 2 Accident. NSAC-80-1, 1980. ed., 448 p., DOI 10.2172/5598769, 1980.

/ERD 01/ Erdmann, W., Sonnenkalb, M., Steinhoff, F., Trambauer, K.: Validierung des Rechenprogramms ATHLET-CD, Validierung des Rechenprogrammsystems ATHLET/ATHLET-CD. Gesellschaft für Anlagen- und Reaktorsicherheit (GRS) gGmbH (GRS), GRS-A-Bericht, GRS-A-2882, 262 p., August 2001.

/ERD 02/ Erdmann, W.: International Standard Problem No. 46 – PHEBUS FPT1 Test Calculations with ATHLET-CD 1.1I. Gesellschaft für Anlagen- und Reaktorsicherheit (GRS) mbH, Technische Notiz, TN-ERD-02/02, July 2002.

/ERD 04/ Erdmann, W.: Nachrechnung des Experiments PHEBUS SFD-B9+ mit dem Rechenprogram ATHLET-CD Mod 2.0A/1.1K. Gesellschaft für Anlagen- und Reaktorsicherheit (GRS) mbH, Technische Notiz, TN-ERD-02/04, August 2004.

/GAU 11/ Gaus-Liu, X., Miassoedov, A., Cron, T., Foit, J., Fluhrer, B., Schmidt-Stiefel, S., Wenz, T.: Test and simulation results of LIVE-L4 + LIVE-L5L. Ed.: KIT Scientific Publishing, KIT Karlsruhe, KIT-SR 7593, 2011.

/GLA 08/ Glaeser, H.: GRS Method for Uncertainty and Sensitivity Evaluation of Code Results and Applications. Science and Technology of Nuclear Installations, Vol. 2008, pp. 1–7, DOI 10.1155/2008/798901, 2008.

/GOL 86/ Golden, D. W.: TMI-2 Standard Problem Package. Ed.: Idaho National Engineering Laboratory (INL), 1986.

/GRS 21/ Gesellschaft für Anlagen- und Reaktorsicherheit (GRS) gGmbH (GRS): Managementhandbuch Kapitel 2.2.3.5: Softwareentwicklung (TKP 03-05). Managementhandbuch, Kapitel 2.2.3.5, Rev. 2, 2021.

/GRS 24/ Gesellschaft für Anlagen- und Reaktorsicherheit (GRS) gGmbH (GRS): Managementhandbuch Kap. 2.2.3.5: Softwareentwicklung (Teilkernprozess TKP 03-05). Rev. 7, 35 p., 18. November 2024.

/HAG 93/ Hagen, S., Hofmann, P., Noack, V., Schanz, G., Schumacher, G., Sepold, L.: 1993-02_Results of SFD Experiment CORA-13_OECD International Standard Problem 31. Ed.: Kernforschungzentrum Karlsruhe, 194 p., 1993-02;

/HAG 94/ Hagen, S., Hofmann, P., Noack, V., Schanz, G., Schumacher, G., Sepold, L.: Behavior of a VVER-1000 fuel element with boron carbide/steel absorber tested under severe fuel damage conditions in the CORA facility. (Results of experiment CORA-W2). DOI 10.5445/IR/270036514, Karlsruhe, 1994.

/HAS 96/ Haste, T., Adroguer, B., Gauntt, R. O., Martinez, J. A., Ott, L. J., Sugimoto, J., Trambauer, K.: In-Vessel Core Degradation Code Validation Matrix. OECD Nuclear Energy Agency (NEA), NEA/CSNI/R(95)21, 1996.

/HAS 18/ Haste, T., Barrachin, M., Fichot, F., Gueneau, C., Journeau, C., Le Tellier, R., Payot, F., Piluso, P., Pontillon, Y., Le Belguet, E., Torkhani, M., Hózer, Z., Bottomley, D., Hollands, T., et al.: In-Vessel Core Degradation in Water-Cooled Reactor Severe Accidents, State-of-the-Art Report Update (CoreSOAR), 1996-2018. Ed.: NUGENIA, 29. December 2018.

/HER 02/ Hering, W., Homann, C., Lamy, J. S., Miassoedov, A., Schanz, G., Sepold, L., Steinbrück, M.: Comparison and Interpretation Report of the OECD International Standard Problem No. 45 Exercise (QUENCH-06). Report FZKA 6722, Forschungszentrum Karlsruhe GmbH, Karlsruhe, January 2002.

/HOF 10/ Hoffmann, M., Hollands, T., Wagner, H.-J., Koch, M. K.: Simulation der Spätphasenversuche ACRR MP-1 und MP-2 mit dem Programmsystem ATHLET-CD und Bewertung der Spätphasenmodellbasis. LEE-59, May 2010.

/HOF 14/ Hoffmann, M., Bratfisch, C., Kruse, P., Koch, M. K.: Validierung und Interpretation der ATHLET-CD Modellbasis, Abschlussbericht. Ruhr-Universität Bochum (RUB), LEE-88, January 2014.

/HOL 10/ Hollands, T., Hoffmann, M., Kruse, P., Wagner, H.-J., Koch, M. K.: Analyse und Bewertung der ATHLET-CD Modellbasis durch Anwendung auf ausgewählte Experimente, Abschlussbericht. Ruhr-Universität Bochum (RUB), LEE-66, December 2010.

/HOL 15/ Hollands, T., Bals, C.: SIMULATION OF LIVE-L4 WITH ATHLET-CD. 16th International Topical Meeting on Nuclear Reactor Thermal Hydraulics (NURETH-16), 2015.

/HOL 16/ Hollands, T., Austregesilo, H., Bals, C., Buchholz, S., Ceuca, S. C., Hristov, H. V., Langenfeld, A., Pandazis, P., Palazzo, S., Preuß, J., Tiborcz, L., Weber, S.: Validierung von Rechenprogrammen zur Simulation des Reaktorkühlkreislaufs unter Stör- und Unfallbedingungen. Gesellschaft für Anlagen- und Reaktorsicherheit (GRS) gGmbH (GRS), GRS-Bericht, GRS-404, 641 p., 2016.

/HOL 19/ Hollands, T., Lovasz, L., Bals, C.: Status of ATF Modelling in AC2, Proceedings of 2019 International Topical Meeting on Accident Tolerant Fuel, Shenzhen, China. 2019.

/HOL 22a/ Hollands, T., Lovasz, L., Gabrielli, F., Carénini, L., Luxat, D. L., Philipps, J.: STATUS OF MODELING OF FeCrAl CLADDINGS IN SEVERE ACCIDENT CODES AND APPLICATION ON THE QUENCH-19 EXPERIMENT. In: Gabrielli, F., Herranz, L. E., Paci, S. (Eds.): Proceedings of the 10th European Review Meeting on Severe Accidents Research (ERMSAR2022), Severe Accident Research Eleven Years after the Fukushima Accident. ERMSAR, Karlsruhe, Karlsruher Institut für Technologie (KIT), 2022.

/HOL 22b/ Hollands, T., Tiborcz, L.: Simulation of QUENCH-19 and QUENCH-20 with AC^2/ATHLET-CD. In: Steinbrück, M. (Ed.): 27th International QUENCH Workshop. Karlsruhe Institute of Technology (KIT), Karlsruhe Institute of Technology (KIT), Karlsruhe, Germany, 27. - 29. September 2022, DOI 10.5445/IR/1000152245, 2022.

/HOL 23/ Hollands, T., Buchholz, S., Di Nora, V. A., Dünne, N., Eckert, D., Junk, M., Krüssenberg, A., Rezchikova, A., Schöffel, P. J., Wielenberg, A.: ATHLET 3.4.0 Validation. GRS-P-1/Vol. 3 Rev. 8, November 2023.

/HOL 25/ Hollands, T., Buchholz, S., Di Nora, V. A., Dünne, N., Eckert, D., Junk, M., Rezchikova, A., Schöffel, P. J., Wielenberg, A.: ATHLET 3.5.0 Validation. Gesellschaft für Anlagen- und Reaktorsicherheit (GRS) gGmbH, GRS-P-1/Vol. 3 Rev. 10, December 2025.

/IAEA 16/ International Atomic Energy Agency (IAEA): Safety Assessment for Facilities and Activities, General Safety Requirements. IAEA Safety Standards Series, GSR Part 4 (Rev. 1), 163 p., ISBN 978-92-0-109115-4, IAEA: Vienna, 2016.

/IAEA 19/ International Atomic Energy Agency (IAEA): Deterministic Safety Analysis for Nuclear Power Plants, Specific Safety Guide. IAEA Safety Standards Series, SSG-2 (Rev. 1), ISBN 978-92-0-102119-9, IAEA, 2019.

/JAC 00/ Jacquemain, D., Bourdon, S., Braemaeker, A. de, Barrachin, M.: PHEBUS FPT-1 Final Report. Ed.: Institut de Radioprotection et de Surete Nucleaire (IRSN), IPSN/DRS/SA/PDF report SA 1/00. IP00/479, 2000.

/JAC 25/ Jacht, V., Scheuer, J., Schöffel, P. J., Wielenberg, A.: ATHLET 3.5 Programmer's Manual. Gesellschaft für Anlagen- und Reaktorsicherheit (GRS) gGmbH, GRS-P-1 / Vol. 2 Rev. 14, 2025.

/JAN 17/ Jankowski, T., Bratfisch, C., Risken, T., Schittek, U., Koch, M. K.: Validierung und Analyse ausgewählter Modelle sowie der Kopplung der Systemcodes ATHLET-CD und COCOSYS (VAMKoS). Ruhr-Universität Bochum (RUB), LEE-102, January 2017.

/KIR 89/ Kirmse, R.: ATHLET Progress from 11/88 to 6/89. 7. June 1989.

/KIR 94/ Kirmse, R., Bestele, J., Glaeser, H., Höppner, G., Hrubisko, M., Petry, A., Pointner, W., Ringer, F. J., Schickel, H., Steinborn, J., Steinhoff, F., Trambauer, K.: ATHLET-Verifikation anhand von internationalen Integral- und Einzeleffekt-Experimenten, Abschlußbericht. Gesellschaft für Anlagen- und Reaktorsicherheit (GRS) gGmbH (GRS), GRS-A-Bericht, GRS-A-2194, 305 p., October 1994.

/KLE 01/ Kleinhietpaß, I. D., Reinke, N., Koch, M. K., Unger, H. E., Wagner, H.-J.: Analyse des "In-Pile"-Experimentes PHEBUS FPT0 basierend auf Simulationsrechnungen mit dem Programmsystem ATHLET-CD. Ruhr-Universität Bochum (RUB), LEE-, No. 2: Bochum, December 2001.

/KLE 03/ Kleinhietpaß, I. D., Reinke, N., Unger, H. E., Koch, M. K., Wagner, H.-J.: Internationales Standardproblem ISP46: Nachrechnung des Experiments PHEBUS FPT-1 mit ATHLET-CD 1.2D/1.1I. Ruhr-Universität Bochum (RUB), LEE-17, March 2003.

/KLE 04a/ Kleinhietpaß, I. D., Drath, T., Koch, M. K.: Ergebnisse der Nachrechnung und Parameterstudien zum Experiment PHEBUS FPT-2 mit ATHLET-CD. Ruhr-Universität Bochum (RUB), LEE-23, August 2004.

/KLE 04b/ Kleinhietpaß, I. D., Drath, T., Unger, H. E., Koch, M. K.: The Debris Bed Experiment PHEBUS FPT-4 and its Simulation with ATHLET-CD. Ruhr-Universität Bochum (RUB), LEE-25, December 2004.

/KRI 22a/ Krist, F., Bratfisch, C., Koch, M. K.: Analysis and validation of fission product release and distribution by simulations of Phébus FPT1 and FPT3 with AC2. In: American Nuclear Society (ANS) (Ed.): 19th International Topical Meeting on Nuclear Reactor Thermal Hydraulics (NURETH-19). NURETH-19, Brussels, Belgium (virtual), 6. - 11. March 2022, ISBN 9789076971261, 2022.

/KRI 22b/ Krist, F., Bratfisch, C., Koch, M. K.: Analysis of the AC2 model basis regarding the fission product release by simulations of Phébus experiments, KERNTECHNIK 2022. Leipzig, June 2022.

/KUA 89/ Kuan, P., Anderson, J. L., Tolman, E. L.: Thermal Interactions during the Three Mile Island Unit 2 2-B Coolant Pump Transient. Nuclear Technology 87, pp. 977-989, 1989.

/LOV 21a/ Lovasz, L., Bals, C., D'Alessandro, C., Hollands, T., Köllein, C., Austregesilo, H., Pandazis, P., Tiborcz, L., Weber, S.: ATHLET-CD 3.3 Models and Methods. Gesellschaft für Anlagen- und Reaktorsicherheit (GRS) gGmbH (GRS), GRS-P-4/Vol 2 Rev. 0, November 2021.

/LOV 21b/ Lovasz, L., Austregesilo, H., Bals, C., Hollands, T., Köllein, C., Luther, W., Pandazis, P., Schubert, J.-D., Tiborcz, L., Weber, S., Wielenberg, A.: ATHLET-CD 3.3 User's Manual, Input Data Description. GRS-P-4/Vol. 1 Rev. 8, November 2021.

/LOV 23/ Lovasz, L., Pandazis, P.: Simulation of an SBO Accident in a PWR with AC2/ATHLET-CD with and without using ATF Cladding Material. In: Nuclear Society of Slovenia (DJS) (Ed.): Proceedings of the International Conference Nuclear Energy for New Europe 2023. NENE 2023, Portorož, Slovenia, 11. - 14. September 2023, pp. 704.1–704., 2023.

/LOV 25/ Lovasz, L., Austregesilo, H., Bals, C., D'Alessandro, C., Hollands, T., Lu, C., Pandazis, P., Tiborcz, L., Weber: ATHLET-CD 3.5 User's Manual. GRS-P-4/Vol. 1 Rev. 10, 2025.

/MCC 87/ McCormick, D. R., Anderson, J. L., Golden, D. W.: TMI-2 Data Summary Report. Ed.: Idaho National Engineering Laboratory (INL), 1987.

/NEA 87/ OECD Nuclear Energy Agency (NEA): CSNI code validation matrix of thermo-hydraulic codes for LWR LOCA and transients. CSNI Report 132, 70 p., March 1987.

/NEA 89/ OECD Nuclear Energy Agency (NEA) (Ed.): CSNI Standard Problem Procedures. CSNI Report, No 17, 1989.

/NEA 00/ OECD Nuclear Energy Agency (NEA) (Ed.): CSNI International Standard Problems (ISP), Brief Descriptions. NEA/CSNI/, R(2000)5, 2000.

/NEA 01/ OECD Nuclear Energy Agency (NEA): Validation Matrix for the Assessment of Thermal-Hydraulic Codes for VVER LOCA and Transients, A Report by the OECD Support Group on the VVER Thermal-Hydraulic Code Validation Matrix. NEA/CSNI/R(2001)4, 249 p., June 2001.

/NEA 04/ OECD Nuclear Energy Agency (NEA): CSNI International Standard Problem Procedures, CSNI Report No. 17 - Revision 4. NEA/CSNI/R(2004)5, March 2004.

/NEA 15a/ OECD Nuclear Energy Agency (NEA): Ability of Current Advanced Codes to Predict In-Vessel Core Melt Progression and Degraded Core Coolability - Benchmark Exercise on the Three Mile Island-2 Plant - Final Report. NEA/CSNI/R(2015)3, 327 p., June 2015.

/NEA 15b/ NEA NSD CSNI: Ability of Current Advanced Codes to Predict In-Vessel Core Melt Progression and Degraded Core Coolability - Benchmark Exercise on the Three Mile Island-2 Plant - Final Report. Eds.: NEA Nuclear Development (NEA), CSNI, 327 p., 2015.

/NOM 87/ Nomura, Y.: PORV discharge flow during the TMI-2 accident. Idaho National Engineering Laboratory (INL), EGG-TMI-7825, July 1987.

/NRC 05/ U.S. Nuclear Regulatory Commission (NRC): Transient and Accident Analysis Methods. Regulatory Guide, No. 1.203, 52 p., 2005.

/ODA 00/ Odar, F.: Software Quality Assurance Procedures for NRC Thermal Hydraulic Codes. Ed.: U.S. Nuclear Regulatory Commission (NRC), NUREG, NUREG-1737, 1. December 2000.

/OEC 93/ OECD/NEA-CSNI: International Standard Problem ISP-31 CORA-13 Experiment on Severe Fuel Damage. Report NEA/CSNI/R(93)17, July 1993.

/OEC 96/ OECD/NEA-CSNI: International Standard Problem ISP-36 CORA-W2 Experiment on Severe Fuel Damage for a Russian Type PWR. Report NEA/CSNI/R(95)20, 1996.

/ONR 19/ Office for Nuclear Regulation (ONR): Validation of Computer Codes and Calculation Methods. Nuclear Safety Technical Assessment Guide, NS-TAST-GD-042 Revision 4: Bootle, March 2019.

/PAN 18/ Pandazis, P., Hollands, T., Gaus-Liu, X., Miassoedov, A.: Experimental and numerical investigation of molten corium behavior in lower head under external subcooling and boiling conditions. Annals of Nuclear Energy, Vol. 120, pp. 888–895, DOI 10.1016/j.anucene.2018.06.020, 2018.

/PAY 10/ Payot, F., Haste, T., Biard, B., Bot-Robin, F., Devoy, J., Garnier, Y., Gullot, J., Manenc, C., March, P.: PHEBUS FP- FPT3 Final Report. Ed.: Institut de Radioprotection et de Sûreté Nucléaire (IRSN), DPAM/DIR-2011-206, 2010.

/PES 19/ Peschel, J. M., Bratfisch, C., Krist, F., Koch, M. K.: Simulation von Spätphasenphänomenen in DWR mit ATHLET-CD. PSS-TR-4, DOI 10.2314/KXP:1694266222, January 2019.

/POH 99/ Pohl, N., Steinrötter, T., Unger, H. E.: Nachrechnung des "In-Pile"-Experiments PHEBUS FPT0 mit dem Programmsystem ATHLET-CD 1.1D/0.2E. Ruhr-Universität Bochum (RUB), RUB E-I-232, March 1999.

/REI 02/ Reinke, N., Kleinhietpaß, I. D., Drath, T., Koch, M. K., Unger, H. E.: Nachrechnungen der Bündelversuche QUENCH-03 bis -06 mit dem Programmsystem ATHLET-CD 1.2D/1.1I. Ruhr-Universität Bochum (RUB), LEE-14, October 2002.

/ROS 12/ Rostechnadzor: Requirements to Quality Assurance Programs of Nuclear Facilities. Federal Rules and Regulations in the Area of Atomic Energy Use, NP-090-11, 7. February 2012.

/SCH 25/ Schöffel, P. J., Di Nora, V. A., Eckert, D., Junk, M., Cron, D. von der, Weyermann, F. C., Wielenberg, A.: ATHLET 3.5 User Manual. GRS-P-1/Vol 1 Rev. 14, 2025.

/SEP 04/ Sepold, L., Hering, W., Homann, C., Miassoedov, A., Schanz, G., Stegmaier, U., Steinbrück, M., Steiner, H., Stuckert, J.: Experimental and computational results of the QUENCH-06 test (OECD ISP-45). Forschungszentrum Karlsruhe (FZK), FZKA-6664, February 2004.

/STA 22/ Stahlberg, G., Bratfisch, C., Koch, M. K.: Preliminary simulation results of the experiments QUENCH-L3HT and QUENCH-ATF-1 regarding high-temperature oxidation mechanisms using the system code AC2. In: Steinbrück, M. (Ed.): 27th International QUENCH Workshop. Karlsruhe Institute of Technology (KIT), Karlsruhe Institute of Technology (KIT), Karlsruhe, Germany, 27. - 29. September 2022, DOI 10.5445/ir/1000152245, 2022.

/STA 23/ Stahlberg, G., Bratfisch, C., Koch, M. K.: Comparative analyses of the QUENCH experiments L3HT and ATF-1 on high temperature oxidation mechanisms using AC2. In: Furstenau, R., Yang, B.-W., Merzari, E., Hassan, Y., Ninokata, H., Cheung, F.-B., Kelly, J., Bajorek, S., Bolotnov, I., Manera, A., Geradi, C., Pointer, W., Chair, X., Choi, K.-Y., et al. (Eds.): Proceedings of the 20th International Topical Meeting on Nuclear Reactor Thermal Hydraulics (NURETH-20). 20th International Topical Meeting on Nuclear Reactor Thermal Hydraulics (NURETH-20), Washington, D.C, 20. - 25. August 2023, ISBN 978-0-89448-793-4, DOI 10.13182/nureth20-39989, American Nuclear Society: Illinois, 2023.

/STE 98a/ Steinrötter, T., Unger, H. E.: Nachrechnung des Bündelabschmelzexperiments CORA-5 mit dem Programmsystem ATHLET-CD 1.1D/0.2E. Ruhr-Universität Bochum (RUB), RUB E-202, October 1998.

/STE 98b/ Steinrötter, T., Unger, H. E.: Simulation der Depositionsphase des Versuchs STORM SR11 mit dem Programmsystem ATHLET-CD 1.1D/0.2E. Ruhr-Universität Bochum (RUB), RUB E-219, December 1998.

/STE 99/ Steinrötter, T., Pohl, N., Unger, H. E.: Nachrechnung des "In-Pile"-Experiments PHEBUS SFD B9+ mit dem Programmsystem ATHLET-CD 1.1D/0.2E. Ruhr-Universität Bochum (RUB), RUB E-230, March 1999.

/STE 00/ Steinrötter, T., Pohl, N., Unger, H. E.: Nachrechnungen der Siedewasserversuche CORA-17 und CORA-33 mit dem Programmsystem ATHLET-CD 1.2B/1.0A. Ruhr-Universität Bochum (RUB), RUB E-259, September 2000.

/STE 03/ Steinhoff, F., Erdmann, W.: Validierung des Rechenprogrammsystems ATHLET und ATHLET-CD, Teil 2: ATHLET-CD. Gesellschaft für Anlagen- und Reaktorsicherheit (GRS) gGmbH (GRS), GRS-A-Bericht, GRS-A-3156, 296 p., October 2003.

/STE 06/ Steinhoff, F., Austregesilo, H., Bals, C., Erdmann, W., Trambauer, K.: Validierung des weiterentwickelten Rechenprogrammsystems ATHLET/ATHLET-CD, (Teil 2: ATHLET-CD). Gesellschaft für Anlagen- und Reaktorsicherheit (GRS) mbH (GRS), GRS-A-Bericht, GRS-A-3348b, October 2006.

/TEP 12/ Tokyo Electric Power Company (TEPCO): Fukushima Nuclear Accident Analysis Report. 503 p., 20. June 2012.

/TIB 22/ Tiborcz, L., Beck, S., Pandazis, P., Hollands, T.: Validation of the Fission Product Transport Module in the Code System AC² 2021. In: Chung-Hwa Nuclear Society (CHNS), National Tsing Hua University (Eds.): NUTHOS-13 2022 Proceeding Book, 13th International Topical Meeting on Nuclear Reactor Thermal-Hydraulics, Operation and Safety. NUTHOS-13, Hsinchu, Taiwan, 5. - 10. September 2022, N13P148, 2022.

/TMI 92/ TMI-2 Analysis Exercise Task Group: TMI-2 Analysis Exercise Final Report. Ed.: OECD Nuclear Energy Agency (NEA), 662 p., 1992.

/TOL 88/ Tolman, E. L., Kuan, P., Broughton, J. M.: TMI-2 accident scenario update. Nuclear Engineering and Design, Vol. 108, No. 1-2, pp. 45–54, DOI 10.1016/0029-5493(88)90055-6, 1988.

/TRA 90/ Trambauer, K., Ball, A., Bruder, M., Loy, D., Schubert, J.-D., Steinhoff, F., Wahba, A.: Entwicklung und Verifikation des Rechenprogramms ATHLET-SA zur Analyse schwerer Störfälle, - Abschlussbericht -. Gesellschaft für Anlagen- und Reaktorsicherheit (GRS) gGmbH (GRS), GRS-A-Bericht, GRS-A-1689, June 1990.

/TRA 96/ Trambauer, K., Bestele, J.: ATHLET-CD Validierung anhand von Integral und Einzeleffektexperimenten. Gesellschaft für Anlagen- und Reaktorsicherheit (GRS) gGmbH (GRS), GRS-A-Bericht, GRS-A-2420, 167 p., December 1996.

/TRA 01/ Trambauer, K., Schubert, J.-D., Schmitz, B.: Weiterentwicklung von ATHLET-CD für die Spätphase der Kernzerstörung, Abschlussbericht. Gesellschaft für Anlagen- und Reaktorsicherheit (GRS) gGmbH (GRS), GRS-A-Bericht, GRS-A-2907, 109 p., June 2001.

/TRA 04/ Trambauer, K., Austregesilo, H., Bals, C., Cester, F., Deitenbeck, H., Hora, A., Lerchl, G., Schubert, J.-D., Voggenberger, T.: Weiterentwicklung des Rechenprogrammsystems ATHLET/ATHLET-CD, Continued development of the computer code system ATHLET/ATHLET-CD. Gesellschaft für

Anlagen- und Reaktorsicherheit (GRS) gGmbH (GRS), GRS-A-Bericht, GRS-A-3215, July 2004.

/WEB 12/ Weber, S., Austregesilo, H., Hollands, T., Bals, C., Köllein, C.: Aktuelle Arbeiten zur Validierung des Rechenprogramms ATHLET-CD, Validierung von Rechenprogrammen zur Simulation von Stör- und Unfällen im Reaktorkühlsystem. Gesellschaft für Anlagen- und Reaktorsicherheit (GRS) gGmbH (GRS), GRS-A-Bericht, GRS-A-3642, 175 p., February 2012.

/WEB 16/ Weber, S., Bals, C., Austregesilo, H., Band, S., Hollands, T., Köllein, C., Lovasz, L., Pandazis, P., Schubert, J.-D., Sonnenkalb, M.: Weiterentwicklung des Rechenprogramms ATHLET-CD, Abschlussbericht. Gesellschaft für Anlagen- und Reaktorsicherheit (GRS) gGmbH (GRS), GRS-Bericht, Vol. 445, GRS-445, 207 p., ISBN 978-3-946607-27-4, Gesellschaft für Anlagen- und Reaktorsicherheit (GRS) gGmbH: Köln, Garching b. München, Berlin, Braunschweig, October 2016.

/WOL 94/ Wolf, J. R., Rempe, J. L., Stickler, A. L., Korth, G. E.: TMI-2 Vessel Investigation Project Integration Report. Ed.: Idaho National Engineering Laboratory (INL), 1994.